The University Of Sheffield.

University of Sheffield

DOCTORAL THESIS

Investigation of doping contrast in gallium arsenide by scanning electron microscopy and atomic force microscopy

Author:
Ran Guo

First Supervisor:
Thomas Walther
Second Supervisor:
Andrew Maiden

A thesis submitted in partial fulfilment of the requirements for the degree of Doctor of Philosophy

in the

Semiconductor Material and Devices Group

Department of Electronic and Electrical Engineering

May 2th 2023

Declaration of Authorship

I, Ran Guo, declare that this thesis titled, "Investigation of doping contrast in gallium arsenide by scanning electron microscopy and atomic force microscopy" and the work presented in it are my own. I confirm that:

- This work was done wholly or mainly while in candidature for a research degree at this University.
- Where any part of this thesis has previously been submitted for a degree or any other qualification at this University or any other institution, this has been clearly stated.
- Where I have consulted the published work of others, this is always clearly attributed.
- Where I have quoted from the work of others, the source is always given. With the exception of such quotations, this thesis is entirely my own work.
- I have acknowledged all main sources of help.
- Where the thesis is based on work done by myself jointly with others, I have made clear exactly what was done by others and what I have contributed myself.

Signed: Ran Guo

Date: 26/05/2023

Abstract

This thesis is a study of dopant mapping in two dimensions with scanning electron microscopy (SEM) and atomic force microscopy (AFM) methods. The measurements have been applied to both p- and n-doped GaAs staircase structures and a GaAs-based light emission diode with p-i-n device structure.

Although dopant contrast mechanisms have been studied for two decades, the explanation of the SEM image contrast is still difficult as secondary electron (SE) emission is dependent on so many factors. Aiming to get a better understanding of the dopant contrast mechanism, cleaved GaAs (110) surfaces of different samples have been investigated from different points of view: as a function of surface treatment by ion milling or simple mechanical cleavage, the primary electron beam energy from 1kV to 5kV, the electron irradiation dose, the working distance used in SE imaging and the beam induced carbon surface contamination.

It was found that ion milling will reduce the dopant contrast as the ion range and damage from ion milling is larger than the typical SE escape depth. Ion milling is therefore not a good method for surface treatment of p-i-n junctions if quantification of the SE image contrast is to be achieved.

The dopant contrast in SEM is changing as a function of beam energy. When the voltage increases, the contrast will be reduced. At 5kV, the contrast of doped layers almost disappears because of SE yield reduction and charging.

For the SEM, Monte Carlo simulation results for different doping types, concentrations and acceleration voltages have been compared with the experimental SE images taken at different primary beam voltages.

The effect of electron dose on contrast has been investigated by using fixed beam current and changing the condenser aperture size. With higher dose, the contrast will first be reduced and finally, for >4keV, be reversed due to the injection of electrons into the p-doped specimen changing the local electron density of states, hence the work function for SE emission is different at high electron doses.

The effect of working distance has been explored by moving the specimen towards the pole-piece and reducing the working distance. The reverse of contrast of SE images of Si doped GaAs at different working distances suggests that the electrical field around pole piece suppresses the SE emission at larger working distances while for small working distances, more low energy electrons in the n-doped region would be emitted.

The carbon contamination during scanning process has been investigated for initially clean GaAs surfaces. By measuring the carbon contamination layer thickness as function of time by atomic force

microscope, we find that even a few nm of carbon deposited on the surface will reduce the image contrast.

Resistive AFM has been utilized to get current and resistance maps of cleaved GaAs specimens. The influence of effective contact area on the lateral resolution has been discussed and the relationship between resistance and doping concentration relation was obtained for a Be doped p-GaAs sample.

The work function measurements by Kelvin probe force microscopy (KPFM) with the LED sample shows that KPFM is an effective way to map the doping related work function of semiconductor materials.

All these studies have provided an understanding of the dopant contrast in SEM and AFM. With well-established dopant mapping techniques, contributions can be made to the characterisation of electrical and optical devices relevant for the semiconductor industry.

Acknowledgements

First and foremost, I would like to thank my supervisor Dr. Thomas Walther for his invaluable guidance and supervision throughout my project. During my PhD study, he spent countless time with me to discuss my research topic. Besides, he has provided a lot of suggestions for my career development.

I would like to express my deep gratitude to Dr. Shiyong Zhang and Dr. Kristian Groom for providing the sample for investigation. I would also express gratitude to Dr. Ian Ross, Dr. Paul Fry and Dr. Le Ma, who have provided most of the training of the equipment for my research.

I would like to say thanks to Dr. Michael Dixon, Steve Murray, and Yukari Dan for the demonstration of LVSEM voltage contrast. I express my appreciation to Dr Louis Pacheco and Emmanuel Lepleux from CSI Instruments, Paris, for providing the C-AFM data. Besides, I am thankful to Dr. Vladimir Korolkov from Park Systems, Nottingham, for his help of giving me insights into the KPFM working principle.

Also, I would like to say thanks to the members of our group, especially Dr. Xiaoyi Wang and Dr. Veerendra Angadi for their friendship and help in the beginning of my research.

Special thanks go to my friend Dr. Yuchen Liu. He helped me a lot with my life and always encouraged me, making me relax again when I feel anxious. I will always cherish our friendship.

Last but wholehearted thanks go to my parents: Dr. Liyan Guo and Mrs Shan Li for their support to my life.

Contents

1 GaAs: structure, properties, and devices

Nowadays, semiconductor devices play an important role in our lives. Semiconductor devices are widely used in communication systems, automatic control systems, consumer electronics etc. The development of these devices has made our life more convenient and easier. For next generation semiconductor devices, we require faster, higher performance and more energy efficient devices. In order to improve the device perfomance, progress in crystal growth, device manufacturing, device packaging and charaterization techniques are needed. Techniques for 2-D dopant profiling are very essential for the semiconductor industry, and dopant profiling by scanning electron microscopy is promising, as it provides high spatial resolution and is non-destructive if used in top-down geometry.

This section introduces some fundamental principles of semiconductor physics and introduces doping of semiconductors. Then, the p-n junction is discussed as it is the most basic structure and used in all semiconductor devices, in particular metal-oxide-semiconductor field-effect transistors (MOS-FETs). This is followed by a short review of semiconductor device characterization techniques. An outline of this thesis is presented at the end of Chapter1.

1.1 The importance of compound semiconductor devices in modern society

In the past 50 years, the developments of semiconductor device technology have enhanced modern life a lot. Semiconductor devices have been commonly used in consumer electronics, manufacturing equipment, communication systems, automatic control systems, medical care instruments and so on. The next generation of semiconductor devices need to have higher speed and power efficiency.

Compound semiconductors can meet those requirements as they generally have higher electron mobility, higher break-down voltages and direct band-gaps compared to Si based devices. Compound semiconductor based optical devices like photodiodes (PD) and laser diodes (LD) can be used in high-speed information communication systems. Light emitting diodes (LEDs) are widely used in display techniques like monitor screens and illumination systems like solid-state lighting to save energy. High electron mobility devices also can be found in base stations, mobile phones and other telecommunication systems [1].

The market size of semiconductor was $ 513 billion in 2019, and is predicted to reach $726 billion with a growth rate of about 5% by 2027 [2]. The growth of market size is mainly due to the growth of the market for smartphones.

1.2 Band structure

The electrical conductivity of a material represents how easily electric charges will flow through the material. It is different from the ionic conductivity (in liquids) resulting from ionic movement. Thermal conductivity which indicates how good the material conducts heat. High electrical conductivity materials like most metals are called conductors. Materials like many ceramics that do not conduct current are called insulators. Semiconductors have a conductivity between conductors and insulators, which can be adjusted by doping. To understand how the semiconductors conduct electricity, we need to understand the concepts of electronic states and energy bands.

1.3 Atoms and their electronic states

An atom is formed by the nucleus and electrons surrounding the nucleus. Those electrons occupy discrete energy states (also called energy levels) starting from the lowest available energy level up to the highest level. Electrons must obey the Pauli Exclusion Principle as they are Fermions. The Pauli

exclusion principle states that two electrons in an atom or molecule cannot have the same sets of quantum numbers, thus no two electrons can have the same quantum state[3].

To describe an electron in a free atom, we need four quantum numbers. First, the principal quantum number (n) describes the energy state of each electron in an atomic main shell. The azimuthal quantum number (l) is determined by the orbital angular momentum. The magnetic quantum number (m_l) is used to distinguish the orbital in a subshell. The spin quantum number (s) describes the spin momentum of the electron.

Figure 1. 1: Energy states of a hydrogen atom. Three possible transitions to the lowest energy level (n = 1) are also shown [4] below shows the electron transitions and the resulting photon energies of one hydrogen atom.

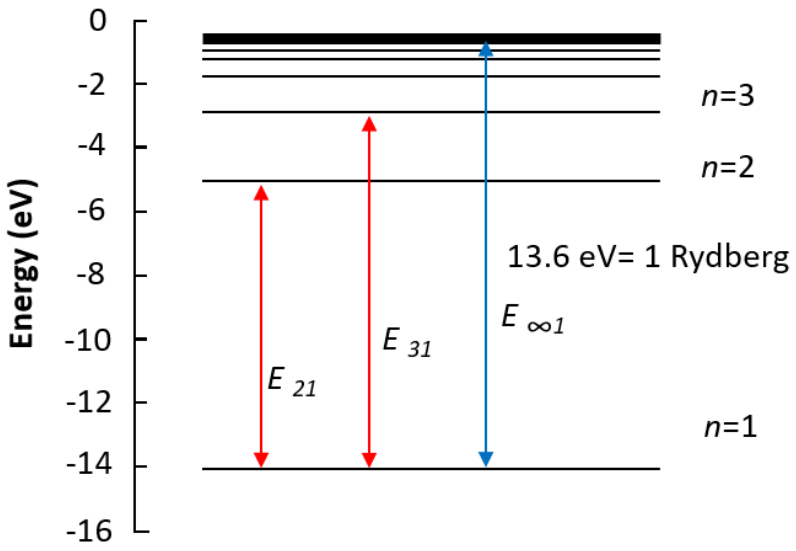

Figure 1. 1: Energy states of a hydrogen atom. Three possible transitions to the lowest energy level (n = 1) are also shown [4].

When crystals are formed with many atoms, the mixing atomic orbitals convert into new hybrid orbitals with certain properties (energies, shapes, etc.) [5]. The combining of the wave functions of atomic orbitals is called hybridization. The total angular momentum J is the sum of total orbital angular momentum and total spin angular momentum vector. So, this gives a new quantum number J for crystals.

$$J = L + S = \sum_i l_i + \sum_i s_i \tag{1.1}$$

1.4 Band structure in crystalline solids

Solids can be identified by the way in which the atoms are placed in the material. Materials without a definite geometrical long range of order (such as glass, plastic, etc.) are amorphous. If atoms of a material are placed in a periodic structure, this kind of material is classified as a crystalline solid. Single crystalline materials are materials with perfect long-range translational order (periodicity). Materials with a high degree of short-range periodicity but no long-range periodicity are called poly-crystalline materials.

The primary material of interest in this thesis is gallium arsenide (GaAs) which is a single crystalline semiconductor. Crystals are categorized by their crystal structure and the underlying lattice. For some

crystals, they have a single atom placed at each lattice point, but for most crystals, they have a combination of atoms called basis associated with every lattice point.

The Bravais lattices, the space groups, face-centred cubic structure and the zinc-blende structure are discussed in the following sections.

1.5 Bravais lattices

Crystal lattices are formed by the lattice translations or by other symmetry operations. Those smallest repeating blocks are called unit cells. A unit cell is described by the lengths of the three axes, *a*, *b*, and *c*, and the three interaxial angles, α, β, and γ. The unit of lengths is Angstroms (Å), and the unit of angles is degrees (°).

The Bravais lattices are the distinct types or configurations in which atoms can be arranged in a crystal. In two-dimensions (2D), there are 5 Bravais lattices, and in three-dimensions (3D) there are 14 Bravais lattices.

The 5 Bravais lattices of 2D crystals are: (1) square lattice, (2) rectangular lattice, (3) centred rectangular lattice, (4) hexagonal lattice and (5) parallelogram lattice.

The 14 Bravais lattices in 3D are grouped into 7 crystal systems: (1) cubic, (2) tetragonal, (3) orthorhombic, (4) hexagonal, (5) monoclinic, (6) trigonal and (7) triclinic [6]. The Bravais lattices are formed by combining one of the seven listed crystal systems with the possible centering types: (1) primitive, (2) base-centred, (3) body-centred and (4) face-centred. As some of the combinations would be equivalent, for example, the monoclinic base-centred lattice is the same as a monoclinic body-centred lattice when shifted by half the unit cell length along crystal axes, there are only 14 Bravais lattice types.

1.6 Space groups

To form the crystal structure of a single-crystalline substance, we use unit cells to repeat the translation symmetry infinitely throughout the crystal. However, sometimes the unit cell contains additional symmetry elements like rotations or screw axes. Under these conditions, we need to describe only one part of it rather than the whole unit cell. In 3D, there are 230 space groups of Bravais lattices with rotation axis, screw axes, mirror planes, glide planes or point of inversions [7]. The diamond and zinc blende lattices belong to cubic group that has constant lattice parameters for all the cell lengths and the angles between the lattice parameters are 90°.

1.6.1 Face-centred cubic lattice and zinc blende crystal structure

There are three kinds of cubic Bravais lattices: simple cubic lattice, the body-centred cubic (bcc) lattice and the face-centered cubic (fcc) lattice, as shown in the Figure 1. 2 below.

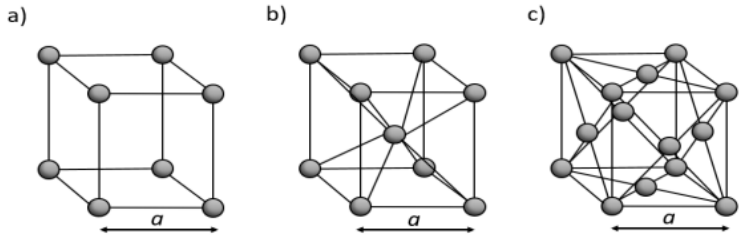

Figure 1. 2: The three types of cubic Bravais lattices. The simple cubic (SC) (a), bcc lattice (b) and the fcc lattice (c) [8].

The diamond lattice is a common crystal structure of elemental semiconductors. Every carbon atom in the lattice has a covalent bond with four neighbouring atoms, forming a tetrahedron. The diamond lattice could be viewed as two fcc lattices, which are displaced from each other by one quarter of the body diagonal. The diamond lattice can be treated as an fcc lattice with a basis of two identical atoms. Silicon (Si) and germanium (Ge) are the typical examples of semiconductors with diamond structure. The cubic zinc-blende structure results from an fcc lattice with a basis made of two different types of atoms as shown in the Figure 1. 3 below.

Many compound semiconductors are comprised of two different elements such as Ga (gallium) and As (arsenic) in gallium arsenide (GaAs). Many other binary compound semiconductors such as indium phosphide (InP) and ternary or even quaternary semiconductors, such as (In,Ga)(As,P), also have the zinc-blende crystal structure.

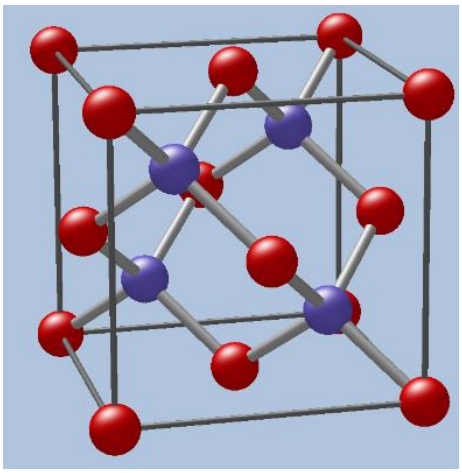

Figure 1. 3: The zinc-blende crystal structure of GaAs. Red atoms are gallium atoms and blue atoms are arsenic atoms. Ga atoms at the corners and faces are shared with neighbouring unit cells, so that each unit cell contains only 4 Ga and 4 As atoms.

1.6.2 Band formation

In solids, when the atoms are brought together, the bonding of electrons between the atoms leads to orbital overlap. However, electrons still need to obey the Pauli Exclusion Principle, which results in the degeneracy of the energy states to be lifted. The discrete energy states in isolated atoms are broadened into bands of electronic states in crystals with many atoms, as shown in Figure 1. 4.

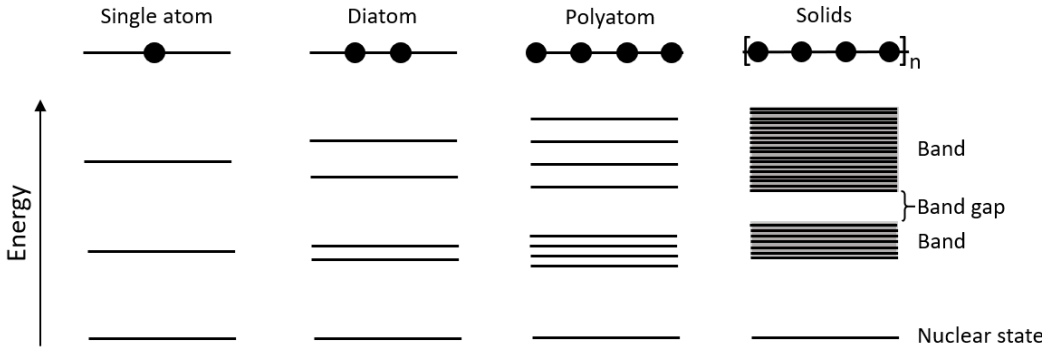

Figure 1. 4: The formation of energy bands [9].

In crystalline materials, many closely spaced energy levels form continuous energy bands. The bands could be regarded as the combination of all the energy states of those electrons surrounding the atom. However, the wave functions of each bound electron overlaps with those from electrons of neighbouring atoms. Due to the Pauli Exclusion Principle, each individual electron state can only be occupied by a spin-up electron and a spin-down electron (forming one orbital), the energy levels of electrons from other orbitals are not the same, so that one obtains a set of closely spaced energy levels, forming an energy band. The energy band model is important in explaining the properties of semiconductor materials and devices. Within the energy band model, we then understand the concept of the energy band-gap and how a partially unfilled band, as shown in Figure 1. 4, becomes conducting.

In this section, we first discuss the free electron model and the Kronig-Penney model. Then we discuss the energy bands of semiconductors and how to obtain a simplified band diagram. The concepts of holes and effective mass are discussed later.

1.6.3 Band filling

The number of electron states in the energy bands is related with the number of atoms in the crystal. Due to the Pauli Exclusion Principle, each energy state can only be occupied by one orbital. Thus, the number of valence electrons in the atoms determines the filling of the bands. How the bands are look like and how the bands are aligned determines the type of the material. This is shown in Figure 1. 5.

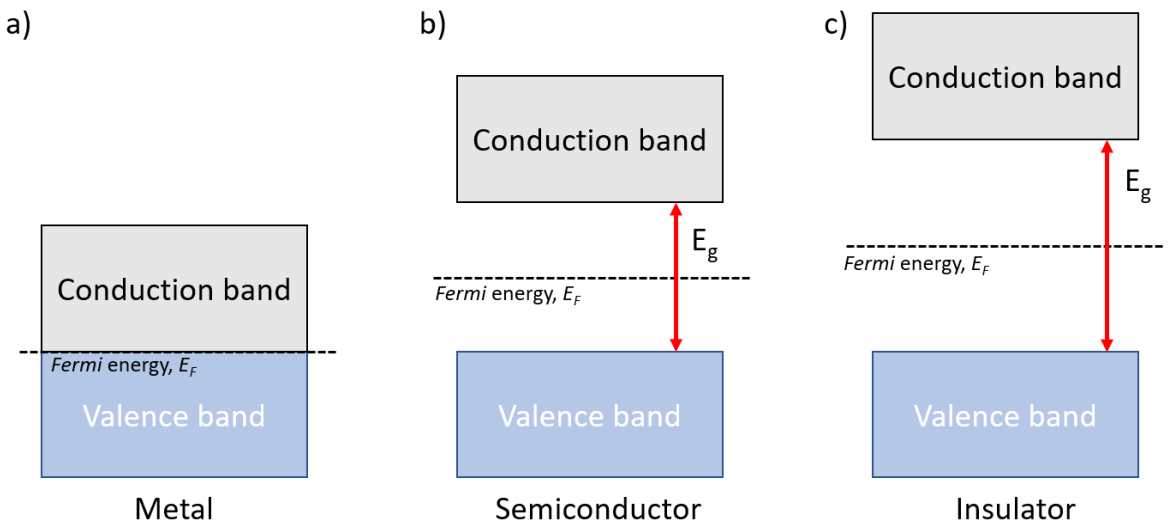

Figure 1. 5: Band occupancies for different types of material. The blue areas represent states that are occupied by electrons and the grey areas are unoccupied levels. The metal will remain conductive down to 0K *as electrons move freely in a partially filled band [10].*

The almost fully filled band is called the valence band (VB) since it is occupied by valence electrons and similarly, the almost empty band is called the conduction band (CB) as electrons are free to move in this band and contribute to the conduction of the material.

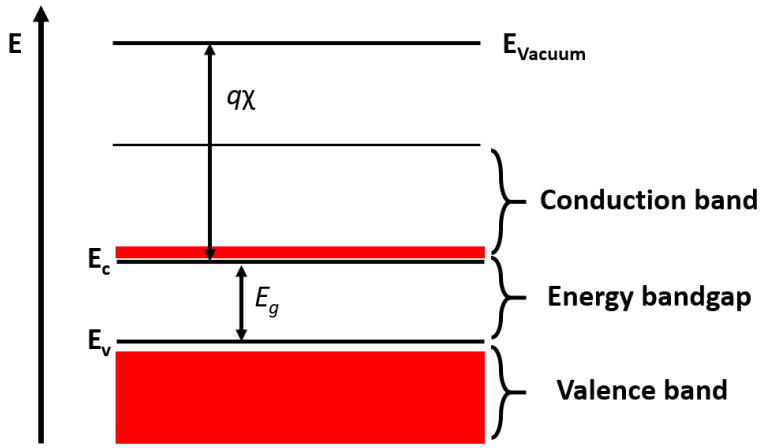

Figure 3. 1

Figure 1. 6: A simple energy band diagram for a semiconductor relative to vacuum level.

The lower line of the conduction band in Figure 3. 1 indicates the bottom edge of the CB and is represented by the symbol E_C. The top of the VB is indicated by the horizontal line with the symbolE_V. The gap between E_C and E_V is called energy band-gap E_g. The distance between E_C and the vacuum level E_{Vacuum} is given by the electron affinity χ multiplied with the charge of an electron, q.

1.6.4 Density of states and Fermi function

The density of states (DOS) for a semiconductor $N_{(E)}$ describes the number of states that can be occupied by the electrons per unit energy and per unit volume, which is important for determining the carrier concentrations and their energy distribution. The probability that a state is actually occupied by an electron is described by the Fermi function $F_{(E)}$.

An increase of the electron energy makes more states available for occupation. There are no states available for electrons to occupy in the band-gap of a pure (intrinsic) semiconductor, meaning the DOS is discontinuous as there are no states available in band-gap. If electrons at the edge of CB want to occupy the states in VB, they must lose a minimum energy of band-gap.

In semiconductors, the degree of freedom for electron movement can be 0, 1, 2 or 3. The dimensions for electron propagation have an influence on the DOS shown in Figure 1. 7. For a three-dimensional semiconductor, the DOS of electrons in the CB is [8]:

$$N_{(E)} = \frac{8\pi}{h^3} m^{*3/2} \sqrt{E - E_c}, \tag{1.2}$$

where *h* is Planck's constant, m^* is the effective electron mass and E_c is the minimum value of CB.

The number of electrons in CB can be expressed as:

$$n = \int_{E_c}^{\infty} N_{(E)} F_{(E)} dE \tag{1.3}$$

The classical free electron model can give a good explanation of electrical and thermal conductivities for metals such as Ohm's Law, however, it fails to distinguish between a metal, a semiconductor and insulators. The probability of an electron occupying an energy level obeys the Fermi-Dirac distribution:

$$F_{(E)} = \frac{1}{e^{(E-E_F)/k_B T} + 1}, \tag{1.4}$$

where E_F is the Fermi level, k_B is the Boltzmann constant and T is the temperature. When the system is at Fermi level, the probability of energy level being occupied is 50%.

The kinetic energy of an electron gas would increase when the temperature is increased, thus some energy states which were empty at absolute 0 K are occupied at finite temperature, leaving some states which were occupied at 0 K vacant. The occupation probability of a state is strongly influenced by the temperature.

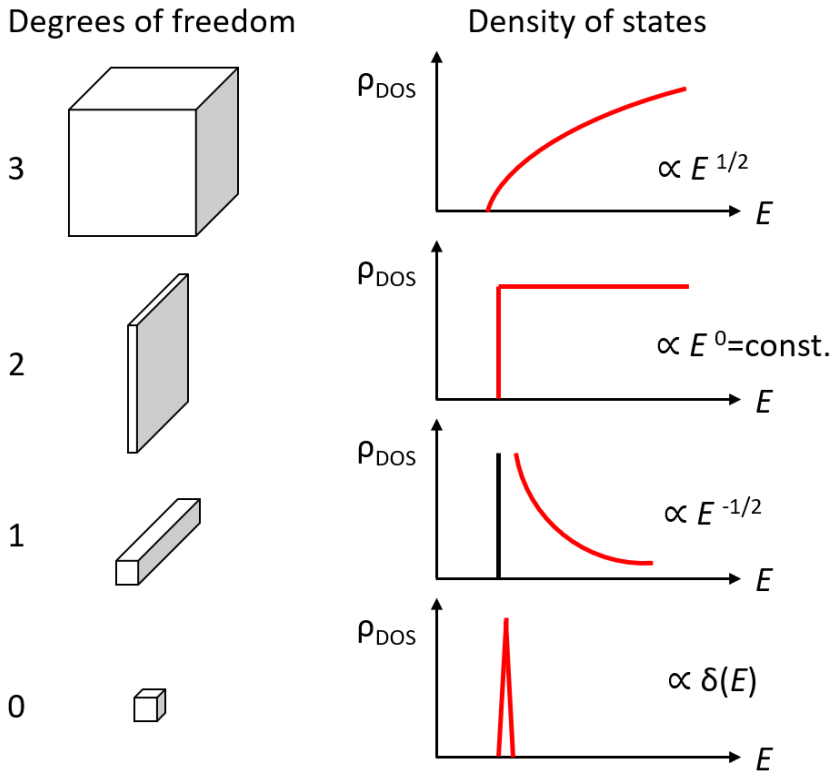

Figure 1. 7: The density of states for semiconductors with different degrees of freedom of electron propagation [11].

1.6.5 The Fermi level

The dashed line in Figure 1. 5 is the Fermi level. At thermodynamic equilibrium, Fermi level could be considered as an energy level that has 50% probability of being occupied. At 0 K, the probability that an electron occupies levels above Fermi energy level E_F is 0, while the probability of an electron occupying levels below E_F is 1. For intrinsic semiconductors without any defects or impurities, E_F is in the middle of valence band and conduction band.

The Fermi energy, E_F, is the maximum energy level associated with a particle that is in thermal equilibrium with the system of interest. This same quantity is called the electro-chemical potential, often denoted by μ, in many thermodynamics textbooks.

1.6.6 Electrons and holes in the material

When a valence electron is activated into the CB, it leaves an unoccupied electron state behind in the VB. This unoccupied electron level in the VB is considered as a quasi-particle of positive mass and positive charge and is called a 'hole'. So, when an electron is promoted from VB to CB, an electron-hole pair is created. This process is shown schematically in Figure 3. 2.

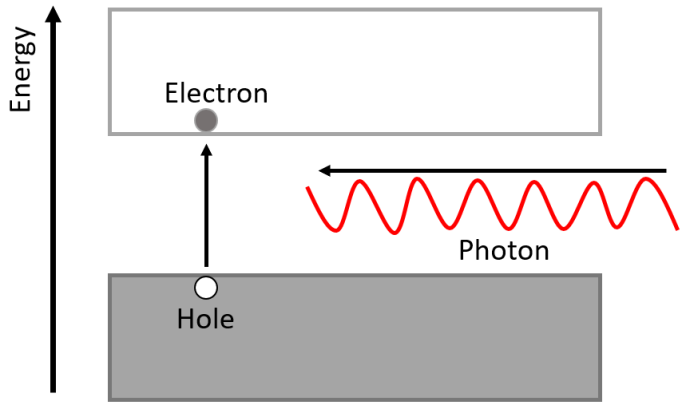

Figure 3. 2

Figure 1. 8: The electron in VB (grey) obtained energy from a photon to move from VB to CB and leaves a hole behind [12].

The band-gap of the semiconductor determines the absorption of light with different wavelengths or photons with different energy. If a photon's energy is smaller than the band-gap of a material, it will pass in the material without being absorbed; if the photon's energy is the same as the band-gap, the photon can promote an electron from VB to CB with ideally no wasted energy so it is absorbed and creates an electron-hole pair; if the photon's energy is larger than the band-gap, the excited electron can release this extra energy as heat before going back to the CB edge.

1.7 Lattice constants and band-gaps

The length of the unit cell of the lattice along a certain direction is called lattice constant. If a compound semiconductor material contains atoms only from the boron group (group III) and the nitrogen group (group V) of the periodic table of chemical elements, it is called a III-V material, such as GaAs, gallium phosphide (GaP) and InAs. Many III-V compound semiconductors have zinc-blende structure, which is cubic and means there is only one lattice constant. Figure 1. 9 shows the band-gaps and corresponding lattice parameters of several III-V semiconductors with the zinc blende lattice (blue) compared to elemental semiconductors with the diamond lattice (orange).

Each semiconductor has its own lattice constant, which is the length of one side of the unit cell of that lattice. For those III-V alloys that have zinc-blende structure (Figure 1. 3), the lattice is cubic and the lattice parameter of these semiconductors is independent of direction. The crystal structure of (Ga,Al,In)(P,As,Sb) alloys is zinc-blende, while the crystal structure of GaN and InN and related alloys is hexagonal [13].

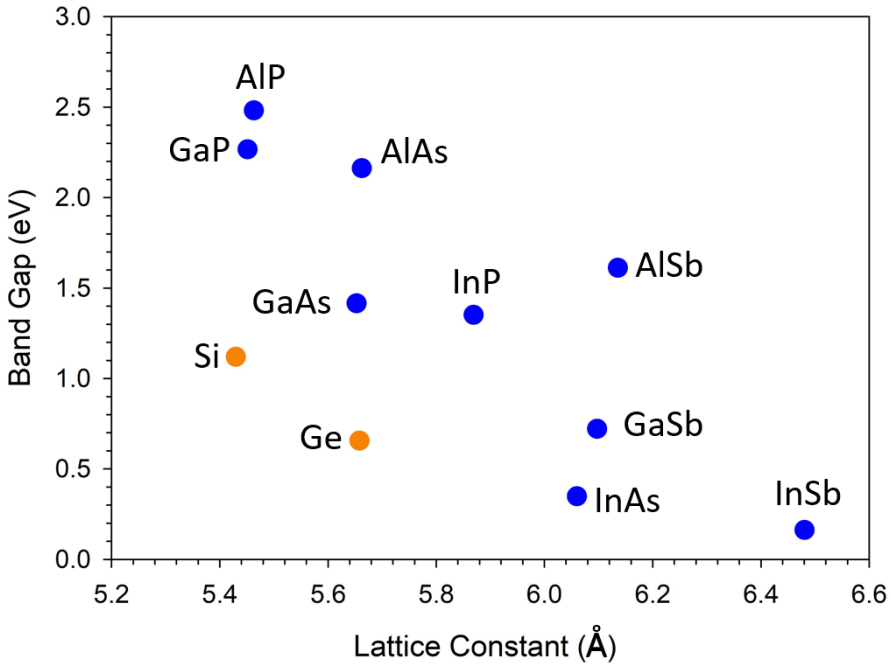

Figure 1. 9: Lattice constant and band-gap of some cubic III-V materials and elemental semiconductors*[14]*.

1.7.1 Temperature dependence of band-gap

When the temperature of a semiconductor is changed, its lattice parameter will be changed too due to thermal expansion. That means, for most semiconductors their band-gap tends to decrease when the temperature is increased. The temperature dependence of the band-gap can be described by using an empirical model [15]:

$$E_g(T) = E_0 - \frac{\alpha T^2}{\beta + T} \qquad (1.5)$$

where E_0 is the band-gap at 0K, α and β are fitting parameters. As temperature can influence the band-gap, some semiconductor devices must be cooled during operation to keep the performance, e.g. power electronic devices [16]. Cooling devices are needed for those semiconductor devices in micro- electronics that use both majority and minority carriers (electron and holes) for example: bipolar transistor, carrier monitoring devices and so on.

1.7.2 Direct band-gap and indirect band-gap

Every electron has its own energy and momentum. In the lattice, the dispersion relation between the momentum and energy of an electron is plotted as in Figure 1. 10. The CB minimum and the VB maximum do not always have the same value of momentum. Therefore, semiconductor materials can be divided into two groups: direct band-gap materials and indirect band-gap materials [8]. If the momentums of VB maximum and the CB minimum are the same, it is called a direct band-gap semiconductor. An electron in the CB wants to lose energy and might emit a photon when coupling with the unoccupied state in the VB.

On the contrary, for an indirect band-gap semiconductor, the VB maximum is not at the same position as the CB minimum. For indirect band-gap material, an electron would have to emit a photon as well as simultaneously generate a lattice vibration called phonon to relax the energy and conserve

momentum. The photon absorption principle is the inverse of photon emission. Figure 1. 10 shows the absorption of direct and indirect band-gap materials. Semiconductor materials with direct band-gaps can efficiently absorb photons of energies above the band-gap and the lifetimes of excited states are shorter, due to the carriers have radiative recombination without phonon interaction. Absorption and emission of photons in indirect band-gap semiconductors are weaker, and carrier lifetimes are much longer.

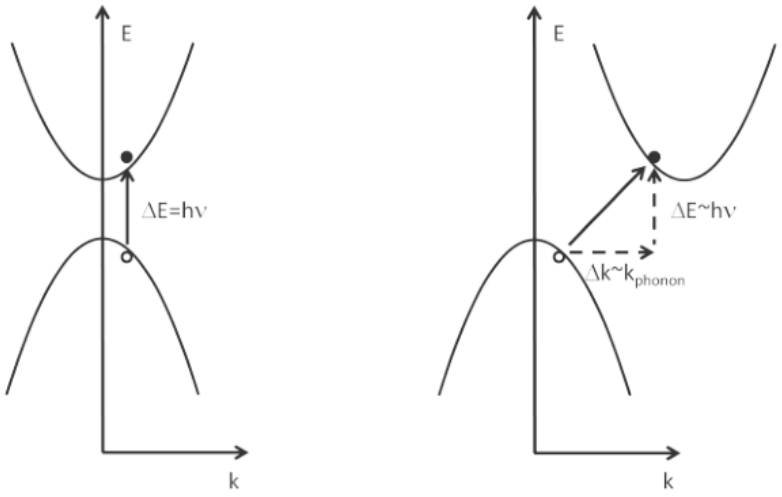

Figure 1. 10 diagram of direct band-gap (left) and indirect band-gap (right) after [17]

If the incident photon energy is larger than the semiconductor band-gap, the photon could be absorbed. An electron in the VB could be promoted into the CB, leaving a hole in VB. In the CB, the electrons will move to the CB edge when the excess energy is thermalized. The electrons can recombine with holes from VB and emit photons with same energy as the band-gap. This is radiative recombination. If defects or impurities are present in the band-gap, the recombination will be influenced by these states. Carriers could recombine at such trap states and release energy by emitting photons or phonons. This mechanism is known as Shockley-Read-Hall recombination [18]. Another non-radiative recombination is Auger recombination; Auger recombination occurs when the energy is transferred to a third electron rather than to a photon.

1.7.3 Alloying

In order to produce semiconductors with different band-gaps, crystal growers will combine different binary materials to form ternary or quarterly III-V alloys. Figure 1. 11 shows the relationship between band-gap and lattice constant of some semiconductors. The discontinuities shown by broken lines are due to the band-gap changing from direct to indirect.

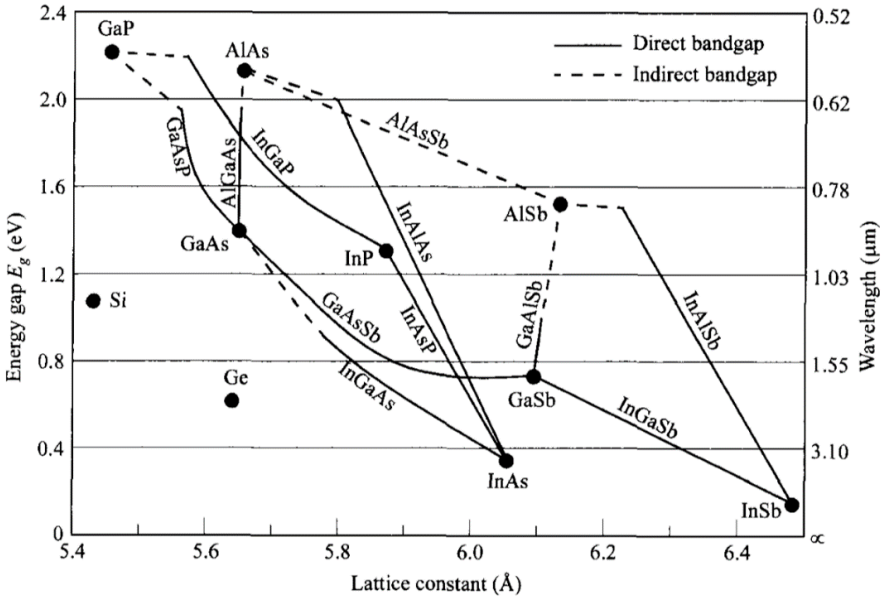

Figure 1. 11. Lattice parameters and band-gap relations for several ternary III-V semiconductor materials [8].

The lattice constant of a ternary alloy can be determined approximately by linear interpolation between the lattice constants of its binary compounds, which is called Vegard's law [19].

The expression is:

$$a_{ABC} = xa_{AC} + (1-x)a_{BC}, \tag{1.5}$$

where a_{ABC}, a_{AC} and a_{BC} are the lattice constant of ternary alloy ABC, the lattice constants of binary compounds AC and BC, respectively and *x* is the fraction of AC component.

The band-gap of alloys can be modelled as [20]:

$$E_{gABC} = xE_{gAC} + (1-x)E_{gBC} + x(1-x)b, \tag{1.6}$$

where E_{gABC}, E_{gAC} and E_{gBC} are the band-gaps of ternary and binary compounds; b is a bowing parameter that depends on the material [21].

1.7.4 Growth

In 1970s, the epitaxial growth of semiconductors has been developed. The first GaAs thin film grown on GaAs substrate was reported in 1971 [22]. There are several epitaxial growth techniques: liquid phase epitaxy (LPE), vapour phase epitaxy (VPE), metal organic vapour phase epitaxy (MOVPE) and molecular beam epitaxy (MBE). As our samples have been grown by MBE, so MBE will be described in the following.

The concept of MBE is quite simple: a lattice substrate is under ultra-high vacuum (UHV ~10^{-10} mbar) condition, high purity elements are thermally evaporated from effusion cells and beams of molecules are adsorbed onto the heated crystalline surface of the substrate. The molecules can move around on the surface before incorporating into the growth front, otherwise they are desorbed from the surface. To grow epitaxial layers with high quality, UHV is necessary as impurities in the chamber can be incorporated easily during the slow growth. The physical deposition process can monitored by Reflection High Energy Electron Diffraction (RHEED) [23].

The substrate temperature must be controlled carefully to enhance the mobility of adsorbed atoms while minimising desorption. The MBE growth temperature is typically lower than in MOVPE as MOVPE needs sufficient temperature to initiate molecular splitting and chemical reactions on the surface, while MBE is a purely physical deposition method. MBE is the state-of-the-art technology for research of new materials as it can prevent the propagation of dislocations within the grown structure by temperature control [24].

1.8 Intrinsic semiconductors

Semiconductors which do not have impurities or only a negligible amount of impurities are called intrinsic. The intrinsic electron density is identical to the hole density as the electron-hole pairs are generated at the same time by thermal activation. The intrinsic carrier concentration is discussed in 1.14.

An intrinsic semiconductor material can also be called undoped semiconductor or i-type semiconductor. The number of carriers in the undoped material is determined by the material itself and not influenced by impurities. When biased, both electrons and hole can move in the material and form small currents.

1.9 Doping of semiconductors

If a small concentration of impurity atoms of different chemical valence substitutes the atoms in a semiconductor crystal lattice, the electrical properties of the semiconductor can be changed. The number of valence electrons of impurity atoms must be different from the atoms being replaced from their lattice site. If the number of valence electrons of an impurity is the same as that of the replaced atom, all electrons will be bonded as before and no excess carriers are generated for conductivity.

When the impurity atom has more valence electrons than the atom which it is going to replace, this kind of atom is called a donor. The donor atom can contribute a free electron to the semiconductor, hence doping with donors will result in n-type semiconductors.

Similarly, if the impurity atom has fewer valence electrons than the atom which will be replaced, this atom is called an acceptor. Acceptors can contribute a free hole for electrical conductivity, hence doping with acceptors will form p-type semiconductors.

Figure 1. 12 below shows the basic chemical bonding of Si. Each Si atom shares four valence electrons with four neighbour atoms in Figure 1. 12(a). (b) and (c) show n-type doping and p-type doping respectively.

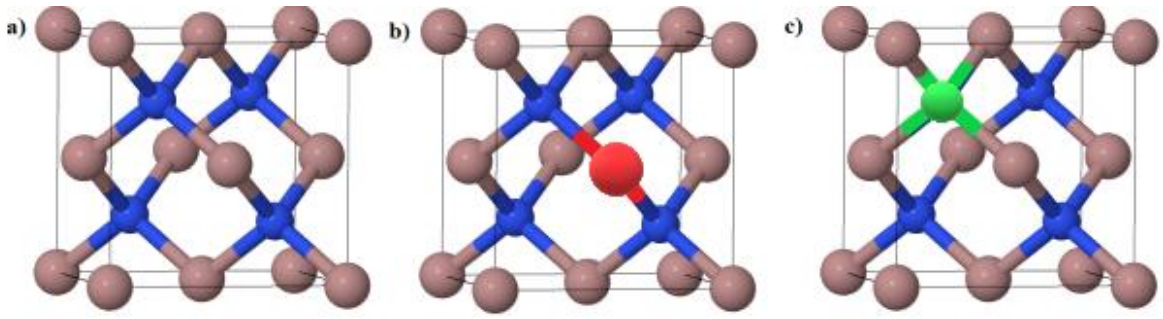

Figure 1. 12: The (a) intrinsic GaAs, Ga atom in blue and As in brown. (b) Be (red) doped p-type GaAs. (c) Si (green) doped n-type GaAs. The size of atom is not scaled with atomic number, it just represents different atoms.

Figure 1. 12 is just the simplest situation for elemental semiconductors. For III-V semiconductors, the doping type also depends on where the dopant atoms replace the atoms in the lattice. Alkaline earth (group II) atoms can be used to replace group III atoms to form a p-type semiconductor. Chromium (group VI) can used as acceptors to replace group V atoms from their site to get n-type semiconductors.

Some atoms (like Si) from the carbon group (group IV) can be used as either donor or acceptor, depending on whether the atoms replace group III or group V atoms in the semiconductor crystal. During MBE growth, Si dopants typically produce n-type GaAs, though they can also form p-type GaAs [25]. To get good quality GaAs epi-layers, the As flux is larger than the Ga flux to achieve As-stabilized growth conditions on which a *(2×4) or c(2×8)* pattern can be obtained by RHEED. When Si is incorporated into GaAs, if the Si atoms replace Ga atoms, they act as donors, while if Si atoms replace As atoms, they act as acceptors. At low temperature ($T \leq 700℃$), Si will prefer to sit on As sites, while at high temperature ($T \geq 900℃$), Si atoms tends to sit at Ga sites and becomes donors. Besides, when As flux is high, Si atoms prefer to replace Ga atoms and act as donors[26]. For the sample used in this research, the GaAs substrate surface is (100), the Si atoms are preferentially incorporated in Ga sites as the surface has excess As atoms relative to Ga atoms, thus Si dopants behave like donors in GaAs (100). If the growth direction is (111) and surface structure (111)A, the Ga atoms have 3 bonds to the surface while As only has 1, then Si atoms will replace As easier and produce p-type GaAs.

In this thesis, beryllium (Be) atoms are used for p-type GaAs doping and silicon (Si) atoms are used for n-type doping. Adding a dopant into GaAs introduces extra energy levels within the band gap. The energy levels are close to the CB in n-type GaAs, and the energy levels are close to the VB in p-type GaAs. Figure 1. 13 shows the schematic diagram of donor and acceptor induced states in n-type and p-type material.

By introducing donors with 5 outer electrons, n-type semiconductors have excess electrons which are not bonded, and these electrons can be moved into conduction band with relatively small energy. Similarly, when doping with trivalent acceptors, free holes are generated, their energy level can be occupied easily by electrons from the valence band.

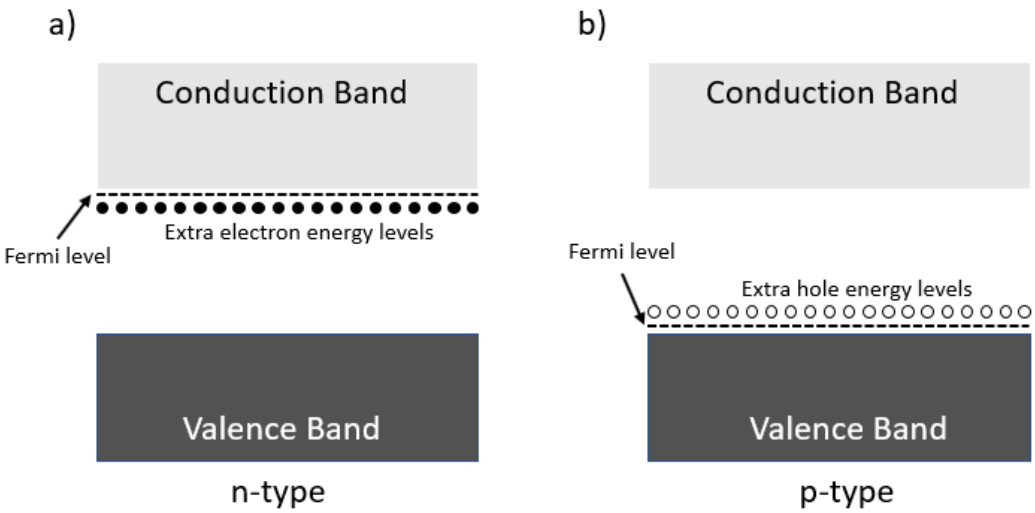

Figure 1. 13: band diagrams of n-type and p-type semiconductors.

1.10 Conductivity

The momentum of a free electron is:

$$\vec{p} = mv = \hbar k \tag{1.7}$$

where ***k*** is the wave vector. In a constant electric field ***E*** and magnetic field ***B***, the force on an electron is:

$$F = m\vec{a} = m\frac{d\vec{v}}{dt} = \hbar\frac{dk}{dt} = -eE - e\vec{v}B \tag{1.8}$$

where $-e$ is the charge of an electron. If $B = 0$, we get

$$k(t) - k(0) = \frac{-eEt}{\hbar} \tag{1.9}$$

In condensed matter physics, the Fermi surface is the surface in reciprocal space (***k*** space) which separates unfilled orbitals from filled orbitals at 0 K [27]. In some semiconductors, like GaAs, the surface is spherical, so the Fermi surface can also be called Fermi sphere. This equation shows that the displacement of an electron gas that fills the Fermi sphere centred at the origin of ***k*** space is moved to a new centre after time *t* when an electric field is applied. Due to collisions of electrons with impurities, lattice defects and phonons, the displaced sphere may be maintained in a steady state in an electric field [28]. If the collision time is τ, the incremental velocity is

$$v = -eE\tau/m \tag{1.10}$$

According to Ohm's Law, if *n* electrons move in a constant electrical field ***E***, the current density is:

$$\vec{j} = nq\vec{v} = ne^2\tau\boldsymbol{E}/m \tag{1.11}$$

1.10.1 Electron conductivity

The electrical conductivity *σ* is defined by $\vec{j} = \sigma\boldsymbol{E}$, so

$$\sigma = \frac{ne^2\tau}{m} \tag{1.12}$$

The electrical resistivity *ρ* is defined as the reciprocal of the conductivity *σ*.

Then for semiconductors, conduction by both electrons and holes needs to be taken into consideration, so the electrical conductivity becomes:

$$\sigma_{semi} = \frac{n_e e^2\tau_e}{m_e{}^*} + \frac{p_h e^2\tau_h}{m_h{}^*} = e[\mu_e(T)n_e(T) + \mu_h(T)p_h(T)] \tag{1.13}$$

where $\mu_e(T)$ and $\mu_h(T)$ are the mobility of electrons and holes, n_e and p_h are the volume densities of electrons and holes, respectively, $m_e{}^*$ and $m_h{}^*$ are the effective masses of electrons and holes. For n-doping semiconductor, the conductivity contribution from minority holes is very small and sometimes can be ignored, thus $\sigma_n \approx ne\mu$. Similarly, for p-doping material, its conductivity is $\sigma_p \approx pe\mu$.

1.10.2 Mobility

From equation 1.13, we notice that both carrier concentration and relaxation time are temperature dependent factors, and that means the resistivity is a temperature dependent parameter.

First, we consider the effects of temperature on charge carrier mobility of a doped semiconductor.

For an ideal crystal lattice, we need to consider lattice scattering by phonons. The lattice vibrations cause the mobility to decrease with increasing temperature.

However, even in the absence of crystal defects, ionized impurities will act as traps interacting with charge carriers. When the temperature is low, carriers move slower than at high temperature, which means they have more time to interact with charged impurities. So, in contrast to lattice scattering, impurity scattering makes mobility decrease when temperature decreases.

Neutral impurity scattering and effects of hole-hole or electron-electron scattering are not as important as lattice scattering and ionized impurity scattering[8]. For neutral impurity scattering, it makes the mobility decrease when temperature decreases, while h-h or e-e scattering is not influenced by carrier concentration or temperature. [29]

For n-doping, there is an empirical relationship between electron mobility and donor concentration N_D [30]:

$$\mu_e = \mu_L/[1+\sqrt{N_D/10^{17}cm^{-3}}] \tag{1.14}$$

where μ_L is the electron mobility due to phonon scattering, for GaAs at 300K, $\mu_L = 10000$ cm^2/V sec.

In 2000, Rezazadeg published the following empirical low-field mobility model for III-V material [31]:

$$\mu_{LF}(N,T) = \mu_{min} + \frac{\mu_{max}(300K)\left(\frac{300K}{T}\right)^{\theta_1} - \mu_{min}}{1+\left[\frac{N}{N_{ref}(300K)(T/300K)^{\theta_2}}\right]^{\lambda}} \tag{1.15}$$

where μ_{min}, μ_{max}, λ, θ_1,θ_2, N_{ref} can be found in the Table 1 below [31].

Material	Electron or hole	μ_{max} (300 K) (cm^2/V s)	μ_{min} (cm^2/V s)	N_{ref} (300 K) cm^{-3}	λ	θ_1	θ_2
AlAs	electron	400	10	5.46×10^{17}	1.00	2.1	3.0
	hole	200	10	3.84×10^{17}	0.488	2.24	3.0
GaAs	electron	9400	500	6.0×10^{16}	0.394	2.1	3.0
	hole	491.5	20	1.48×10^{17}	0.38	2.2	3.0
InAs	electron	34 000	1000	1.1×10^{18}	0.32	1.57	3.0
	hole	530	20	1.1×10^{17}	0.46	2.3	3.0
InP	electron	5200	400	3.0×10^{17}	0.47	2.0	3.25
	hole	170	10	4.87×10^{17}	0.62	2.0	3.0
GaP	electron	152	10	4.4×10^{18}	0.80	1.60	0.71
	hole	147	10	1.0×10^{18}	0.85	1.98	0.0
$Al_{0.3}Ga_{0.7}As$	hole	240	5	1.0×10^{17}	0.324	⋯	⋯
$In_{0.52}Al_{0.48}As$	electron	4800	800	3.0×10^{16}	1.10	⋯	⋯
$In_{0.53}Ga_{0.47}As$	electron	14 000	300	1.3×10^{17}	0.48	1.59	3.68
	hole	320	10	4.9×10^{17}	0.403	1.59	⋯
$In_{0.49}Ga_{0.51}P$	electron	4300	400	2.0×10^{16}	0.70	1.66	⋯
	hole	150	15	1.5×10^{17}	0.80	2.0	⋯

Table 1. Fitting parameters for GaAs in the low-field mobility model [31]

The total mobility is then approximated by combining all the different scattering events using Matthiessen's Rule [32]. When lattice scattering dominates, the mobility decreases with temperature, while when impurity scattering dominates, the mobility increases with temperature. In practices, only lattice scattering dominates at room temperature, observing impurity scattering needs very low

temperature as carriers move slower and have more time to interact with impurities at low temperature.

$$\frac{1}{\mu} = \frac{1}{\mu_{impurities}} + \frac{1}{\mu_{lattice}} + \frac{1}{\mu_{defects}} + \cdots \tag{1.16}$$

1.11 Doping concentration dependence of semiconductor conductivity

At temperature T, if we denote the density of allowed states as $g_c(E)$ in the conduction band (CB) and $g_v(E)$ in the valence band (VB), n_c as the number of electrons per unit volume in CB, and p_v as the number of holes in VB, one gets [33]

$$n_c(T) = \int_{E_c}^{\infty} g_c(E) \frac{1}{e^{(E-\mu)/k_BT}+1} dE, \tag{1.17}$$

$$p_v(T) = \int_{\infty}^{E_v} g_v(E)[1 - \frac{1}{e^{(E-\mu)/k_BT}+1}]dE$$

$$= \int_{-\infty}^{E_v} g_v(E)[\frac{1}{e^{(\mu-E)/k_BT}+1}]dE. \tag{1.18}$$

where E_c is the energy at the bottom of CB, E_v is the energy at the top of VB, n_c and p_v are only affected by the chemical potential or Fermi level μ at given temperature.

In Equations (1.16 and 1.17), for a semiconductor at room temperature:

$$E_c - \mu \gg k_BT, \tag{1.19}$$

$$\mu - E_v \gg k_BT. \tag{1.20}$$

Thus, we can simplify the statistical factors to substitute the Fermi distribution by the Boltzmann distribution in Equations (1.17 and 1.18):

$$\frac{1}{e^{(E-\mu)/k_BT}+1} \approx e^{-(E-\mu)/k_BT}, \; E > E_c; \tag{1.21}$$

$$\frac{1}{e^{(\mu-E)/k_BT}+1} \approx e^{-(\mu-E)/k_BT}, \; E < E_v. \tag{1.22}$$

Thereby, Equations (1.17) and (1.18) reduce to

$$n_c(T) = N_c(T)e^{-\beta(E_c-\mu)}, \tag{1.23}$$

$$p_v(T) = P_v(T)e^{-\beta(\mu-E_v)}, \tag{1.24}$$

where $\beta = 1/k_BT$, so

$$N_c(T) = \int_{E_c}^{\infty} g_c(E)\, e^{-\beta(E-E_c)} dE, \tag{1.25}$$

$$P_v(T) = \int_{-\infty}^{E_v} g_v(E) e^{-\beta(E_v-E)} dE. \tag{1.26}$$

The level densities can be taken to be [33]:

$$g_{c,v}(E) = \sqrt{2|E - E_{c,v}|}\frac{m_{c,v}^{3/2}}{\hbar^3\pi^2} \tag{1.27}$$

where the integrals in equations (1.25) and (1.26) then give

$$N_c(T) = \frac{1}{4}\left(\frac{2m_c k_B T}{\pi\hbar^2}\right)^{3/2}, \tag{1.28}$$

$$P_v(T) = \frac{1}{4}\left(\frac{2m_v k_B T}{\pi\hbar^2}\right)^{3/2}. \tag{1.29}$$

Here, m_c is the effective mass of an electron in the CB and m_v is the effective mass of a hole in the VB. To calculate the electron density n_c and hole density p_v, we need to know the value of Fermi level μ. However, multiplying these two densities, their product is independent of μ:

$$n_c p_v = N_c P_v e^{-E_g/k_B T} = n_i^2 \tag{1.30}$$

where E_g is the band-gap of the material. For intrinsic semiconductors, the electrons in CB only come from VB, leaving holes after they were excited, thus $n_c = p_v \equiv n_i$. The value of n_i is the square root of Equation (1.30):

$$n_i(T) = [N_c(T)P_v(T)]^{1/2} e^{-\frac{E_g}{2k_B T}} \tag{1.31}$$

The chemical potential μ in Equations (1.23) and (1.24) for the intrinsic case can be provided [33]:

$$\mu_i = \frac{1}{2}(E_c + E_v) + \frac{3}{4}k_B T \ln\left(\frac{m_v}{m_c}\right). \tag{1.32}$$

The temperature dependence of intrinsic carrier concentration is given by [28]

$$n_i(T) = 2\left[\frac{2\pi kT}{h^2}\right]^{\frac{3}{2}} (m_e{}^* m_h{}^*)^{\frac{3}{4}} \exp\left[\frac{-E_g}{2kT}\right] \tag{1.33}$$

where h is Plank's constant, E_g is the band-gap of material. For GaAs, the intrinsic carrier concentration is 2.1×10^6 cm^{-3} at 300 K [8].

To determine the total carrier concentration of a doped semiconductor, we need to consider electric charge neutrality in the semiconductor

$$p_h - n_e + N_D^+ - N_A^- = 0 \tag{1.34}$$

For fully ionized dopants, N_D^+ and N_A^- are equal to doping densities. Then we can get the carrier concentration for doped material.

Considering that only donor atoms but no acceptors are present, then the electron concentration in thermal equilibrium is [28]

$$n_e = \frac{N_D^+}{2} + \sqrt{\left(\frac{N_D^+}{2}\right)^2 + n_i^2}, \tag{1.35}$$

with donor concentration N_D^+. If the doping concentration is much larger than intrinsic carrier concentration, $n_e \approx N_D^+$, and the conductivity is mainly determined by majority electrons.

The acceptor conductivity calculation is a bit more complex, due to the multiplicity of valence bands.

For GaAs, we can obtain the effective mass values from [32]e, $(0.043\pm0.005)\mathrm{m}_0$ the influence of doping concentration on conductivity and resistivity are shown in Table 2.

N_D^+(atoms/cm^3)	n_e	n_h	μ_e(cm^2 V^{-1} s^{-1})	μ_h(cm^2 V^{-1} s^{-1})	$\sigma(\Omega^{-1}\ \mathrm{cm}^{-1})$	ρ(Ω.m)
9×10^{17}	9×10^{17}	4.9×10^{-6}	2778	491.5	400	2.5
1.2×10^{18}	1.2×10^{18}	3.68×10^{-6}	2591	491.5	498	2.01
2.14×10^{18}	2.14×10^{18}	2.06×10^{-6}	2249	491.5	771	1.3
3.8×10^{18}	3.8×10^{18}	1.16×10^{-6}	1953	491.5	1189	0.84

Table 2. The electrical properties of four different doping levels for n-type GaAs

The intrinsic GaAs conductivity at room temperature (300K) is 0.46Ω^{-1}cm^{-1} [8], the resistivity is 2173 Ωm. Doping thus changes the electrical properties significantly.

1.12 Epitaxial Growth of Semiconductor

To dope semiconductor materials, diffusion or ion implantation methods are widely used in industry. In the diffusion method, impurities are typically diffused into the material from the surface due to Fick's first law of diffusion [35]. The dopant concentration is controlled by temperature and diffusion time.

Ion implantation can achieve more precise control of impurities' location by using a high energy ion beam bombarding a semiconductor substrate during growth. The ion energies used for ion implantation are typically in the range from keV to MeV; lower energy ions with 1keV-10keV can be used, but the penetration depth would be very small [36]. In section 3.3.3, simulations of doping GaAs with Be or with Si by SRIM2013 have been presented. After implantation, to get desired electronic contribution from dopants in the semiconductor, the material needs to be annealed in order to reduce lattice damage and to electrically activate the dopant. At high temperature, dopant species can move from intersititial to substitional lattice sites and the amorphous damage region from ion implatation can be recrystallized [37].

Diffusion and ion implantation are post-growth doping methods. When doping seminconductor devices during frabrication, diffusion and ion implantation allow the creation of non-uniform profiles either with depth or spatially controllled by photolithography. Ion implatation is better for mass production as it has better reproducibility and controllability. If dopants are added during crystal growth, it can result in a laterally uniform doping [38]. And to get the desired electronic properties, only a very thin layer needs to be doped during synthesis of semiconductor devices.

For our sample, the doping staircases were achieved by growing doped epitaxial layers on top of the GaAs substrate by molecular beam epitaxy (MBE). The dopant concentration is influenced by the temperature of the dopant cells and the growth rate. For MBE , it is easy to epitaxially deposit a thin layer but it is neither cost nor time efficient to dope semiconductors for industrial mass production as deposition of layers is very slow. As an example, the growth rate of GaAs is 0.15 mololayers per second at 1175 K Ga effusion cell temperature and cannot be localised [39].

1.13 The p-n junction

A p-n junction is consisting of an interface between a p-type semiconductor region and an n-type semiconductor region, see Figure 1. 14. The p-n junctions are widely used in diodes and transistors.

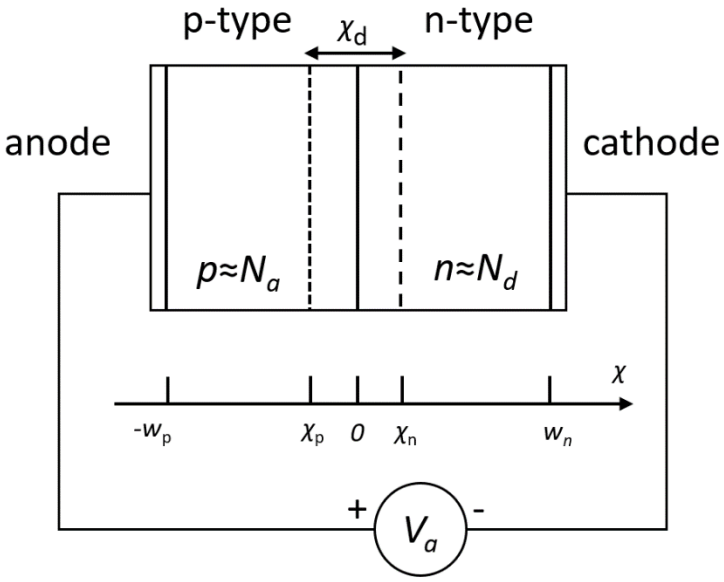

Figure 1. 14: A schematic of p-n junction with forward bias. The doping concentration is roughly the same for both sides.

The p-type region has excess holes that can diffuse across the junction to the n-type region due to concentration gradient of carriers, leaving negatively charged ions behind. For Be-doped GaAs, Be dopants replace Ga atoms, and Be dopants with 2 outer electrons will catch an additional electron from As atoms, leaving holes in the VB of As atoms. Similarly, the n-type region has excess electrons that can diffuse to the p-type region by concentration gradient, leaving positively charged ions behind. For Si-doped GaAs, if a Si atom replaces a Ga atom, three electrons will combine with a As atom, the fourth electron is free to move in CB, leaving positive ionized Si behind. The diffusion of carriers forms the diffusion current. The space charge areas left behind are depleted of mobile carriers, forming a depletion region which extends a distance of x_n and x_p into n- and p-type regions. The total width of depletion region is x_d. This space charge region then builds up an electrical field at the junction, making the carriers drift and forms a drift current in opposite direction to the diffusion current. When the magnitudes of diffusion current and drift current are equal and their direction is opposite, the voltage across the space charge region is called built-in potential, V_{bi}.

If the p-n junction is biased, the conduction properties of the junction will be changed. We call the junction forward biased when the positive terminal is connected to the p-type region, similarly, the junction is reverse biased if the positive terminal is connected to the n-type region. Increasing forward bias will decrease the potential barrier at the junction, hence increasing the current flowing across the p-n junction. Increasing the reverse bias will increase the potential barrier at the junction, which will reduce the current flow.

The depletion width is also changed with bias. Forward bias reduces the depletion width as carriers are pulled towards the junction. Reverse bias expands the depletion region as carriers are pulled out from the junction, resulting in a reduction of current flow across the junction.

The band diagram of a p-n junction is shown in Figure 1. 15 below.

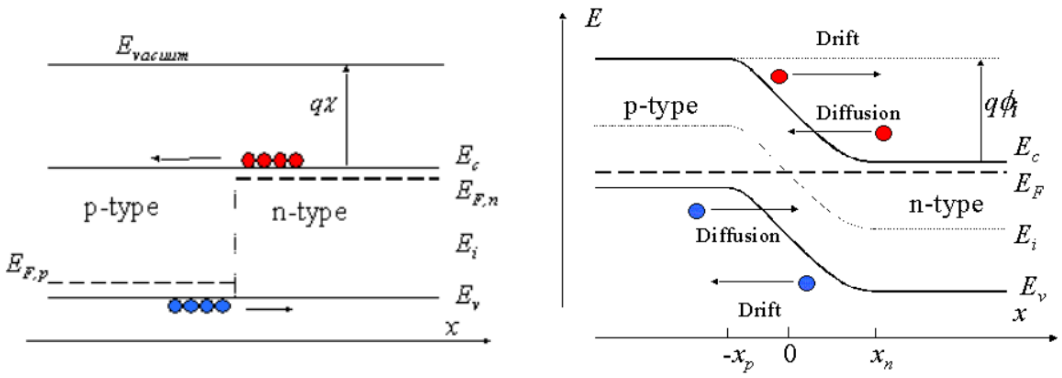

Figure 1. 15: Energy band diagram of the p-n junction before (a, left), and after the diffusion and drift currents balancing each other at thermal equilibrium (b, right).

1.14 Doping in GaAs and doping induced Fermi level shift

At temperature T, if we denote the density of states as $g_c(E)$ in the conduction band (CB) and $g_v(E)$ in the valence band (VB), n_c as the number of electrons per unit volume in CB, and p_v as the number of holes in VB, one gets [33]

$$n_c(T) = \int_{E_c}^{\infty} g_c(E) \frac{1}{e^{(E-E_F)/k_BT}+1} dE, \qquad (1.36)$$

$$p_v(T) = \int_{\infty}^{E_v} g_v(E)\left(1 - \frac{1}{e^{\frac{E-E_F}{k_BT}}+1}\right) dE = \int_{-\infty}^{E_v} g_v(E)\left(\frac{1}{e^{(E_F-E)/k_BT}+1}\right) dE \qquad (1.37)$$

where E_c is the energy at the bottom of CB, E_v is the energy at the top of VB, n_c and p_v are only affected by the chemical potential or Fermi level E_F at given temperature.

If the binding energies of the donors and acceptors are small so they can all be ionized at room temperature, the ionic densities N_D^+ , N_A^- are equal to the corresponding doping densities.

Assume only donor doping ($N_A^- = 0$) and donors are fully ionized ($N_D^+ = N_D$), then from Equations (1.30) and (1.34), we get:

$$n_c - p_v = N_D^+ = N_D \qquad (1.38)$$

$$(1.38)(n_c - \frac{n_i}{n_c})^2 = N_D^2 \qquad (1.39)$$

$$(n_c + \frac{n_i}{n_c})^2 = N_D^2 + 4n_i \qquad (1.40)$$

$$2n_c = \sqrt{N_D^2} + \sqrt{N_D^2 + 4n_i} \qquad (1.41)$$

$$n_c = (N_D/2) + (n_i{}^2 + (N_D/2)^2)^{1/2} \qquad (1.42)$$

Similarly, for p-doping,

$$p_v = (n_i{}^2 + (N_A/2)^2)^{1/2} - (N_A/2) \qquad (1.43)$$

We note that Equations (1.42) and (1.43) have the form [33]

$$n_c = e^{\beta(\mu-\mu_i)} n_i, \qquad (1.44)$$

$$p_v = e^{-\beta(\mu-\mu_i)} n_i \tag{1.45}$$

Therefore

$$\frac{\pm N_{D(A)}}{n_i} = 2\sinh\beta(\mu-\mu_i). \tag{1.46}$$

$$\Delta\mu = \mu - \mu_i = k_B T \operatorname{arsinh}\frac{\pm N_{D(A)}}{2n_i}. \tag{1.47}$$

Equation (1.47) shows how much the chemical potential is shifted from the intrinsic level by doping. We need to know the intrinsic carrier density n_i, to do the calculation.

Due to different assumption of temperature and effective mass of the carriers, the intrinsic Fermi level calculation for GaAs has different results[33] [8] [40] [28] [41].

As intrinsic density n_i for GaAs used in this report is $2.1 \times 10^6\ cm^{-3}$ from Ioffe insitute[42]. The work function shifts for different doping levels are listed below:

For a pure GaAs (110) surface, the work function values have been measured by Kelvin contact potential difference method [43] and scanning tunnelling microscopy [44]. Some calculation results match the experimental value of work function well [45]. The final work function shifts then can be calculated by equation (16) and the results are listed in Table 0.4

1.15 Charge carriers at thermal equilibrium in doping staircase samples and p-i-n sample

When undoped GaAs and n-type GaAs are brought together, if the conduction band (CB) and valence band (VB) were aligned, the corresponding flat-band diagram would be as shown in Figure 1. 16:

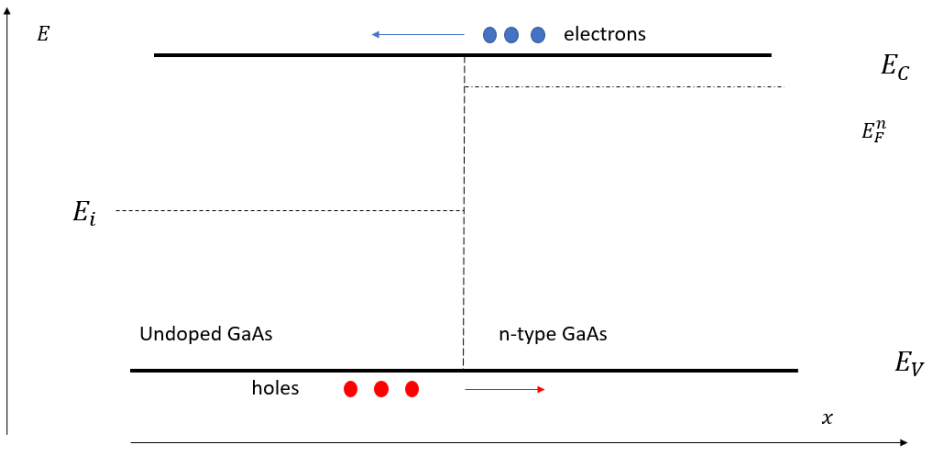

Figure 1. 16 Schematic flat-band diagram of merging undoped GaAs region with n-doped GaAs region.

In the flat-band diagram in Figure 1. 16, the Fermi energies are not aligned, and it is not an equilibrium diagram as electrons/holes could lower their energy by crossing the interface. As the name suggests, the band edges are horizontal and there is no net charge in the material. After the diffusion of electrons and holes, thermal equilibrium is obtained as shown in Figure 1. 17.

The depletion region ranges from $-x_p$ to x_n , the sum of the two depletion layer widths is the total depletion width x_d. The charge of ionized donors and acceptors forms an electric field ($\bar{E}$), which makes the carriers drift in the opposite direction. When the diffusion and drift of carriers are balanced, the material reaches thermal equilibrium and the Fermi energy is constant across the interface region.

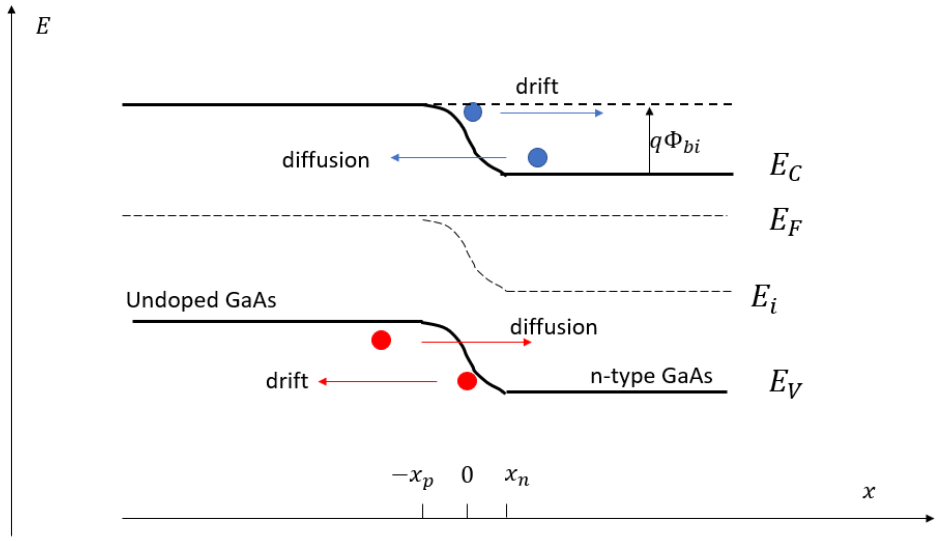

Figure 1. 17. The band diagram of undoped GaAs with n-doped GaAs region in thermal equilibrium.

We have the general equation (1) for the space charge ρ(x), and the Poisson equation (1.64):

$$\rho = q(p - n + N_d^+ - N_a^-) \tag{1.63}$$

$$\frac{d^2\Phi}{dx^2} = -\frac{\rho}{\varepsilon_0} \tag{1.64}$$

$$x_d = x_n + x_p \tag{1.65}$$

For our case, on an undoped GaAs layer with $N_A = p_i$, an n-doped GaAs layer with $N_d = 3.8 \times 10^{18}\ \mathrm{cm}^{-3}$ is grown, so the nominal charge density is then given by:

$$\rho = \begin{cases} 0 & \text{for} \quad x < -x_p \\ N_A & \text{for} \quad -x_p < x < 0 \\ N_D & \text{for} \quad 0 < x < x_n \\ 0 & \text{for} \quad x > x_n \end{cases} \tag{1.66}$$

Then the Poisson equation becomes

$$\frac{\mathrm{d}^2\Phi}{\mathrm{d}x^2} = \begin{cases} 0 & \text{for} \quad -\infty < x < -x_p \\ \frac{q}{\varepsilon_s} N_A & \text{for} \quad -x_p < x < 0 \\ -\frac{q}{\varepsilon_s} N_D & \text{for} \quad 0 < x < x_n \\ 0 & \text{for} \quad x_n < x < \infty \end{cases} \tag{1.67}$$

and the boundary conditions are:

$$\Phi = 0 \quad \text{for} \quad x = -x_p$$

$$\begin{aligned} \frac{\mathrm{d}\Phi}{\mathrm{d}x} &= 0 \quad \text{for} \quad x = -x_p \\ \Phi &= \Phi_{bi} \quad \text{for } x = x_n \\ \frac{\mathrm{d}\Phi}{\mathrm{d}x} &= 0 \quad \text{for} \quad x = x_n \\ x_p \times N_a &= x_n \times N_d \quad \text{for charge neutrality} \end{aligned} \tag{1.68}$$

The solution of the Poisson equation should be:

$$\Phi(x) = \begin{cases} \frac{q}{2\varepsilon_s} N_A \cdot (x_p + x)^2 \quad \text{for} \quad -x_p < x < 0 \\ \Phi_{bi} - \frac{q}{2\varepsilon_s} N_D \cdot (x_n - x)^2 \quad \text{for} \quad 0 < x < x_n \\ \frac{q}{2\varepsilon_s} N_A \cdot x_p^2 = \Phi_{bi} - \frac{q}{2\varepsilon_s} N_D x_n^2 \quad \text{for } x = 0 \\ 0 \quad \text{anywhere else} \\ ; \end{cases} \tag{1.69}$$

From equation (1.69), we get the built-in potential of the depletion region:

$$\Phi_{bi} = \frac{q}{2\varepsilon_s} N_D x_n^2 + \frac{q}{2\varepsilon_s} N_A \cdot x_p^2 \tag{1.70}$$

From Figure 1. 17, in thermal equilibrium, the Fermi energy is constant throughout the system, the built-in potential equals the difference between the Fermi energies, E_F^n and E_F^i, divided by the electronic charge:

$$\Phi_{bi} = \frac{E_F^n - E_F^i}{q} \tag{1.71}$$

Assuming x_d is known, x_n and x_p can be calculated by combining equations (1.65) and (1.68):

$$x_n = \frac{N_A}{N_A + N_D} x_d \tag{1.72}$$

$$x_p = \frac{N_D}{N_A + N_D} x_d \tag{1.73}$$

Substituting equations (1.72) and (1.73) into (1.70) yields:

$$x_d = \sqrt{\frac{2\varepsilon_s}{q}\left(\frac{1}{N_A} + \frac{1}{N_D}\right)\Phi_{bi}} \tag{1.74}$$

From equation (12), the solutions of x_n and x_p are:

$$x_n = \sqrt{\frac{2\varepsilon_s}{q}\frac{N_A}{N_d}\frac{1}{N_A + N_D}\Phi_{bi}} \tag{1.75}$$

$$x_p = \sqrt{\frac{2\varepsilon_s}{q}\frac{N_D}{N_A}\frac{1}{N_A + N_D}\Phi_{bi}} \tag{1.76}$$

This result shows that we can treat an interface of n- or p-doped GaAs to undoped GaAs like a diode. We need to consider the diffusion of carriers before they recombine. The diffusion length L_{dif} is the

average distance that the excess carries can travel before recombination, and it depends on the lifetime τ and mobility μ of the carrier:

$$L_{dif} = \sqrt{\tau \cdot \mu \frac{k_B T}{e}}, \tag{1.77}$$

where k_B is the Boltzmann constant, *T*=300 K at room temperature and *e* is the charge of an electron. For GaAs, the minority carrier lifetime is about 10^{-8} s^{-1}[46], and the mobility of the holes is about 400 cm^2 V^{-1} s^{-1} [8], so the calculated diffusion length of minority carriers in doped GaAs is about 3μm. However, the minority carrier lifetime of n-type GaAs changes with the doping concentration: when doping concentration $N_D < 10^{18}$ cm^{-3}, the lifetime τ is a constant; when the doping concentration $N_D > 10^{18}$ cm^{-3}, the carrier lifetime reduces when the doping level increases [47]. This is because defects associated with donor complexes and precipitates are formed [48], and these defects will act as hole capture centres [49], [50]. Thus, the carrier diffusion length for $N_D = 3.8 \times 10^{18}$ atoms/cm^3 would be smaller than 3μm.

Figure 1. 18 below shows the interface simulation for n-doped/i GaAs and the electronic field and potential calculated by a Poisson solver code called Padre [51].

(a)

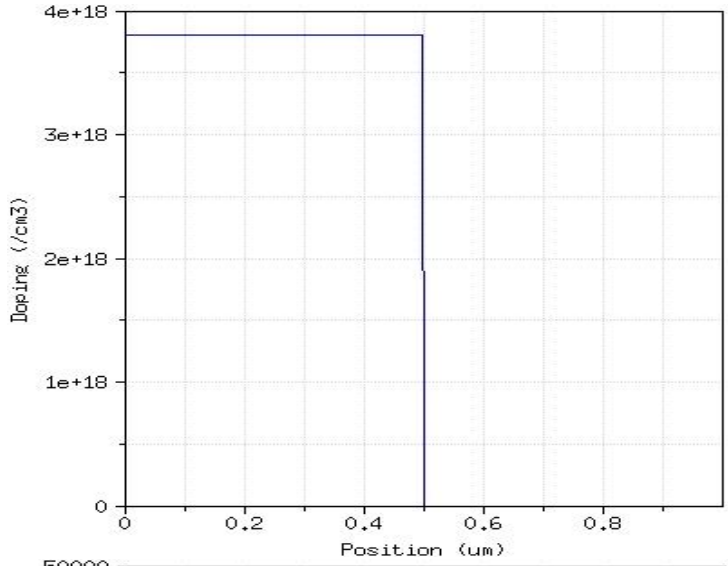

(b)

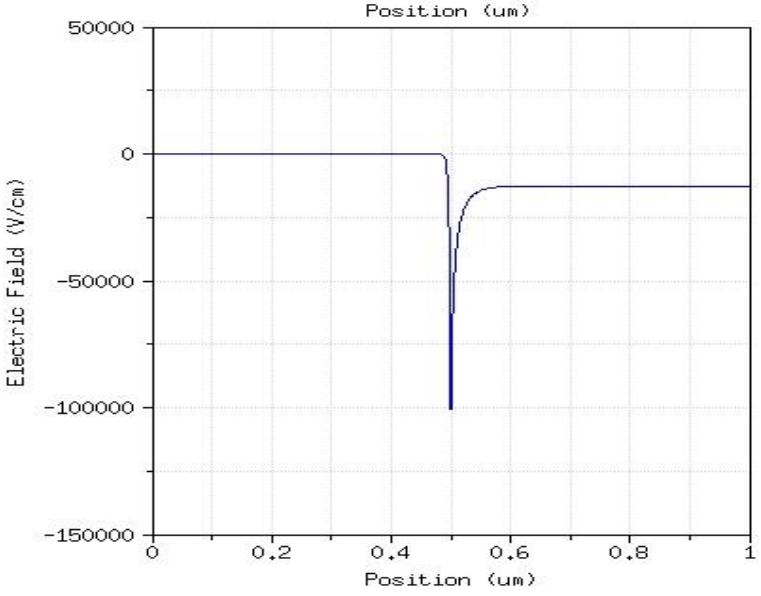

(d)

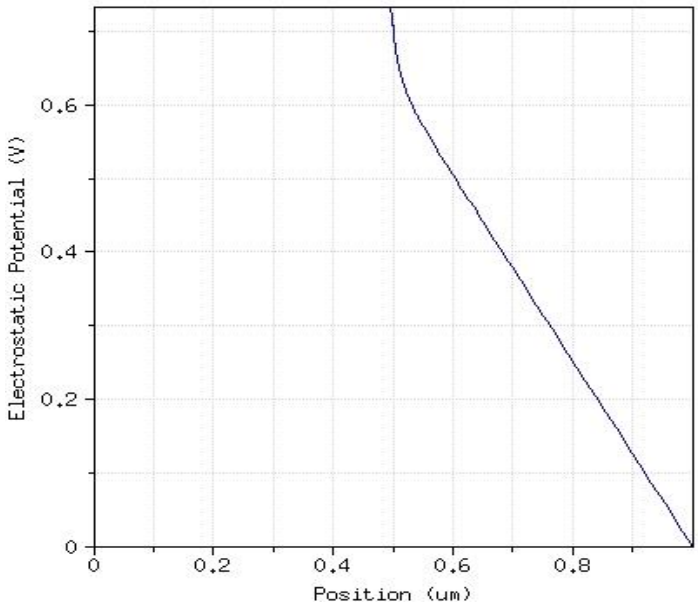

(c)

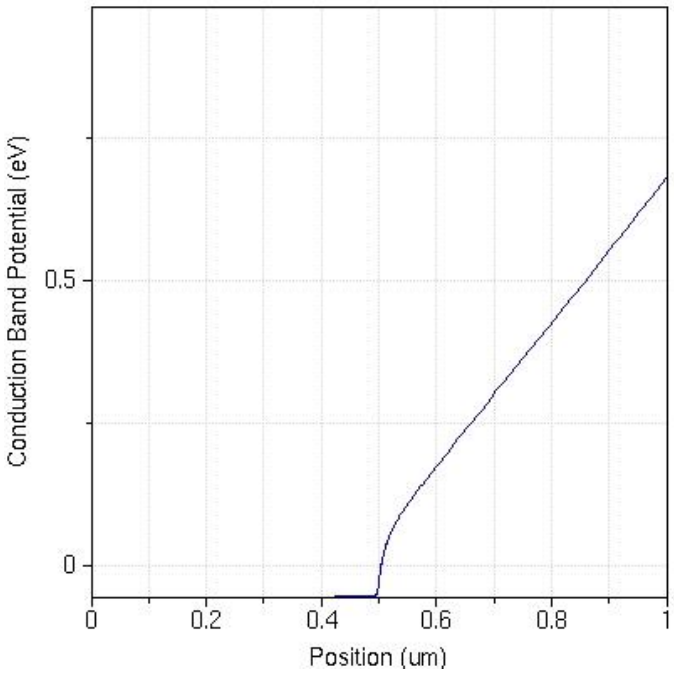

Figure 1. 18 : The electric field (b) ,the electric potential (c) and conduction band (d) across an n-doped / undoped GaAs interface (a) of 3.8×10^{18} atoms/cm^3 Si doped GaAs (on the left) to undoped GaAs (on the right).

1.16 GaAs based devices

GaAs and other III-V compound semiconductors have advantages like direct band-gap and high electron mobility that are not found in Si or Ge. As GaAs has a 1.42 eV band-gap at room temperature, which is larger than that of 1.12 eV of Si, the wide band-gap gives GaAs superior high temperature performance. By taking these advantages, GaAs has commercial application in GaAs based power electronics, GaAs based integrated circuits, light emitting diodes and lasers.

1.17 GaAs for power electronics

The desired properties of power electronic devices include high switching speed, high temperature capability, wide bandwidth, simple biasing. Power field effect transistors (FET) based on III-V materials have better electrical characteristics when compared with their counterparts made of Si. GaAs FET devices are frequently used today in mobile phones, mobile base stations and other custom-made electrical devices [52], [53]. GaAs metal-oxide-semiconductor field effect transistor (MOSFET) has an oxide layer between the metal and the semiconductor resulting in a higher drain current, lower leakage current than metal-semiconductor field effect transistor (MESFET) [54]. The MESFET has similar structure to a MOSFET. MESFET has a metal contact onto the GaAs, forming a Schottky barrier. GaAs MESFET devices are widely used in radio frequency (RF) amplifiers [55]. Heterojunction bipolar transistors (HBJT) based on GaAs for high performance systems are in demand for commercial and military applications too [56].

1.18 GaAs for high frequency integrated circuits

Integrated circuits (IC) based on GaAs have been developed for a long time [57] and the large scale production of GaAs ICs has been achieved in the 1990's [58]–[60]. For ICs, optical fibre components fabricated monolithically on the same substrate are important to avoid lattice mismatch; GaAs deep level LEDs (introducing energy levels in the band-gap so that the light emission wavelength is increased) for fibre optics have also been developed [61].

Both digital and analogue ICs based on GaAs have been produced. Digital ICs are used for logic gates, frequency dividers, microprocessors and so on [62]–[64]. Analogue ICs are used in amplifiers, switches, modulators and frequency converters in communication systems [65]–[67].Analogue bandwidth is the sinusoidal frequency range of the circuit works on, in digital ICs, the digital signals are square wave signals which made of 0 and 1, digital bandwidth is refer to the bit rate through the channel.

1.19 GaAs for light emitting diodes, laser diodes and solar cells

Since 1962, GaAs has been used in near-infrared laser diodes (LD) as it has a band-gap of 1.42 eV and so emits infrared light around 870nm wavelength. Usually, GaAs is used in alloys to tune the emission wavelength [68]. GaAs is also used as material for high performance solar cells as it has better performance in high temperature environments [69], [70], and its band-gap is close to the Shockley-Queisser limit that describes the theoretically calculated maximum efficiency of a single p-n junction photovoltaic solar cell [71]. The maximum photovoltaic conversion efficiency is around 33.7 % for a band-gap of 1.5eV [71].

1.20 Semiconductor device analysis technology

The major semiconductor device characterization methods in research are: failure location analyses (such as by focused ion beam etching, electron beam induced current in SEM and so on) [72]–[74] , electron microscopy analysis (such as SEM and STEM) [75], local composition analysis (such as by energy dispersive X-ray (EDX) spectroscopy) [76], dopant profiling (SIMS), dopant contrast (SEM, holography) [77], [78] as detailed in Chapter 2, stress mapping (X-ray diffraction) [79], chemical state analysis at high spatial resolution by electron energy loss spectroscopy (EELS) [80], [81].

With high spatial resolution and rapid imaging speed, SEM is potentially good for 2D dopant profiling. However, SEM dopant profiling is not widely used in industry. This is due to the poor reproducibility as the contrast will decrease or even disappear as the electron beam irradiation is enhanced, and a quantitative interpretation of SEM images is difficult. In order to get more understanding of the SEM

image contrast, experiments using GaAs staircase samples with different doping layers have been imaged at different beam voltages and electron doses.

1.21 Aims and objectives

With the development of electron guns and improvements of detectors, Perovic *et al.* reported in 1995 that doping contrast of SE intensity depends on the type of doping and is sensitive to the doping concentration [82]. However, there are still some problems in the 2D dopant profiling of semiconductor devices.

The first problem is due to the sample preparation because ion milling will reduce the contrast needed for detection. For silicon samples, it has been reported that the contrast from ion milled samples is only half of the contrast from a cleaved surface [83]. It has been demonstrated that focused ion milling (FIB) by 30kV Ga ions generated 99±7 nm amorphized layer for GaAs; though the amorphous layer thickness is smaller than that of 237±23 nm amorphous layer reported for Si under same condition, it is still thick [84]. Furthermore, FIB may also generate surface roughness in compound semiconductors. That means ion milling will lead to a decrease in contrast and an increase of surface roughness, which will result in low sensitivity for dopant profiling [85]. Hence, it is difficult to achieve sensitive 2D dopant profiles across semiconductor devices that are difficult to cleave well. To reduce the influence of amorphous layer thickness, reducing the dose and accelerating voltage would be helpful. By reducing the voltage and beam current, 2nm amorphous layer thickness on GaAs sample has been achieved by Ga ion milling at 2kV and 0.02nA for 30 seconds of milling time [86].

The second problem is that the dopant contrast will decrease or can even disappear as a result of electron beam irradiation [87]. This is common in semiconductor devices and would lead to poor reproducibility [88]. So, it is worth to investigate the mechanism.

The last problem is how to interpret the SEM images. As most compound semiconductor devices consist of more than two kinds of materials [89], the potential variation at heterojunction interfaces will also influence the dopant contrast. This makes the interpretation of SE images difficult, as the contrast will not only come from the doping. To get more accurate dopant profiles for such compound semiconductor devices, it is necessary to take the influences of heterojunctions into account [90].

Overall, it is very important to explore the dopant profiling mechanism and SE contrast as a practical method of 2D dopant mapping, which can benefit the research, development and industry production of semiconductor devices.

In this chapter, the basics of semiconductor device physics and importance of GaAs based compound semiconductors have been discussed.

The purpose of this thesis is to discuss the contrast mechanism using secondary electrons in SEM obtained at different voltages and for different detectors.

The materials used in the experiments are GaAs based doping staircase samples and LED device structures. As the GaAs has similar crystal structure and electrical properties as many other III-V materials, investigation of dopant profiling in GaAs by SEM and AFM can be applied to other compound semiconductors like InAs and other GaAs based ternary alloys. Though InP is much softer than GaAs, it can still be manually cleaved and if the sample size is cut to 50×50 μm^2, it can still be handled. However, if the layers are strained, macroscopic curvature will occur due to lattice mismatch and epitaxial layers roll up. But it is a different research area, in our work we have not looked into strained layers.

Previous dopant profiling work has been discussed in Chapter 3 and 4, with much attention paid to SEM and AFM work on dopant profiling.

In Chapter5 the characterization of GaAs staircase samples and GaAs based LED sample will be discussed in detail. Also, the dopant profiles of the samples have been compared with Monte Carlo simulations.

A summary of the results and promising future work is presented in Chapter 6.

2 Literature Review on semiconductor characterization methods

2.1 Introduction of techniques most used in semiconductor device characterization

The electrical conductivity of semiconductor materials ranges from 10^{-8} to 10^{3} $\Omega^{-1}cm^{-1}$ [91]. This conductivity is sensitive to temperature and impurities as discussed in Chapter1. This makes semiconductors very essential for electronic devices [8].

By impurity doping, the number of active electrons in the material can be modified. The electrical and optical properties can be controlled by doping. By fabricated into electronic devices, semiconductor applications can be found in industry and modern life easily. As electronic device dimensions are scaling down, the demand for nanoscale semiconductor device characterization is increasing. None destructive high spatial dopant concentration mapping at nanometre or sub-nanometre level is important for the semiconductor device industry [92].

In this review chapter, we discuss the most commonly used methods for dopant detection. The dopant contrast in SEM and dopant mapping in KPFM are discussed in detail.

2.2 Dopant characterization technology

After doping a semiconductor, it is important to evaluate the doping profiles as dopants are intentionally introduced impurities that dramatically change the electrical properties of semiconductors [93]. Thus precise dopant measurement is important for semiconductor device development and production. The common tools for dopant investigation are:

0D (with no spatial information): photoluminescence (PL), Hall effect measurements

1D (line scan): SIMS, Capacitance-Voltage measurenents (C-V), Spreading Resistance Profiing (SRP)

2D (mapping): cathodoluminesence (CL), AFM, KPFM, TEM, SE imaging in SEM

3D (volume distribution): atom probe tomography [78].

2.3 Standard electrical measurements

There are many types of electrical measurements to measure electrical quantities of a material or system, such as the voltage measurements for electrical potential difference between two points with voltmeter; the electron current measured by ammeter; the resistance measurement with ohmmeter; Hall effect used for measuring the carrier concentration [94], [95]; capacitance measurement with digital voltmeters; and so on. The electrical contacts for these measurements are usually made by clamps or probes with a dimension larger than modern semiconductor devices.

2.4 Secondary Ion Mass Spectroscopy (SIMS)

Secondary Ion Mass Spectrometry (SIMS) can obtain the dopant concentration directly with excellent elemental sensitivity (<ppm) [96]. In SIMS, the sample of interest is bombarded with heavy ions such as Ar^{+} or O^{-} with high energy, the sputtered atoms from the specimen surface are then analysed by a mass spectrometer as the local surface recedes.

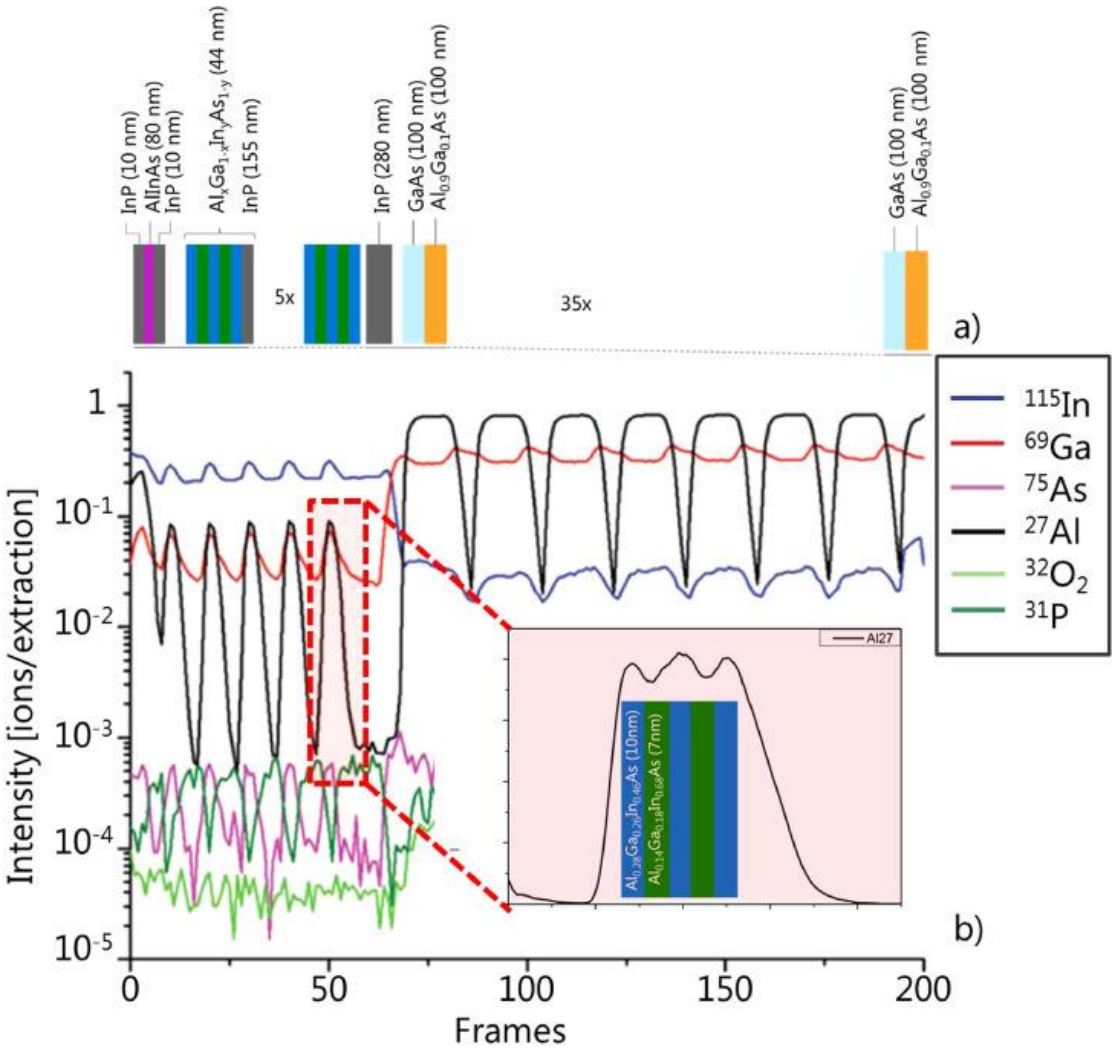

*Figure 2. 1.*SIMS profiles of a laser diode with vertical cavity. The ion beam was a 260pA, 20keV Ga^+ beam *[97]*.

The major advantage of SIMS is that it is sensitive to dopant concentrations even in concentrations as low as 10^{13} cm^{-3} but it can also detect dopant concentration as high as 10^{21} cm^{-3} [98]. The accuracy of the SIMS measurements is highly dependent on the quality of standards [99], [100]. Surface contamination such as by carbon and / or oxides will not influence SIMS results as different atoms have different masses but there are matrix effects and surface effects due to the need to build up a stable sputter yield. The matrix effect is that the elemental ion yield depends on the surrounding chemical species [101]. Surface effect refers to the surface structure or morphology, surface orientation will also influence secondary ions yields [102], [103]. Although it has these advantages, SIMS is a destructive technique and it is time consuming [104]. And it detects impurity concentrations no matter whether the dopants are electrically active or not [98].Scientists today also use SIMS to obtain 2D dopant distribution images: high resolution and high sensitivity elemental imaging has been achieved [105]. For SIMS imaging, there are the microprobe mode and the microscope mode [106].

In the microprobe mode, the focused ion beam probe scans over the area to be analysed in a raster manner like in an SEM. The sputtered ions are collected with a mass spectrometer and counted to reconstruct the image pixel by pixel. Hence the lateral resolution of microprobe mode depends on how good the ion beam can be focused. By using liquid metal ion source, such as Ga^+ or In^+, the probe size can be reduced to 20-40nm [105], [107], [108].It is an extremely time-consuming technique

considering its field of view, though it is good as a calibration experiment for other dopant profiling tools.

In the microscope mode an unfocused ion beam is used to irradiate the sample. The mass spectrometer itself acts as a microscope as the distribution of ions is magnified and recorded when passing the spectrometer and then, ions are transferred onto a 2D position sensitive detector [105]. The optics of the mass spectrometer, image magnification and the pixel density on the detector will limit the resolution of microscope mode SIMS to μm range [105]. It is faster than microprobe mode but has poorer resolution. Also, the unfocused beam will reduce the beam intensity which influences the secondary ion generation rate; thus, a better ion source with higher current density is needed for this mode.

2.5 Transmission Electron Microscopy (TEM)

Physicists discovered in the 20th century that particles like electrons possess a wavelike character. Louis de Broglie proposed the following relationship between wavelength λ, and the momentum amplitude p of a particle [109]:

$$\lambda = \frac{h}{p} = \frac{h}{mv} \ , \tag{2.1}$$

where *h* is Planck's constant, v stands for the speed of the particle and m stands for the mass. From equation (2.1), electrons that have high speed will have a short wavelength. As electrons are charged particles that can be focused by magnetic lenses, an electron beam allows a specimen to be imaged at better spatial resolution than conventional light microscopy due to the Rayleigh criterion describing the resolution Δx, of an optical diffraction-limited system with collection angle α [110]:

$$\Delta x \approx \frac{0.61\lambda}{\sin \alpha} \tag{2.2}$$

The numerical aperture (NA) of an optical system is defined by $NA = n \sin \alpha$, where *n* is the refraction index for the medium in which the lens is working. For light in vacuum, the refraction index is one. To improve resolution, one can reduce wavelength or increase the collection angle. The invention of transmission electron microscopy (TEM) has given researchers the opportunity to view objects at the atomic level. TEM characterization methods are widely used to reveal the structure and chemical properties of materials.

2.5.1 Electron-specimen interaction

When an electron beam is incident on an electron transparent specimen, the interactions between atoms and incident electrons can be many, as illustrated in Figure 2. 2.

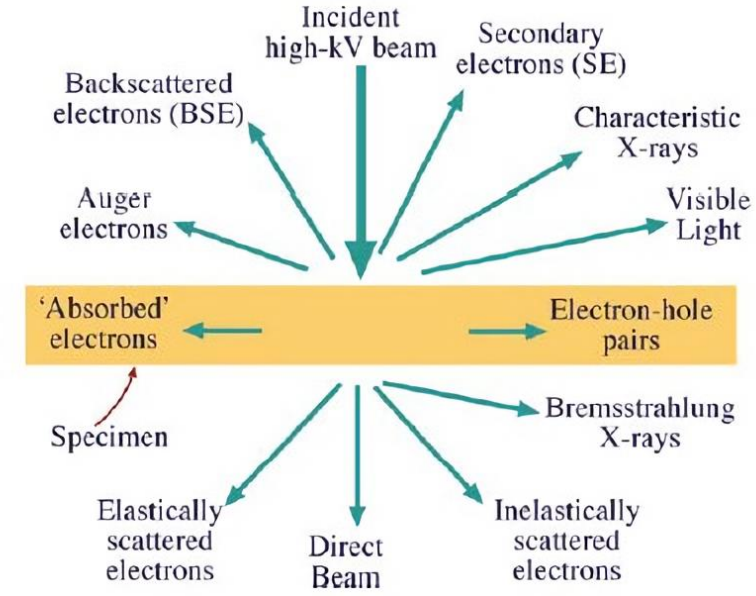

Figure 2. 2.Signals generated by the interaction of the primary electron and material.

Electrons can be viewed as a kind of radiation which can ionize material and produce secondary electrons during the interaction [111]. Most secondary electrons (SE) are brought to rest within the interaction volume, however, only those SE generated close to the specimen surface have a large possibility to escape from the specimen and can be collected by a positively biased detector [112]. SE imaging reveals properties of surface structures (topography) and is exploited in the scanning electron microscope (SEM).

Electrons that get through the specimen in a straight direction without undergoing any angular deviation constitute the direct beam and are exploited in the transmission electron microscope (TEM).

As atomic nuclei are positively charged, an electron will deviate from the incident direction due to the Coulomb force. This interaction between the fast electron and nucleus is called elastic scattering. The angle of deflection is in the range of 0-180°. This kind of scattering has high momentum transfer, but hardly any energy transfer. The direct beam and all backscattered electrons are dominated by elastic scattering.

Interactions between fast electrons and bound electrons are inelastic due to their similar weights. By inelastic scattering, the transmitted electrons will lose some energy. The energy lost can be released in form of X-rays, cathode luminescence (CL), or secondary Auger electrons [113].

By detecting those signals, one can perform different types of analysis, such as: collecting backscattered electrons [114] and inelastic electron scattering for EELS [115].

Conventional TEM images have hardly any information about the doping concentration. In order to detect a p-n junction, one can make use of selective etching to convert doping concentration into thickness differences [116]. The contrast due to thickness can be used to identify the p-n junction. Holography by using an electron biprism in the TEM has demonstrated 2D dopant mapping wherein the phase shift in a hologram is proportional to the electronstatic potential distribution at the p-n junction [117]. The spatial resolution of holography can be better than 10nm and 0.1V sensitivity of

potential difference[118], while SEM also has sub 10nm resolution but detection rang from 10^{16}-10^{20} cm^{-3}[119].

2.6 Scanning Probe Microscopy (SPM)

For all the SPM methods described in sections 2.2.5-2.2.8, each technique has its own advantages and disadvantages. Most of the SPM methods require good surface preparation and are difficult to apply to Si based semiconductors where it is difficult to get well-defined cross-sections by cleaving. Furthermore, the field of view of SPM is usually small.

2.7 Scanning Tunnelling Microscopy (STM)

STM has been used for p-n junction delineation by detecting differences in tunneling current [120]. The conductive tip induces band bending at the surface; hence the tunneling current depends on dopant type and concentration. By incorporating current-voltage spectroscopy it is possible to identify differently doped regions and depleted regions [121].

The STM can achieve atomic level spatial resolution for GaAs and other III-V materials [122]. The STM needs to work in UHV condition at low temperature to avoid contamination during the measurement. The tunneling current is measured and the conductance related to the doping concentration can be calculated for known bias and tip-sample separation [121]–[123]. However, the surface states and the tip induced surface band bending limit the accuracy of dopant profling, and the dopant concentration needs to be larger than typically 10^{18} cm^{-3} to be detectable [123].

2.8 Scanning Spreading Resistance (SSR) profiling

SSRP is a simple method to measure eletrically active dopant concentrations. SSRP determines the carrier concentration based on the sequential measurement of the resistance between two metal probes placed on the sample surface (metal or semiconductor). Figure 2. 3below is a sketch of a sample beveled at a shallow angle being measured by SSRP. A depth profile of resistivity ρ can be geranerated at different position x_i.

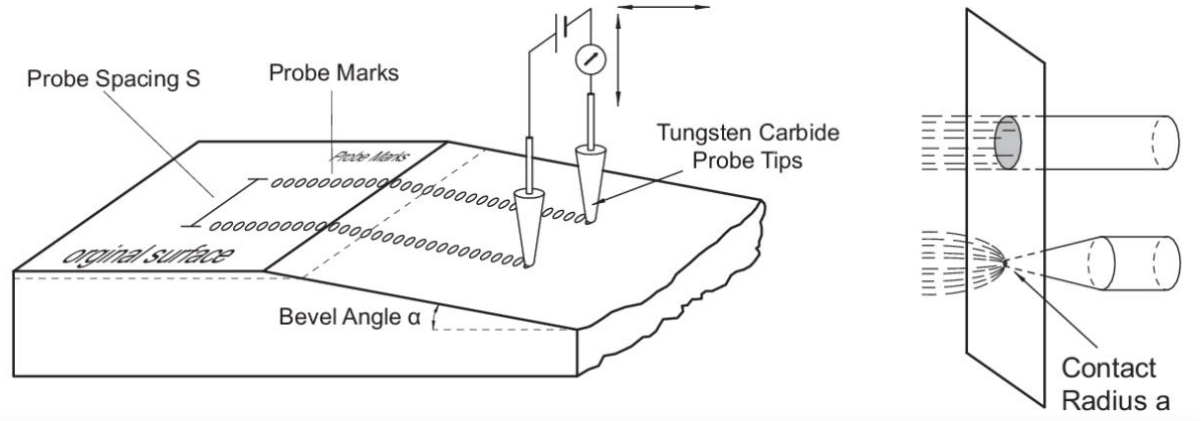

Figure 2. 3.Dual probe measurement of surface resistance [124].

The current flowing (*I*) through the probes spreads out into the sample and is measured and as the applied voltage is already known, one can get the measured resistance R_{meas}. For the two probes of different geometry shown in the right part of Figure 2. 3, when the tip is pointed, the current can

spread over at the contact point, and effective contact radius needs to be considered. The measured resistance is dominated by current spreading effect if the contact radius *a* is small and the distance *S* between two probes is short. That means the spreading resistance occurs between the electrical contact and is representative of the local surface resistance.

The measured resistance R_{meas} consists of the spreading resistance R_{sp} generated by current spreading, the resistance of the circuit including probes R_{set} and the barrier resistance R_{cont} from contact between probe and sample surface [124]:

$$R_{meas} = R_{sp} + R_{set} + R_{cont} \tag{2.3}$$

The contact barrier resistance can be evaluated by calibration [125], while the resistance of the system can be measured by simply connecting the two probes together.

The spreading resistance (R_{sp}) is calculated by using Ohm's law. Then the resistivity of the semiconductor (ρ) at different points is obtained using the equation:

$$R_{sp} = \frac{\rho}{2\pi r} \tag{2.4}$$

where *r* is the radius of area the probe current spreads over.

Using an n-type semiconductor as an example, the conductivity σ_n is related to its carrier concentration n and electron mobility μ_n by

$$\sigma_n = q\mu_n n = \frac{1}{\rho} \tag{2.5}$$

$$n = \frac{1}{\rho q \mu_n} \tag{2.6}$$

From the resistivity we can get the carrier concentration at room temperature [95], [126], [127]. When using SSRP, the carrier type cannot be determined as SSRP only measures the resistivity to obtain majority carrier concentration.

The resolution of SSRP depends on the finite geometrical size of the tip; 10nm resolution can be achieved [128]. SSRP measurements are very sensitive to dopant concentrations from 10^{15}-10^{20} cm^{-3}. Like most SPM techniques, the sample preparation and surface conditions are important for SSRP. With development of diamond coated Si tips, the resolution is inproved as SSRM works at relatively high tip pressure to make good electreical contact, otherwise the resistance between tip and sample surface is measured [129].

2.9 Capacitance-voltage profiling (CV)

C-V profiling is a well-developed technique that can provide qualitative doping data. It measures the capacitance between a reverse biased semiconductor sample and a metallic probe tip. A depleted region is formed between the sample and the tip due to the reverse DC bias. The capacitance-voltage relation is obtained by measuring the capacitance between tip and sample at various voltages. The doping concentration is inversely proportional to capacitance so the carrier density can be directly extracted from the C-V curve, then converted into a depth profile by calculating the depletion region width from the measured capacitance [130]:

$$n = \frac{2}{q\varepsilon_0\varepsilon_r A^2}\left[\frac{d}{dV}\left(\frac{1}{C^2}\right)\right]^{-1} \tag{2.7}$$

where A is the area of interaction, which can be modeled and *d* is the depletion depth given by

$$d = \frac{A\varepsilon_0\varepsilon_r}{C} \tag{2.8}$$

C-V measurements are fast and non-destructive, and sensitive to dopant levels as low as 10^{14} cm^{-3} [130]. The doping concentration measured by C-V method is the combination of effective doping concentration and electrically active defects. However, the spatial resolution is limited by the calculated depletion region width. C-V is widely used as a 1D profiling technique as the capacitance is measured as a function of the applied voltages. For a p-n junction or MOSFET sample, the width of depletion region will be changed when varying the applied voltage. The relationship between depletion width and bias can be used for dopant profiling of the semiconductor material [131], [132]. The main disadvantage of 1D C-V profiling is that the resolution is limited by the Debye length in low doped regions and that this method is insensitive to highly doped regions [133].The Debye length is the distance in a semiconductor over which the electirc field affects carrier distrubution. It could be regarded as a screening effect as charges are increasinggly electrically screened.

2.10 Scanning Capacitance Microscopy (SCM)

Scaning capacitance microscope (SCM) is a method that combines C-V and AFM, where a conductive probe contacts the sample surface and scans across to map the electrostatic capacitance, extending C-V profiling to 2D imaging with the increase of computing speed.

In SCM measurement, the metal tip is sometimes coated with an insulating oxide layer, so when the tip is in contact with the speciemen surface, it forms a metal-insulator-semiconductor capacitor. When scanning the tip over the sample, the capacitance variations can be recorded, hence the 2D carrier concentration map is obtained. By reducing the oxide layer thickness, the sensitivity of SCM measurements can be improved as the thickness of dielectric is reduced to increase capacitance.

The SCM has a high spatial resolution due to the use of conductive AFM probe [134]. With a high frequency capacitance sensor, the capacitance between conductive tip and specimen can be measured. Like most scanning probe techniques, SCM also requires high quality probes and clean specimen surface conditions to obtain good 2D dopant maps [135].

The spatial resolution of SCM can be improved by reducing the tip size of cantilever, however, the capacitance measurement sensitivity will reduce too as the area of interaction is reduced.

2.11 Dopant Profiling with the SEM

As mentioned before, a TEM specimen needs to be electron transparent. That means if the specimen is not made very thin, electrons will only be scattered or even absorbed within the specimen. Since TEM cannot provide the capability of examining bulk specimens, scientists developed the scanning electron microscope (SEM) which makes use of backscattered electrons (BSE) and secondary electrons (SE). The image formation in SEM is using the scanning principle as its name suggests: primary electrons are focused into a small electron probe and the probe position is controlled by electromagnetic fields. Deflection coils scan in two perpendicular directions over a rectangular area of the specimen [113]. By collecting signals from each scan point, the SEM image finally will be formed and can be displayed on a screen. A schematic diagram of SEM is shown Figure 2. 4. The BSE detector and SE detector are located at different positions of the optic column. The electrons collected by the detectors are converted into digital electric signals and amplified for display on screen.

In previous studies [23]-[36][136], SEM has been demonstrated as a powerful tool for locating p-n junctions or structures consisting of alternating strips of doped and un-doped layers.

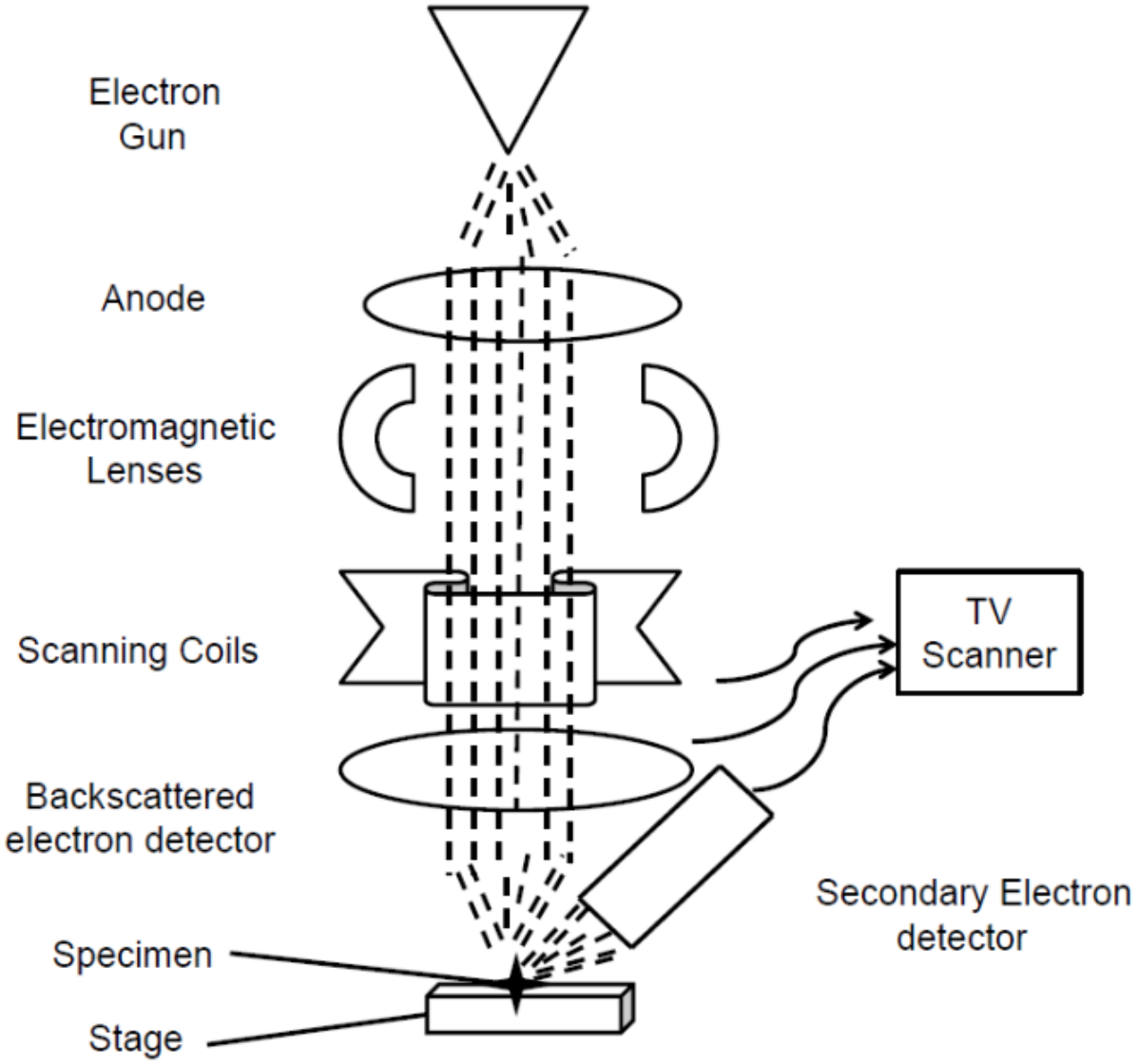

Figure 2. 4.Schematic diagram of SEM[137]

Backscattered-electron images can provide indirect compositional information of the specimen, because the cross-section for backscattering of a single atom is proportional to the square of its atomic number [113]. Low-loss electron imaging can be obtained by energy filtering of the BSE signal. Though a reduction of signal intensity is accompanied with energy filtering, simulations have shown that the interaction volume is further reduced by increasing the retarding energy of filtering system, the energy filter SEM can provide more accurate dopant mapping for GaAs/AlAs multilayers [139]. This is because energy filtering can decrease the mean intensity of two regions, thus the image contrast is enhanced [140].

SE imaging is not only a rapid technique for analysis of integrated circuits [141] but also a promising tool for characterising electrically active dopant concentrations at high resolution and sensitivity [139]. Perovic et al. demonstrated it to be a sensitive tool for 2D dopant distribution mapping at nanometre scale spatial resolution and ppm concentration levels [142]. In fact, SEM dopant profiling can be widely used in failure analysis of MOSFETS [143], lasers [144], ICs [145] and solar cells [145]. Researchers have made a lot of effort to improve the doping contrast, especially for n-type material [146]. By adjusting the bias of the ET-detector, one can reduce the total number of electrons collected as SEs with higher

energies cannot reach the detector any longer. In such an energy filtered SE image, *n*-type material can even be brighter than *p*-type material [140].

2.12 Energy spectrum of electron signals in SEM

From beam-specimen interaction, signals near the surface can leave surface and be detected. The signals could be BSEs, SEs, Auger electrons, X-rays and photons. If we plot the collected electron energies versus the counts of electrons, we will get an energy spectrum of electrons that escaped from the surface, as shown in Figure 2. 5.

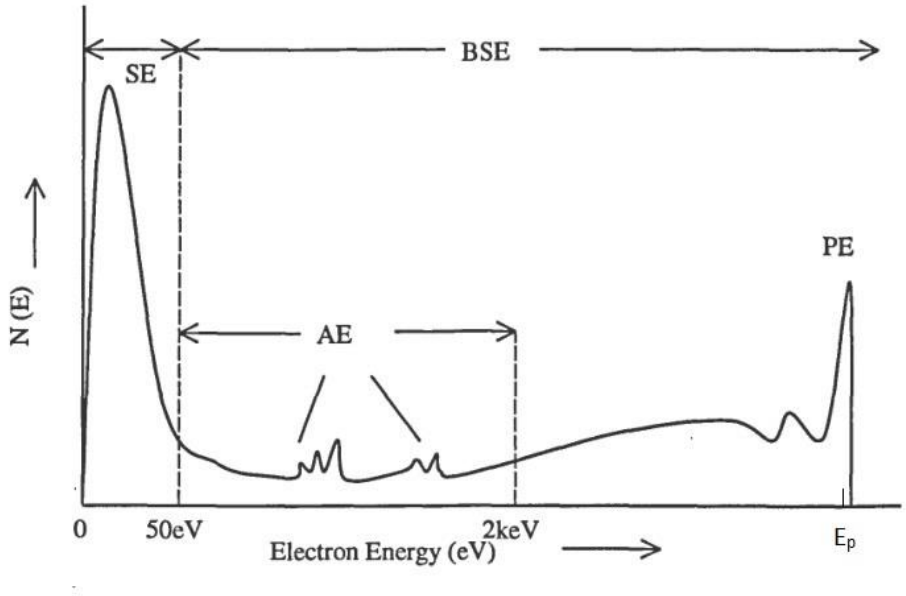

Figure 2. 5.The energy spectrum of electrons emitted from specimen surface with incident primary electron energy Ep [75].

2.13 Electron range and excitation volume

When primary electrons are incident on the specimen surface, they will travel a distance before they leave or rest in the specimen. This finite distance will be influenced by the primary electron energy and the material property of the specimen.

The interaction volume is formed as the electron can diffuse in the specimen after being scattered. As the electron trajectories are in random directions, the interaction volume is formed. All the SEM signals are generated within this interaction volume. The shape of the interaction volume is like a pear and its dimensions are of several micrometres depending on the primary beam energy and what signal is considered.

Figure 2. 6 shows how the interaction volume size reducing with beam energy reduction. The interaction volume is simulated by the program “Monte Carlo Simulation of Electron Trajectory in Solids” (CASINO3.3.04) [147]–[150].

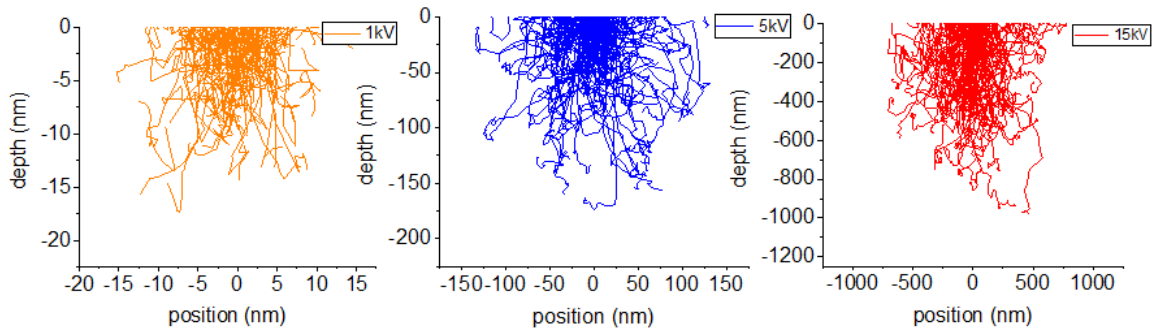

Figure 2. 6. Screen shot of interaction volumes in GaAs as function of electron energy from Monte Carlo simulations.

The electron range is the average distance travelled by the electrons before they rest in material, and can be expressed as [151] :

$$R_{KO} = \frac{0.0276 A_m E_p^{1.67}}{\rho Z^{0.889}}, \tag{2.9}$$

where A_m is the atomic weight in g/mol for the target material, E_{p} (keV) is the primary electron energy; Z is atomic number of the material and ρ is the material's density in g/cm^3.

2.14 Escape depth of SEM signals

Escape depth λ_{esp}means the depth from which BSEs, SEs, Auger electrons and X-rays generated by the primary beam can escape from the surface of the specimen as illustrated in Figure 2. 7. The escape probability B_{esp} of the SEM signals at depth x decreases with the escape depth λ_{esp}: $B_{esp} \propto e^{-x/\lambda_{esp}}$ [152].

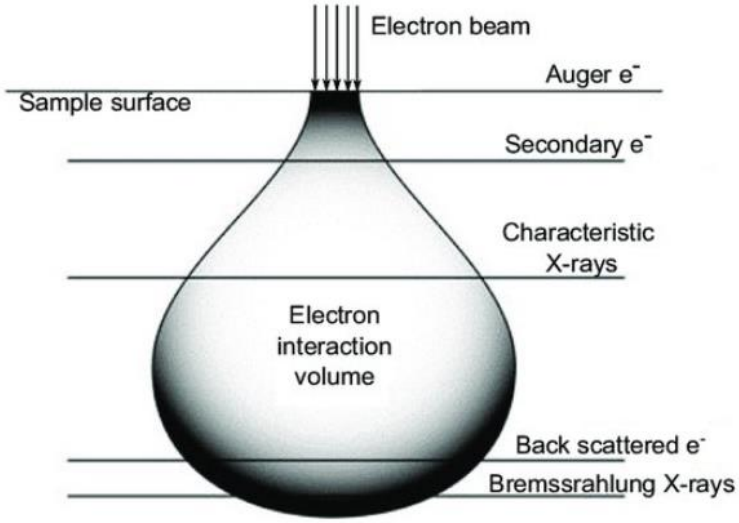

Figure 2. 7. Schematic sketch of signal emission within the interaction volume [153].

The energies of most SEs are very small, that means SEs generated at deep regions of the interaction volume will lose their energy and come to rest in the specimen after a few times of scattering. The escape depth for most metals are 0.5 to 1.5 nm [75], for most insulators the escape depths are 10-20 nm [66]. The escape depth for semiconductors are 0.5 to 5 nm [154]. For GaAs, the calculated mean escape depth is about 1.3nm for 1 kV to 5 kV primary beam energy [155].

Backscattered electrons are emitted without energy loss. The escape depth of BSEs is about half of the penetration depth and at least 5 times the SE escape depth [75]. Auger electron escape depth is only a few surface monolayers due to their low energy [156]. Escape depth for X-rays is about 1µm as it is an electromagnetic wave which has high transmission power [157].

2.15 SE signal in the SEM

Conventional scanning electron microscopy (SEM) has been used as a functional tool for 50 years after the secondary electron detector (SED) was invented by Everhart and Thornley in 1960 [158]. The electrons with energies below 50 eV are generally denoted as SEs and those SEs have four main origins [151].

Figure 2. 8 below illustrates the different types of SEs collected by Everhart-Thornley (E-T) SED.

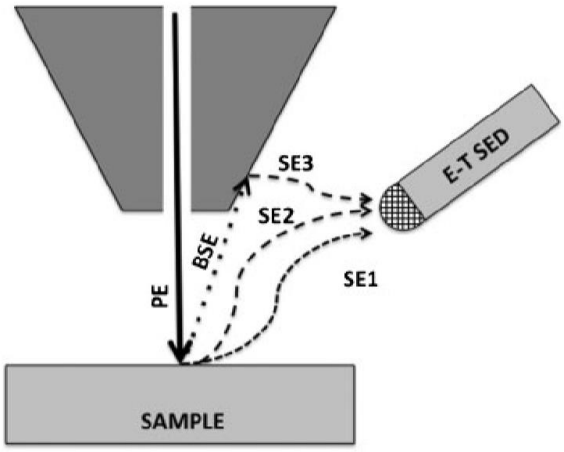

Figure 2. 8. SE signals collected by E-T SED (after Goldstein et al., 2003) [151].

From Figure 2. 8 it is clear that "SE1" come from primary beam-sample interaction, "SE2" are generated by delocalised BSE leaving the sample surface, "SE3" are collected when BSEs collide with the SEM pole piece or other components of the SEM, and "SE4" come from interaction between primary electrons with SEM column components [151]. Both "SE1" and "SE2" are useful for dopant contrast as they are generated within the sample surface and they are indistinguishable from each other as from their energy (<50meV) and distribution. However, "SE2" will add noise to the signal. Furthermore, "SE2" is related to the BSE surface distribution, thus "SE2" will show some sensitivity to the atomic number [151]. The contribution of each SE signal for gold crystal specimen at 30kV,20-40 pA beam current have been measured as 9% SE1, 28% SE2, 61% SE3 and 2% SE4 [151] with a cold emission SEM (JEOL JFSM 30)[159]. An E-T detector can attract some of the SE3 and SE4 which results in image noise increase.

Another kind of detector is the in-lens detector which is also called through-the-lens detector (TLD). This kind of detector is located in the objective lens and collects SEs directly over the scanned area, which means the field of view is quite small [151]. The in-lens detector is efficient in collecting SE1 and SE2, meanwhile SE3 and SE4 are suppressed, hence the dopant contrast sensitivity is improved [160]. To ensure the better contrast, the TLD detector is used for SEM imaging in this study.

2.16 SE yield as a function of angle of incident beam

The secondary electron yield δ is defined as the number of emitted secondary electrons per primary electron. The SE yield is found to be increasing with incident angle θ, where the normal incident angle is $\theta = 0°$:

$$\delta(\theta) = \delta_0 \sec(\theta), \tag{2.10}$$

where δ_0 is the SE yield at normal incidence of primary beam. With a beam tilt angle θ, the maximum penetration depth is reduced by $\cos(\theta)$, hence the escape probability will be increased. It can be concluded that increasing the beam tilt angle θ will give small escape depth of secondary electrons.

2.17 SE yield as a function of incident beam energy

The SE yield δ measurement of incident electron energy in the 1-100keV range has shown the SE yield decreases when primary electron energy is increased above a certain threshold V_{max} [75]:

$$\delta \propto E_p^{0.8} \lambda \sec(\theta), \tag{2.11}$$

where λ is the inelastic mean free path that is an average distance over which an electron is inelastically scattered, for GaAs, λ is 5nm [161].

The SE yield as a function of primary beam energy is shown in Figure 2. 9below. The plot indicates the SE yield first increases with rising primary energy, reaching a peak of δ_{max} at V_{max}, and decreases with further increase of beam energy. This can be explained by the penetration depth and escape depth of SEs. When $R \ll \lambda_{esp}$, the SEs can be emitted from surface easily, but the small number of primary energy electrons only create few SEs. While for $R \gg \lambda_{esp}$, although more inelastic scattering of electrons happens, the exponential reduction of escape probability at deeper depth will reduce the SE yield. As discussed in section 2.3.4, secondary electron can be generated from different inelastic scattering events, which means the number of secondary electrons sometimes can be (much) larger than the number of primary electrons. When $\delta = 1$, the number of incident primary electrons is equal to the secondary electrons generated.

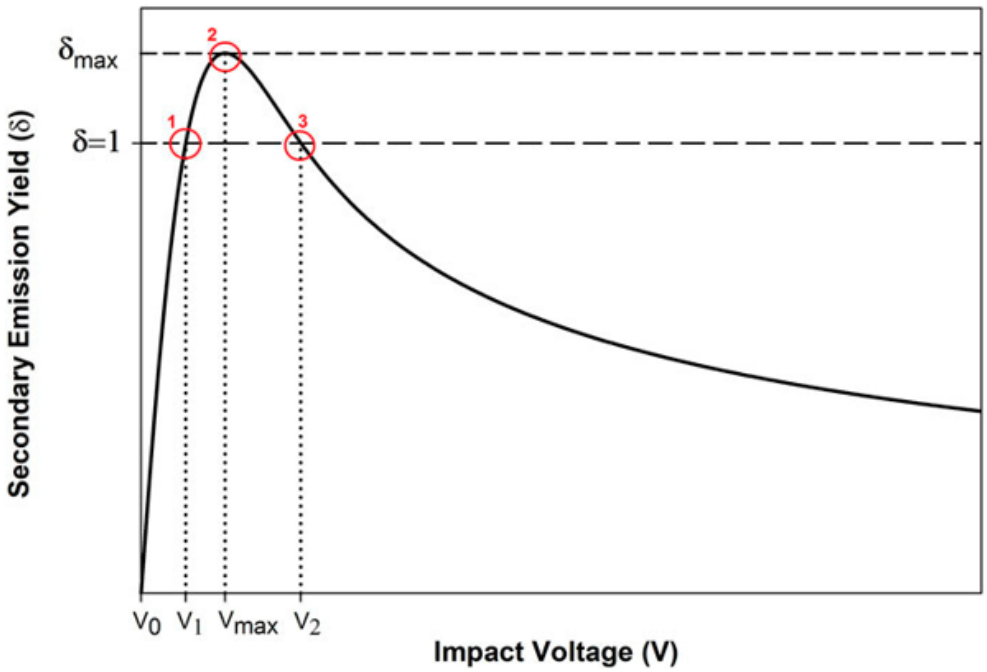

Figure 2. 9. SE yield as a function of beam energy [162].

2.18 Secondary Electron Detection

As the E-T SED is a wide bandwidth detector, it will collect all these electrons, SE1-SE4. As described above, SE2 and SE3 are not generated by the primary electron beam, which will limit the SE image resolution and reduce contrast by smearing out image details, while SE4 contrast is not even related to any sample characteristics.

Low-voltage SEM (LV-SEM) with primary beam energies from 100 eV to 5 keV has been developed as a low energy primary beam has a lower penetration depth and smaller interaction volume with the specimen, which means LV-SEM is more sensitive to specimen surface details. The LV-SEM image can provide information different from conventional SEM images. This is due to the LV-SEM imaging mechanism.

Figure 2. 10is a sketch of the electron optical so-called Gemini column from Zeiss [163].

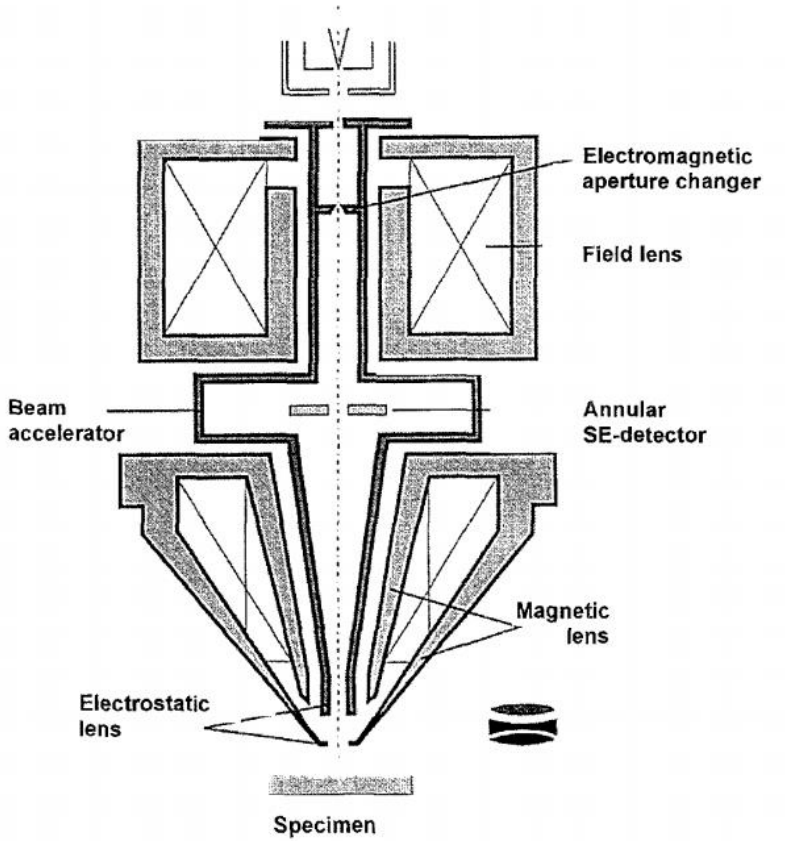

Figure 2. 10. The electron optical column of SEM with in-lens detector [163].

In Figure 2. 10, the Gemini lens system has a beam booster or accelerator inside the column. The electrons from field emission gun (FEG) will first be accelerated to several kilovolts and then decelerated to the primary beam energy at the pole-piece at the end of the electron column. This retarding field acts as an electrostatic lens and will also accelerate SEs into the column and focus them onto the annular detector which is called in-lens (i-L) detector [163].

Microscopy studies have noted that the i-L SED image is dominated by SE1 while the E-T SED image is dominated by SE3 and SE4 signals [164]–[166]. For doped sample imaging, it is better to use an in-lens detector as the image is mainly formed by the SE1s from the primary interaction between beam and specimen. It is important to realise that the energies of SE1 are generally lower than SE2 [165], [167]. Based on a spectroscopy study, it has been reported that if the retarding field is 8 kV, the field will preferentially collect the low energy SE1 signal [167]. Thus, the beam booster will also act as an energy filter to attract SE1 to the i-L SED while filtered SEs dominated by SE2 are collected by E-T SED to form a material contrast more similar to a Z-contrast type image. This column is not an immersion lens while the FEI UHR mode is an immersion lens.

Figure 2. 11 below shows the geometry of an E-T detector.

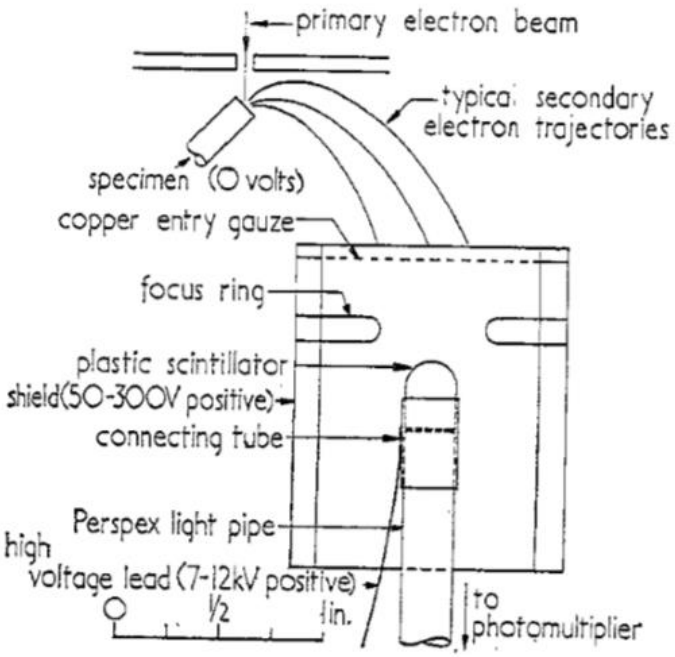

Figure 2. 11. Diagram of E-T SED [158].

In Figure 2. 11, the secondary electrons are collected and focused onto a scintillator inside a Faraday cage. During this process, the low energy SE signal will also be filtered out by trapping low energy electrons on the wires of the cage. That means that a conventional E-T SED is a SE2 detector in practice. To collect low energy electrons with E-T SED, one needs to increase the working distance (e.g. >50mm) to let electrons accelerate over longer path lengths.

In summary, the low voltage image formed by i-L SED contains a smaller energy range of electrons, dominated by SE1, the conventional SEM image by E-T SED is a material contrast without much surface-related information.

2.19 Dopant contrast mechanism

The intensity of secondary electrons emitted from a semiconductor surface is very sensitive to the doping: p-type regions appear usually bright while n-type regions are dark under standard imaging conditions (so-called doping contrast) [168]. To explain this phenomenon, Perovic et al. proposed it is due to surface band bending [82]. Howie et al. suggested that external electrical fields called patch fields should be considered for profiling electrical junctions [169]. The detection range of SE dopant contrast is from 10^{16}-10^{20} atoms/cm^3 for a p-type Si sample [170]. A spatial resolution of 19nm was achieved by Venables et al. [87] for B-doped Si. N-type Si dopant contrast with spatial resolution of 1nm has been demonstrated by Frank et al. with slow electrons in 2019 [171]. Though the uncertain of experimental condition and noise during the SEM observation impede the quantifications of doping contrast, the two-dimensional mapping can be empirical quantified relies on calibration of one-dimensional SIMS profile for Si p-n junction or p-doping patterns on n-doped substrate[172]. The spatial resolution is limited by the probe size. It has been suggested that to get near atomic spatial resolution, the microscope would need to have 0.1nm probe size[173], which is impossible to achieve in low-kV SEM. In this work, the aim is to better understand the doping contrast mechanism in the view, investigate the contrast from staircase sample with small variation of doping levels rather than a p-n junction and try to combine SPM methods with SE image to quantify the SE contrast.

In case of profiling thin doped films, doping contrast is relative to surface band bending by the charge induced electrical field.

The SEs are generated by core-electron excitation; before these electrons reach the detector, they will have to overcome the energy barrier of the material called work function [8]. If we assume the energy of an excited electron is E' and the work function of material is Φ, Fermi energy is E_F, then only the electrons with energy $E' > E_F + \Phi$ can escape from the material. The escape probability $P(E)$ of SE electrons can be defined as the ratio of SEs escaping from the semiconductor surface to the total number of SEs generated.

2.19.1 Band-bending effect

In practice, semiconductor specimen surfaces are often not clean due to contamination or oxidation following cleavage in air. This will give rise to surface states and results in surface band bending as shown in figure 2.12 below [82]. This band-bending effect is significant, for example, 0.05 monolayers of oxygen could produce 0.15eV band-bending [82].

Figure 2. 12(a) shows the case in which no band bending occurs in the semiconductor (which consists of equally wide alternating strips of n- and p-regions) near the surface while the vacuum level bends towards opposite directions for different doping types. For smaller work function material (n-type dopants), its surface barrier is reduced while for p-type dopants (larger work function), the surface barrier is increased [174]. This is called graded barrier effect. In practice, the presence of surface states means that the Fermi level is pinned near the middle of the gap, as illustrated in Figure 2. 12(b). In the presence of internal fields, the potential outside the surface would be curved along perpendicular direction of the surface [82]. The band bending effect will attract carriers to the surface thereby changing the vacuum level shape from Figure 2. 11(a) to (b), which is the reason why E_c bends stronger than the local vacuum level.

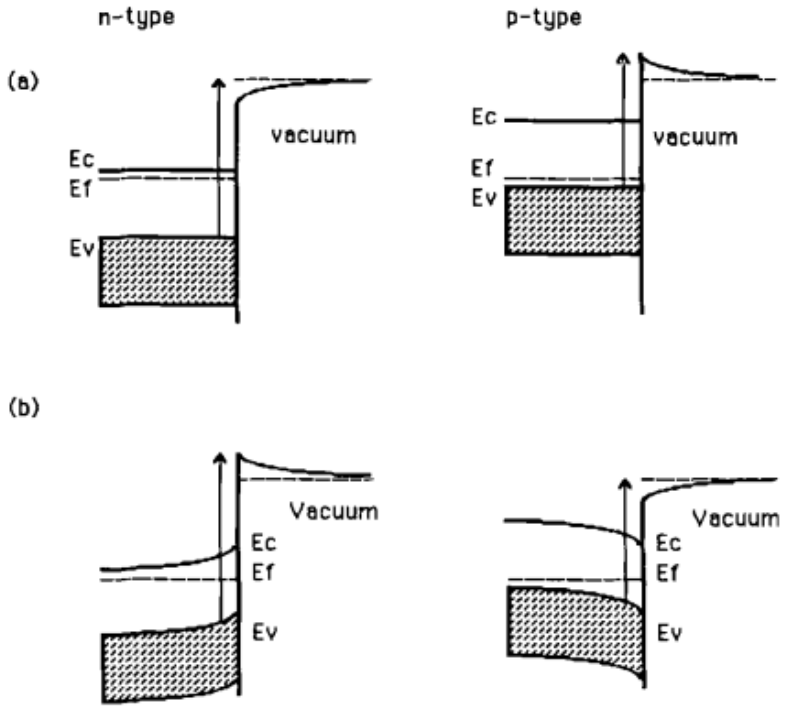

Figure 2. 12.The schematics of surface band bending for different doping types, (a) no band bending at the semiconductor surface versus (b) the Fermi level of differently doped semiconductors is pinned by surface states [82].

When the depletion length is smaller than the penetration depth of primary electrons, the electron affinity (from CB edge to vacuum level) of p-type material is less than that of n-type region. From Figure 2. 12(b), it is clear to see a smaller energy *E*' is needed for *p*-doped material than for *n*-doped material to excite an electron from the valence band into vacuum.

When the depletion length is larger than the penetration depth of primary electrons, n- and p-regions have same affinities, but the internal electric field will accelerate electron toward surface in p-type region, while the internal field will push back the electrons in n-type region. The lower energy barrier of *p*-doping surface compared to that of *n*-doping means the SE emission threshold is decreased for *p*-type material and increased for *n*-type material. Thus, the larger yield of SEs in *p*-type semiconductor results in brighter images compared to *n*-type material under the same condition.

Additionally, the shape of the surface barrier in vacuum would be different for n- and p-doped regions. The potential outside the surface would curve along the perpendicular direction of the surface, but the direction of the potential curve is opposite for different doping type. The barrier of the p-type region surface is less than n-type, and the grade shape of the barrier gives rise to low energy SE production. Therefore, SE emission would be greater still for *p*-type material than *n*-type [82].

2.19.2 Patch field effect

The patch field effect was first reported in 1968 by Plows [175] where an external field would result in deflection of the electron trajectories in SEM. Using a negatively charged particle on a specimen surface, the particle will have some 'shadow' around it due to the SE emission is reduced in the distorted electrical field around the particle [75].

For a p-n junction, one needs to consider a further step. Due to the existence of patch fields, SEs above p-region experience acceleration away from specimen which results in a larger probability to be

collected, whereas those SEs above n-region are accelerated towards specimen. That is another reason why p-doped regions appear brighter than n-regions in SE images.

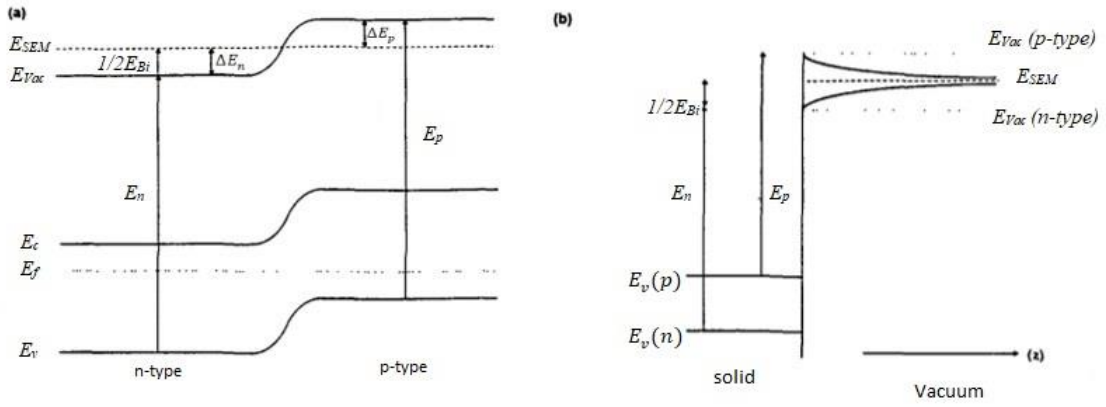

Figure 2. 13.The band structure of a p-n junction. (a) For p-doped region, SEs need E_p for emission (from VB to local vacuum level) while for n-region, SEs need E_n+1⁄2 E_{Bi}. E_{Bi} is the built-in potential due to space charge distribution. The vacuum level far away from surface is in the middle of local vacuum levels (b) Band diagram of SE emission [176].

However, in this patch field mode, the SEs are ionised only from VB, the SEs from CB are neglected. Besides, the ionisation of electrons in VB to vacuum level is assumed to be independent of the doping. Experiments on patch field effects on Si p-n junctions have been performed by Elliott [177].

2.19.3 Metal -semiconductor contact effect

Besides the surface band bending and patch field effect, now we consider the effect of the surface thin film which is consisting with contamination or unknown composition. A metal-semiconductor contact (M-S) should be considered as it can form Ohmic or Schottky barriers on the surface to influence the SE emission.

During SEM imaging, the beam is scanned over the area and hydrocarbons would crack and form a contamination layer. This layer is reported to be graphitic by using Auger electron spectroscopy [178]. If the work function Φ_m of the metallic layer is larger than the work function of specimen Φ_s, it will form a Schottky barrier and SE emission becomes lower. If $\Phi_m < \Phi_s$, an Ohmic contact is formed and the electrons pass the layer with low resistance.

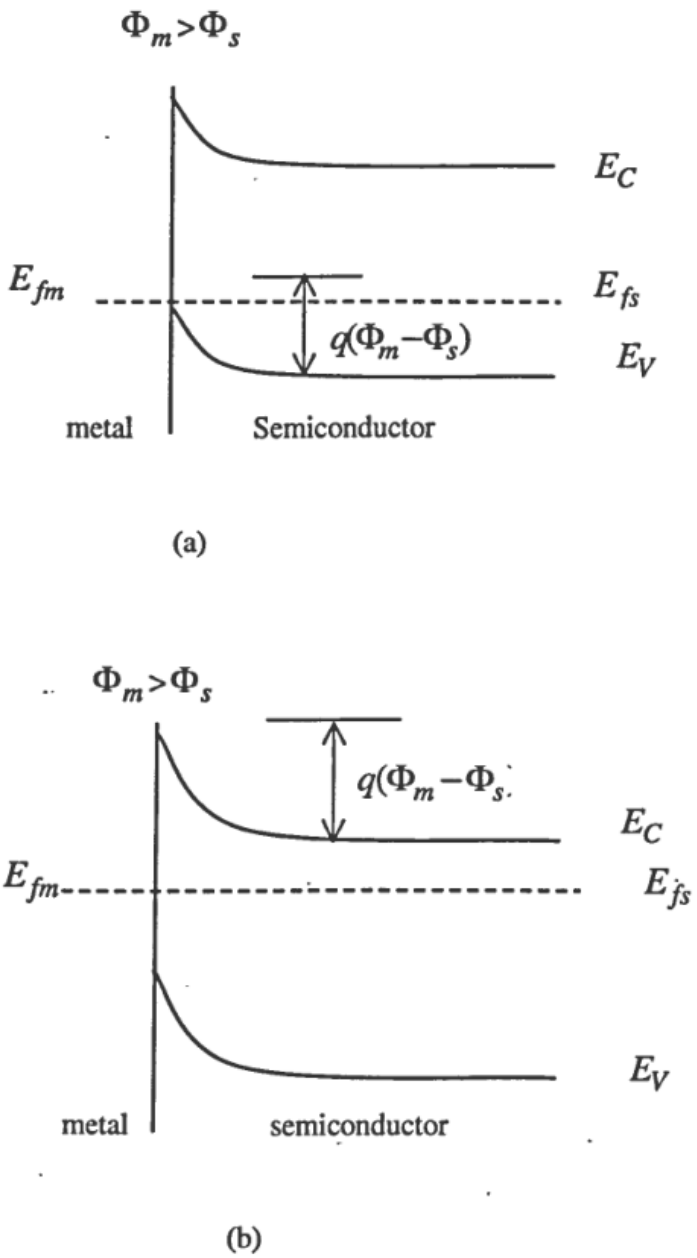

Figure 2. 14.The energy band diagram of (a) Ohmic contact on p-region, (b) a Schottky contact on the n-region [179].

Furthermore, the M-S contact model also indicates the contrast can be inversed due to specimen coating with metals of different work function. It was reported that by coating chromium and nickel on same doped Si, the contrast was inverted [179].

2.19.4 SE Contrast in the SEM

The displacement of Fermi level relative to the band edges in bulk is the basis of doping contrast. However, in addition to reasons above, refraction at semiconductor-vacuum interface influences the doping contrast due to a change in the collection angle of the detector [180]. These effects make it difficult to find a quantitative model for SEM dopant profiling.

The doping contrast mechanism is related to the electrical field inside and outside the specimen. The SE image contrast can be defined by the formula below [180] :

$$C = \frac{I_1 - I_2}{I_2} \tag{2.12}$$

Here I_1 and I_2 represent the intensity of two adjacent areas where $I_1 > I_2$. As the background intensity is usually very small, the contrast can be expressed as a function of SE field-dependent escape depth, λ_{esc}, and SE escape probability, B, which depends on the effective electron affinities [181]. In solid state physics, electron affinity is defined as the energy needed for an electron in the bottom of conduction band to move into the vacuum level just outside the semiconductor. Then

$$C = \frac{\lambda_{esc}^1 B_1}{\lambda_{esc}^2 B_2} - 1, \text{where } B = \int_0^\infty P(E) N_{SE}(E) g_c(E) dE, \tag{2.13}$$

where $P(E)$ is the quantum mechanical escape probability sensitive to doping, $g_c(E)$ is the density of states in the conduction band and $N_{SE}(E)$ is the SE energy distribution.

In this research, SEM is used to investigate cleaved GaAs specimens. SE images have been taken of doped regions, and the contrast and doping relation have been explored. The results of SEM imaging will be discussed later in chapter 3.

2.19.5 Backscattered Electrons

Those electrons that interact with the specimen elastically or inelastically and leave the specimen surface for detection with energies larger than 50 eV are called backscattered electrons (BSEs). There are three type of BSEs: first, the BSEs only elastically scattered without energy loss; second, the diffused electrons inelastically scattered more than once with loss of energy; third, the Auger electrons.

BSE signals are important in SEM as the contrast is dependent on the specimen atomic number *Z*, which gives so-called *Z*-contrast. The target with higher atomic number will appear brighter than lower atomic number material due to higher degree of elastic scattering. Figure 2. 15 shows the Monte Carlo simulation results of BSE yield for different pure targets showing how the BSE yield varies as a function of *Z* for 5 kV and 15 kV beam energies.

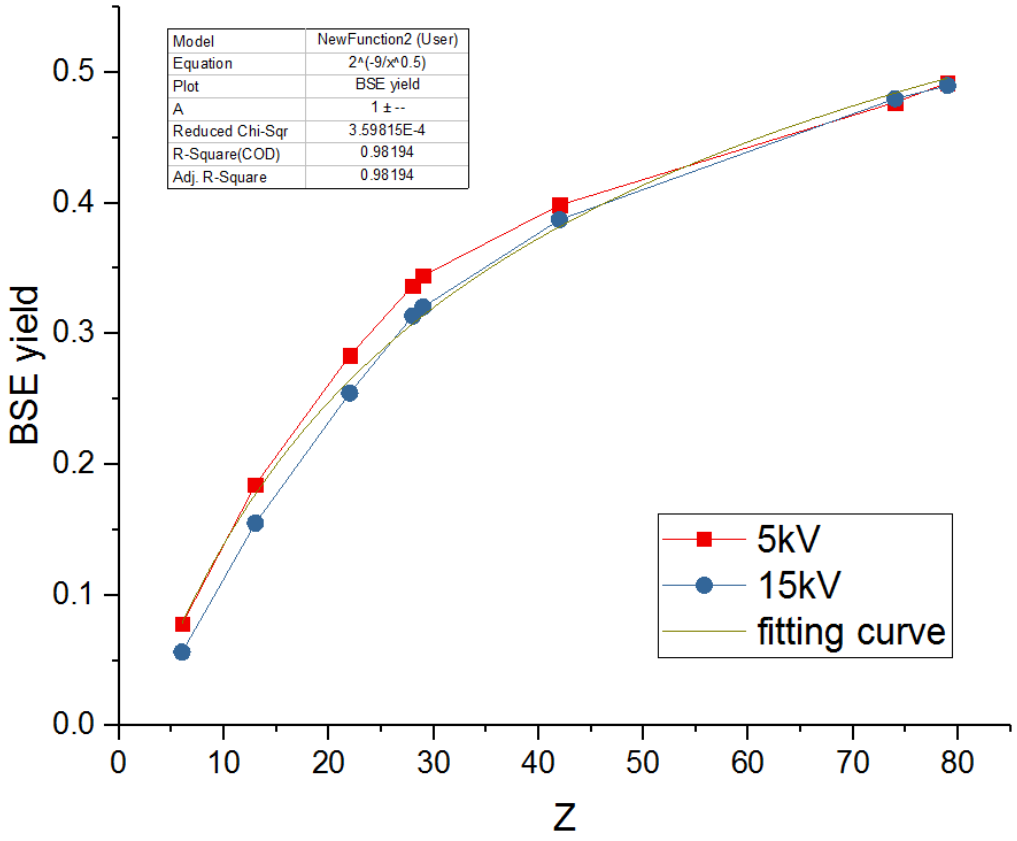

Figure 2. 15.The BSE yield increases with increasing atomic number Z for high beam energy. For electron energy less than 10keV, BSE coefficient increases when energy decreases at small Z, the curves will be identical at large Z [182].

There are two types of BSE detectors: solid state detectors (SSD) and scintillator detectors. The SSD is made of a p-n junction. When BSEs are collected by the Si, electron-hole pairs are generated, and the reverse biased SSD separates the electron-hole pairs to get a current. But the response of SSD is slow. A scintillator detector has faster response but is more expensive than SSD [183].

2.19.6 X-rays

By using an energy-dispersive X-ray (EDX or EDS) detector, the characteristic X-ray signals can be collected to analyse chemical information. Figure 2. 16 shows the generation process of X-rays by a primary electron beam. When the core electron is displaced by inelastic scattering of primary electron, the electron from an outer shell will fill this vacancy, and the energy difference between the levels can be released as an X-ray (or alternatively, an Auger electron). There are K_α, K_β and L_α X-ray emission peaks for the fluorine atom shown in Figure 2. 16 corresponding the LK, MK and ML shell transitions of electrons.

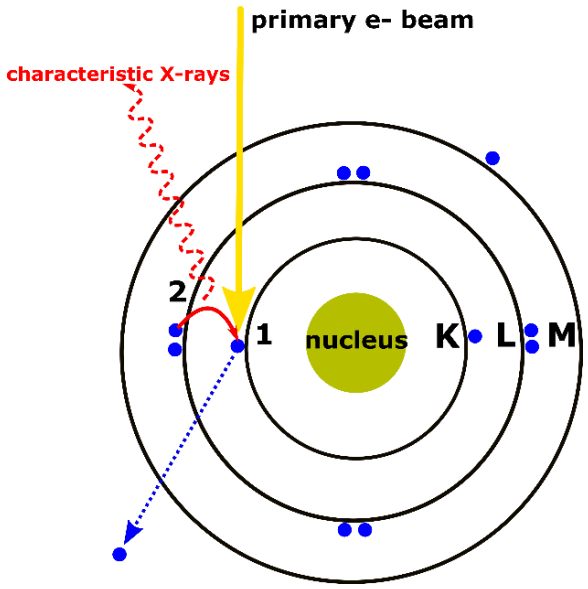

Figure 2. 16.The characteristic X-ray generation process in a fluorine atom [184].

The emitted X-rays can be collected with a silicon drift detector or a thicker Si:Li. The X-ray spectrum or elemental mapping can be used for element identification. EDX can also do quantitative analysis of the element's concentration with good calibration standards [151].

2.19.7 Auger electrons

Auger electrons can also be generated by incident electrons if the energy transferred to sample atoms knocks out core electrons in the sample, e.g. from the K-shell. An electron of higher energy level (L) of target atom will fill the hole. If this energy loss is transferred to another electron in the M shell, this electron in M shell is released as Auger electron as shown in Figure 2. 17. The peaks in the Auger electron spectrum are labelled according to the shells involved in the Auger electron generation. Figure 2. 17 shows the KLM transition.

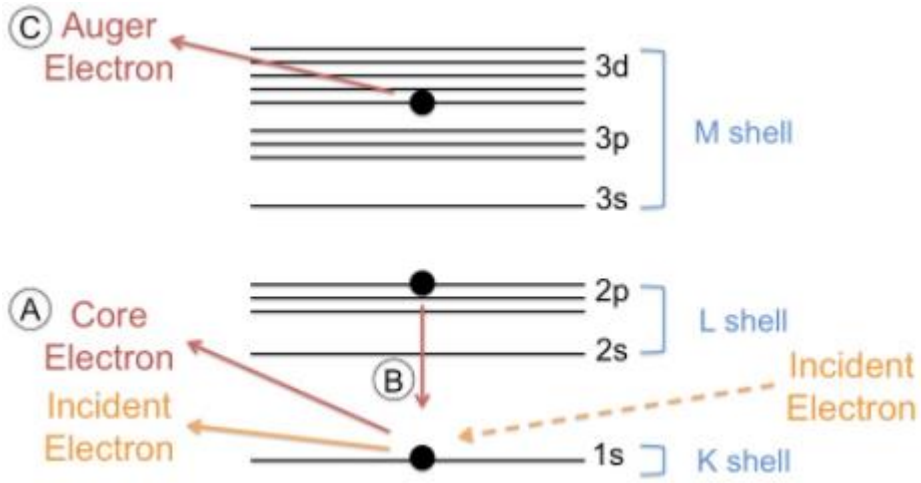

Figure 2. 17 Diagram of the Auger electron generation [185].

2.20 Contamination of the sample during SEM imaging

When the specimen is handled in air, natural-occurring compounds of hydrogen and carbon atoms will be formed on the exposed surface. To avoid hydrocarbon deposition, one can cleave the specimen in UHV and image it directly after cleaving. However, even in UHV the presence of hydrocarbon is

unavoidable. Hydrocarbon molecules can be formed from the diffusion pump and grease of vacuum seal.

Once the electron beam breaks hydrocarbon bonds and H_2O and CO_2 are evaporated, some carbon atoms are left behind in the scan area. Then, thin carbon films of a few nm would be deposited on the specimen surface. As discussed, the SEs have short escape depth, so the SE emission is strongly reduced by carbon contamination and surface oxides. In STEM, the quantification of carbon contamination during observation and its suppression by plasma cleaning has been reported in 2010[186].

The SEMs used in this work have mechanical and turbo pumps. So, in order to have better vacuum condition and minimize carbon contamination, the pumping time applied is longer than the default time. With turbo pump, the vacuum level of 10^{-6} Pa can be achieved. Besides, to reduce charge build up, small beam current is used by selecting the smallest aperture size. The image acquisition time (frame time) is also carefully selected in order to avoid contamination layer build-up while getting good signal-noise ratio. Unfortunately, no liquid nitrogen cold finger or metallic copper seal or ion pump is available for any of the SEMs used in this work.

2.21 Oxidation influence on SEM imaging

The reactivity of oxygen with GaAs under ambient conditions is low, and the multi-layer oxide on the surface will prevent the GaAs be further oxidized [187]. By measure the GaAs [100] surface with X-ray photoelectron spectroscopy(XPS) at 30 and 60^o tile angel, a multi-layer model which contains $Ga(OH)_3$ at outer surface, Ga_2O_3 and As_2O_3 form a glass phase but change to a separate phase in another layer and oxide layer with elemental arsenic atom diffusion is proposed. Under certain conditions, the oxidation of GaAs has been studied as the thin gallium oxide film in metal-oxide-semiconductor (MOS) devices influences the device properties significantly [188]. Hence, the oxide growth under electrochemical environments was studied in [189],[190],[191], [192],[193], and thermal, photo or plasma enhanced oxidation was studied in [194],[195] and [193]. The measurement by X-ray photoelectron spectroscopy of oxide thicknesses grown in air shows that native oxide forms as islands and then builds up to a 2nm thin film [196], and this film shows a multilayer structure of oxides of different phases [187]. For fresh cleaved GaAs, the 1.5nm wide amorphous oxide can be detected under 45^o projection in a high resolution JEOL TEM [197] [198].

The surface oxide will have some influence on the dopant contrast. Experiment of in-situ cleaved Si and Si cleaved in ambient with 3 minutes exposure to air shows that the contrast of a Si p-n junction is 10% for in-situ cleaving while reduced to 5% for ex-situ cleaving [199]. The oxidation speed for Si (111) plane is reported to be 5-7 Å in 5-10 minutes [200]. The secondary electron yield is mainly from the top part of interaction volume, and if we use low accelerating voltage (such as 1kV) the SEs are generated from the top 20 Å of the specimen, which means at least 25% of sample depth is affected by the silicon dioxide.

For GaAs, it is reported that GaAs (100) oxidation process takes ten of hours in dry ambient [201]. Though the oxidation of GaAs is much slower than Si and the 1-2nm surface oxide cannot be prevented, it is still worth to store the sample in vacuum container to avoid further wet oxidation in moist air for reuse of the samples.

2.22 Dopant profiling based on scanning probe microscopy

2.22.1 Scanning tunnelling microscopy and atomic force microscopy

The tunnelling effect was found in the 1930s, however the first successful experiment of tunnelling through a vacuum gap was achieved in 1981 when scientists at IBM Rüschlikon lab solved the vibration problems related to scanning probe microscopy [202]. In their report, the building vibration was avoided by installing the vacuum chamber on a heavy bench floating on rubber tubes. The internal vibrations of the system were minimised by static magnetic levitation of the tunnelling unit. They first performed vacuum tunnelling with controllable tunnel distance for a Pt plate and W tip at room temperature and non-ultrahigh vacuum.

Since then, scanning tunnelling microscopy (STM) has become an effective technique for two-dimensional real space surface studies. For most applications, the fine metal tip is brought near and scanned over the specimen surface, the distance between tip and surface is adjusted to keep the finite and measurable tunnelling current constant.

The tunnel current J_T is sensitive to gap width s, i.e., $J_T \propto V_T \exp(-A\Phi^{1/2}s)$, where Φ is the work function and $A \approx 1$ if distance s is on the scale of Å [203]. For constant tunnel current, the work function changes must be compensated by changes of gap width, s. As in Figure 2. 18, the tunnel distance can be controlled with piezo P_z by changing voltage V_z. That is why STM can be used for measuring the work function.

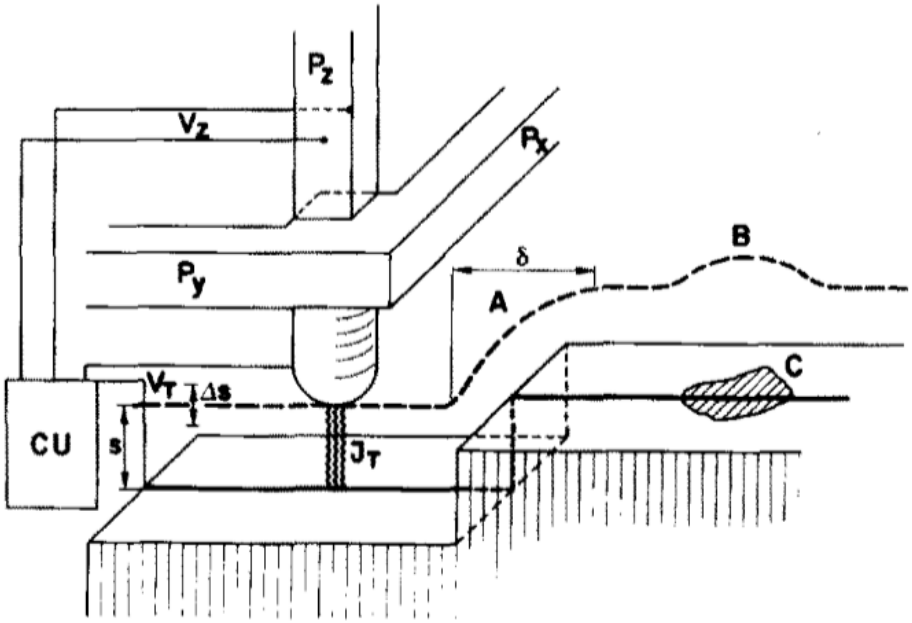

Figure 2. 18. The sketch of STM scanning over a stepped surface. Part CU is a control unit and C is contamination [203].

As Figure 2. 18 shows, the work function shift can be detected by modulating s by Δs with constant tunnelling current. When the tunnelling gap distance is changed by Δs, the response of tunnelling current is ΔI, so the work function can be obtained [204]:

$$\psi = 0.95 \left(\frac{\Delta \ln I}{\Delta s} [\text{Å}] \right)^2 \tag{2.14}$$

Another important factor is the curvature radius of the metal tip. It influences the lateral resolution. Some reports model the tip as a locally spherical potential well as shown in Figure 2. 19.

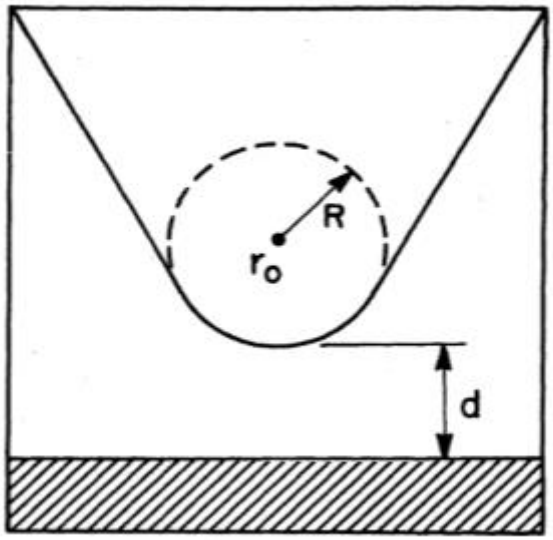

Figure 2. 19.Schematic of the tunnelling metal tip and surface. The tip has arbitrary shape but its end is assumed as spherical [205].

The transition probability P for transfer of an electron from one side to another is [206]:

$$P = \frac{2\pi}{\hbar}|M|^2\rho_f \tag{2.15}$$

where *M* is the transition matrix element and ρ_f is the energy density of final states.

The tunnelling current is [205]:

$$I = \frac{2\pi}{\hbar}\sum_{\mu,v} f(E_\mu)[1 - f(E_v + eV)]|M|^2\delta(E_\mu - E_v), \tag{2.16}$$

If we replace the tip with a point probe, and consider low voltage and room temperature, the current *I* is influenced by the local density of states at E_F.

$$I \propto \sum_v |\varphi_v(\overrightarrow{r_0})|^2\delta(E_v - E_F) \tag{2.17}$$

For tunnelling current calculation, we also need to know the factor $|M|$; Bardeen showed that [206]

$$M_{\mu v} = \frac{\hbar}{2m}\int d\vec{S}(\varphi_\mu^*\vec{\nabla}\varphi_v - \varphi_v\vec{\nabla}\varphi_\mu^*) \tag{2.18}$$

For comparison, Kelvin Probe force microscope (KPFM) was invented in 1991 [207]. This technique is based on an atomic force microscope (AFM) platform and can measure the surface potential difference between two different materials at the nanoscale [208]. KPFM applies a bias between metal tip and sample and detects electrostatic forces bending the cantilever together with the tip-surface interaction. The image is a superposition of the topography and potential distribution of the surface [209].

The electrostatic force between tip and surface at distance *z* and voltage *V* for AFM is:

$$F = \frac{1}{2}\frac{\mathrm{d}C}{\mathrm{d}z}V^2, \tag{2.19}$$

where *C* is the capacitance between sample and tip, *z* is the distance between them.

The applied voltage *V* can be assumed as the sum of [209]

$$V = \left(V_{cp} + V_{dc} + V_{\text{induced}}\right) + V_{ac} \sin \Omega t, \tag{2.20}$$

where V_{cp} is contact potential, V_{dc} is applied dc voltage between tip and sample, V_{induced} is the extra voltage applied to the system and V_{ac} a sinusoidal voltage and Ω is the frequency.

The capacitors between sensor plane and sample surface can be considered as three capacitors in parallel. Then the force can be written as:

$$F = \frac{1}{2}\left(\frac{\mathrm{d}C_{cantilever}}{\mathrm{d}z} + \frac{\mathrm{d}C_{cone}}{\mathrm{d}z} + \frac{\mathrm{d}C_{apex}}{\mathrm{d}z}\right)V^2 \tag{2.21}$$

The best condition requires having just tip to apex interaction involved, in such case the force can be rewritten as

$$F = \pi \varepsilon_0 \left(\frac{r}{z}\right) V^2 \tag{2.22}$$

where *r* is the apex sphere radius (30-50 nm).

Figure 2. 20 shows the STM tip scanning over a sample surface. The tip-surface distance is kept the same to keep the tunnelling current and force constant, the adatom A varies its position along with the AC bias and will modulate the tunnelling current and probe force.

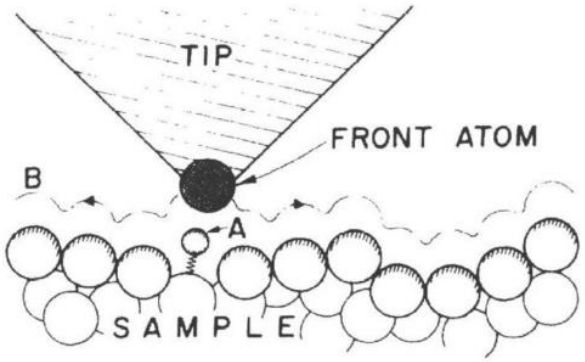

Figure 2. 20. STM tip scanning along the contour B to keep the tunnelling current constant [210].

If the work function of tip and sample surface overlap and the distance *z* is small enough, the electrons can tunnel through the vacuum barrier. When voltage is applied between tip and specimen surface, the tunnelling current can be measured.

STM is an invaluable tool for surface science, however, the limitation is that STM samples must be conductive to make sure current flows between the biased tip and surface. Binnig and his colleagues found that during STM measurements, there are significant forces between atoms and by measuring these forces on the tip, one can obtain an atomic force microscope (AFM) image [210].

Figure 2. 21 shows the basic sketch of an AFM configuration. The tip is mounted on a cantilever, and the atomic force between tip and sample will bend the cantilever. The deflection of cantilever is then detected by a deflection sensor. The most common method of cantilever deflection measurements is the beam-deflection method [210]. Laser light is used to reflect at the back of cantilever and then collected by a position sensitive detector. There are also other methods like: piezoelectric detection [211], Laser Doppler vibrometer [212], capacitive detection [213] and piezo resistive detection [214]. The beam deflection method is most popular due to its simple operation, without any special requirement for cantilever as it does not require electrical contact, and the sensitivity is high [215].

The fine approach to and scanning of the sample are controlled by the piezo scanner. Compared to STM, the tunnelling tip is replaced by the force sensing cantilever with a tip.

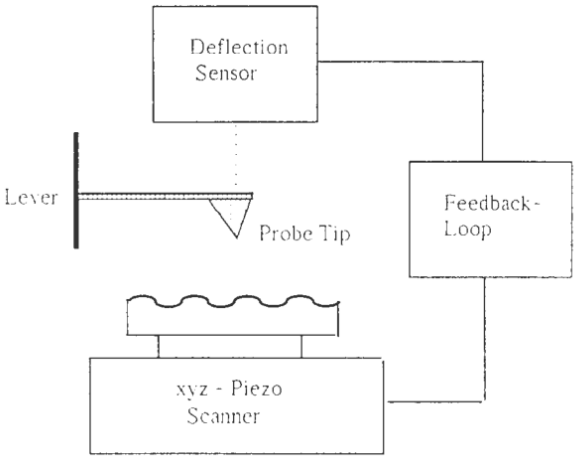

Figure 2. 21. Scheme of an AFM [216].

2.22.2 From conductive AFM to KPFM

As we discussed, the STM provides topography information in relation with the change of tunnelling resistance, thus STM is restricted by the specimen conductivity. When researchers used the atomic force signal to replace the tunnelling current signal, the AFM was developed at IBM [210].

The AFM technique can be expanded to magnetic force microscopy (MFM) [217], electrostatic force microscopy (EFM) [218] and Kelvin probe force microscopy (KPFM) [207] by choosing appropriate AFM tips. STM/AFM based microscopy is often called scanning probe microscopy (SPM).

The quantitative study of surface potential is difficult with EFM as the electrostatic force detected in not only influenced by surface potential but also the capacitance between tip and sample surface. By cooperating Kelvin measurement method into EFM, the surface potential can be obtained by KPFM. The first KPFM measurement reported detection of potential differences of 0.1 mV and spatial resolution of 50nm [207].

2.22.3 Contact potential difference (CPD)

During the KPFM measurement, the contact potential difference (CPD) between the conductive probe and semiconductor surface is recorded. The CPD is a result of the work function difference of the two materials. As we know, the work function is the energy required for removing an electron from material to the vacuum level, with an expression:

$$q\psi = (E_C - E_F) + \chi, \tag{2.23}$$

where χ is the electron affinity which represents the energy needed to remove an electron in the bottom of the CB to vacuum [219]. The typical electron affinity of GaAs is 4.07 eV and Si 1.39 eV [108].

For n-doping and p-doping material, the work function can be estimated by equations below, respectively:

$$q\psi_n = \left(\frac{E_g}{2} - k_B T \ln\frac{N_d}{n_i}\right) + \chi. \tag{2.24}$$

$$q\psi_q = \left(\frac{E_g}{2} + k_B T \ln\frac{n_i}{N_a}\right) + \chi. \tag{2.25}$$

When the electrical contact of two material is made, the free charges will move to align the Fermi energy till equilibrium. A sketch of CPD measurement is shown in Figure 2. 22.

2.22.4 KPFM measurement principle

Kelvin probe force microscopy (KPFM) is widely used in studies of alloys [221], surface analysis [222] and photovoltaic effects in solar cells [223]. As the basic idea of KPFM is to measure the potential difference between the conductive probe and the specimen surface, it is also called surface potential microscopy. KPFM is only possible in a conductive atomic force microscope (AFM) and KPFM is commonly used for nanoscale electrical characterization [224].

KPFM is sensitive to the carrier concentration from 10^{15} to 10^{20} atoms/cm^3 with 100nm lateral resolution for n-doped Si [225]. The resolution of KPFM can be improved to 40nm by using a Si tip coated with gold(Au) for AlGaAs/GaAs multilayer structure [226]. KPFM experiments for GaAs dopant profiling performed in ultra-high vacuum illustrated 20nm resolution [227]. The spatial resolution of KPFM has achieved atomic level [163] and the energy resolution can be 5-20meV [228]. However, the charges at sample surface and the calibration accuracy will influence the quantification of doping concentration [229]. Compared with a standard SEM, KPFM has a spatial resolution of 10nm [163] and the work function shift is measured by detecting the contact potential difference (CPD).

Figure 2. 22 shows how to measure the work function by Kelvin probe.

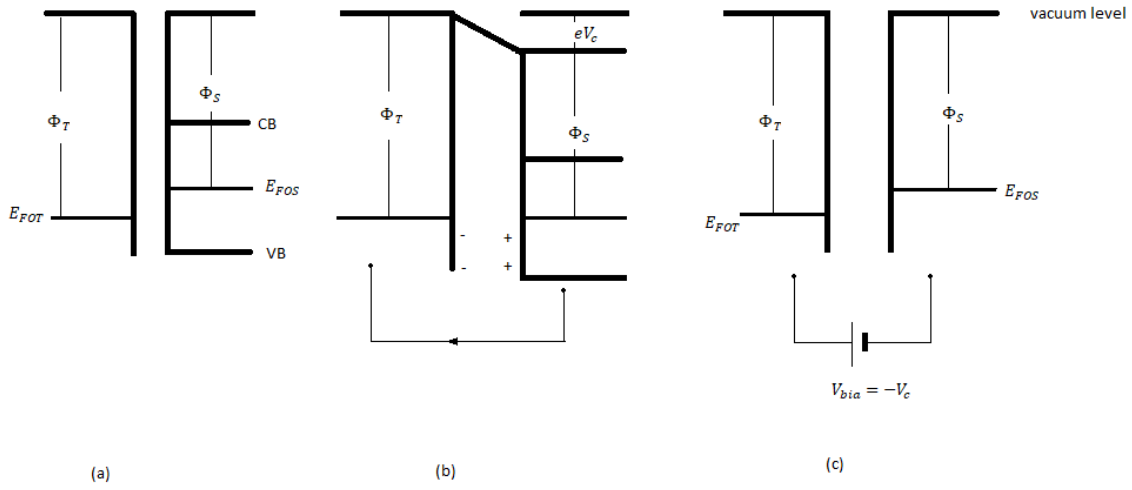

Figure 2. 22. Energy diagrams for measuring contact potential difference. (a) metal tip (left) and semiconductor specimen (right) without connection. (b) electrical contact between tip and specimen. Electrons flow from low work function to high work function to equalize the Fermi levels, EF0. (c) external bias applied to the capacitor to neutralize any charges at the interface.

As shown in Figure 2. 22(a), a metal tip with work function Φ_T has been brought near to a semiconductor with work function Φ_S. In Figure 2. 22(b), the metal tip and semiconductor have been connected and electrons flow from the semiconductor to the metal to make Fermi energies the same on either side. This leaves holes behind in the semiconductor, indicated as positive charges. The potential between two materials is established like a capacitor and this potential is equal to the work function difference between both materials. This potential V_c is called contact potential difference (CPD) or surface potential. In Figure 2. 22(c), a bias is applied to the capacitor to make the surface charges disappear. Now we get:

$$eV_{bias} = -eV_c = \Phi_s - \Phi_T \tag{2.26}$$

When applying a superposition of a DC and an AC voltage to the AFM tip, the AC voltage generates oscillations of the tip and changes the capacitance and electrostatic force as the tip-surface distance z changes, the DC voltage nullifies the forces from CPD. If ΔV is the potential difference between tip and surface, we get:

$$\Delta V = V_{app} - V_C = V_{DC} - V_C + V_{AC}\sin(\omega t), \tag{2.27}$$

where V_{app} is the applied voltage that is the sum of DC voltage V_{DC} and AC voltage $V_{AC}\sin(\omega t)$.

The electrostatic force F_{el} is related to ΔV and the capacitance gradient $\partial C/\partial z$ between tip and surface:

$$F_{el} = -\frac{1}{2}\Delta V^2 \frac{\partial C}{\partial z} \tag{2.28}$$

This equation consists of three parts when inserting the above expression for ΔV:

$$F_{el} = F_{DC} + F_{\omega} + F_{2\omega}, \tag{2.29}$$

$$F_{DC} = -\frac{\partial C}{\partial z}\left[\frac{1}{2}(V_{DC} - V_C)^2\right] \tag{2.30}$$

$$F_{\omega} = -\frac{\partial C}{\partial z}(V_{DC} - V_C)V_{AC}\sin(\omega t) \tag{2.31}$$

$$F_{2\omega} = -\frac{1}{4}\frac{\partial C}{\partial z}V_{AC}^2[1 - \cos(2\omega t)] \tag{2.32}$$

The electrostatic force will influence the oscillation of the AFM cantilever with applied voltage V_{app}. KPFM uses a lock-in amplifier to extract the term F_{ω}. The output signal of the lock-in amplifier is proportional to the difference between V_{DC} and V_C. When the output signal is nullified and F_{ω} is adjusted to zero, V_C equals the applied voltage V_{DC}. To form a surface potential map, the value of V_{DC} is acquired for every point of the surface.

KPFM can be divided into amplitude modulation KPFM and frequency modulation KPFM [230], [231]. It is based on whether KPMF modulates the amplitude of the cantilever oscillation or the resonant frequency of the cantilever.

However, KPFM has its disadvantages. First, for measuring the surface potential using KPFM one needs to know the work function of the probe. This means the KPFM probe must be calibrated very well to guarantee accuracy [232]. KPFM also requires a flat surface, e.g. in the form of a well cleaved facet of the specimen, as an abrupt change in topography will influence the capacitance gradient and disturb the measurement [233]. Besides, KPFM measures the averaged surface potential over a finite area, so any surface topography information or height difference on the sample surface may reduce the accuracy of measurement and the work function of the probe needs to be calibrated carefully [232], [234].

3 Experimental methods on dopant profiling in FEGSEM

3.1 Description of samples grown by molecular beam epitaxy

Undoped GaAs substrates of 2 inches diameter and 350μm thickness have been used for growing the samples by Dr. Shiyong Zhang in the Semiconductor Materials and Devices group in the Department of Electronic & Electrical Engineering, University of Sheffield. First, the substrate was baked at 600°C to remove the surface oxide layer, then 4 doped layers were grown at 580°C by supplying Ga, As and dopant (Be or Si) at the same time for the doped layers. The growth rate was estimated as 0.5 monolayers/second (1/4 of the lattice constant). The doping concentration of each layer was controlled by the temperature of the effusion cells. For the staircase samples, no cap layer was grown. The LED sample VN790 has been supplied by Dr Kristian Groom, also from the University of Sheffield.

3.2 Sample description

Figure 3. 1 reports the structure of the two differently doped GaAs samples studied. The layers we are interested in are 200-300nm thin, and the substrate is much thicker than the layers. Prior to cleaving small pieces from these specimens, the substrates need to be thinned from their back sides by mechanical grinding to a remaining thickness in the range around 0.1mm.

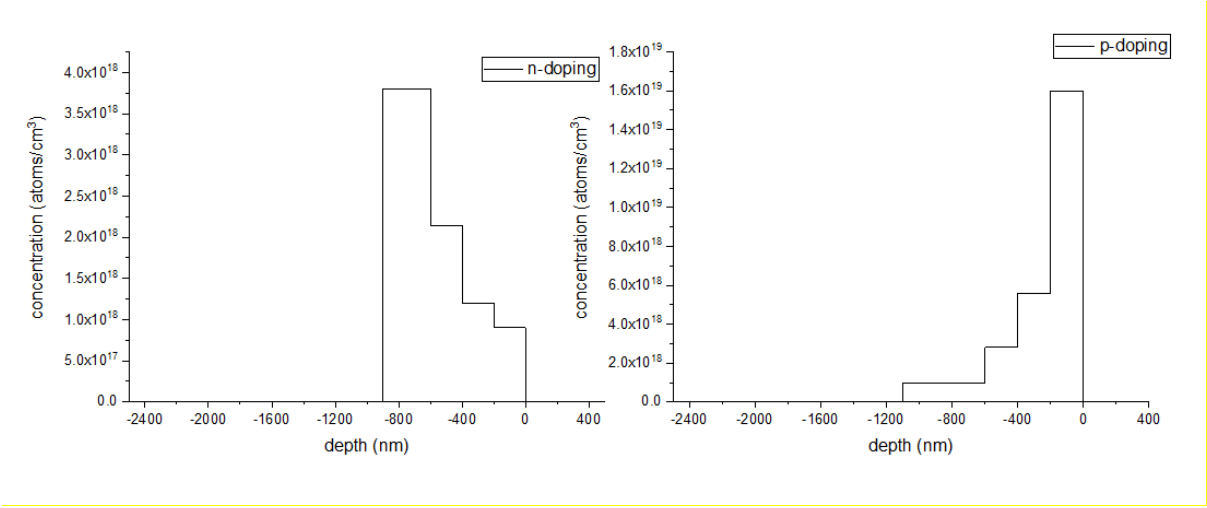

Figure 3. 1: The nominal doping concentration versus depth for differently doped GaAs staircase samples, the growth direction is left to right.

3.3 Sample preparation for SEM and AFM imaging

3.3.1 Specimen thinning by mechanical grinding and polishing

The first thickness reduction by grinding was done by fixing the samples to a standard metal or glass cylinder. First, one needs to heat the cylinder, put a little mounting wax on the glass slide and mount the GaAs block for grinding and polishing the substrate back side to make the wafer piece thin enough for cleaving. Grinding started with 400 grit silicon carbide paper. No force should be applied to the cylinder during the process. When grinding, one should hold the cylinder horizontally and move it in a trajectory of "∞". The thickness changes can be measured by a micrometre screw. The grinding paper and rotation speed for polishing should be changed as the specimen becomes gradually thinner.

polishing paper grit	specimen thickness (µm)	rotation speed (rpm)
400	500-1000	90
800	300-500	80
1600	200-300	70
2400	100-200	60
4000	<100	60

Table 3.1: overview of the polishing paper and rotation speed selection relative to specimen thickness.

After grinding by 4000 grit paper, the specimen should be removed from the cylinder and be washed with solvents very carefully. N-butyl acetate is first used as it has high solvency power, then acetone is used for removing the remaining organic substances, following by isopropanol and, finally, the sample was cleaned with ethanol which has highest purity level (>99.9%) to minimise any contamination.

3.3.2 Manual cleavage

As the diameter of both bulk GaAs substrates is 2 inches, wafer pieces must be cut into smaller sizes in the first step.

The specimen cleaving process is depicted in Figure 3. 2. All cleaving is performed on a rubber pad in the fume cupboard. The reason for using a rubber pad is that rubber is soft, easy to clean, and it will not move during cleaving. The scratch direction should follow the lattice orientation as the fracture will preferentially be along <100> directions with {110} type facets for zinc-blende or sphalerite structure. One may need several iterations to get the desired cleavage size with clean and cleaved GaAs (110) surfaces. In this work, the cleaved pieces are about 2 mm wide and 4mm long, so it is best to use a ruler for marking the cleavage positions.

As GaAs single crystal has zinc-blende structure, the scribe can break GaAs wafer pieces easily if the scribe lines are aligned with the preferential {110} cleaving planes. The (110) plane is orthogonal to (001). That means when scribing the (001) growth plane of GaAs wafer along [110] direction as shown in Figure 3. 2 below, the crack of scribe line propagates along (110) and $(1\bar{1}0)$ cleavage planes.

The cleavage of a Si wafer is more difficult due to the diamond structure that needs higher cleavage energy compared to GaAs. For GaAs it takes 1 J/m^2 to cleave a (110) plane [235]. For GaAs wafer, {110} planes are the preferential cleavage planes, as <110> orientation is the intersection of (001) plane and {111} planes, where the {111} slip planes are easier to generate dislocation and plastic deformation[236]. A Si wafer can be cleaved along <110> or <111> directions [237]. For Si wafer, cleavages in <111> type directions are preferred as crack propagation in {111} planes need less surface (cleavage) energy (1.36 J/m^2) than cleaving energy of 1.69 J/m^2 in {110} planes and 1.71 J/m^2 in {100} planes[238].

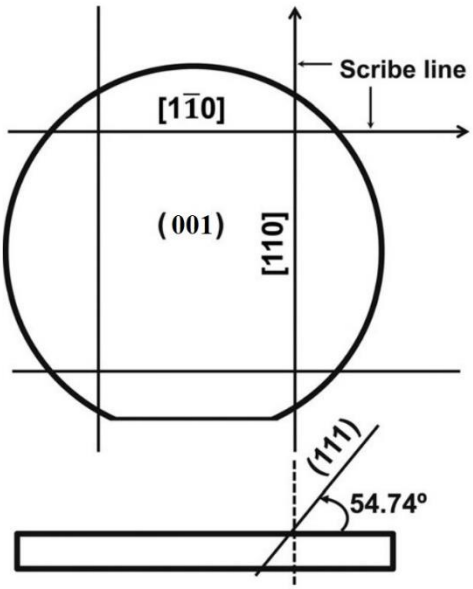

Figure 3. 2. The scribe lines of GaAs and Si (001) wafers [239].

The <110> directions are identified by the perpendicular direction of the primary orientation flat (OF) of the wafer. By the cleaving process, dust is generated. One must clean the rubber pad for the next steps. All GaAs waste generated during the cleaving should go into the red rubbish bin for toxic waste. When breaking small pieces of wafer, like 5mm*5mm, toothpicks are used to press at the back side of the pieces. The tips of fine tweeters are quite shape and the force at the contact point of the tip and sample would be too large.

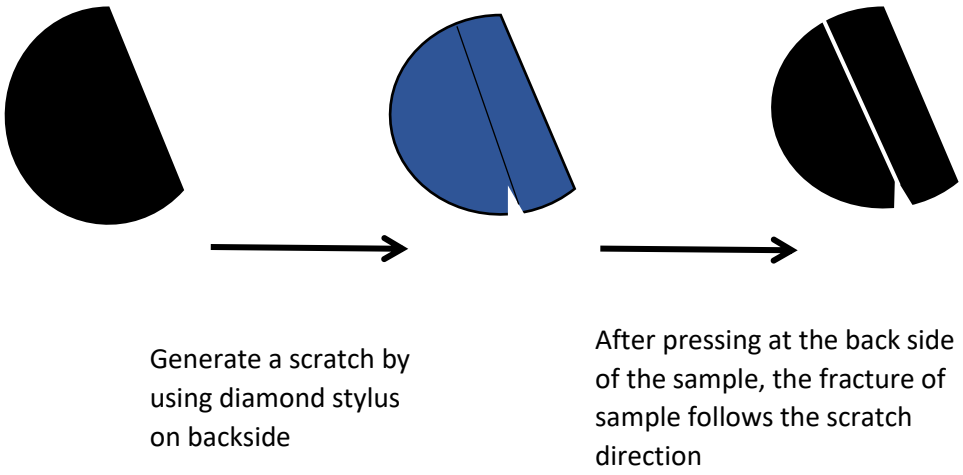

Figure 3. 3. Specimen cleaving process.

3.3.3 Ion milling

The ion milling systems use ionized argon ions to sputter the sample surface, the material on sample surface will be removed, making the surface flatter. Compared to cutting and polishing, ion milling can make extremely flat surfaces without artefacts like scratches, smearing or other damages. Ion milling is a popular method for specimen preparation for electron microscopy as it is fast and convenient [240] but it is not suggested as preparation method for our samples.

Due to ionized ions bombarding the material surface, after ion milling, the immediate surface crystal structure is destroyed and becomes amorphous. This amorphous layer can be 20nm thick for 1kV ion beam and would be 500nm for 10kV as shown in Figure 3. 7, while the interaction volume of secondary electrons for low-kV SEM is even smaller than this depth, which means SE contrast will disappear. Figure 3. 4 is an SE image of the Si doped staircase sample after argon ion milling, showing no contrast from the 200nm doped layers.

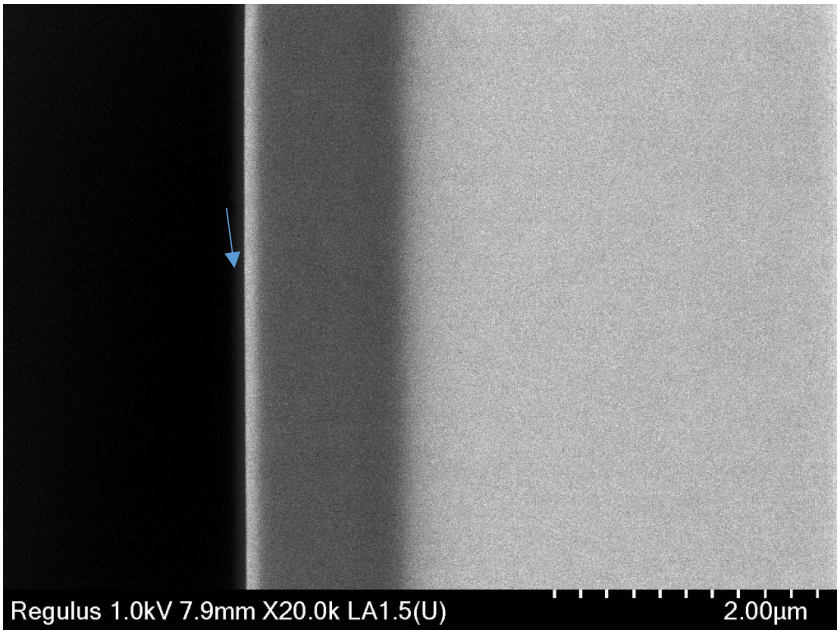

Figure 3. 4. Si doped GaAs staircase sample after ion milling (argon ions,10kV) with shallow angle (5° to surface,85°incident angle) for 5mins. Image from Dan Yukari, Hitachi. Arrow points to sample edge.

As discussed in Chapter 2, the SEs are emitted from the top of the interaction volume, especially for low voltage SEM, and the SE escape depth is only several nm from the surface. When the surface is treated with ion milling, the ion range is much larger than the SE escape depth. Here, we used the Stopping and Range of Ions in Matter (SRIM) software [241] to explore the ion milling effect. The incident angle is 0° when beam is normal incident to the surface.

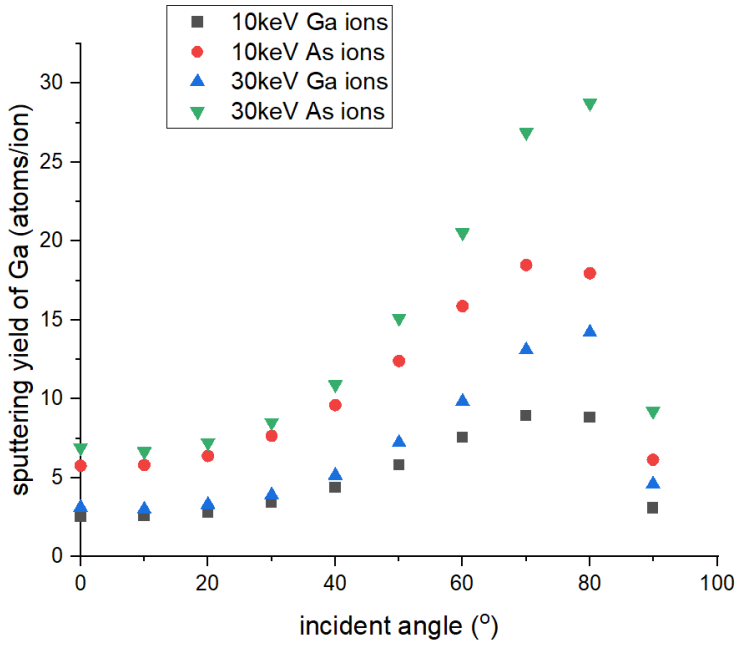

Figure 3. 5. The sputtering yield of Ga atoms from GaAs target for Ar+ ion bombardment from vertical incidence (0°) to specular incidence (90°). The sputtering yield is decreased at large incident angle due to the reduction of momentum transfer.

Figure 3. 5 shows that the sputter yield of 30 keV ions is always higher than that for 10 keV ions. This is due to higher energy ions producing more inelastic scattering events before they have lost so much of their energy that they cannot knock off any more target atoms and are stopped in the material. As atoms always have a higher sputtering yield than Ga atoms due to the surface binding energy of As atoms being less than that of Ga atoms [241], [242], meaning it is easier for As atoms to leave the surface.

The As atom sputtering yield is increasing from 0-80° and decreasing from 80-89.9°. The sputter yield is related to two mechanisms; the first mechanism is that the primary ion knocks off a surface atom directly, the second mechanism is that the ions are reflected inside the target and create recoils of target atoms at the surface.

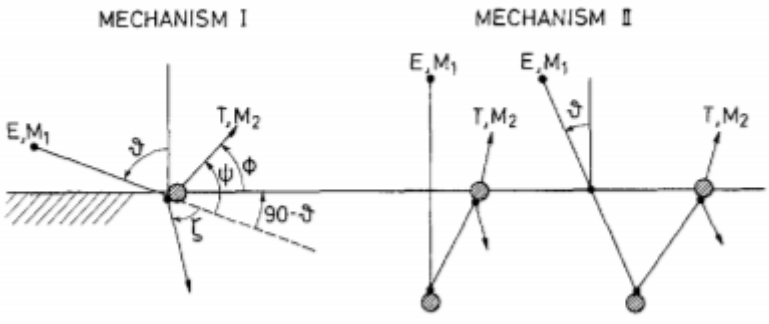

Figure 3. 6. Atom sputtering mechanism for light ions [243].

If the ion beam is incident normally, the second mechanism is more efficient than the first because the first mechanism reflects ions back with small energy transfer. If the projection of the incident angle on the surface is larger, more momentum is transferred onto the surface and

the first mechanism dominates sputtering, hence the probability of a surface atom to get enough energy for being sputtered by direct knock out is relatively increased.

The decrease of As atom sputtering yield at angles from 80-89.9° can be explained by the increasing reflection of incident ions at the specimen surface. Light incident ions are mostly reflected at the first layer of target atoms, as has been proved by simulation [244]. Besides, at glancing angles, the momentum transfer of incident ions to target atoms is small, so target ions cannot get enough energy to be sputtered. The explanation for the Ga atom sputtering yield decreasing from 70° is similar.

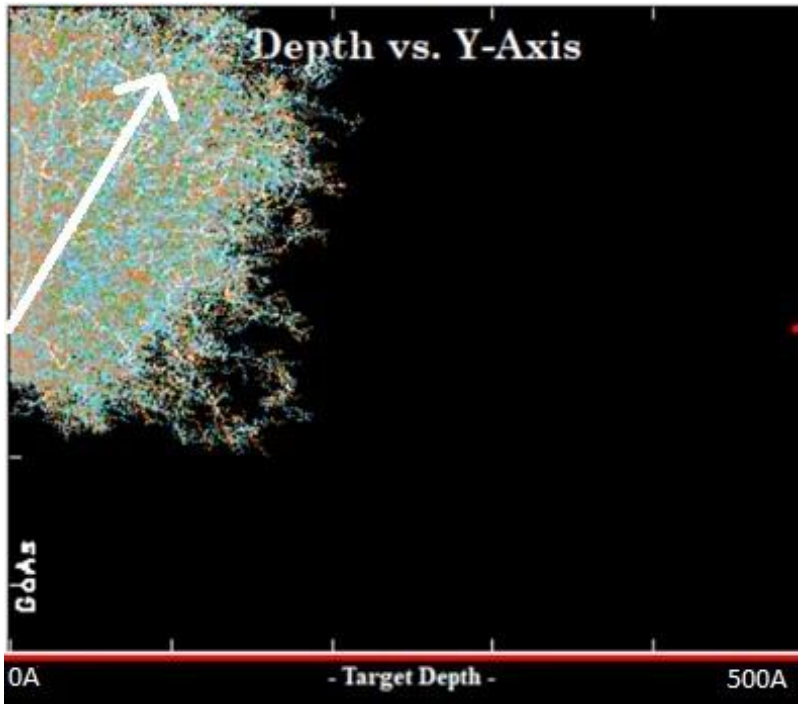

Figure 3. 7. The ion range of Ar+ ion milling GaAs target at shallow angle. The white arrow indicates the direction of incidence.

The ion range is 20 nm for 10kV Ar^+ ion milling of GaAs target at shallow angle, which is much higher than the SE escape depth. The damage depth due to ion milling is much larger than the SE yield depth which is the reason why the contrast of layers disappears in Figure 3. 4.

3.3.1 Mounting specimen on pin stubs for SEM observation

For observation, the cleaved specimen pieces are mounted onto standard JEOL SEM stubs by adhesive carbon pads, so that the {110} cleavage surfaces can be observed without much tilt. The mounting strategy is to mount the longest VN790 samples (5 mm length and 75 μm thickness) as a reference in the centre. The three samples (2 mm length and 200 μm thickness) on the left, perpendicular to the VN790 samples, are the Be doped samples with region of interest (ROI) towards the bottom edge. Another four samples (3 mm length and 100 μm thickness) on the right are Si doped samples with ROI towards the top edges.

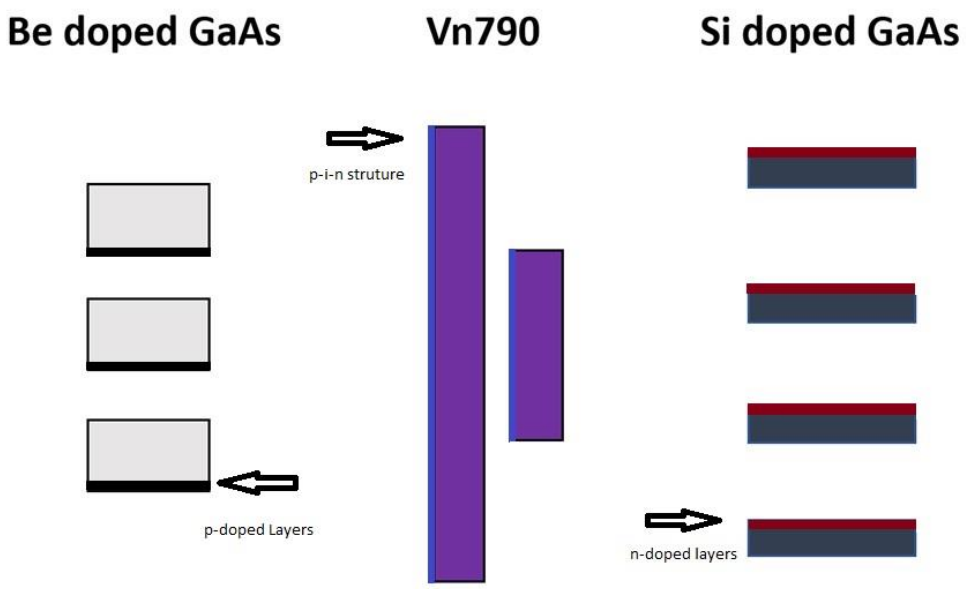

Figure 3. 8. Schematic of top view of the mounted specimen on a stub with carbon conductive adhesion pad. The arrows are pointed to the doped layers of interest, where black region is p-doped layers, blue region is the p-i-n structure and red region represents n-doped layers.

3.4 SEM specifics

The field emission SEM used in this work is a Raith FEG-SEM EO 1530 operating with SmartSEM software provided by Zeiss. Its schematic is plotted in Figure 3. 9. The pixel averaging method (image build-up by scanning every pixel for one time at controlled scan speed) is used for scanning a single frame. The time of scanning a frame is controlled by a scan speed parameter, *n*. If the number *n* describing the scan speed gets higher, the scan speed actually becomes lower. The dwell time per pixel in ns is given by $100 \times 2^{n-1}$. The product of beam current with exposure time gives the accumulated electron dose. For example, if we used scan speed 6 and the beam current is 100pA, the dwell time per pixel would be 3.2μs, scanning a single frame of 1024×768 pixels (7148nm×5360nm area) will take 2.6s and the accumulated electron does is [245]:

$$N_{does} = \frac{I_B t}{qA} = 4.24 \times 10^{19} \text{ electrons/nm}^{-2}$$

The carbon contamination experiment was performed with Hitachi Desktop SEM TM3030 plus [246]. Also, some experiments with bias electrode in the pole-piece were demonstrated by Yukari Dan with the address Hitachi High-Tech Europe, Sci-Tech Daresbury, Cheshire, WA4 5LY.

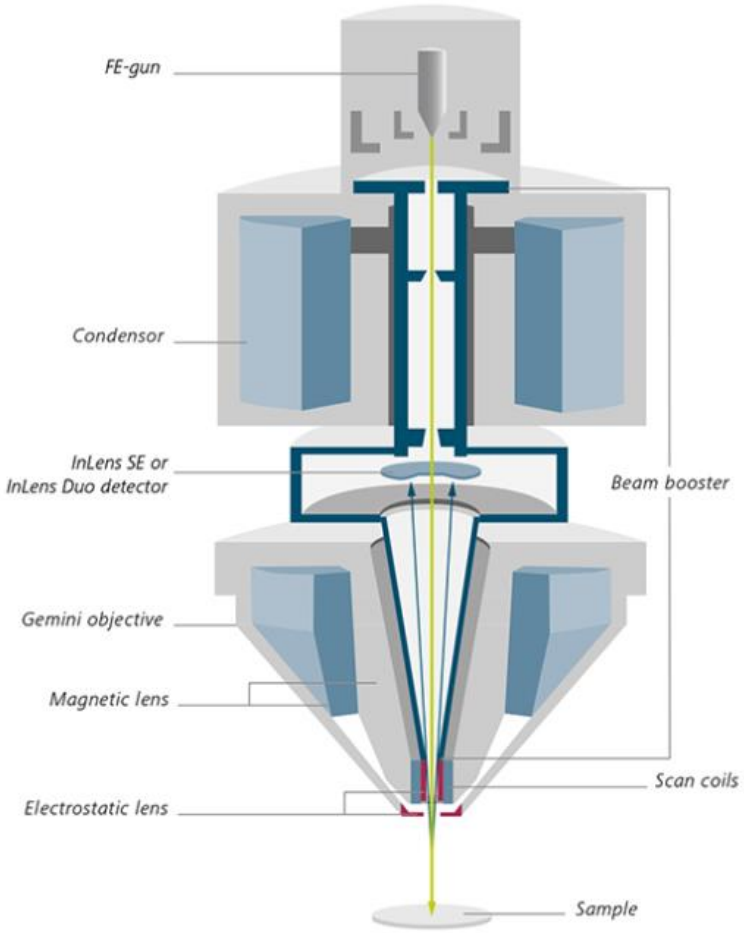

Figure 3. 9. The schematic of Raith SEM[247].

The relationship between the aperture size and electron dose for scan speed 6 single frame scan with area of 7148nm×5360nm is listed in Table 5.

Condenser aperture diameter (μm)	Beam current (pA)	Electron dose
7.5	6.25	2.65×10^{18}
10	11.11	4.71×10^{18}
15	25.0	1.06×10^{19}
20	44.44	1.88×10^{19}

Table 3. 1. The relationship of condenser aperture size and beam current.

3.5 Sample transfer and storage

After the sample is mounted on to standard SEM stub, it is put into a storage tube for pin stubs. The storage tube can shield the specimen on the stubs, so that they will not be touched by someone's finger accidently and thereby preventing contaminating the sample. And it will also protect the sample from collision with the vacuum container during sample transfer between the sample preparation laboratory and SEM laboratories. The GaAs sample is very fragile with less than 100μm thickness used in this work, and as the cleaved specimen is smaller than 2mmx2mm, attention should be paid to prevent touching the surface and specimen edges and corners when using tweezers.

The container used for fast sample transfer between labs has a hand pump. The vacuum level is not as good as in a sealed container for sample storage with an electrical pump. However, the oxidation of GaAs in air is slow as discussed in section 2.21, it is sufficient to do fast transfer so that samples can be reused if necessary. The sample exposure time to ambient is typically less than 3min. The sample may not suffer from much oxidation during transfer process as it takes ten of hours for oxide layer build up on GaAs, but 1.1-1.5nm surface oxide cannot be avoid by all means if the cleaving surface be exposure to the air shown in Thomas' previous work[197].

3.6 Deposition of Carbon contamination

When the electron beam scans an area for long time, a thin layer of hydrocarbon will be deposited on the sample surface. This experiment is designed for explore the relationship between carbon layer thicknesses and scanning time. In this experiment with Hitachi TM3030 plus, the scanning window is successively increased from 60kX, 30kX, 15kX, 7kX to 4kX (as the scanned area is increased when decreasing the mag), and each window is scanned for 30 minutes using 15kV voltage.

The thickness of carbon contamination during electron beam irritation has been measured by AFM.

3.7 AFM based measurement

3.7.1 The resistive AFM principle

The resistive AFM experiments were performed on both doping staircase samples and one p-i-n structure LED sample at CSI instrument, France. The aim is to measure the doping concentration and to compare AFM results with SEM results. The resistivity of intrinsic GaAs is quite high at room temperature. First, the intrinsic carrier concentration of GaAs is 2.1×10^6 cm^{-3} [248]. The low intrinsic concentration of carriers makes GaAs crystals 'semi-insulating' with a specific resistivity of 10^7-10^9 Ω.cm. This resistivity is larger than that of Si, but still smaller than that of insulators like silicon dioxide and glass [249].

The resistive AFM is a kind of probe station for local conduction measurement: a voltage is applied between cantilever tip and specimen while the probe is in contact mode; then the tip is stationary at any point before being moved to the next point to get the current map of the selected region. The changes of current and resistance are recorded by an external amplifier, and a digital signal processor will choose the gain to optimize the measurement. The resistance detection range for resistive AFM with a high performance amplifier (HPA) can be 10^2 -10^{12} Ω [250].

The first resistive AFM experiment was achieved in 1993 in studies of the local tunnelling current through a thick silicon dioxide layer [251]. Since the first resistive AFM on metal surfaces in 1996 [252], resistive AFM has become more and more popular in semiconductor research, for characterising Si solar cells [253], heterojunctions [254], GaAs nanowires [255] and so on. Generally, resistive AFM measurements can investigate the effect of local changes of the electrical properties, such as doping [256] or dielectric properties [257], [258].

The GaAs samples were again prepared by manual cleavage, and then the samples were mounted onto a metal disc with a conductive carbon pad. It is necessary for the bottom of sample to make good electrical contact with the metal disc. The current flow from tip to sample (or sample to tip, depending on the bias) is the product of current density and the effective area (which is limited by the tip size and local resistivity) through which electrons can flow. The resistance measured by resistive AFM is the current passing from top of the sample contacted with the probe to the bottom of the sample contacted by an electrode [259]. As a constant voltage is applied between the tip and the metal disc

carrying the sample, the local current through the cantilever tip is measured as well as the surface topography information if the tip is moved.

As most of SPM techniques, the lateral resolution of resistive AFM is high. At the beginning of the development of instrumentation, 8 nm spatial resolution of native oxide film grown on p-type Si (100) substrate has been demonstrated [260]. A recent study of the local conductivity of titanium dioxide crystal surface in UHV has demonstrated atomic resolution [261].

As resistive AFM requires conductive probes and can work in contact mode or in tapping mode, probes for resistive AFM are not only more expensive but also wear out faster than traditional AFM tips. The degradation of conductive AFM tips increases the cost of experiments and reduces the reliability of data. There are many types tips for resistive AFM, such as the standard Si cantilever coated with approximately 100nm of metal thin film [251], Si probe coated with doped diamond [262] or Si probe coated with graphene [263].

The CAFM experiment was performed by Emmanuel Lepleux, from CSI instrument in Paris. The instrument is Nano-Observer AFM microscope. A diamond coated conductive Si tip is used. The tip bias is alternating current (AC) of 1.71nA with 5.14×10^{4} Hz, the sample is biased with 4.9×10^{-7} V with one side grounded to earth.

3.7.2 Surface potential mapping by KPFM

Frequency modulated Kelvin probe force microscopy (FM-KPFM) is used in this study to investigate the surface potential of the doped GaAs cleaved {110} type facets. FM-KPFM is a kind of tapping mode AFM where the cantilever is oscillating at its resonance frequency. If there is no interaction between tip and surface, the cantilever's resonance frequency will be constant. When the tip is brought near to a specimen surface, the cantilever oscillation will be changed and can be detected by a photodetector with lock-in amplifier, and the signal will be fed back into the servo motor to control the height of tip above the specimen surface.

Amplitude-modulated KPFM is a two-pass procedure where the surface topography is obtained by tapping mode AFM in a first loop and the potential is detected in a second loop. The sketch below in Figure 3. 10 shows the schemes of FM-KPFM and AM-KPFM.

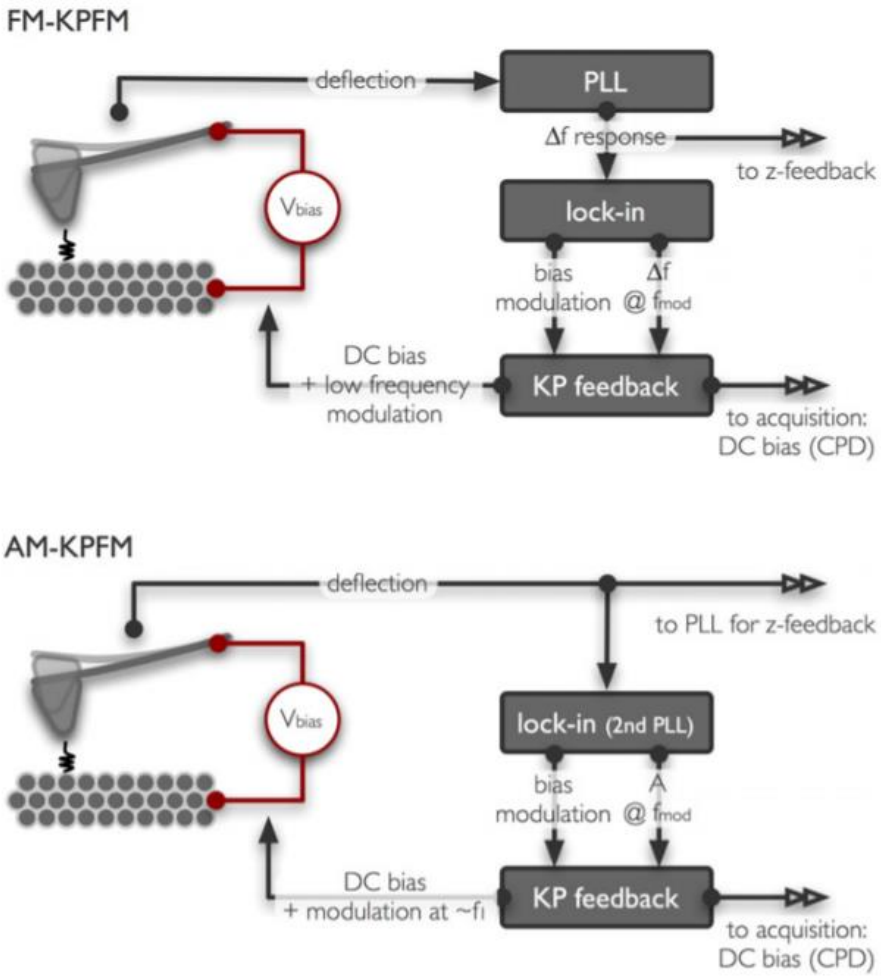

Figure 3. 10. FM-KPFM and AM-KPFM loop.

The specimen is mounted vertically onto a conductive metal plate with carbon conductive pad as shown in Figure 3. 11. Not all of the samples were investigated in first instance and the Si (n-type) and Be doped (p-type) samples did not show good contrast due to oxidation of the surface in humid air. The scan rate used was 0.5Hz, the cantilever height was 350nm above the sample.

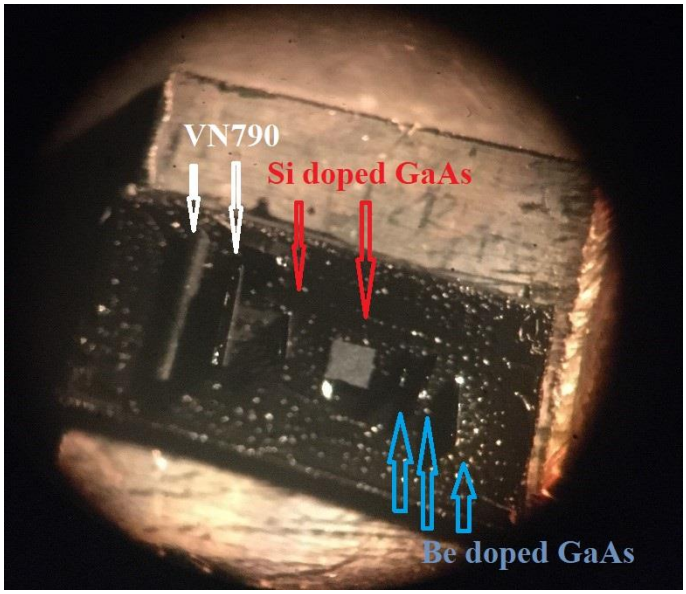

Figure 3. 11. Overview micrograph, taken through the eyepiece of an optical microscope . The samples were mounted on to a piece of Al metal cleaned by 99.9% acetone in the following sequence from left to right: VN790, Si doped GaAs and Be doped GaAs.

The KPFM images are acquired using a Park NX20 AFM in sideband KPFM mode by Dr Vladimir Korolkov from Park System UK Ltd, Nottingham. The cantilever used was a Multi75G Si tip without coating.

4 SE dopant contrast mechanism

4.1 Monte Carlo simulation of SE yield of doped GaAs at different voltages

The simulation results by CASINO version 3 [147] of backscattered electron (BSE) coefficient and secondary electron (SE) yield for different doping levels from percent level down to part per trillion (ppt) level have been shown in Figure 4. 1 and Figure 4. 2.

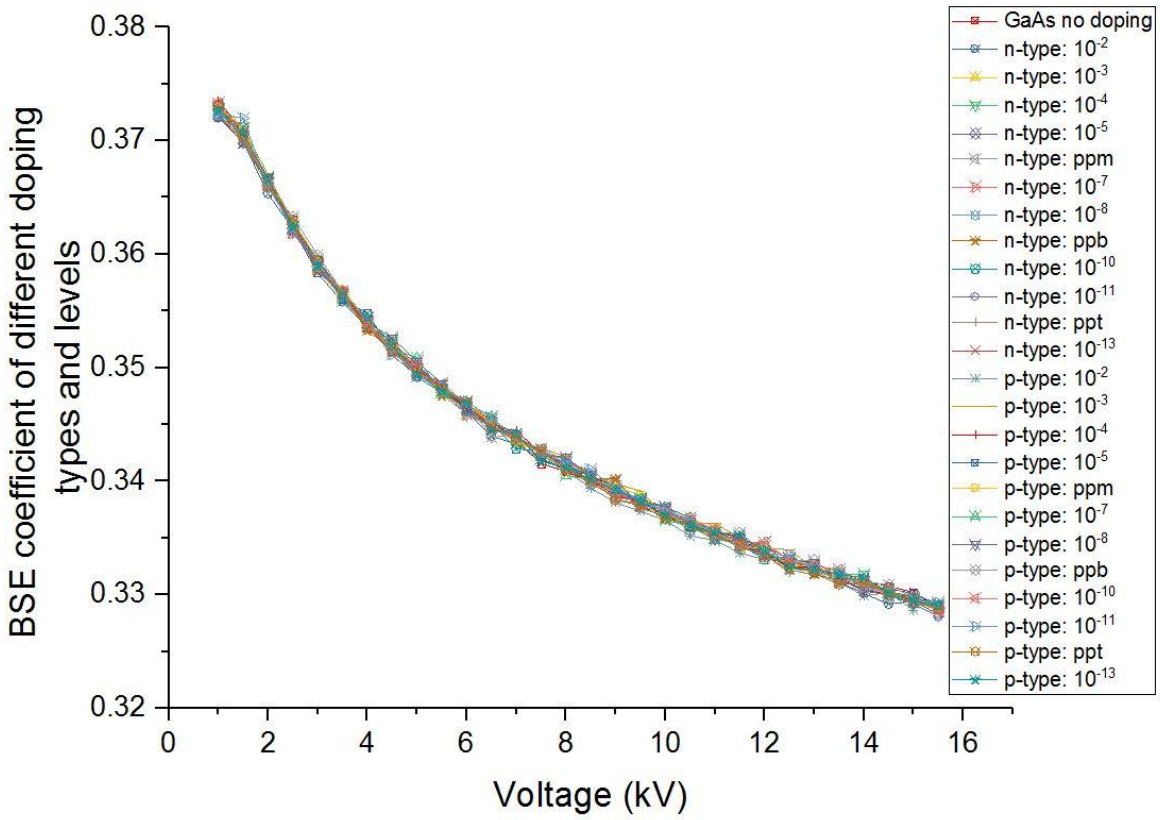

Figure 4. 1. Backscattering coefficient, η, simulated as a function of accelerating voltage for normal incidence for differently doped GaAs by CASINO_3.3. For the simulation parameters of intrinsic GaAs, its density is 5.32 g/cm³, work function is 4.77eV, 10nm beam diameter with Gaussian distribution, 2000000 simulated electrons , Monsel model for cross section and ionisation potential.

From Figure 4. 1, it is clear that the BSE coefficient η is decreasing with increasing electron energy. Besides, we notice that different doping types and levels have negligible influence on the BSE yield within statistics as the average scattering power and density remain basically unchanged.

Figure 4. 2 is a double-logarithmic plot of the SE yield versus primary electron energy for homogeneously doped GaAs. It demonstrates the SE emission is strongly depending on the acceleration voltage. When the number of n-type dopants in GaAs increases, the SE yield is predicted to become larger because the work function is reduced by n-doping. For p-doping, the work function gets larger and SE yield decreases when concentrations go higher. This only holds, however, if the complete specimen is uniformly doped and there are no surface charges.

The relationship between SE yield, δ, and primary electron energy, *E,* can be expressed as $\delta \propto E^{\alpha}$, where α is the slope of the double-logarithmic plot. In this simulation, the slope $\alpha \approx -0.960 \pm 0.0017$ (with R^2=0.9999) obtained here for GaAs is larger than the value in Reimer's book that reports

the slope α is –0.8 for Al and Cu [75]. This is because the SE yield is increases monotonically with atomic number Z and saturates when Z is several tens (Z>50)[264].

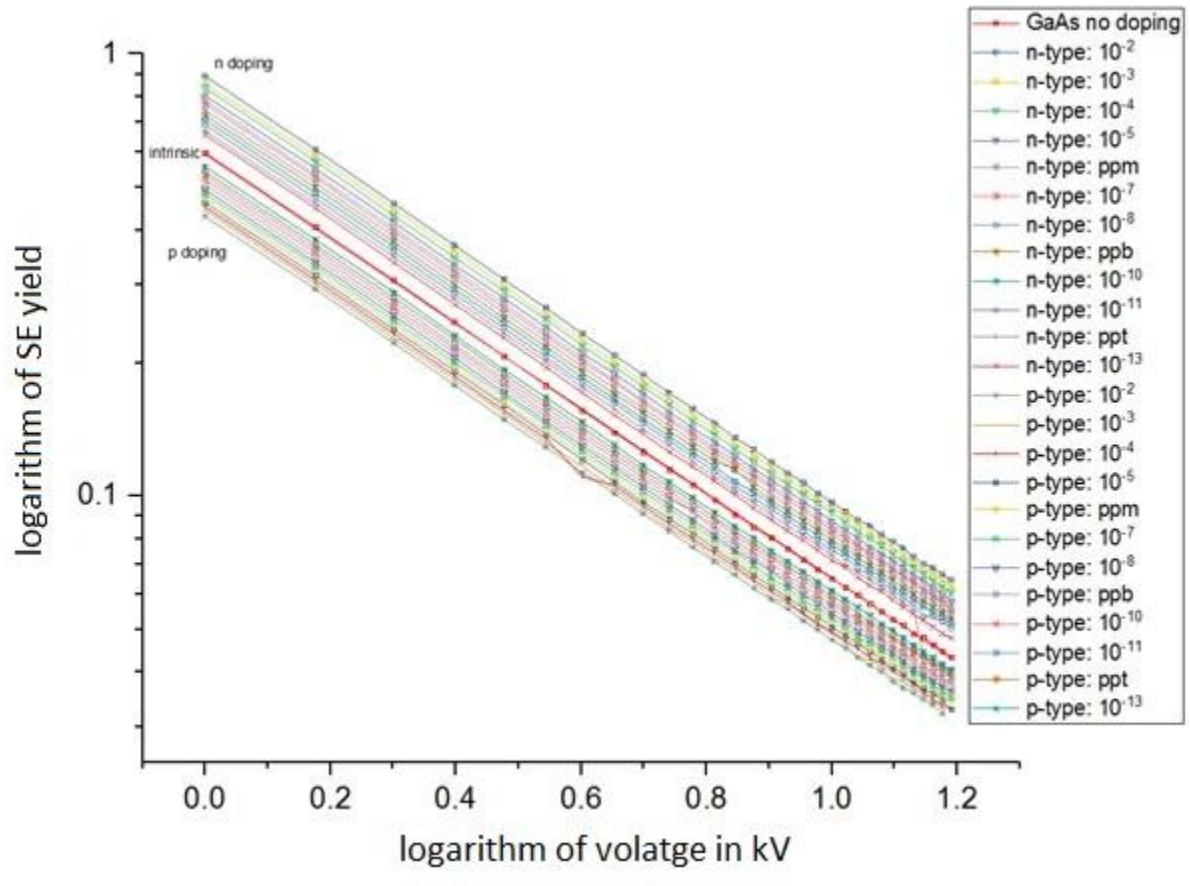

Figure 4. 2. Decrease of the SE yield with increasing electron acceleration voltage for different doping types and concentrations. Simulation parameters are the same with those in Figure 4.1.

4.2 SE imaging of doped GaAs at various voltages

4.2.1 Be doped GaAs sample

The Be doped GaAs staircase sample has been imaged by pixel average method using 9 frames. Without much drift, 9 frames could be averaged to get one noise reduced image. Thus, a total of 10 images would be recorded for each scan area. The nominal aperture size used was 7.5µm, which provides the smallest electron radiation dose as semi-insulating GaAs is quite sensitive to the beam.

A side sketch of the sample is shown in Figure 4. 3 for better understanding of the geometry of the staircase sample.

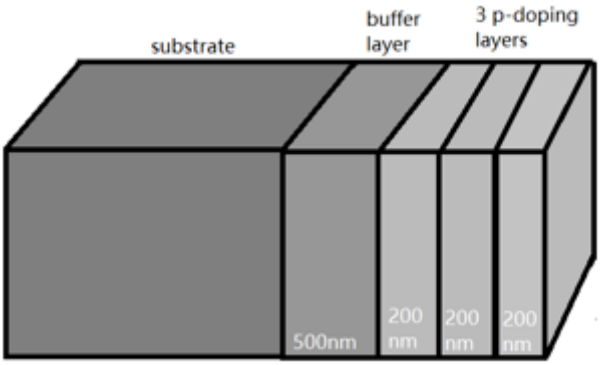

Figure 4. 3. A side oriental sketch of the sample corresponding to the SEM image and intensity profile.

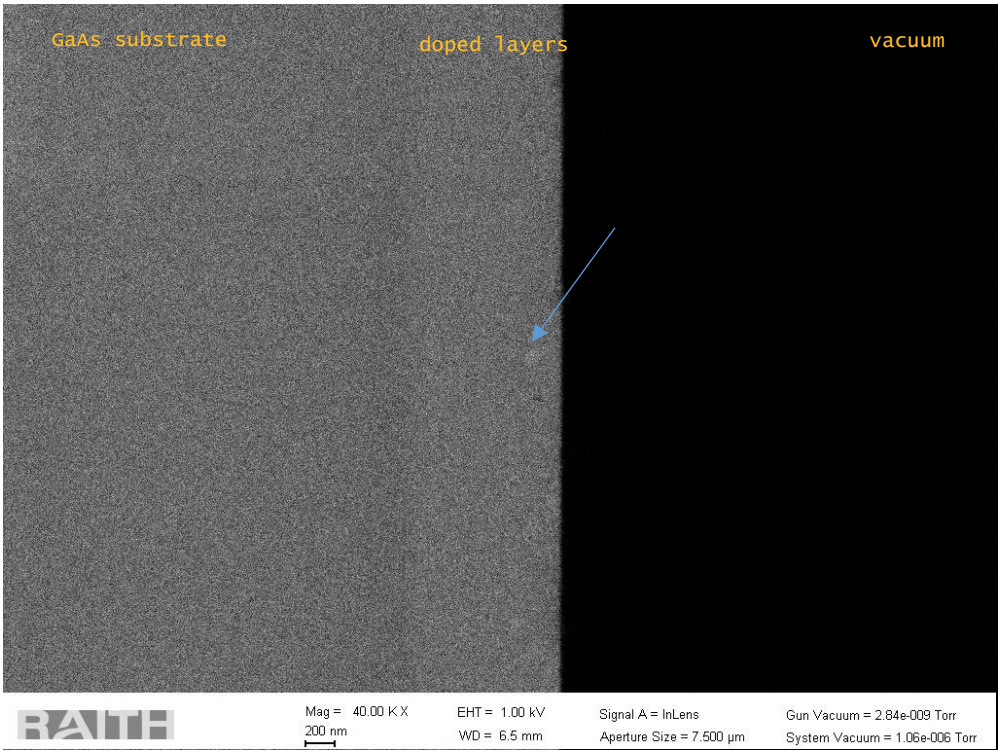

Figure 4. 4. SE single frame at 1.0kV. Arrow points to a bright patch near the edge of Be doped GaAs staircase sample

We can see bright patches in the top 200nm layer in Figure 4. 4, which might be a result of Be dopant segregation [265]. If no segregation was present, the top layer should be laterally uniform. The nominal doping concentration of the top layer is 1.6×10^{19} cm^{-3}, which corresponds to 350 ppm.

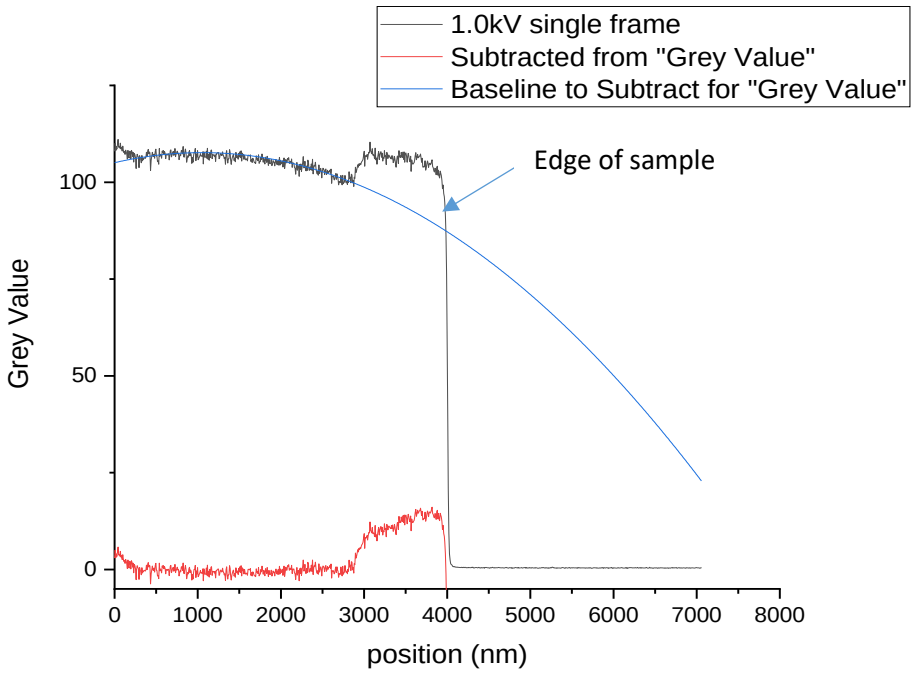

Figure 4. 1. The grey level profile of Be doped GaAs single frame at 1.0 kV.

The contrast in substrate region is not constant due to charging. So, a second order polynomial background fit was fitted where the left side showed charging, and the red line is the background subtracted data in Figure 4. 4.

We can get the fractional intensity increase if we divide the intensity increase by the extrapolated background grey level (blue baseline).

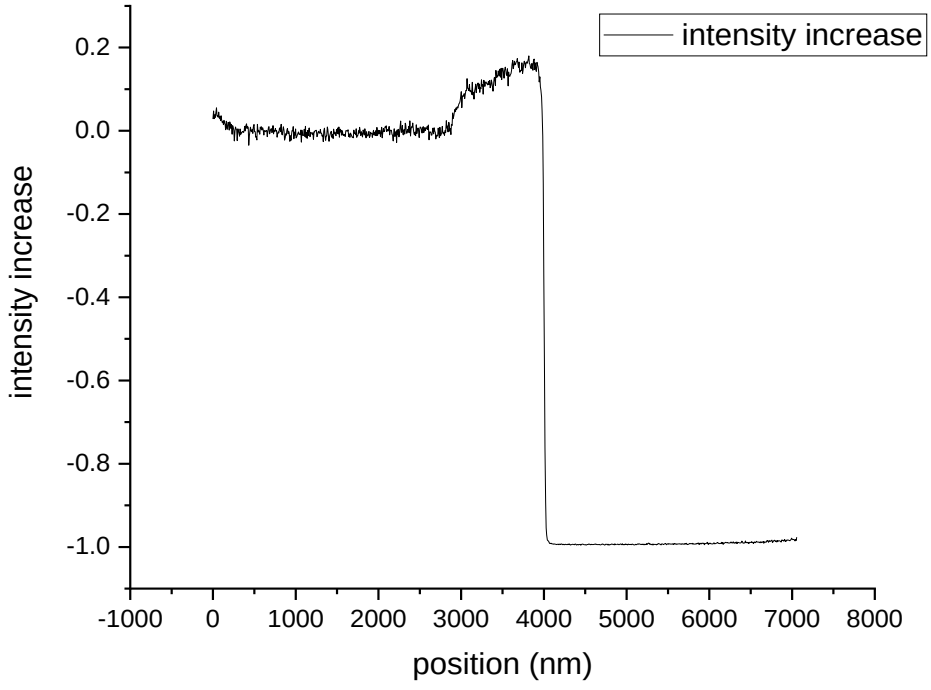

Figure 4. 2. Line profile of the fractional intensity increase in p-doped GaAs at 1 kV.

We can clearly see the doped buffer and vaguely the three thinner doped layers in Figure 4. 3, though the noise level is quite high. This is due to the scan speed of 2.6s per frame being relatively fast; the way we can reduce the noise is to average 9 frames of SE images for the same scan area. Drift must be avoided, otherwise the averaged image would become blurred. When charged carriers are accumulated at the surface, some drift will happen. So, we can reduce the drift by reducing surface charges. When the specimen was mounted, conductive silver paint has been used to join the specimen and carbon pad to ensure better specimen conductivity. When taking the images, by selecting the smallest aperture size (7.5µm), the charging of specimen can be reduced as it decreases the beam current. Besides, by carefully selecting the scan speed, images with good signal-noise ratio can be obtained while avoiding charging effects during long inquisition times.

Figure 4. 3 is the average image of Be doped GaAs staircase and the signal to noise ratio (SNR) is improved by a factor of 3. The bright patches are still visible in Figure 4. 3, indicating drift correction has worked.

Figure 4. 3. The averaged image of 9 consecutively acquired frames.

A single line profile is obtained by vertical averaging of the entire image using the Gatan Digital Micrograph software to generate the averaged line profile. If the sample surface is not oriented perfectly vertical, the direction of line scan can be adjusted to make sure it is vertical to sample surface. In the subtracted intensity profile shown as the red line in Figure 4. 4, we can identify the buffer layer and the three doped layers, however, the contrast of the top layer is lower than expected, which might due to the segregation of Be so that not all dopants are electrically activate.

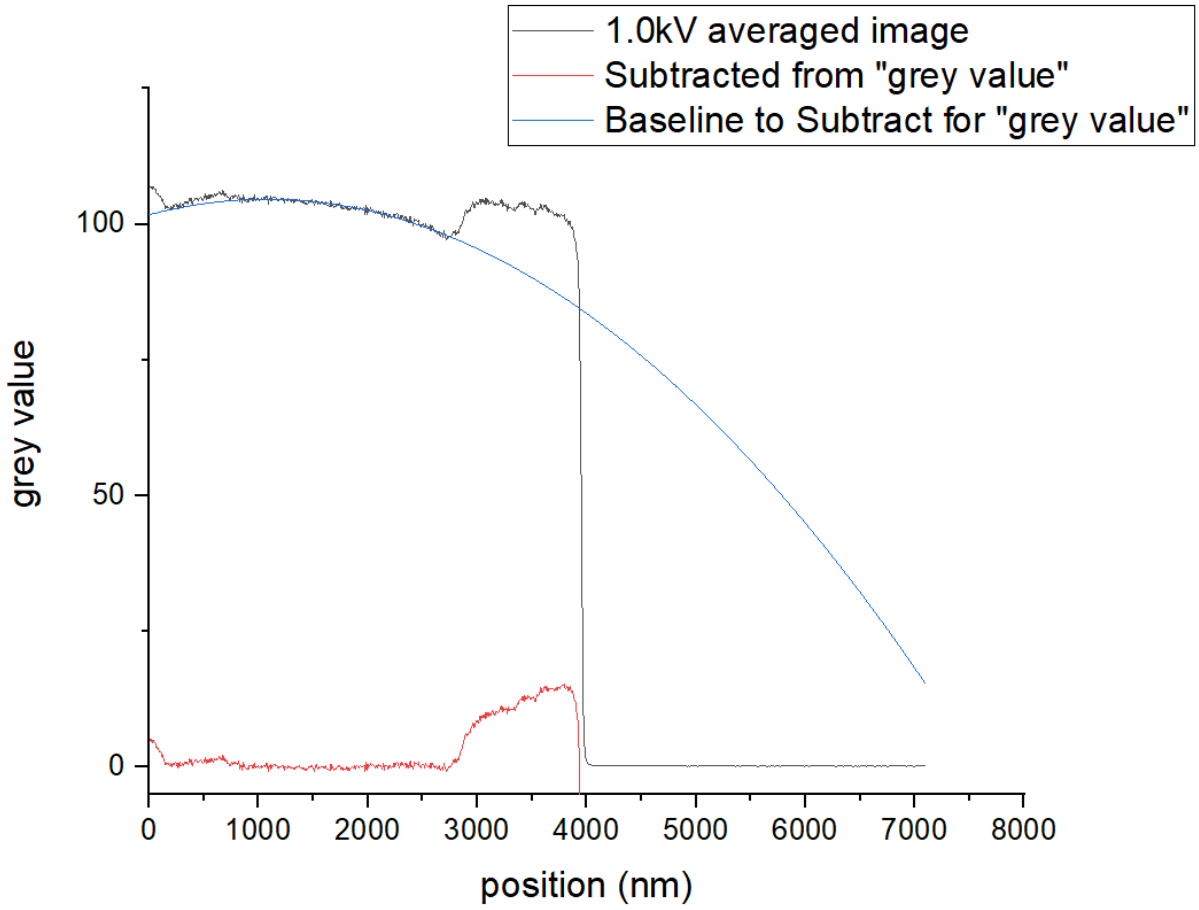

Figure 4. 4. Profile of averaged SE image intensity at 1.0kV and background subtraction profile, for Be-doped p-GaAs staircase sample

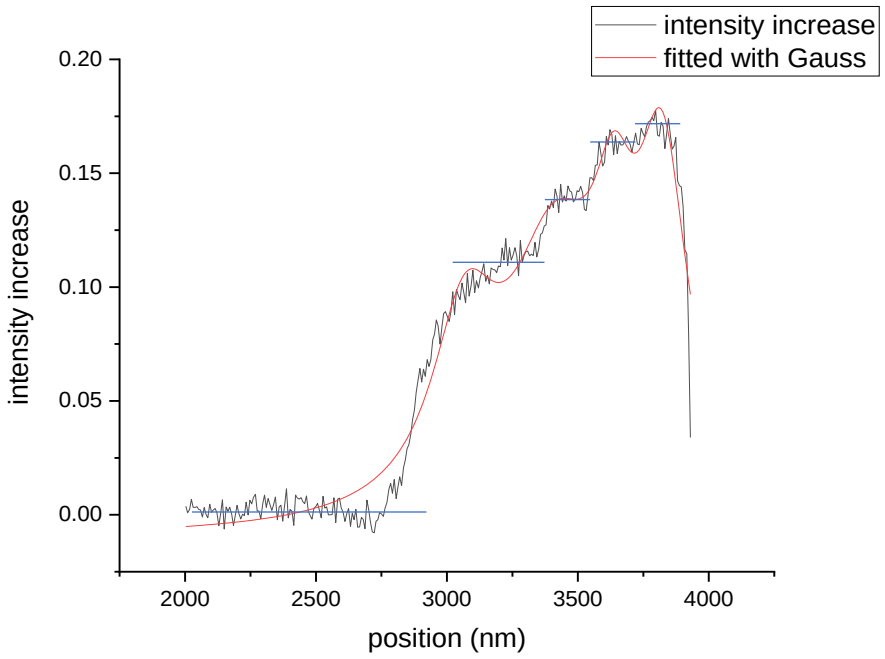

Figure 4. 5. SE intensity increase relative to GaAs for 9 averaged frames of 1.0kV images of Be doped GaAs staircase sample.

After taking 1.0 kV in-lens SE images, the scan window was moved to a fresh area and 1.5 kV images were taken at same magnification and aperture settings.

The SE intensity profile of 1.5 kV Be doped GaAs staircase sample is plotted in Figure 4. 6.

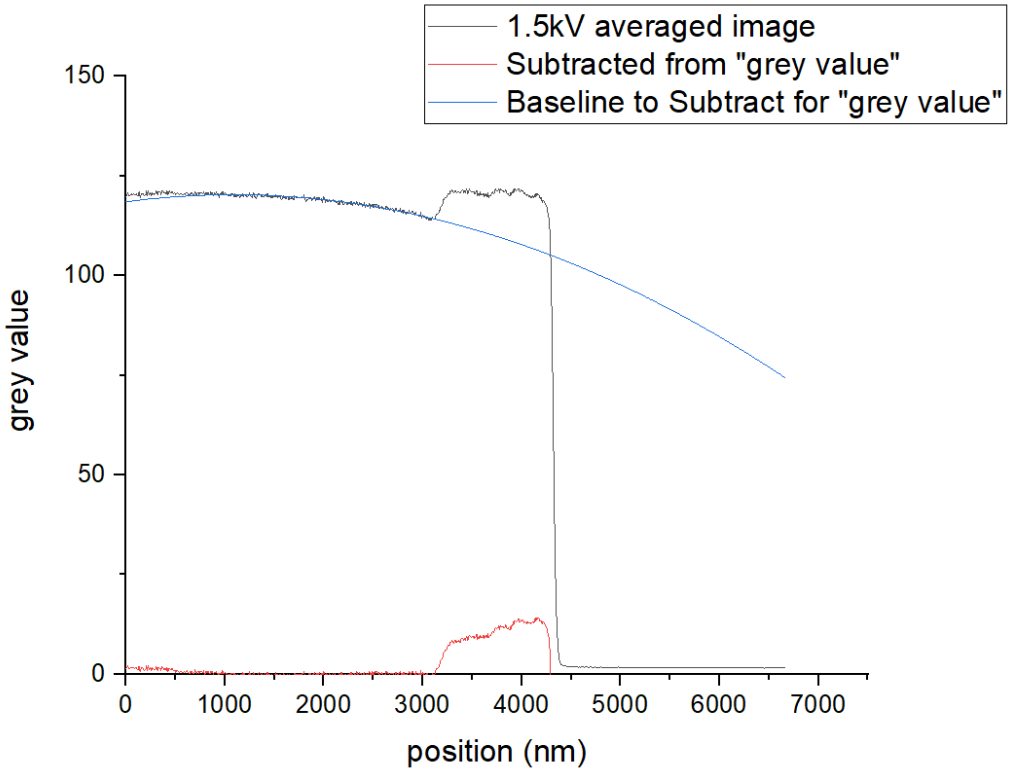

Figure 4. 6. SE profile of Be doped GaAs averaged image at 1.5kV.

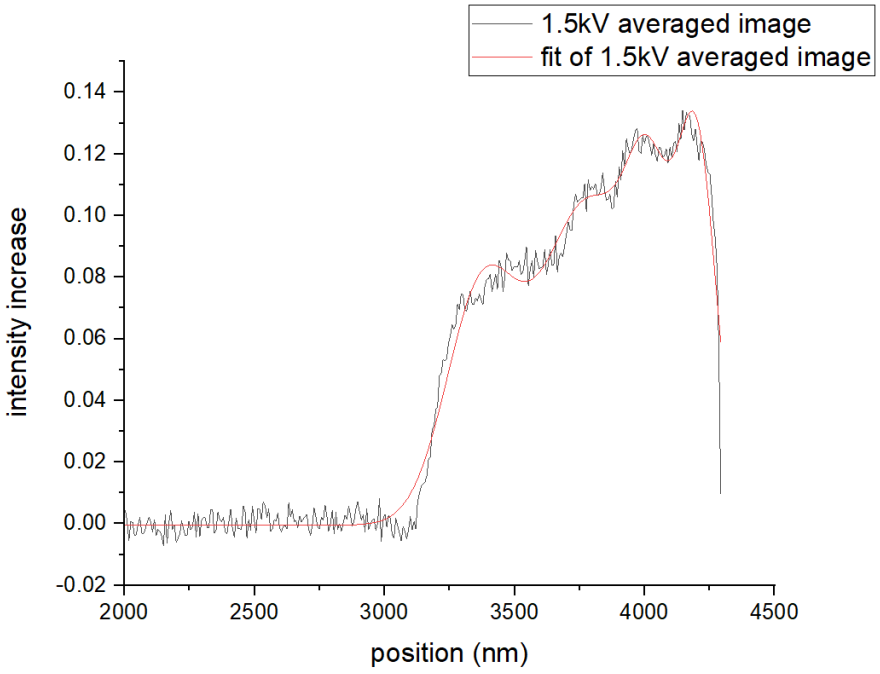

Figure 4. 7. SE intensity increase for averaged 9 frames of 1.5kV images of Be doped GaAs staircase sample.

After fitting the intensity increase fraction curve, we can better distinguish the three doped layers and the buffer layer in the 1.5 kV image intensity increase profile.

The grey scale profile and background subtraction for 2 kV acceleration voltage are displayed in Figure 4. 8.

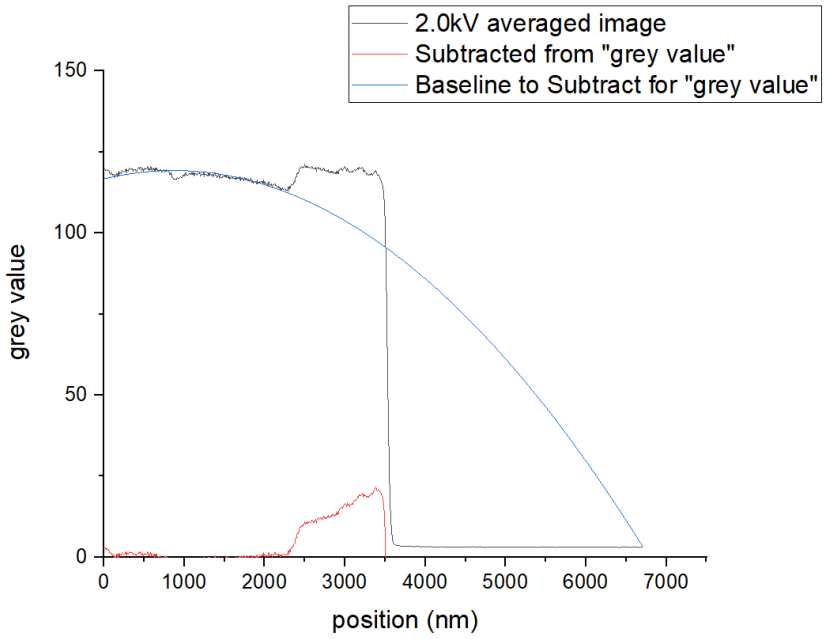

Figure 4. 8. Profile of Be doped GaAs averaged image at 2.0 kV.

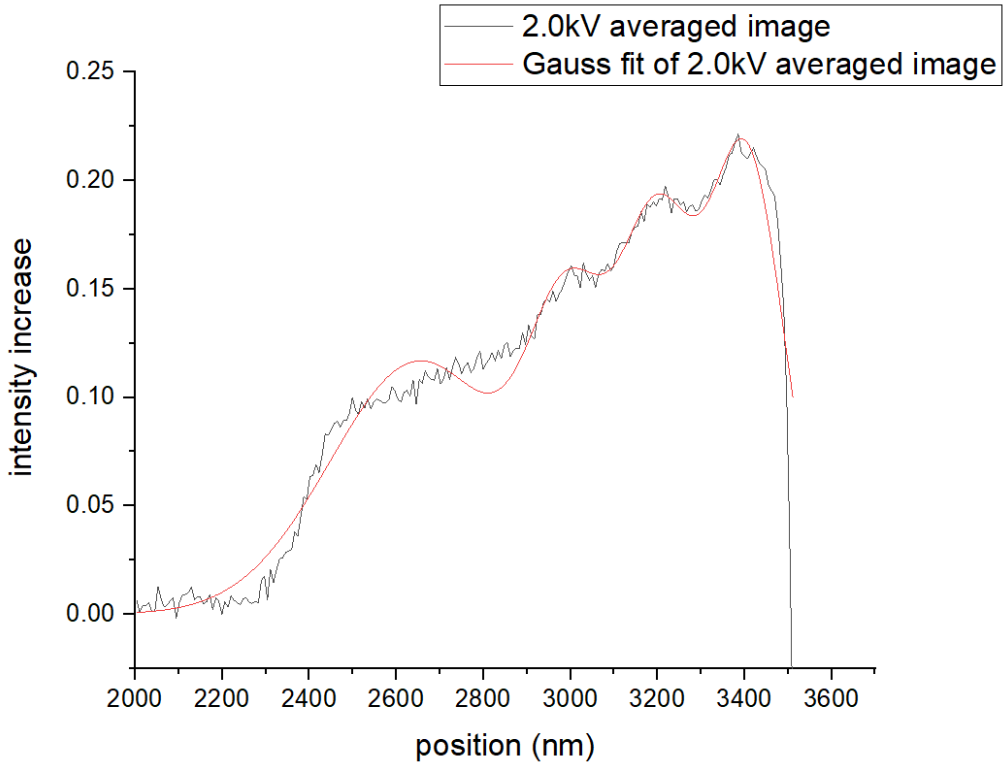

Figure 4. 9. The relative SE intensity increase for 9 averaged frames of 2.0 kV SE images of Be doped GaAs staircase sample.

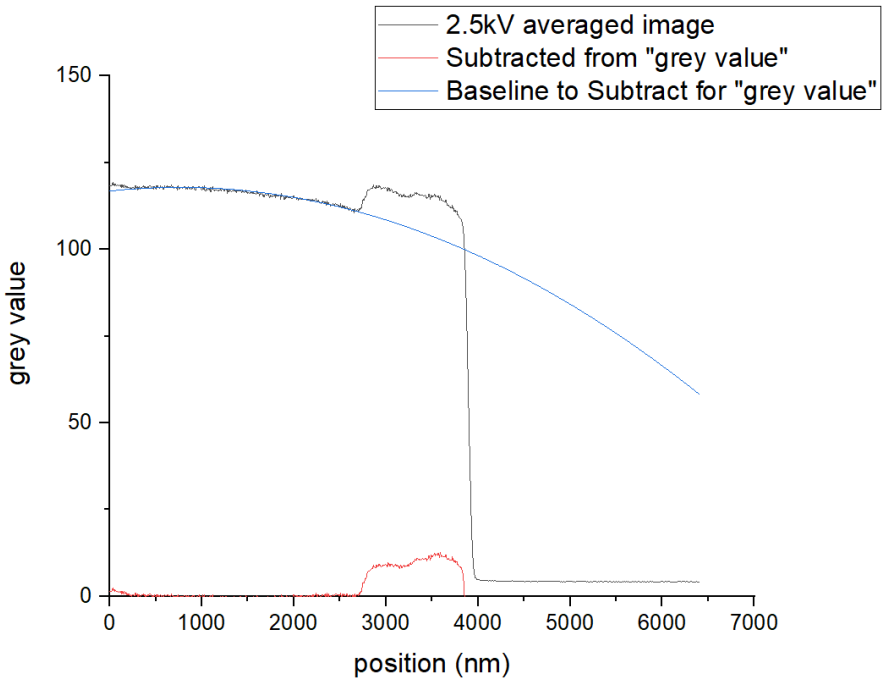

Figure 4. 10. Profile of Be doped GaAs image (9 averaged frames) at 2.5 kV beam voltage.

The profile of Be doped GaAs image with 2.5 kV beam voltage is a bit blurred, the fractional intensity increase illustrated in Figure 4. 11, which is noisy and and the fit quality is not very good. The first layer still shows some bright dots which might be segregated dopant atoms.

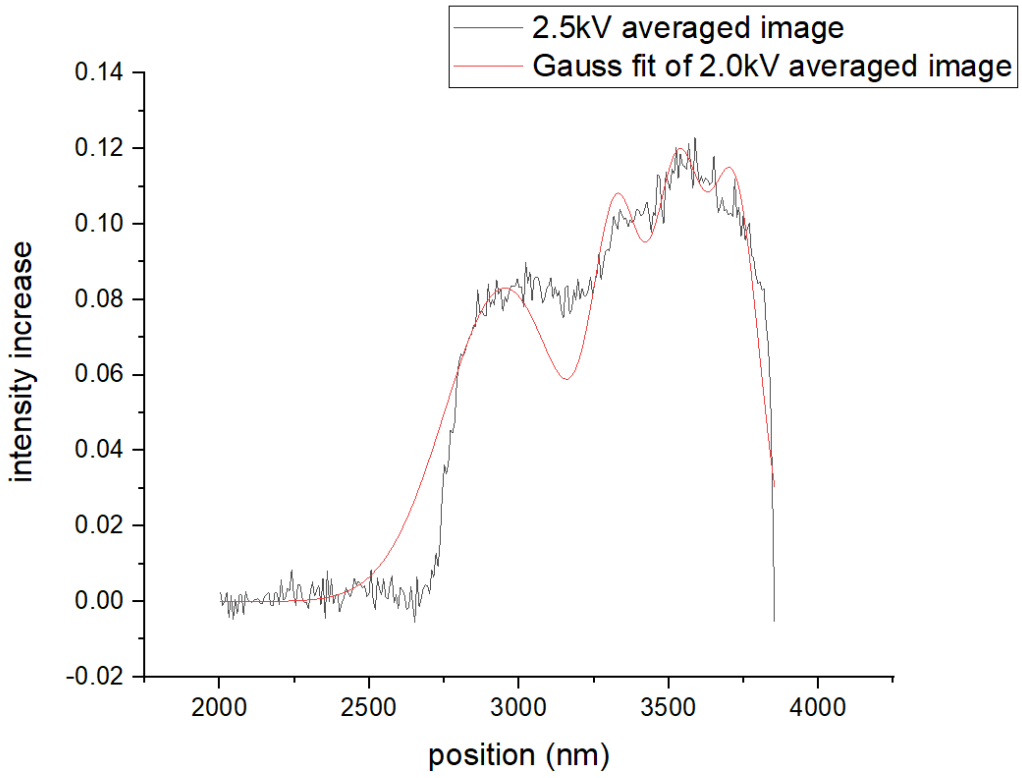

Figure 4. 11. The fractional intensity increase for 9 averaged frames for 2.5 kV SE images of Be doped GaAs staircase sample.

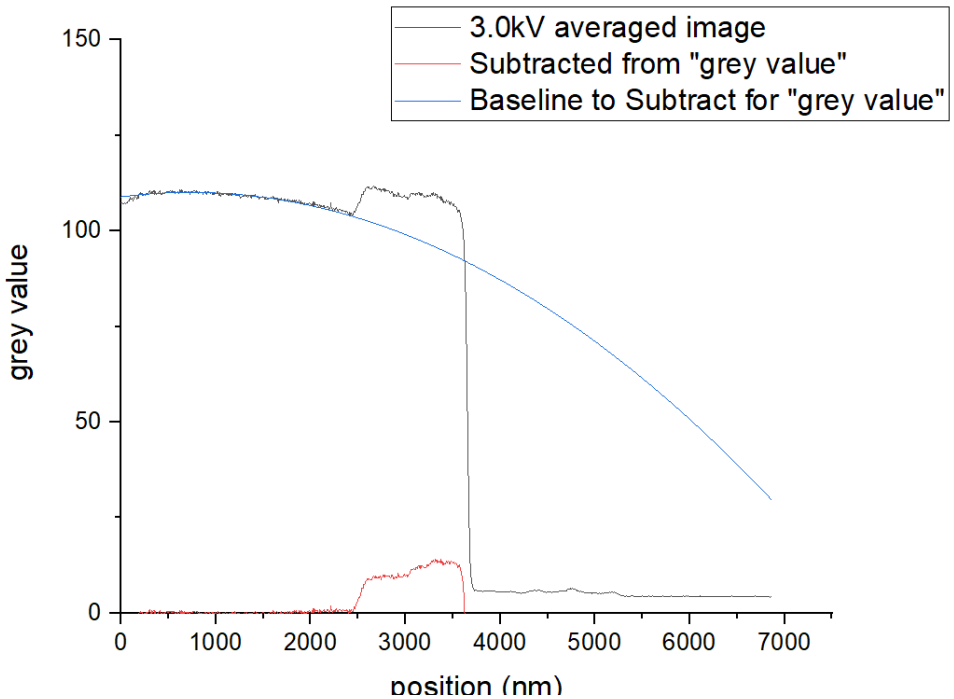

Figure 4. 12. Grey value profile of Be doped GaAs averaged image at 3.0 kV beam voltage.

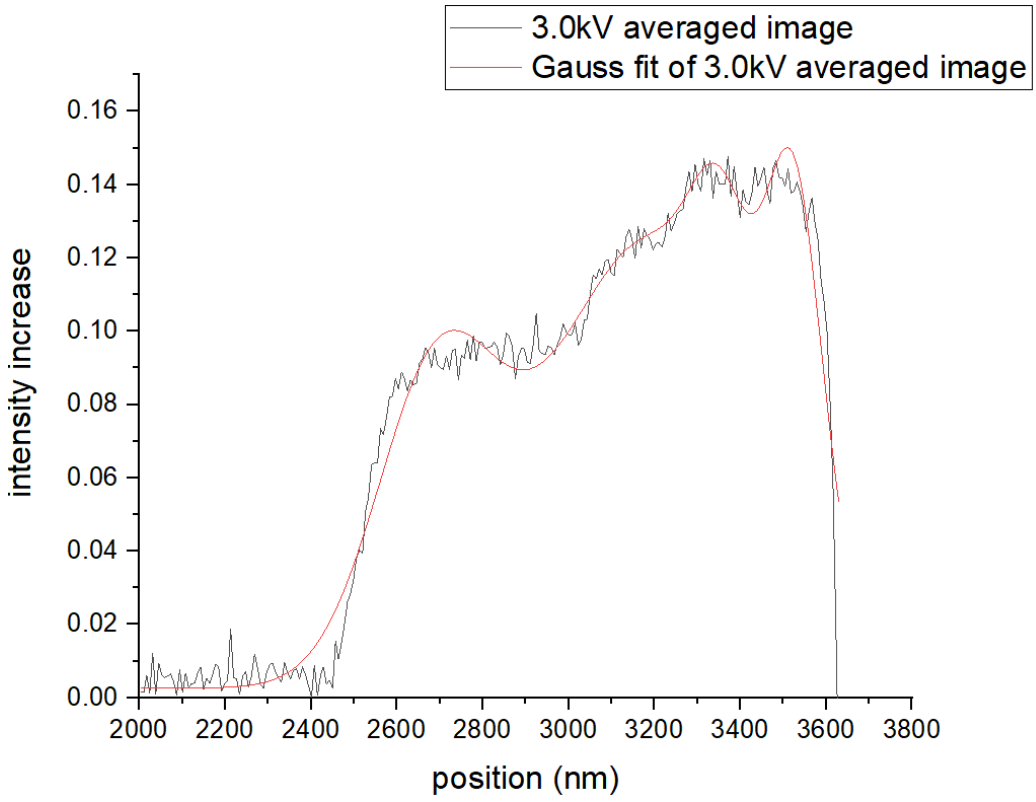

Figure 4. 13. The fractional SE intensity increase for 9 averaged frames at 3.0 kV of Be doped GaAs staircase sample.

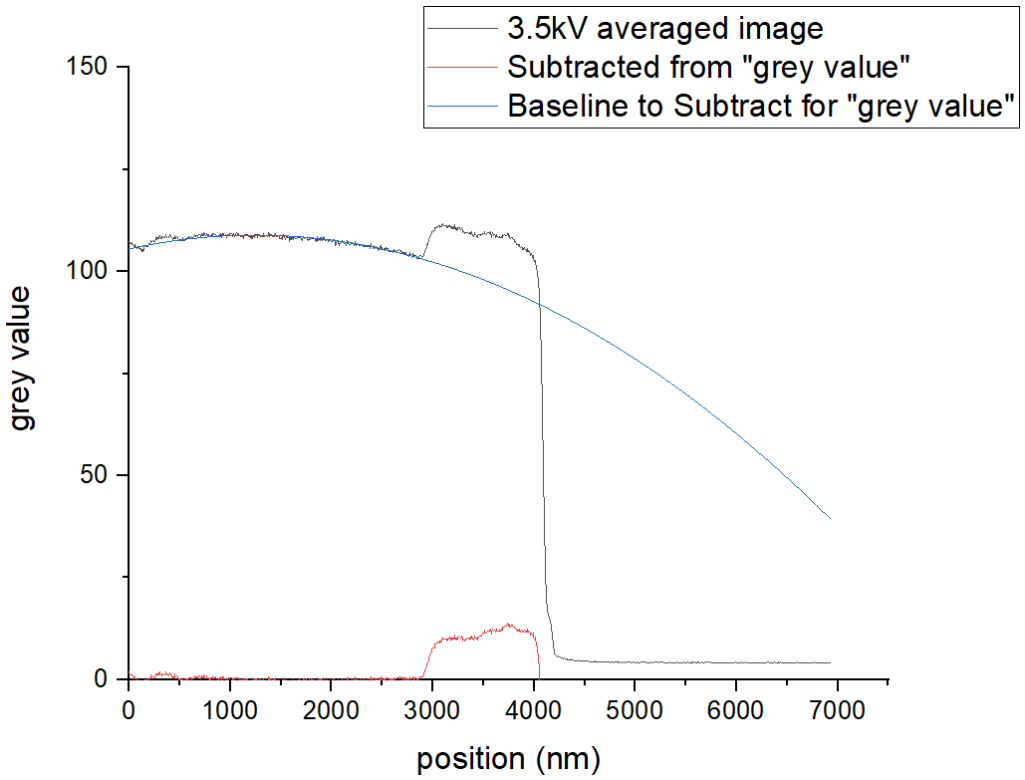

Figure 4. 14. Grey value profile of Be doped GaAs averaged SE image at 3.5 kV beam voltage.

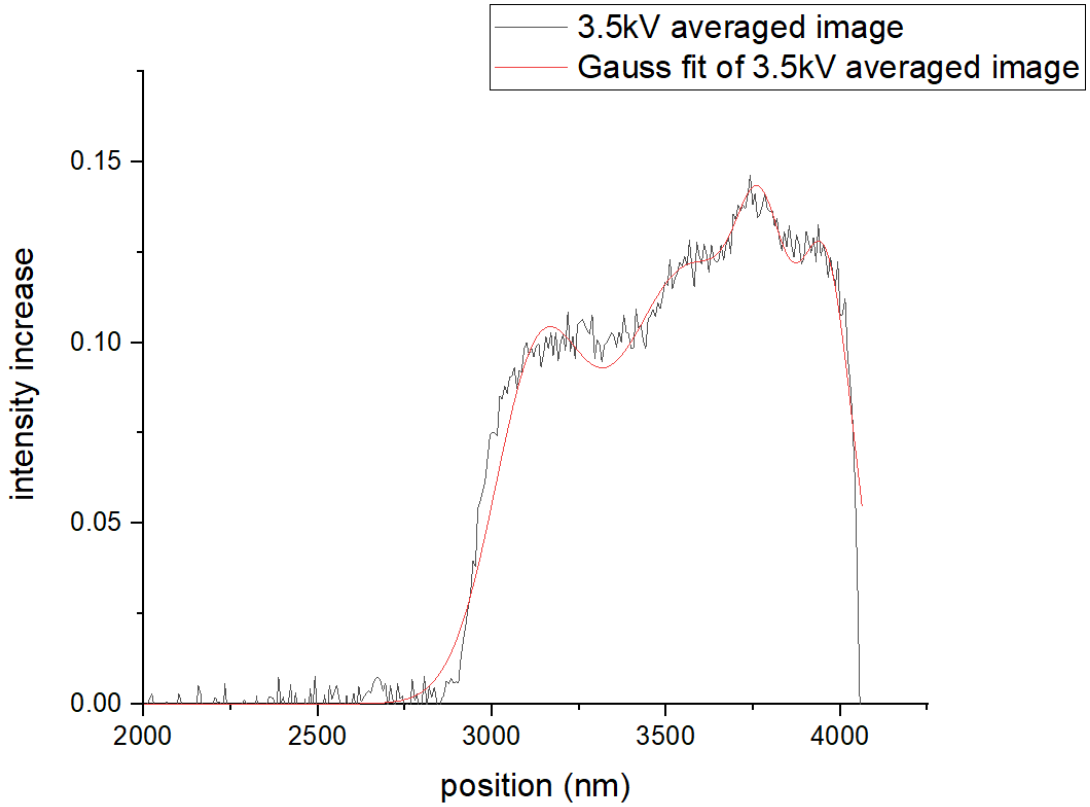

Figure 4. 15. The relative SE intensity increase for averaged 9 frames of 3.5 kV SE images of Be doped GaAs staircase.

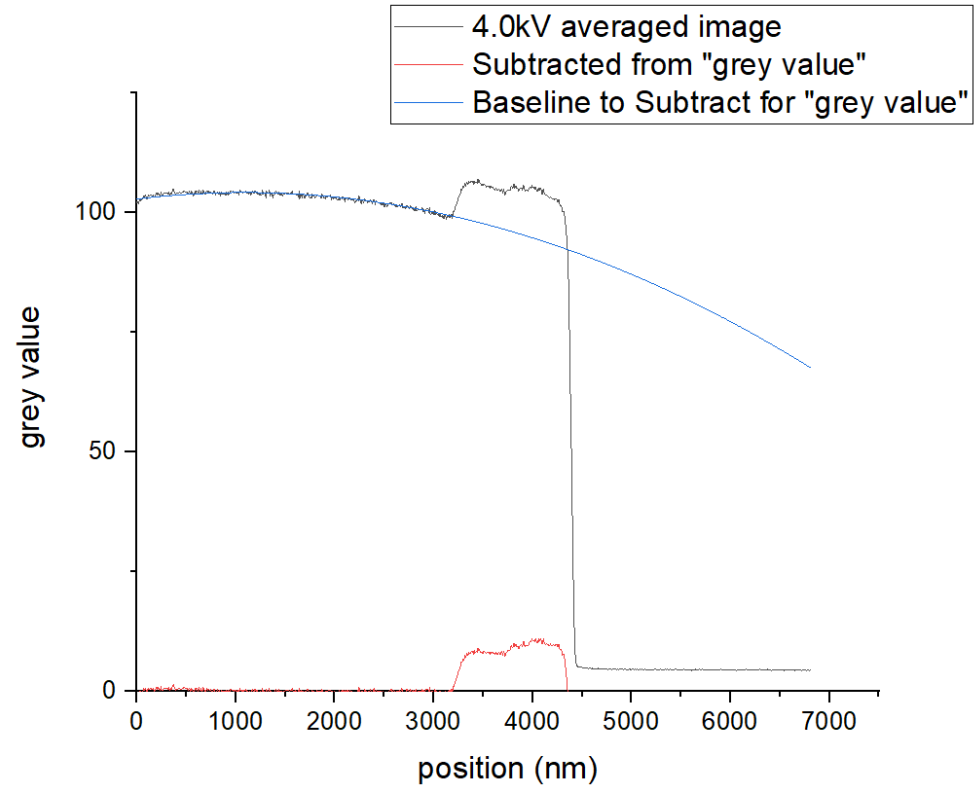

Figure 4. 16.Grey value profile of Be doped GaAs averaged image at 4.0 kV beam voltage.

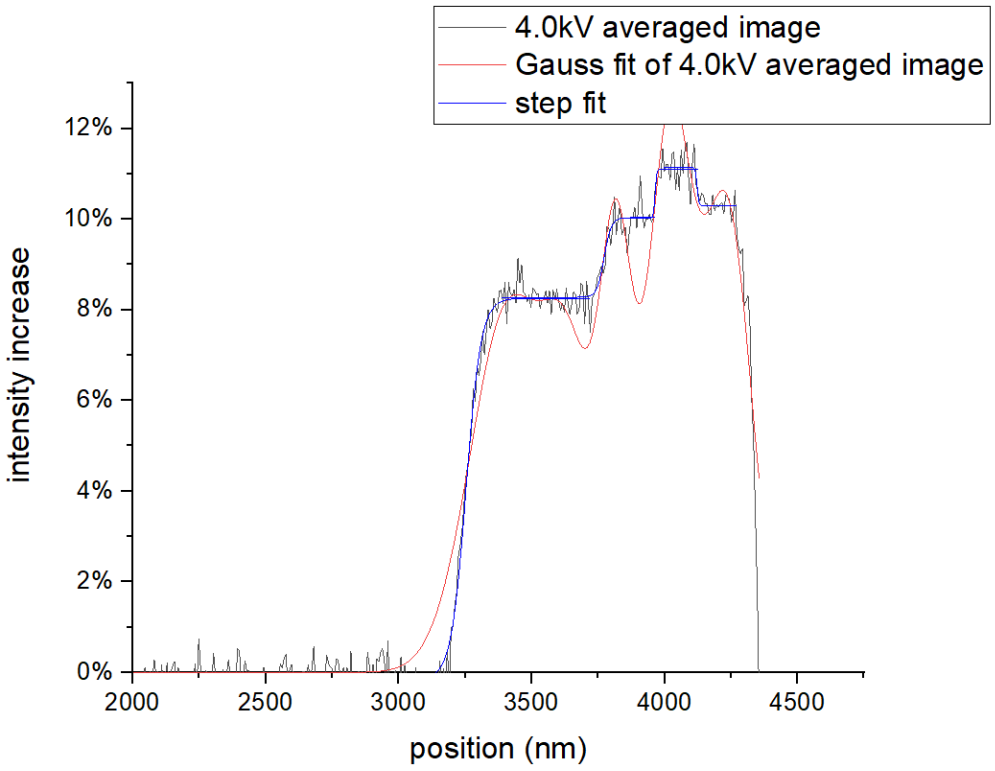

Figure 4. 17. Relative SE intensity increase for averaged 9 frames of 4.0 kV SE images of Be doped GaAs staircase.

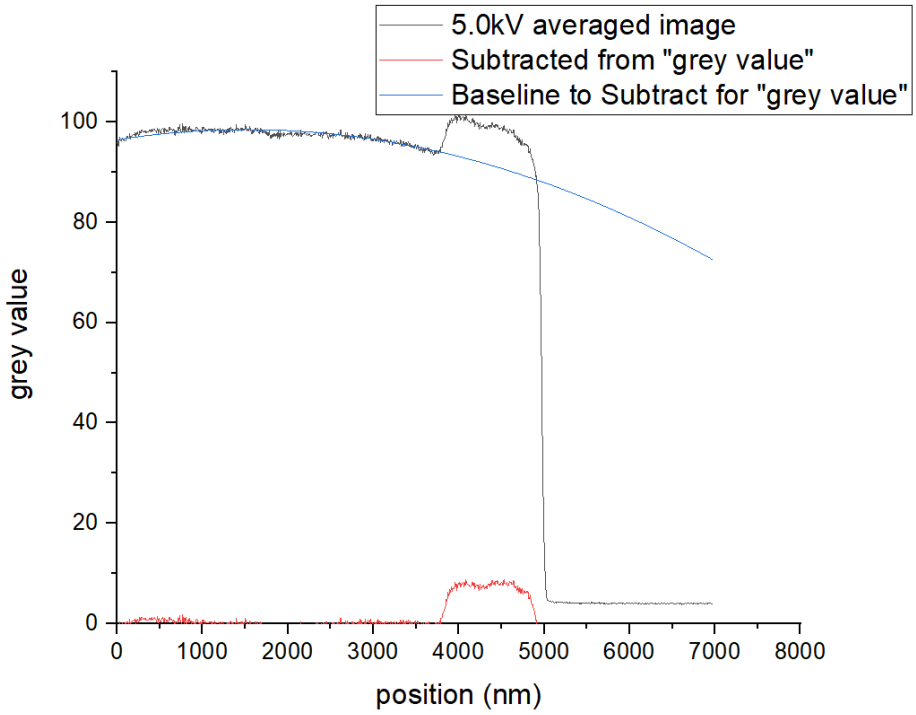

Figure 4. 18. Grey value profile of Be doped GaAs averaged image at 5.0 kV beam voltage.

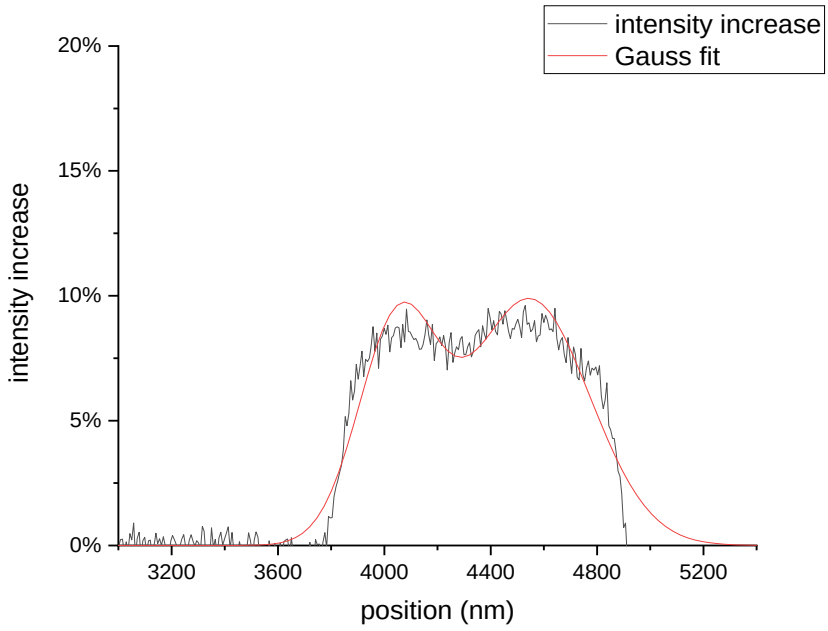

Figure 4. 19. Relative SE intensity increase for averaged 9 frames of 5.0 kV SE images of Be doped GaAs staircase.

4.2.2 Si doped GaAs sample

The Si doped GaAs sample has also been investigated by FE-SEM Raith EO at voltages from 1.0 kV to 5.0 kV but only images and profiles for 1-2 kV are shown in the following because the difference of the raw SE intensity data from the doped layers is too small to give interpretable contrast at higher voltages. The aperture size was again 7.5µm diameter and the scan speed 6, which means the pixel

dwell time is 3.2µs, and the time for a single frame was 2.6 s. For each scan area and different beam voltages, a total of 9 frames were captured.

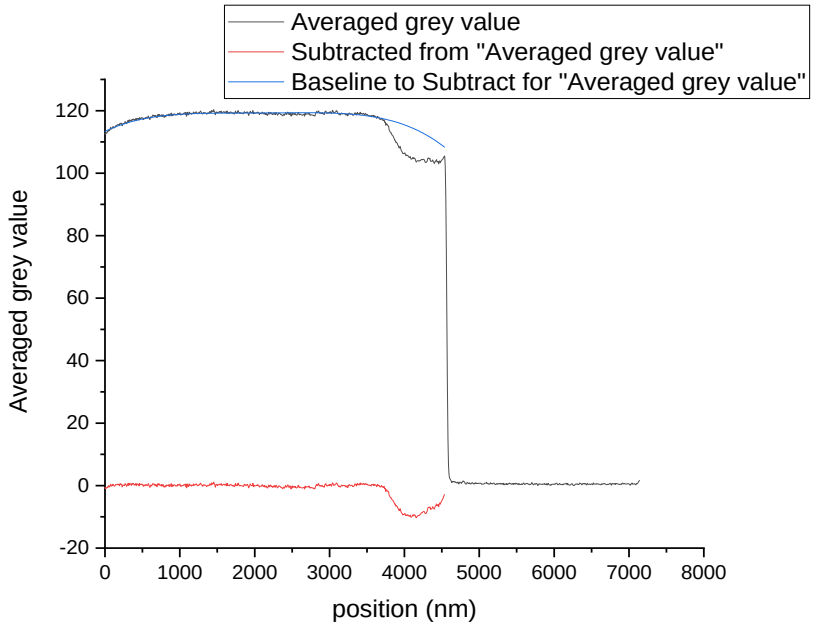

Figure 4. 20. Grey value profile of Si doped n-GaAs averaged SE image at 1.0 kV beam voltage.

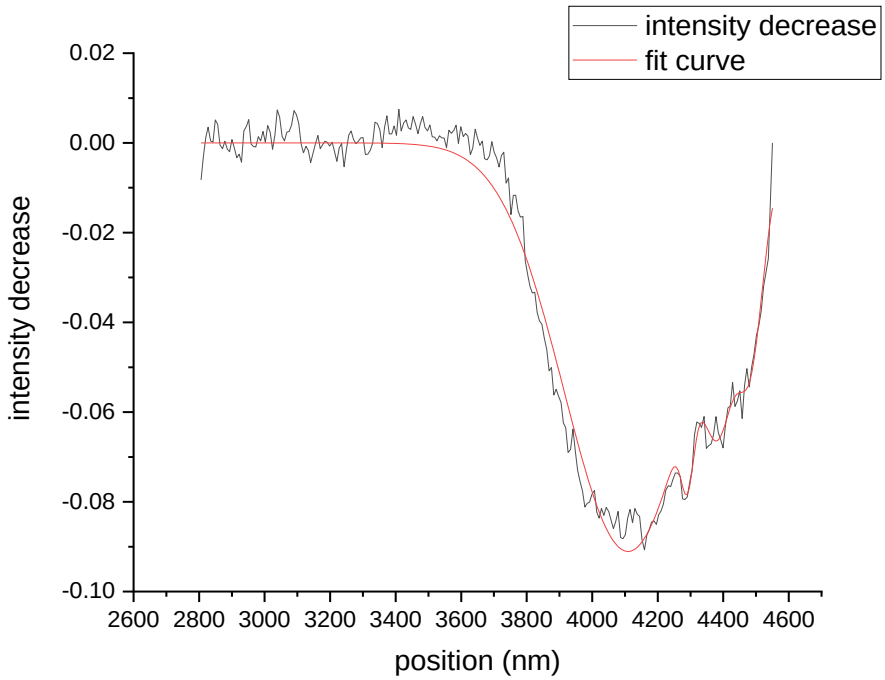

Figure 4. 21. Relative SE intensity decrease for averaged 9 frames of 1.0 kV SE images of Si doped GaAs staircase.

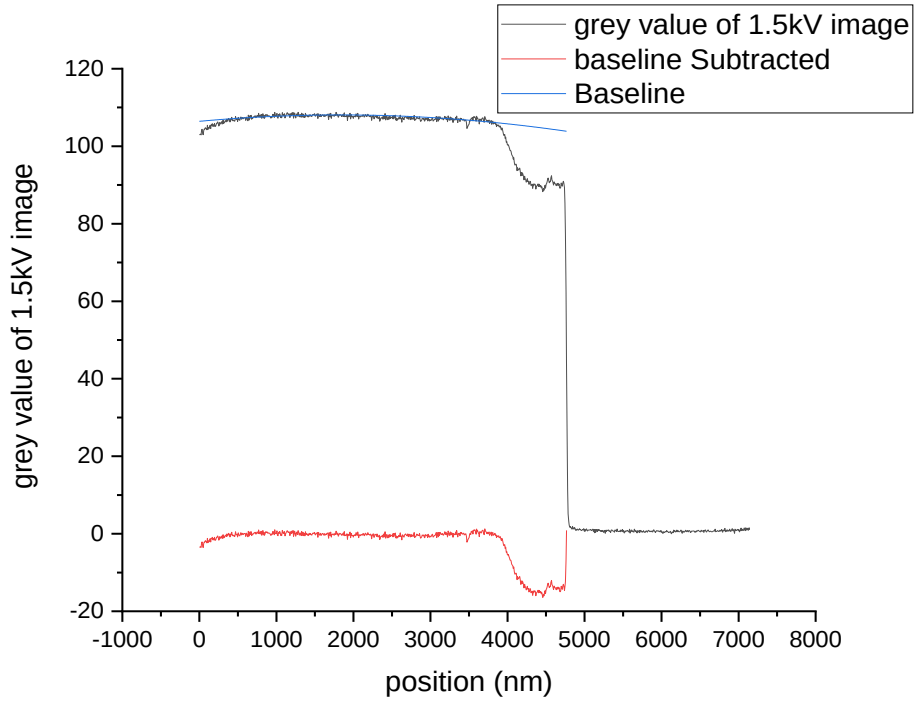

Figure 4. 22. Grey value profile of Si doped GaAs averaged SE image at 1.5 kV beam voltage.

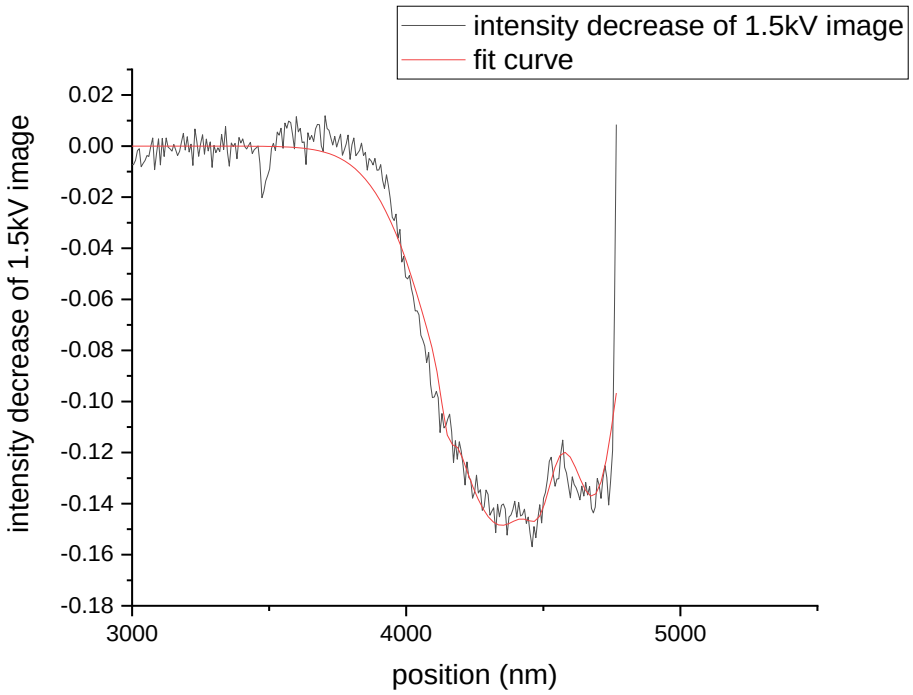

Figure 4. 23. Relative SE intensity decrease for averaged 9 frames of 1.5 kV SE images of Si doped GaAs staircase.

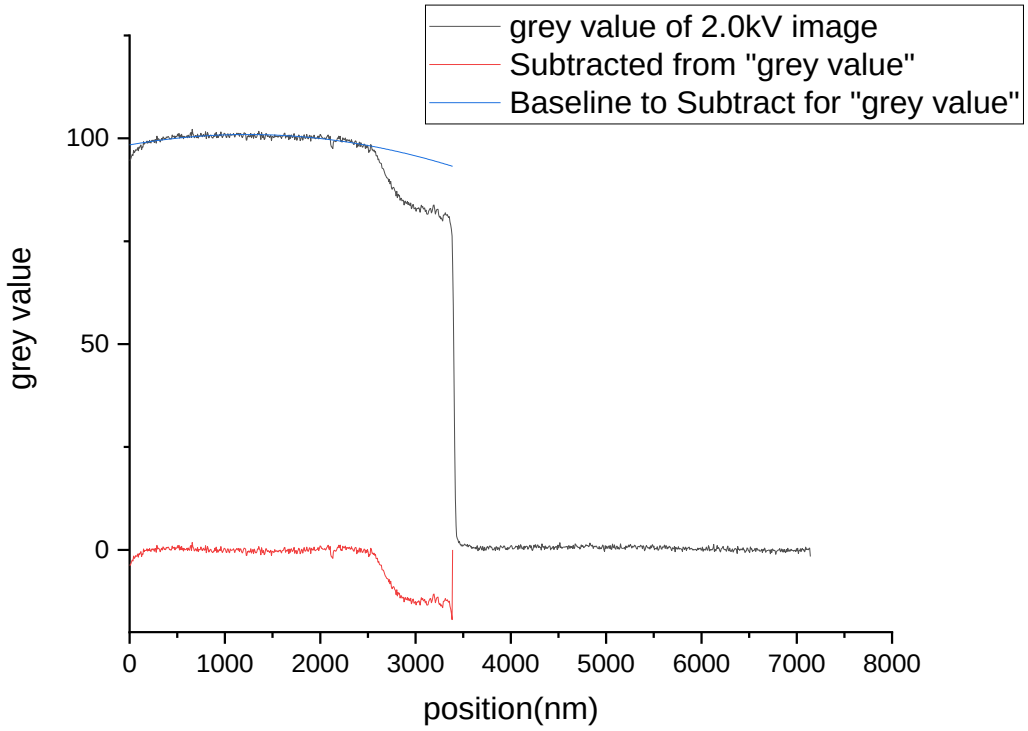

Figure 4. 24. Grey value profile of Si doped GaAs averaged SE image at 2.0kV beam voltage.

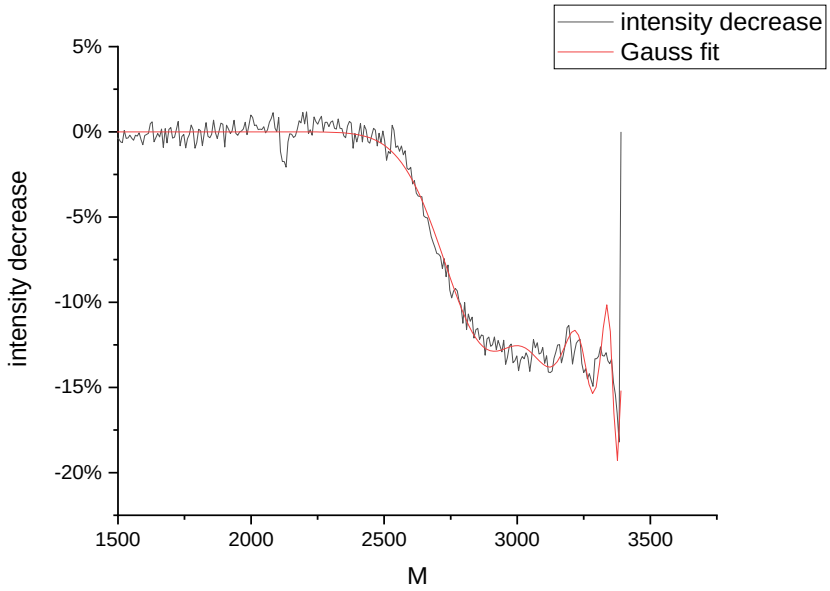

Figure 4. 25. relative SE intensity decrease for averaged 9 frames of 2.0 kV SE images of Si doped GaAs staircase.

4.2.3 Discussion

The contrast ratio, *R*, of the doped layers relative to the undoped region can be obtained by:

$$R = \frac{I_{\text{doped layer}} - I_{\text{extrapolated from undoped}}}{I_{\text{extrapolated from undoped}} - I_{\text{black level}}}, \tag{3.1}$$

Then, the SE image contrast can be plotted as a function of doping concentration. In this research, all images are recorded as unsigned 8-bit data, which means the intensity ranges from 0-255. The intensity of doped region is estimated by second order polynomial extrapolation, and the region of the carbon pad is used as an approximation of the black level.

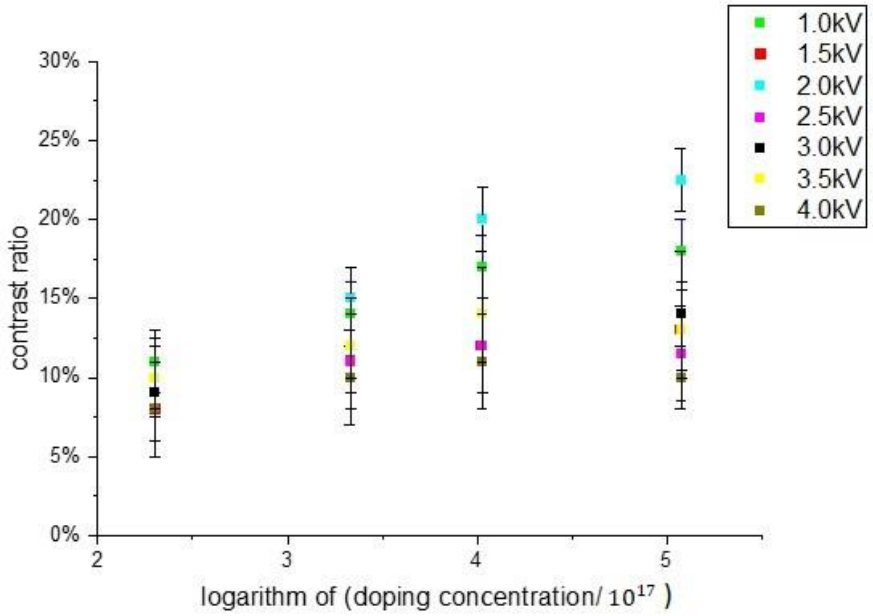

Figure 4. 26. The doping contrast of Be doped GaAs (p-type).

As we can see, the contrast of Be doped GaAs shows a general increase with increasing doping concentration. When in equilibrium, the Fermi level of higher doped p-region is aligned with lower doped p-region, so electrons from highly doped regions need to overcome lower energy barrier for SE yield, this is why highly p-doped region appears brighter than lower doped region. This explains why the SE yield of Be doped p-GaAs increases with doping concentration in Figure 4. 26.

Although an increase of p-doping concentration will increase the work function so electrons need more energy to escape from the surface, this only applies to bulk and is not the dominating effect in low voltage SEM (1-5 kV) of areas with different doping levels where the Fermi levels between all layers need to be adjusted to account for thermal equilibrium.

The smallest work function of Be-doped buffer layer is 5.43 eV (calculated value based on doping concentration) and the carbon film work function is 5.1 eV [178]. Contamination during scanning can reduce the image intensity but the carbon on the surface will only form an Ohmic contact of small resistance that will have a small electronic influence on the SE yield. However when contamination build-up is strong. The atomic number effect will be significant as the SE signals are generated from contamination rather than the sample itself.

The dopant contrast sensitivity starts to go down at 4 kV, and it is very hard to distinguish the three doped layers. This is due to the SE yield decreasing when the beam voltage increases. The electron beam is better focused at higher accelerating voltages, however, the SEs are generated within 50-100nm under the surface and the interaction volume increases dramatically with beam voltage, so we get best SE images for 1.5kV-2kV.

The top p-layer of nominal 1.6×10^{19} Be atoms/cm^3 did not show a contrast as high as expected; this might be due to some Be dopant atoms segregating, as several of the SE images have shown small bright patches in that top layer only.

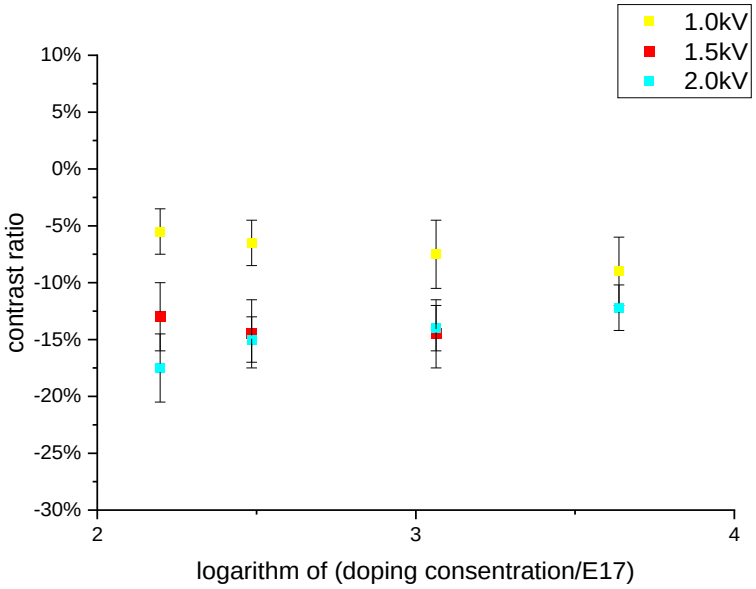

Figure 4. 27. The doping contrast of Si doped n-GaAs

4.3 The influence of electron dose on secondary electron image contrast

To explore the relationship between doping contrast and beam induced electron dose, different apertures are used. The standard aperture size is 30µm diameter, which provides a beam current of around 100pA. When the aperture diameter is reduced by a factor N, then the beam current is reduced by a factor of N^2; for example, for 7.5µm diameter, the beam current is reduced to 1/16 of 100pA, i.e. ≈6pA. Scan speed for 1 frame is 2.3s.

At least 9 frames of SE images were taken for different illumination apertures of diameters 7.5µm, 10µm, 15µm and 20µm. For apertures of 15 and 20µ diameter, we could see charge build-up at the surface of GaAs in the form of stripes parallel to the surface that varied in position in consecutive frames. The images below show the 1st frame and the 9th frame for the 20µm aperture, demonstrating how rapidly charging occurs on the sample surface within 20 seconds of scanning. The corresponding difference in dose is 20s x 44pA / e = 5.5 billion electrons over an area of 165 electrons/nm^2.

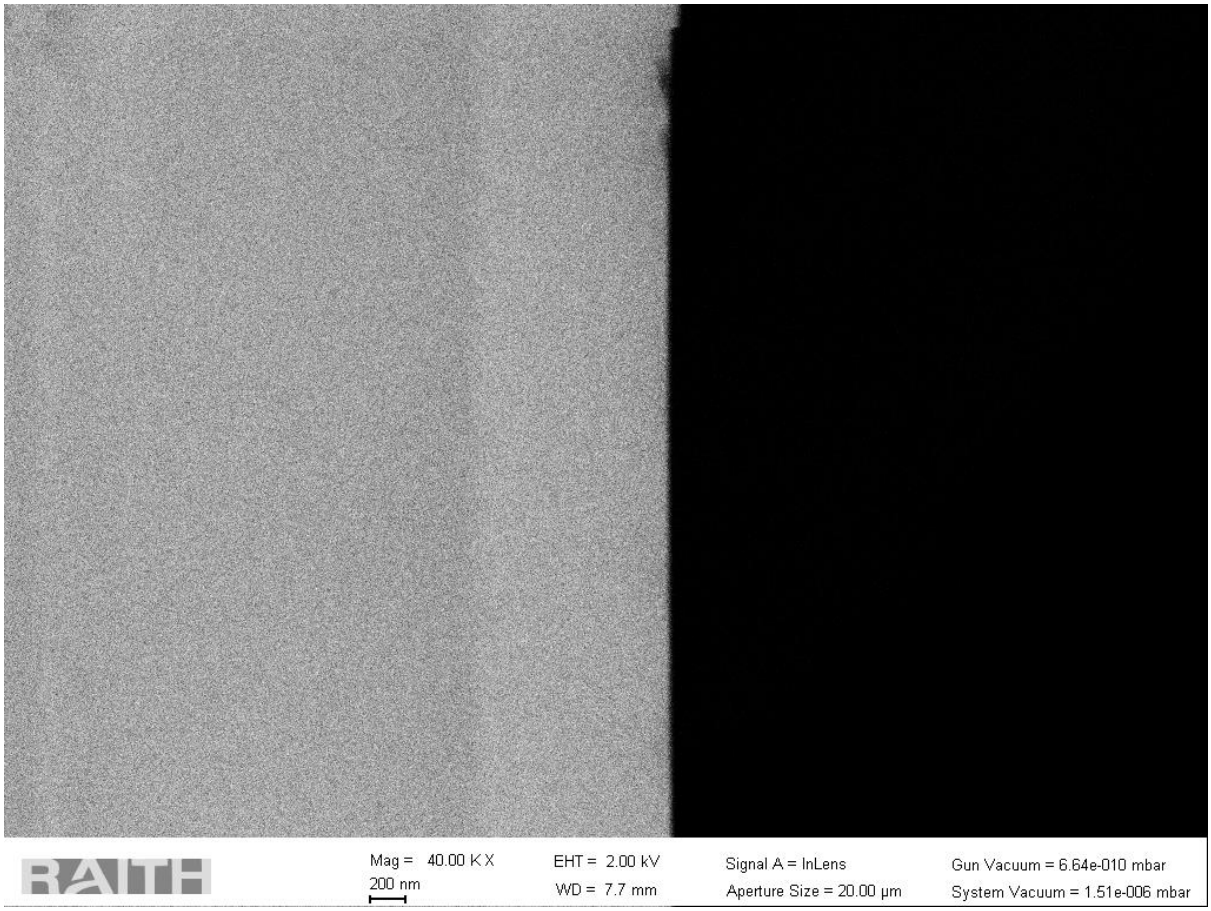

Figure 4. 28. The first frame for 2.0kV SE imaging of p-GaAs staircase sample with 20µm condenser aperture.

Figure 4. 29. The ninth frame for 2.0kV SE imaging with 20µm condenser aperture. Charging manifests itself in the form of two white vertical stripes being formed, one on the left of the image and one near the interface between the intrinsic GaAs and the doped buffer. The region marked by the box also shows the build-up of a carbon contamination layer.

By comparing Figure 4. 28 and Figure 4. 29, we also notice carbon deposition due to hydrocarbon on the surface accumulating before being cracked by the electron beam. That means even with a scan speed of 3.2µs per pixel and 2.3s for a single frame, the increase of electron dose will reduce the image contrast significantly. This sensitivity of GaAs to the beam can also explain why we chose the smaller aperture for investigating the influence of beam voltage on dopant contrast.

As we want to reduce the noise while avoiding charging, I used only frame 1 to frame 4 to form an averaged image for each aperture. As the SNR improves by the square root of averaged frames, this will improve the SNR by a factor of 2.

The image shown in Figure 4. 30 is an example of 4 averaged single frames of Be doped GaAs staircase sample at 2.0kV with in-lens SE detector using 7.5µm aperture size.

Frame number	Aperture size (μm)	Beam current (pA)	Total electron dose (electrons/m^2)
1	7.5	6.25	2.6×10^{18}
2	10	11.1	9.4×10^{18}
3	15	25.0	3.2×10^{19}
4	20	44.4	7.5×10^{19}

Table 4. 1. The total electron dose increases when taking successive frames.

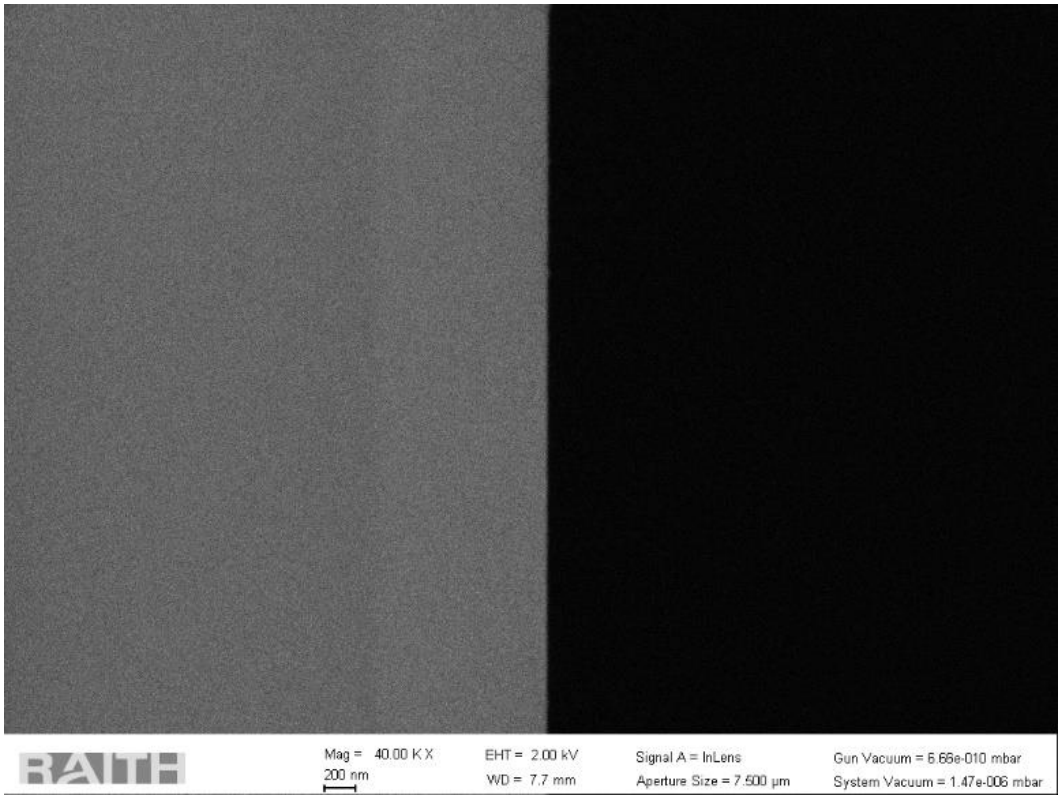

Figure 4. 30. The averaged SE image at 2.0kV with 7.5μm aperture of Be doped GaAs specimen.

The greyscale profiles of the averaged images taken at 2.0kV by using different apertures are plotted and aligned in Figure 4. 31.

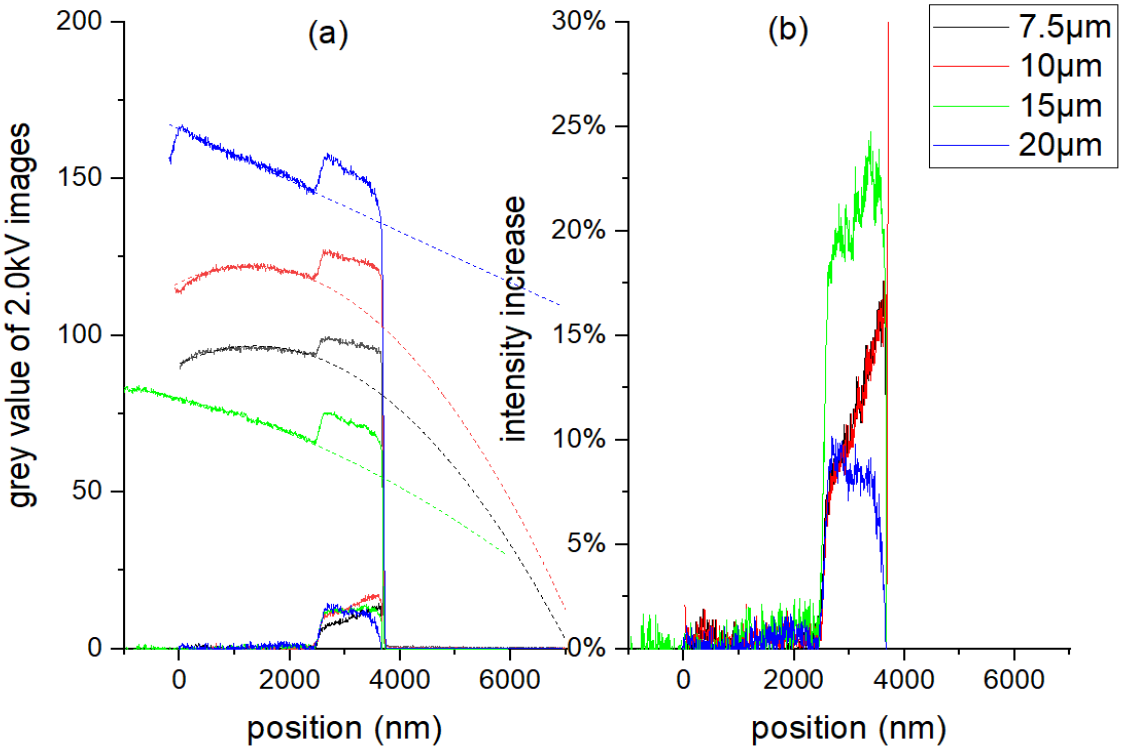

Figure 4. 31. The SE image profiles of 2.0kV images acquired with different condenser apertures. (a) extrapolation of non-linear background. (b) fraction of intensity increase shows influence by the beam current.

To analyse the image contrast, we first need to get the black level of the image. Ideally, one should always have one image with gun valve closed, but the region of carbon pad can be a sufficiently good approximation as the carbon region is 1-2mm below the focusing point and is grounded. By subtracting this black level, intensity profiles are set to zero in the carbon region. A non-linear background is then fitted to the undoped GaAs substrate region by a parabola function to model the intensity variation in the undoped region over a sufficiently long distance. This background is then extrapolated into the doped regions.

It is interesting that the curvatures of the intensity line-traces in the undoped GaAs region are different for very low beam currents (strong curvature) and high beam current (more linear) in Figure 4. 31(a). For low beam current and very high beam current, the curvatures in the resulting net line-traces of doped GaAs seem to be opposite while the one for medium beam current which is using the 15µm aperture shown in green line.

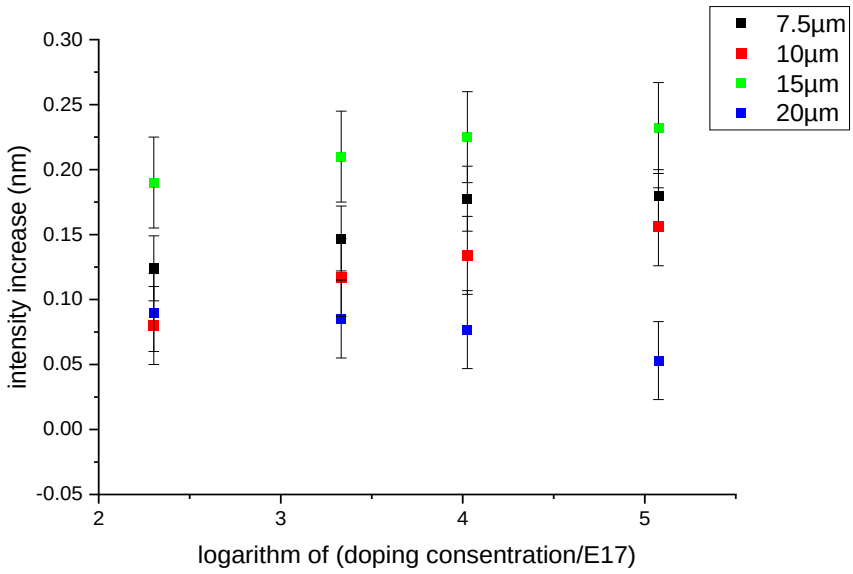

Figure 4. 32. The fraction of intensity increase vs doping level for p-doped GaAs sample for different condenser apertures.

4.4 Influence of working distance on image contrast

The Raith EO FEG-SEM used in this study has a Gemini lens system built by Zeiss. Gemini lens (which is a compound lens consists of the magnetic lens with an electrostatic lens placed behind the specimen) was first applied to improve the optical performance of the pure magnetic design from Carl Zeiss[266]. For conventional SEM with immersion lens, the energy of 1keV is available and Gemini lens extend the energy down to 100eV. The resolution for DSM 982 SEM with Gemini column can achieve 4nm resolution at 1keV and 1.2nm at 20keV[267], the 10.17nm spot size at 100eV can be achieved by using program to control the lenses in Gemini column [268].

The immersion objective lens was first described by German scientists in 1930 [269]. The sample was used as cathode to emit electrons and the electrons leaving sample surface passed through the electrical field between sample and an anode above the sample. With other electrodes between the sample and anode, electrons can be focused to form an image. The immersion objective lens can be also called cathode lens [270]. The scheme of the cathode lens is shown in Figure 4. 33 below.

This means the electrical field lines emerge from the opening within the objective lens. In SEM image, the electrical field between tip and sample is illustrated in Figure 4. 33. When the sample is far from the pole piece, the electrical field will suppress the emission of secondary electrons and when the sample has a very small working distance, typically less than 3mm, the electrical field will accelerate those secondary electrons, thus low energy SEs will get energy to pass the energy barrier and the SE yield increases with the help of external field.

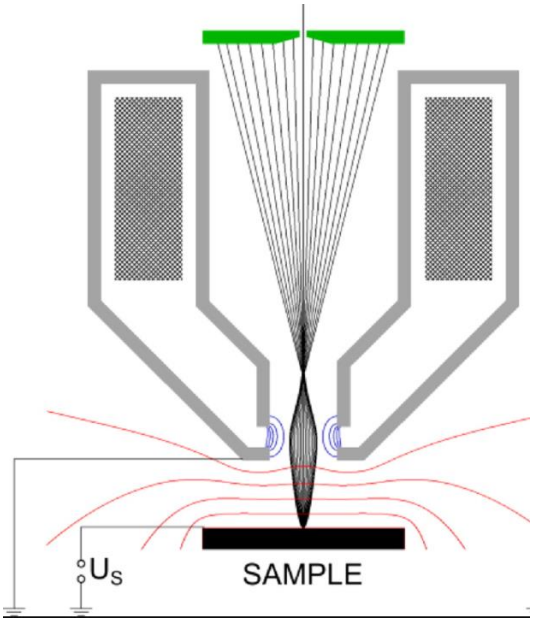

Figure 4. 33.The external electrical field has an impact on SE emission; the red lines are equipotential lines, the field lines would be perpendicular to them [271].

For a Gemini SEM, though the lens will provide superb resolution at low electron beam energies, the field between sample and column is more complicated as the magnetic and electrostatic fields overlapping. So, it would be help to check the influence of working distance on image contrast too. As shown in Figure 3. 9, the beam booster is used in Gemini column will create the electrostatic field. For beam boosters used in latest Gemini 500 Carl Zeiss Microscope, the beam booster is report to be fixed at 8kV for accelerating voltages larger than 0.1keV[272]. Thus we must consider the electrostatic field in Raith SEM used in this work with similar Gemini column.

As changing the working distance allows the user to change the intensity of the field which affect the specimen surface, Sarka et. al reports that at short WD (1mm), the in-lens detector will collect electron with higher kinetic energies and more SE2s as the electrostatic field is very strong; at middle WD (3mm), the collection efficiency will go down with weaker field influencing the sample surface, the in-lens detector can still detect some SE2 but its contribution to total SE intensity is reduced; and at long working distance (>5mm), the influence of electrical field on sample surface is weakest, and low energy SEs are attracted and collected by the detector[272].

Comparing to an immersion lens SEM, SEM with a Gemini column using long WD still can attracts the SEs to the detector rather than suppress the SE emission. This is the reason why we did not get any useful SE images in the FEI 50 SEM with 9mm working distance at 1-5kV.

To investigate how the working distance (WD) influences the dopant contrast, the n-doped GaAs staircase sample was used to take in-lens SE images with 7.5µm condenser aperture at 2.0kV. The working distance has been changed from 2mm to 7mm.

The image profiles are plotted in Figure 4. 34. It shows that when the working distance is larger than 4mm, the contrast of layers is opposite to that image contrast measured at working distance

smaller than 4mm. the image intensity of doped layers at 4mm working distance is almost constant, i.e. there is little contrast. For working distances less than 4 mm, the low n-doped regions appear brighter than highly n-doped regions. For working distance larger than 4mm, the low n-doped regions appear darker than the highly n-doped regions.

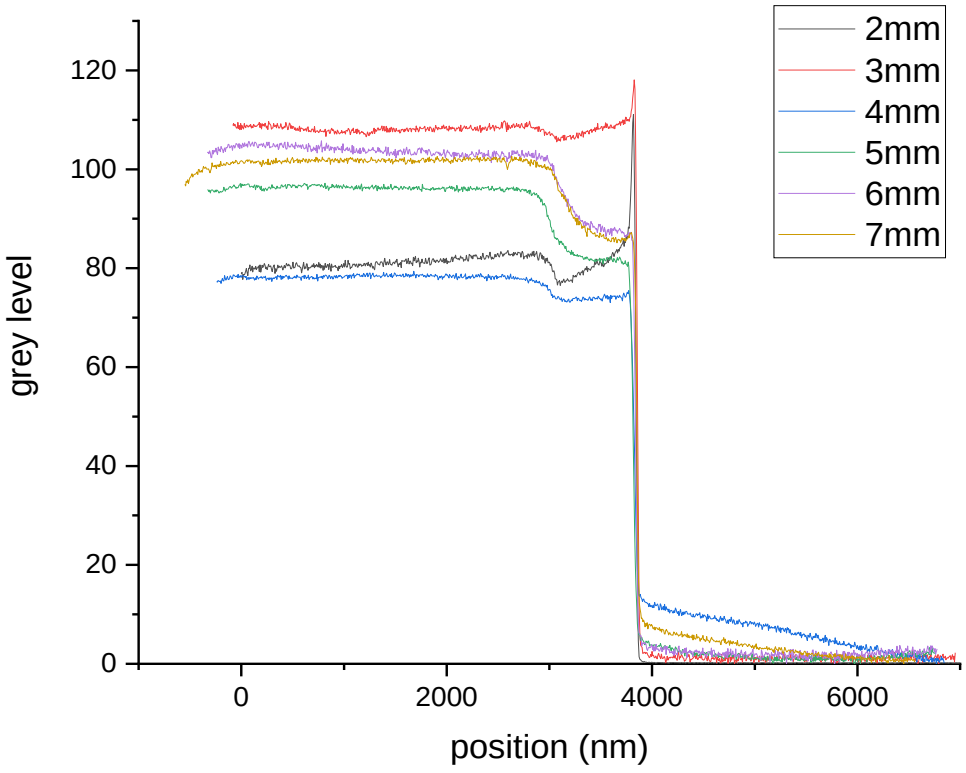

Figure 4. 34. The intensity profiles of Si doped GaAs images taken at scan speed 6, 40kX, 2.0kV and 7.5µm aperture with different working distances. Remember the highest doped layers are those near the buffer as the n-doping staircase is reversed in direction compared to the p-doping staircase.

In Figure 4. 34, the contrast inversion has been shown for working distance 2 and 3mm. This could be due to strong electrical field attracts more SE2 at small WD. As shown in the appendix, the outer most layer has highest Si dopant concentration and doping decreases towards buffer layer, so we expect more BSEs from outer layer and less from inner layers. In previous discussion in section 2.15, we know SE2 is a result of BSEs interacts with the specimen, the inversion of contrast suggests the higher BSE yield for layers of higher doping levels, and this matches our expectation. For middle WD of 4mm, we start to see the reduction of SE2 which means the electrical field on sample starts to be reduced. And for long working distance (>5mm), SE2 are suppressed to get optimized SE image for dopant contrast. Our result shows similar results of how working distance of a SEM with Gemini column influences the in-lens SE image contrast with others' work[272].

4.5 Influence of carbon contamination

Figure 4. 35 is an SE image of an undoped GaAs substrate at 15kV before carbon deposition.

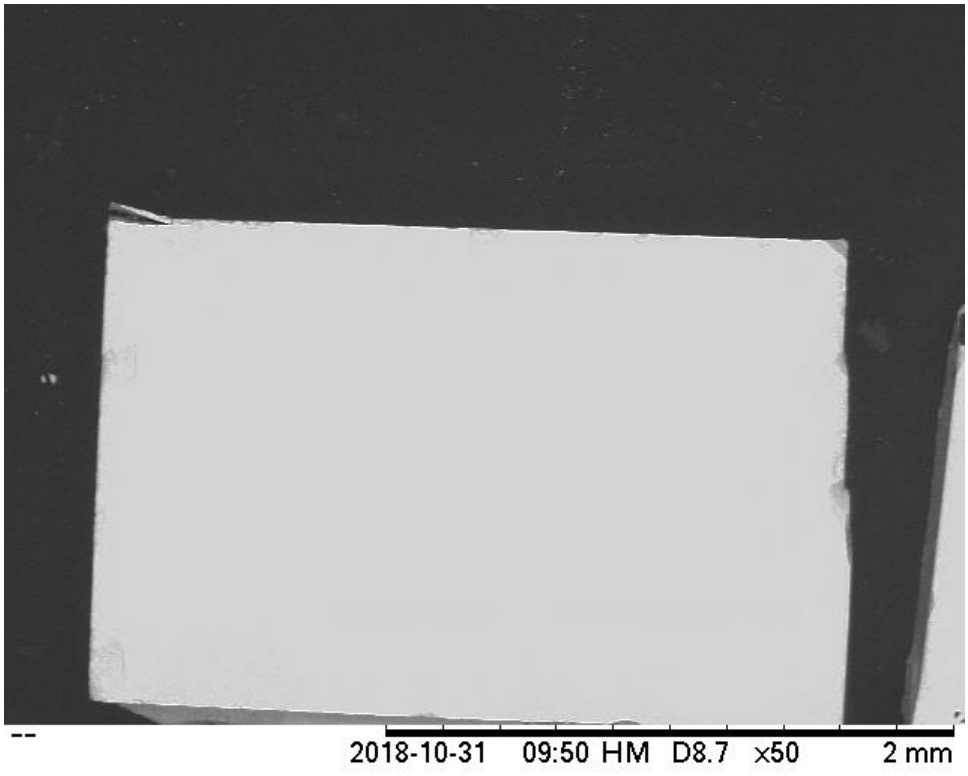

Figure 4. 35. The GaAs specimen before carbon deposition at 15kV, 50X mag, 8.7mm working distance fast scan, BSE mode.

In Figure 4. 35, we noticed that no leaving residuals appear at the GaAs surface and the specimen is very clean before carbon deposition. Then, we started intentional carbon deposition by scanning an electron beam very slowly repeatedly near the edge of specimen, first at high magnification, then at successively smaller magnifications, thereby increasing the field of view and reducing the contamination build-up each time. The region studied is at the mid-top of the specimen, this makes it easier to locate the region in following experiments.

After the carbon deposition of successively decreased scan windows (high mag first), the SE and BSE overview images shown in Figure 4. 36 and Figure 4. 37 were recorded.

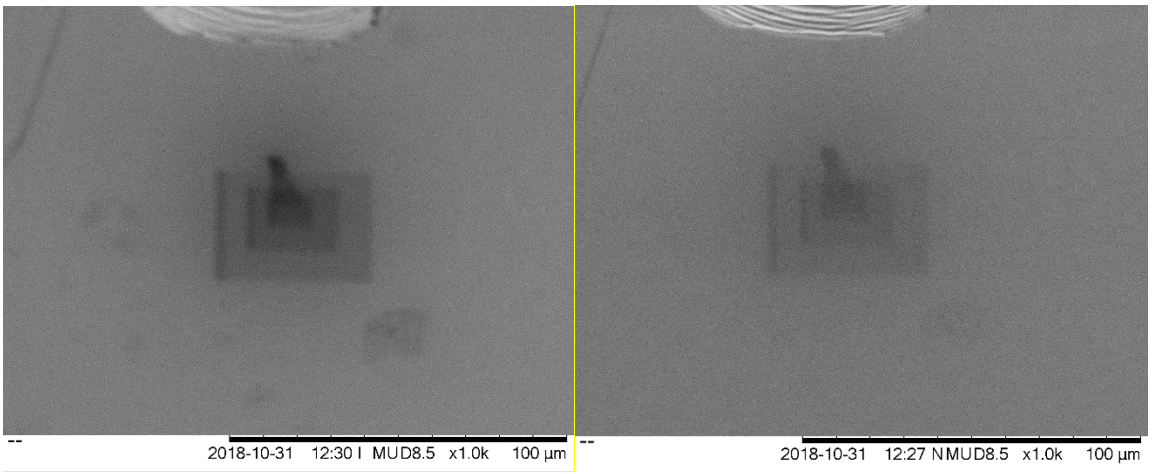

Figure 4. 36. SE images of 5kV (left) and 15kV (right) of GaAs surface after repeated scans over different field of views.

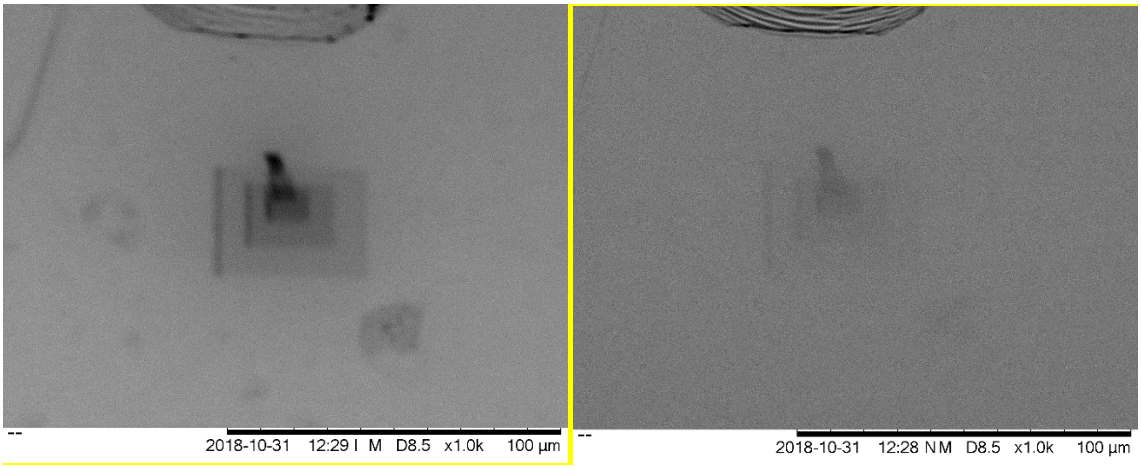

Figure 4. 37. BSE images of 5kV (left) and 15kV (right) of GaAs surface after repeated scans over different field of views.

Figure 4. 37 and Figure 4. 37 shows overlays of 5 carbon layers corresponding to 5 scanning windows. The smaller the scan window is, the thicker and darker the region becomes.

For SE images in Figure 4. 36, the contrast mechanism is complex. The plasmon energies are 24 eV for carbon and 15.8 eV for GaAs [273], and excited plasmon can decay and transfer their energy to conduction electrons near the Fermi level, creating more SEs. After SEs diffuse to the surface, only SEs with energies higher than work function can escape from surface barrier. The work function of carbon is 4.9 eV which is larger than GaAs 4.73eV. Besides, the SE2 also need to be considered, thus $\delta = \delta_{PE} + \beta\eta$, where δ is the SE yield, δ_{PE} is the SE1 yield from primary electron (PE), η is the BSE yield and $\beta = 2 - 3$ is the factor that tells us how many SE2s one gets from BSEs. All these factors discussed result in the intensity decrees with carbon thickness in Figure 4. 36.

For Figure 4. 37, this can be explained by the atomic number density of carbon being less than that of GaAs: carbon generates fewer BSEs than GaAs. The scanning window of 60kX magnification is inclined compared to other windows. When checked with optical microscope, the structure has no difference with or without a tilt angle relative to perpendicular direction. As 60kX is the highest mag, it may require higher focusing power for the lenses, this could be the reason why 60kX mag window inclined with other windows. Or it is due to the sample drift during the observation.

For both BSE and SE images in Figure 4. 36 and Figure 4. 37, the left edge of the rectangular windows is darker than other parts of the corresponding window. This is because the SEM scans in a raster manner, before it starts to scan the next line, the beam is briefly parked at the starting point for a while (typically a few µs). This is called fly-back and is to reduce scan distortions.

After SEM imaging, the carbon deposited specimen is scanned by atomic force microscope to obtain the thickness of the windows. The line scan result is shown in Figure 4. 38.

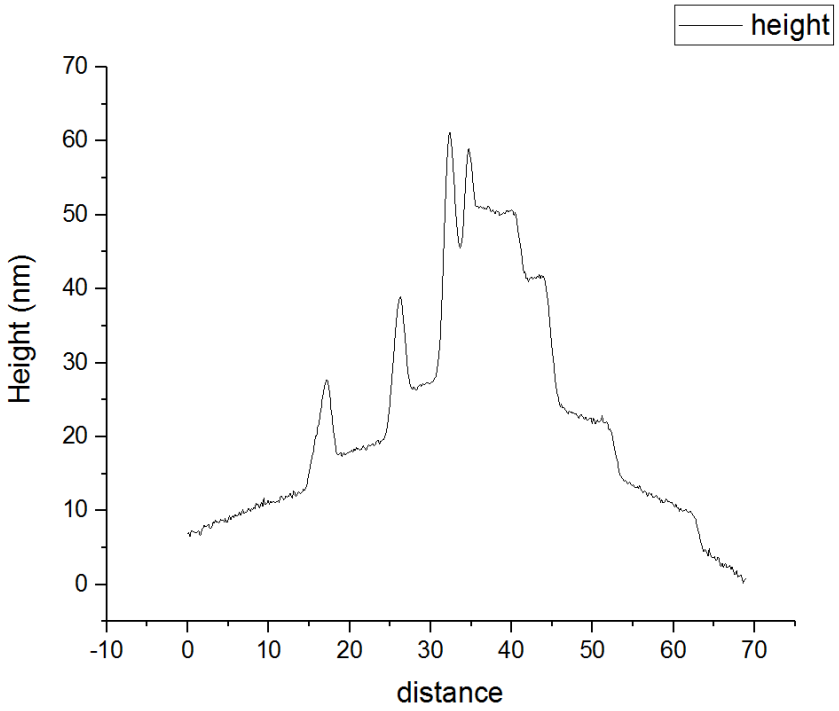

Figure 4. 38. The line profile of carbon deposited region by Bruker Dimension Icon AFM in tapping mod.

The peaks at left side of steps are due to the probe staying at the begin of a scan line at start of scanning each line. The total height for different carbon layers in the plateau regions are shown in Table 4. 2.

magnification	4kX	7kX	15kX	30kX
Carbon thickness (nm)	12±2	21. ±2	37. ±1	46. ±1
Window size (μm^2)	1440	481	87.5	9.45

Table 4. 2. The carbon thickness for successively decreased scan windows

Figure 4. 39 below plots the relation between carbon thickness and magnification.

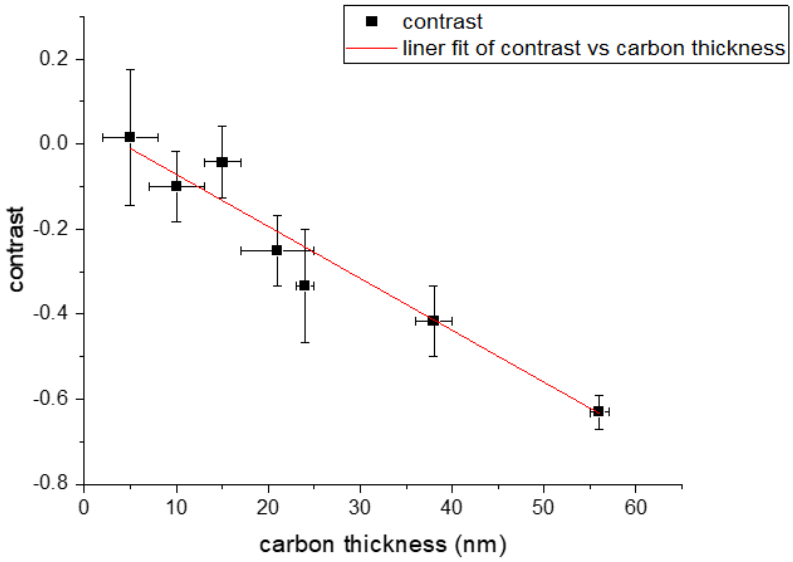

Figure 4. 39. The influence of carbon thickness on SE contrast at 5kV.

It is clear that the carbon thickness is increased when imaging at higher magnification. With same scan speed and duration, the scanning times is increased for smaller regions as the scanning during is 30mins for all the windows and scan window changes by factor of 2 which means pixels size changed by the square root of 2.

After the sample is scanned by AFM, EDX images have been taken for the same area for an hour to avoid noise and accumulate sufficient X-ray signal for carbon layers, but unfortunately, the EDX map in Figure 4. 40 have not shown the carbon structure.

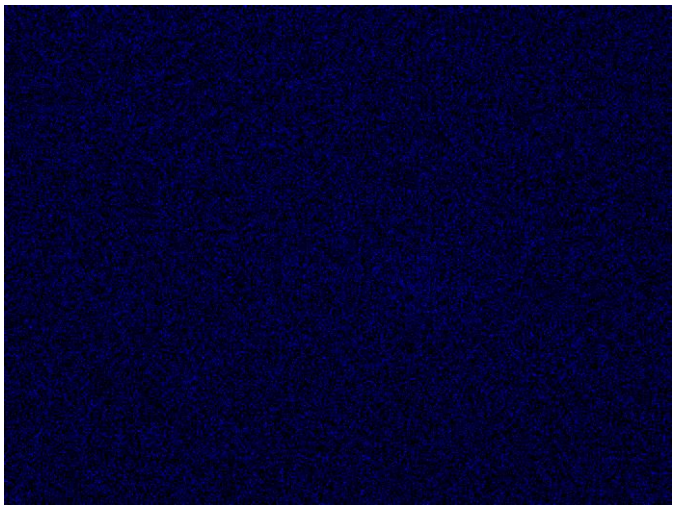

Figure 4. 40. Carbon K map of the contamination structure.

The counts of X-rays from carbon are fewer than from GaAs.

4.6 Effect of etching of the Si doped GaAs sample

For a cleaved GaAs specimen surface, an oxide layer will be formed in ambient environment. This oxide layer is considered to add an extra barrier to electron emission [274]. To avoid the oxide layer influencing the doping contrast, we designed a wet chemical etching experiment using bromine in methanol solution to remove surface oxide. The etch rate for GaAs depends on the bromine concentration in the solution, for high etch rates 5-20% of bromine concentration is used, while for light etches or polishing 0.1-1% is used [275]. We selected low bromine concentration to perform light etch, as the typical oxide layer thickness of GaAs substrates is about 1-3nm [276].

The bromine-methanol etchant must be used very carefully as both liquids are toxic and bromine is highly corrosive. A risk assessment form and information about control of substances hazardous to health (COSHH) form must be provided. The etching process is performed in a fume cupboard under supervision. The concentration we used was 17µL bromine (>99.9%) in 10mL methanol (>99.99%), yielding 0.17% bromine concentration by volume. Figure 4. 41 is a photo of the bromine-methanol solution in a petri dish. The n -GaAs samples have been dipped into the solution for 5, 20 or 60 seconds.

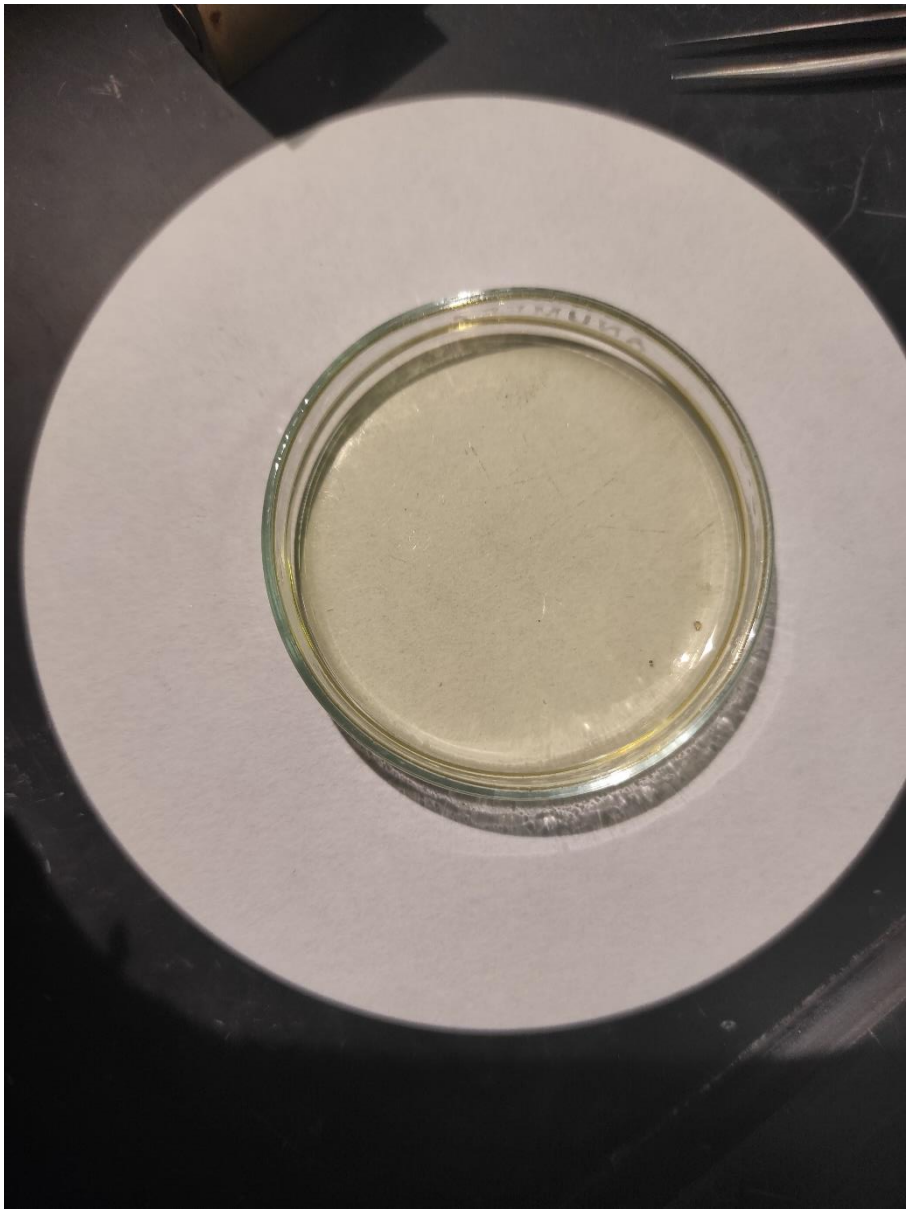

Figure 4. 41. The 0.17% bromine-methanol solution in petri dish shows a light yellow colour. A total volume of about 10mL is used.

Figure 4. 42 is a 1.5kV SE image of the 5s etched n-type GaAs staircase sample.

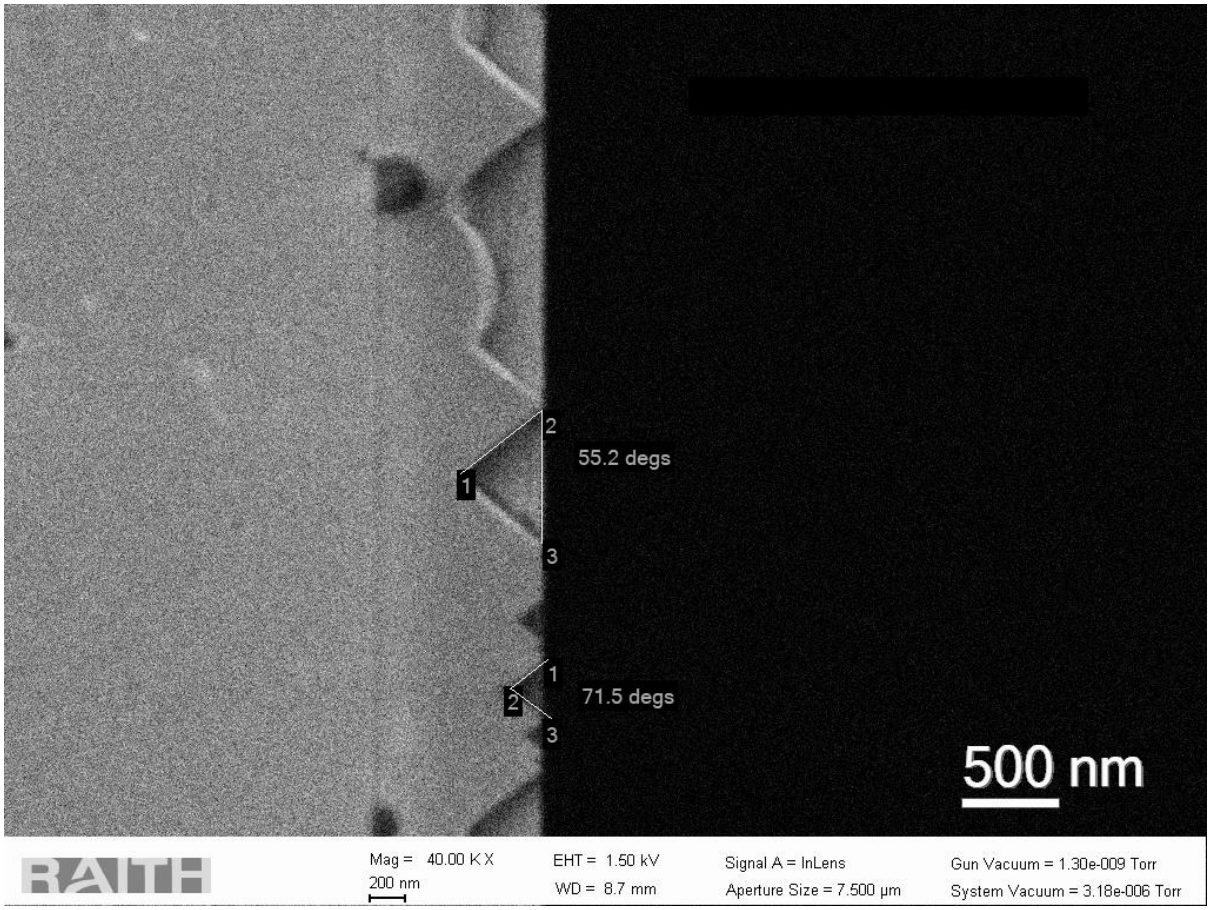

Figure 4. 42. 1.5kV SE image by Raith SEM of n-GaAs etched in 0.17% bromine-methanol etch for 5s etch time.

From Figure 4. 42, the etch pits are the dominant etching effect. The maximum etch depth is about 400nm after 5 seconds of reaction time, corresponding to an etch rate of 80nm/s. This etch rate is too high for our purpose as we only need to remove oxide layer less than 5nm. From the shape of the etch pits, we find the preferential etching of GaAs occurs on (111) and $(\bar{1}11)$ planes. As shown in the annotation of Figure 4. 42, angle 1 is 55.2°, which is very close to the intersection angle of 54.7° between (100) and $(1\bar{1}1)$ planes. The angle 2 below is measured as 71.5°, which is close to the intersection angle of 70.5° between (111) and $(\bar{1}11)$ planes.

For better understanding, the crystallographic planes are drawn in Figure 4. 43, the different planes in cubic system are represented by their different Miller indices.

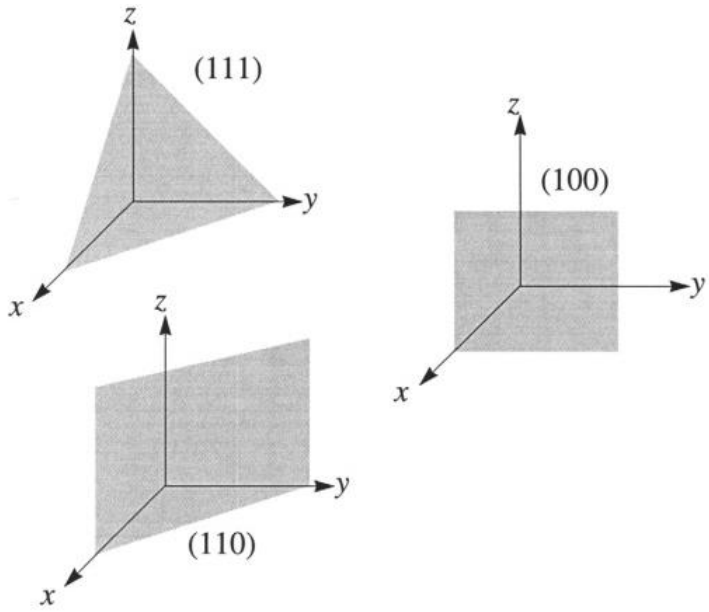

Figure 4. 43. Crystallographic planes in the cubic system and their Miller indices[277].

The intersection angle between ($h_1k_1l_1$) and ($h_2k_2l_2$) in cubic materials is calculated by:

$$\cos\theta = \frac{h_1k_1 + h_2k_2 + h_3k_3}{\sqrt{(h_1^2 + k_1^2 + l_1^2)(h_2^2 + k_2^2 + l_2^2)}}$$

Figure 4. 44 is the SE image of n-GaAs staircase sample etched by 0.17% bromine-methanol for 20s.

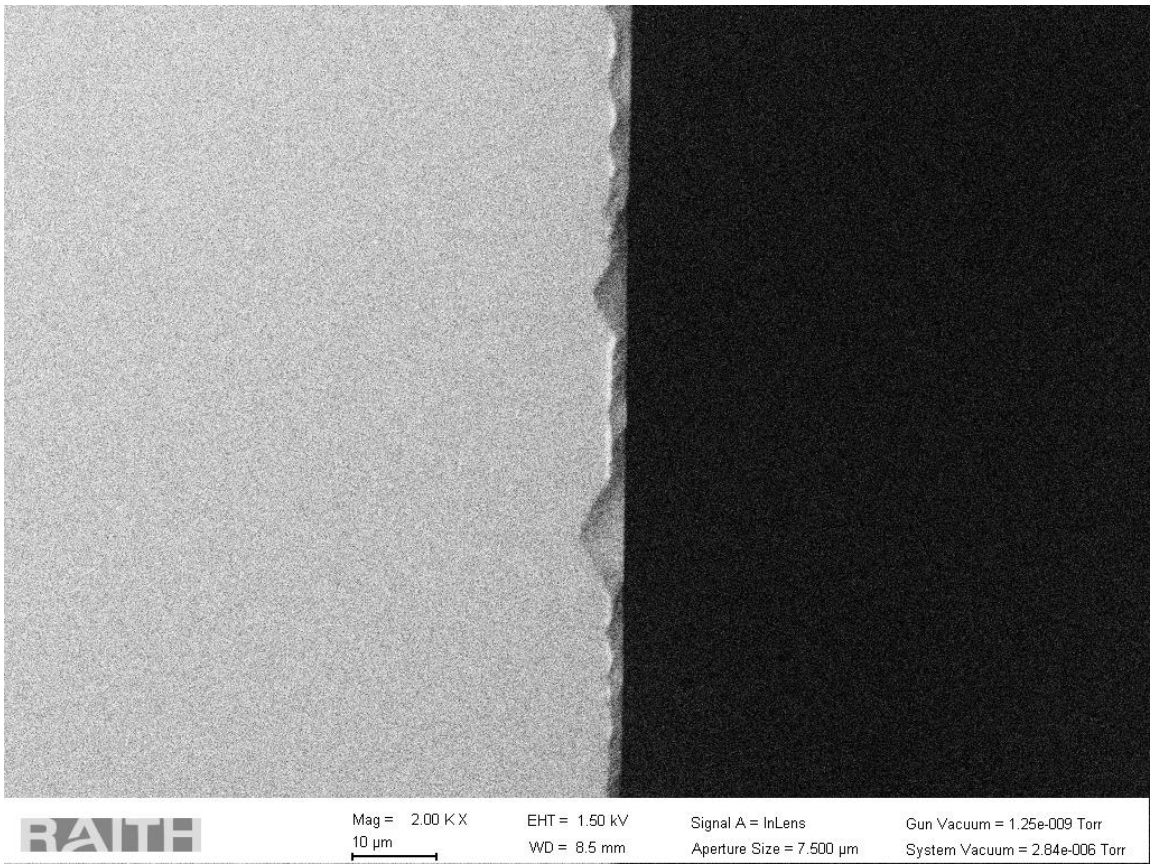

Figure 4. 44. 1.5kV SE image of n-GaAs etched in 0.17% Bromine-methanol for 20 s by Raith SEM.

From Figure 4. 44, we notice that the etching effect is even stronger, the etch depth here is 2-3µm. When etching GaAs for 20 seconds, the most important staircase structure of the n-GaAs sample has been completely etched away.

The notches in Figure 4. 44 are tetrahedral in structure and look different from Figure 4. 42. In Figure 4. 42, the direction of etching is mainly $[0\bar{1}0]$, [111] and $[\bar{1}11]$, while in Figure 4. 44, the preferential etch planes are (211), $(2\bar{1}1)$ and $(1\bar{1}1)$. Preferential etching at higher Miller indices has been reported for GaAs wet etching using bromine-methanol and H_2SO_4-H_2O_2 in 1971 [278]. This preferential etching can be used to form GaAs (211) substrates for MBE and liquid phase epitaxial growth [279], [280].

Figure 4. 45 also shows the 20s etching effect but at higher magnification. From the image, we notice that the surface after etching is not smooth as after a fresh cleavage. These shallow etch pits will make additional topography contrast, and it is difficult to measure doping contrast when there is significant surface roughness present. It has been reported that the polishing action is poor when bromine concentration is above 0.05% [281].

For the longest etching time, dip GaAs staircase samples into bromine-methanol for 60 seconds, the image is shown in Figure 4. 46.

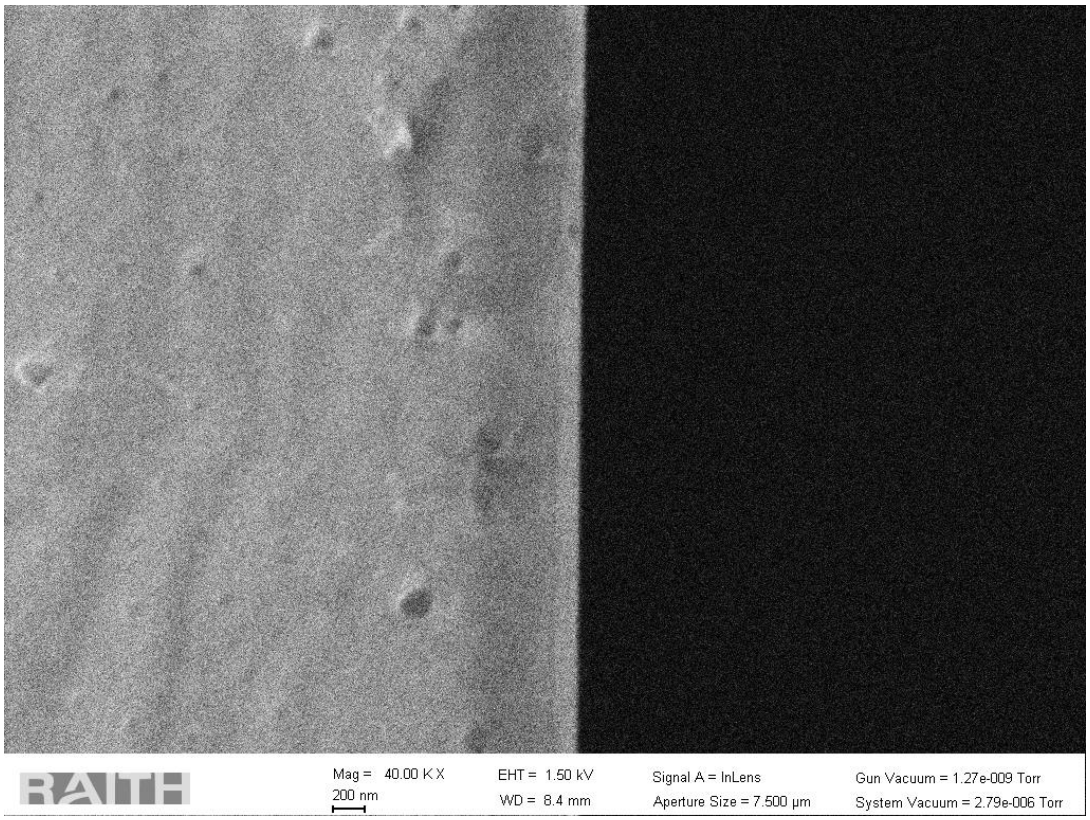

Figure 4. 45.1.5kV SE image at 40kX of n-GaAs etched in 0.17% bromine-methanol for 20s

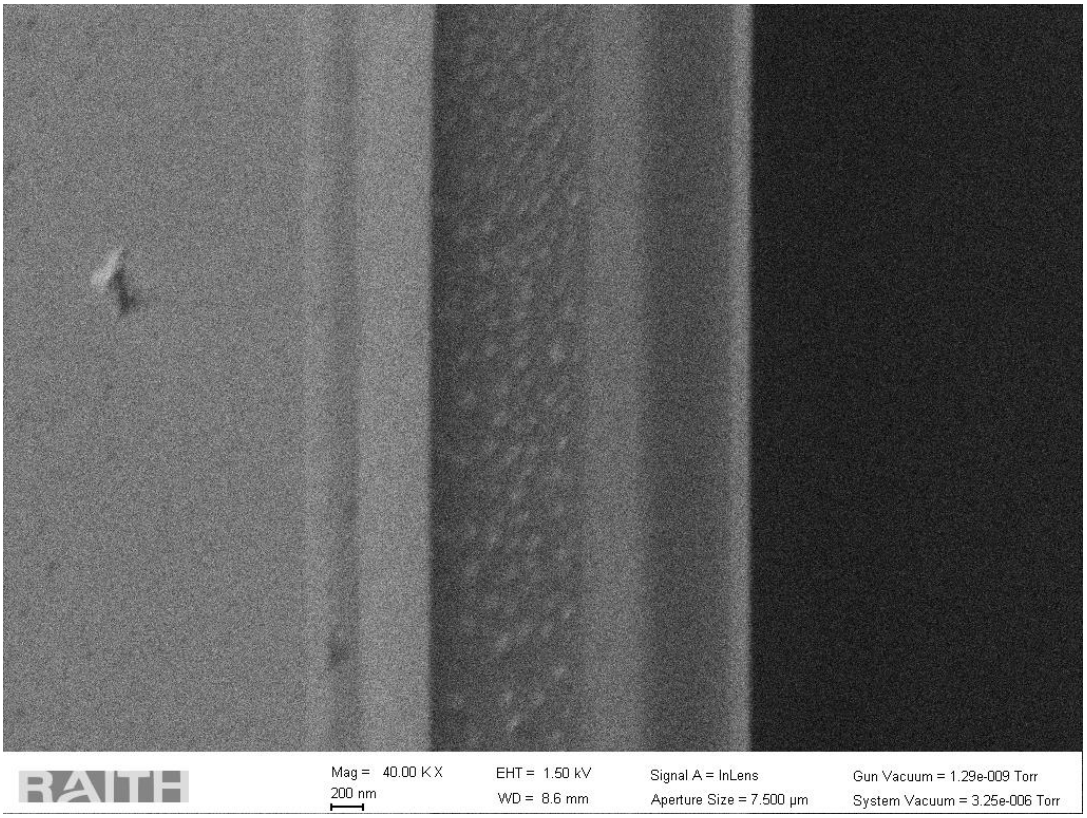

Figure 4. 46. 1.5kV SE image at 40kX of n-GaAs etched in 0.17% bromine-methanol for 60s

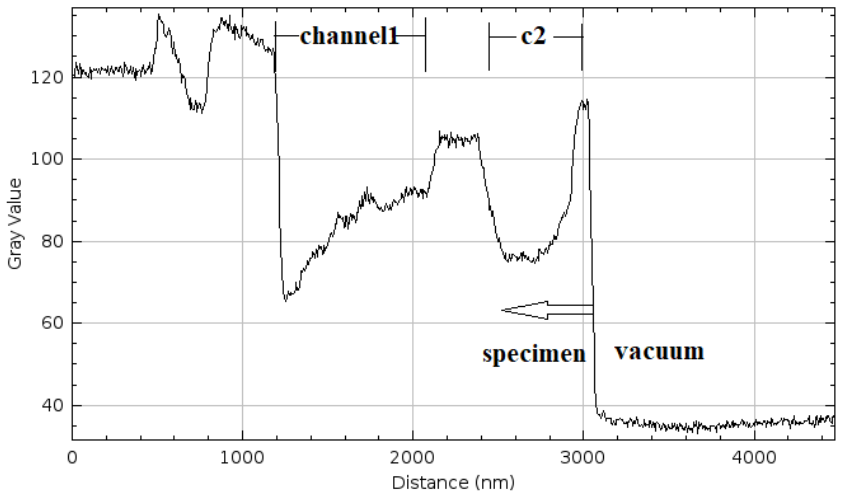

Figure 4. 47. The SE intensity profile of 1.5kV SE image at 40kX of n-GaAs etched in 0.17% bromine-methanol after 60s

As we can see, the 60s etched n-GaAs specimen shows a 750-800nm deep feature labelled 'channel1' in Fig. 4.51 with many spots in it. I guess this is due to the etching speed of GaAs being different in various directions. The white etch pits look like tetrahedral located in the channel, they may be dislocation etch pits [282]. Such a phenomenon has been discussed in the preferential etching of GaAs and its etched profiles with thick patterned aluminium oxide layer [278]. In our case, we do not have a designed window, but selective etching may occur due to intrinsic dislocations. Defect induced selective etching for GaAs using bromine-methanol has been discussed in [283], [284]. Figure 4. 46 suggests why it is essential to have buffer layers when designing semiconductor devices.

Noticeably, the width of etch channel1 is about 800nm. This might suggest a p-n junction is formed at the interface of undoped GaAs and buffer. Report on p-n junction detection by etching can be found in [285], [286], and when an electrical field is present, the etch speed will be enhanced further. If we assume the junction is abrupt, the depletion width is 800nm, 0.75V basis and the doping level of n-type buffer layer is $1.0\times10^{18}cm^{-3}$, the calculated p-type concentration is about $3\times10^{15}cm^{-3}$.

Why then should a nominally undoped GaAs substrate show p-type properties? The answer could lie in the crystal growth of GaAs ingots. GaAs can be grown under As-rich condition or Ga-rich condition. If As melts is larger than a critical composition (As-rich), the wafer material will show n-type and high resistivity electrical properties [287], while under Ga-rich condition, GaAs wafer would be p-type and low resistivity [288]. Besides, As diffusion which can form inclusions in the wafer can also make bulk GaAs p-type [289]. As point defect concentration has been reported to be at least 10^{16}-10^{17} cm^{-3} by examination in TEM [289]. This magnitude is an order of magnitude higher to the value $3\times10^{15}cm^{-3}$ we obtained from SEM experiment of etched n-GaAs staircase sample.

The topography contrast in channel2 (c2) is perhaps due to the etch speed increasing with doping concentration. In addition, the variation of GaAs substrate region on the left of channel1 may be due to the dislocation density showing an 'S' shape as a function of depth in GaAs wafers [288].

From our etching experiment, the etch rate of 0.17% bromine-methanol is approximately 80nm/s for [010] direction and 45nm in [111] direction. Compared with literature, the 0.25% bromine-methanol was reported to have 15nm/s for GaAs[100] and 2nm/s for GaAs[111] direction [278]. The increased etch rate in our experiment may be due to doping [290].

5 Resistive AFM measurements of GaAs based doping staircase samples and p-i-n LED sample

5.1 Result and discussion of CAFM measurement

5.1.1 Be-doped GaAs staircase sample

Figure 5. 1 below shows the topography (a) and CAFM measurement (b) of the Be doped GaAs staircase sample.

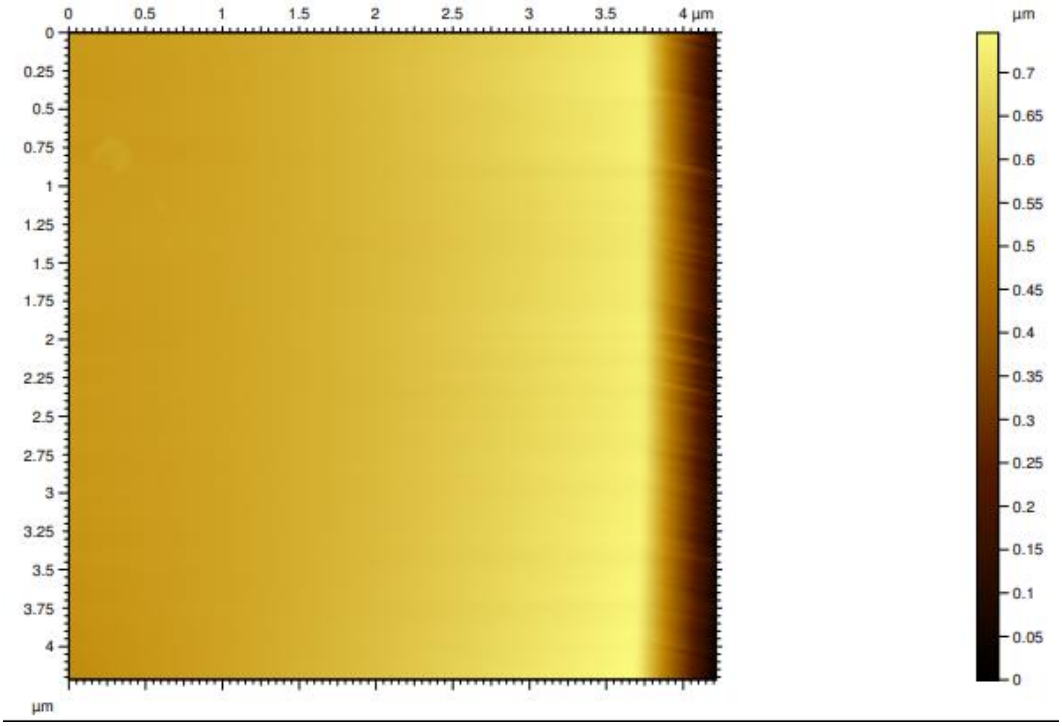

Figure 5. 1. The topography of Be doped GaAs obtained by Nano-observer AFM microscope from CSI instrument, data recorded by Emmanuel Lepleux. The scanned area is $4.5 \times 4.5\ \mu m^2$.

As Figure 5. 1 shows, there is an apparent topography slope on the right-hand side of the image and the depth is about 700nm over a lateral width of only 450nm. That means there is a slope of $\tan(\theta_t) = \frac{450}{700} = 0.64$, i.e. the tilt angle $\theta_t = 57°$. This angle is close to the angle between [111] and [100] plane which is 54.7° and the facet is likely to be {111} type. As GaAs is a binary material, the atoms of {111} type planes can be either Ga or As atoms. Such polar surfaces have different work functions (which range from 4.306-4.831eV due to the electron removal from metal-like surface) to the (001) growth plane with 5.013eV calculated work function and normally {111} planes are no cleavage planes in the sphalerite lattice [291]. For Ga rich (111)A surface, the work function is 4.01eV, while for As rich (111)B surface, the work function is 4.71eV, as measured by Auger electron spectroscopy [292]. The GaAs (110) surface has a work function of 4.74eV which is similar to (111)B surface.

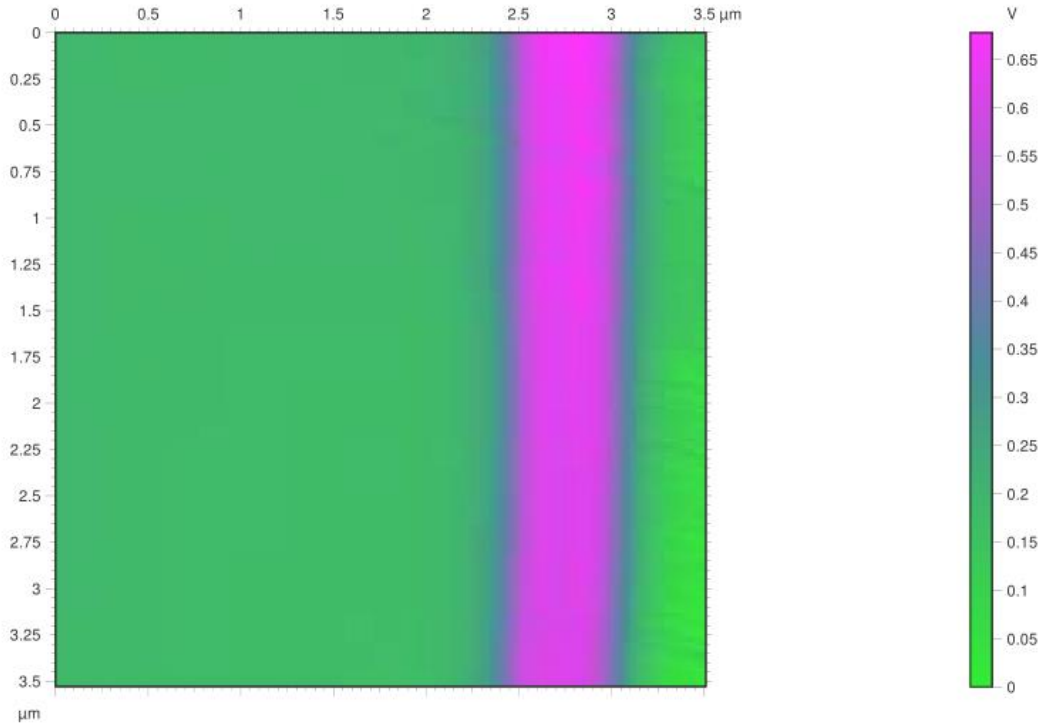

Figure 5. 2. The work function map of the Be doped GaAs

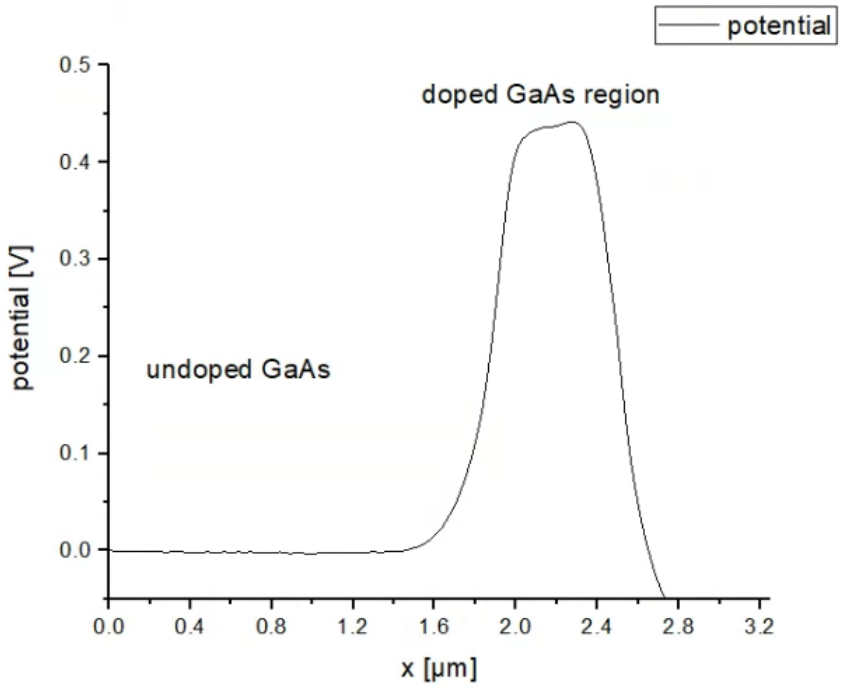

Figure 5. 3. The work function profile of the potential map in Figure 5. 2.

In the CAFM potential profile, we can only see one doped layer which appears about 600nm wide. Considering the tilt angle of 57°, the facet starts thereafter the 1600nm wide layer on the flat is around 400nm in projection; the actual length should be $400 \times \mathrm{cosec}(57°) \approx 750$nm, which probably only contains the 3 heavily doped 200nm layers.

The detection sensitivity is low for the three doped layers, this might be due to the difference between the work functions for these doped layers being small or that the sample cleaved so unfortunate that

the cantilever, in trying to follow the sloping surface, could not establish proper measurement conditions for resistive AFM. Using the highest nominal doping concentration of 1.6×10^{19} atoms/cm^3 in the topmost layer compared with the buffer layer of 10^{18} atoms/cm^3, the work function difference is only expected to be about 0.07eV from Equation 1.62. In Figure 5. 3, there is a little variation of potential signal in middle of doped GaAs region, however it is hard to identify where it comes from as the doping concentration induced work function differences are too small.

The work function measured in the doped GaAs region is 0.44eV larger than in the undoped region, however, the expected work function shifts induced by doping the buffer and the three top layers would be 0.76, 0.74, 0.72 and 0.69eV, respectively, calculated with Equation 1.62. The measured work function difference between doped and undoped region is only 58% of what we expected. I would suggest this might be due to the rapid oxidation of GaAs surface in air especially for the polar facet imaged. CAFM is a surface work function measurement method, which means that oxidation or contamination of the specimen surface would have significant influence on the accuracy of results. Besides, the CAFM detects the electrostatic force gradient and the work function obtained is the averaged work function of the area under the probe thus may not work well on a steep slope.

If we assume the oxidized surface consists half of gallium oxide (4.1eV work function), and half of doped or undoped GaAs, a roughly estimate of the average work function for the doped area ($\approx$5.5eV work function) would be $5.5 \times 0.5 + 4.1 \times 0.5 = 4.8\text{eV}$; for undoped region, the average work function would be $4.7 \times 0.5 + 4.1 \times 0.5 = 4.4\text{eV}$. The work function difference of doped and undoped region when half of the surface is oxidized would then be $\approx$0.4eV.

Although some of the specimens had been freshly cleaved before being put into the AFM, a large fraction of the surface seems to have been oxidized.

The potential map from Park system of the Be doped GaAs samples number 4 and 5 showed even less contrast of 100meV of doped layers and undoped layer due to the presence of humidity on the sample surface.

Figure 5. 4 below shows the surface topography of the Be doped GaAs staircase sample from resistive AFM measurement without steep slope. The sample is a little bit inclined, with a 0.25µm depth over a lateral width of 4µm. The overall tilt angle is about 0.0625 rad, or 3.5°.

Figure 5. 4. The surface topography information of Be doped GaAs specimen in resistive AFM.

Figure 5. 5 and Figure 5. 6 are the current and resistance maps of the same region of the Be doped GaAs staircase sample. The noise level in the undoped region on the left is low, indicating the good quality of the resistance measurement.

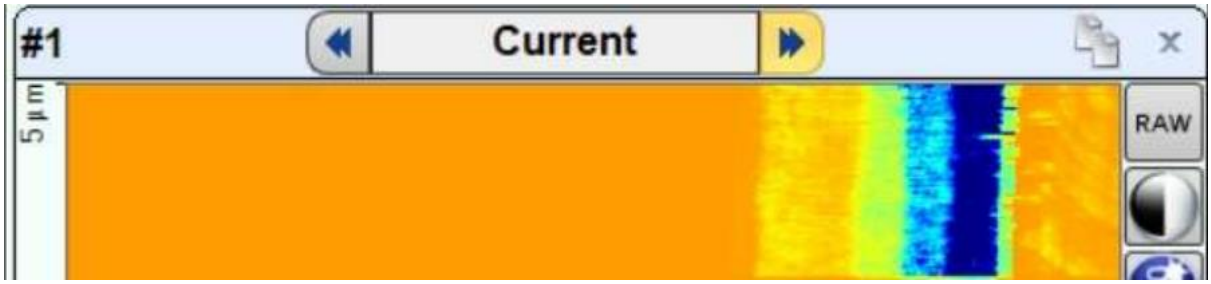

Figure 5. 5. The current map of the Be doped GaAs which reveals all the doped layers.

Figure 5. 6. The resistance map of the Be doped GaAs which reveals all the doped layers.

Figure 5. 7 and Figure 5. 8 plot the current flow and resistance between the conductive AFM tip and sample stage. In Figure 5. 7, we can clearly identify the buffer layer and three doped layers; the layer thicknesses from the edge are: 220, 209, 232 and 450 nm (from topmost layer to the buffer layer). The measured doping layer thickness appears to be a bit larger than the nominal thickness of 200 nm, and the buffer layer is 10% thinner than the nominal width of 500nm. The SEM image in Appendix of Hitachi SEM reported the layer thicknesses as 198, 198, 213 and 516 nm, respectively. The apparent broadening of three doped layers and apparent shrinking of the doped buffer layer in the resistive AFM image, and the line profiles of current and resistance maps are plotted in Figure 5. 7 and Figure 5. 8.

The resistance of three doped layers is low due to their high doping concentration: the higher the doping concentration, the lower the resistance. The nominal doping of buffer layer is 10^{18} atoms/cm^3, while the neighbouring doping layer is 2.8×10^{18} atoms/cm^3, ideally the resistance of buffer layer is 2.8 times larger than the neighbouring doping layer. From the resistances map, we find the resistance of buffer layer is 0.039GΩ, while the neighbouring doping layer has resistance of 0.0085GΩ.The resistance of the buffer layer is much higher than expected due to the functional abilities of buffer layer in MBE growth to reduce defects and diffusion of impurity atoms. As the buffer layer is used to create a smooth surface and avoid the impurities in and on the surface migrate towards the epitaxial layer, there are might be some defects present in the buffer layer. These defects act as carrier traps, and will reduce the electrical conductivity of buffer layer.

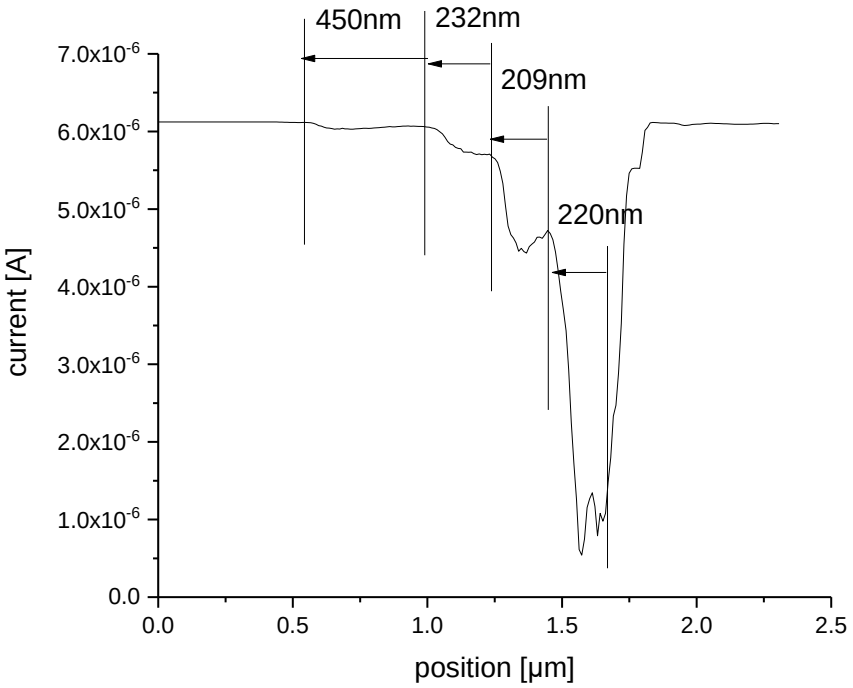

Figure 5. 7. The profile of current map for Be doped GaAs staircase. The sample is grounded and the tip bias is 1.7129V.

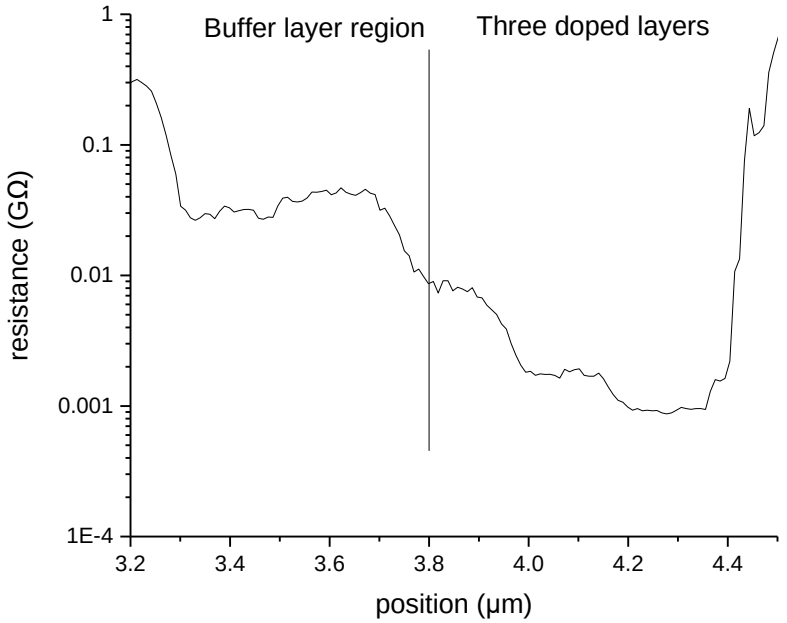

Figure 5. 8. The resistance of the buffer layer and three doped layers of Be doped GaAs staircase sample.

For MBE growth, no matter how good the substrate preparation is, it is still very difficult to get an atomically smooth surface as step-flow growth condition requires super saturation (which is the ratio between incident vapour flux and the equilibrium desorption flux from the surface) of atom flux on a surface will not exceed a critical value, which means nucleation on terraces does not occur and the steps are perfect sinks for incoming chemical species [293]. For a GaAs substrate, which is easily

oxidized, the annealing of GaAs at high temperature to remove the oxide makes the surface even rougher. Thus, the oxide desorption process at high temperature leads to surface roughening and re-construction. A subsequent buffer layer grown at lower temperature is needed to facilitate growth of smooth layers and sharp interfaces. The growth of the buffer layer contains initially a lot of defects and dislocations which can trap carriers and reduce conductivity [294].

That is probably why the resistance of the buffer layer is high in Figure 5. 8. As discussed in the beginning of this chapter, there are reports of atomic resolution resistive AFM achieved on insulators in UHV [13], but there are no reports of atomic resolution resistive AFM for metals. This is because the lateral resolution of resistive AFM is determined by the effective contact area, A_{eff}, between the cantilever tip and the sample. For metals, there are many free electrons in the crystal that conduct current easily. This de-localised electron gas results in a larger value of A_{eff} for metals. For isolators, on the other hand, the current transport is confined to the atoms around the tip, thus $A_{\mathrm{eff}}^{\mathrm{metal}} > A_{\mathrm{eff}}^{\mathrm{insulator}}$.

For the three highly doped layers, the effective contact area is increased compared to the intrinsic case, though probably not as large $A_{\mathrm{eff}}^{\mathrm{metal}}$; for the buffer layer with higher resistance, the effective contact area is smaller than for the higher doped layers. If the actual tip contact area were assumed to be constant during the resistive AFM imaging process, then the region with higher resistance would appear shrunken and the region of lower resistance would appear broadened.

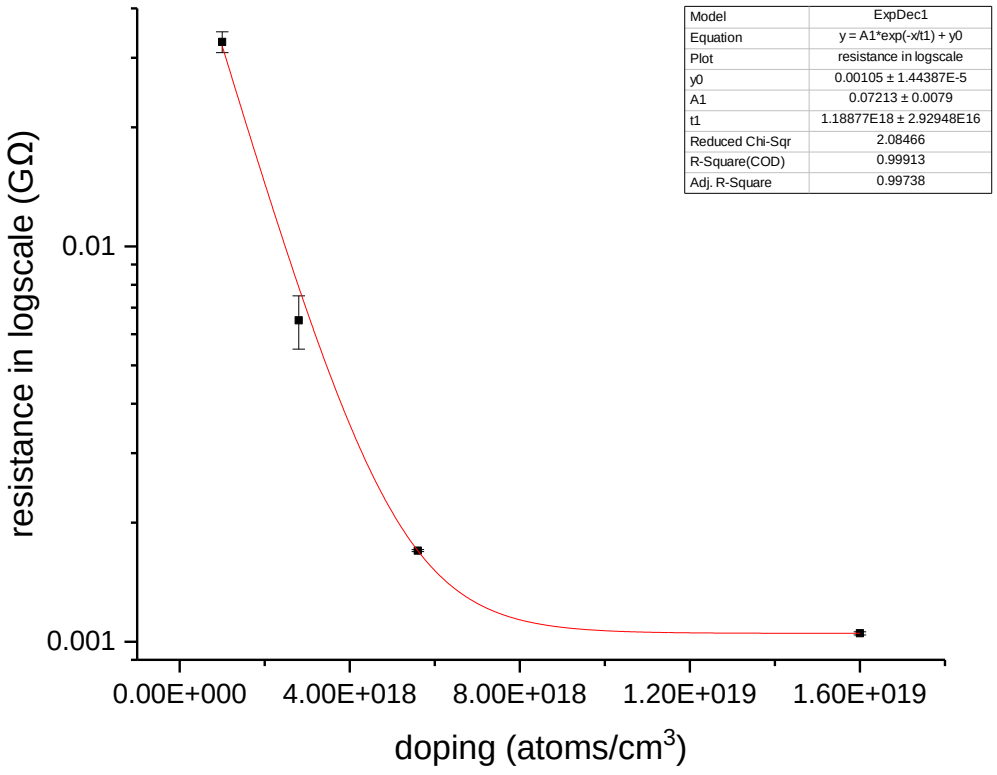

Figure 5. 9. The resistivity (on log scale) of Be doped GaAs from resistive AFM as a function of doping concentration.

5.1.2 VN790 sample

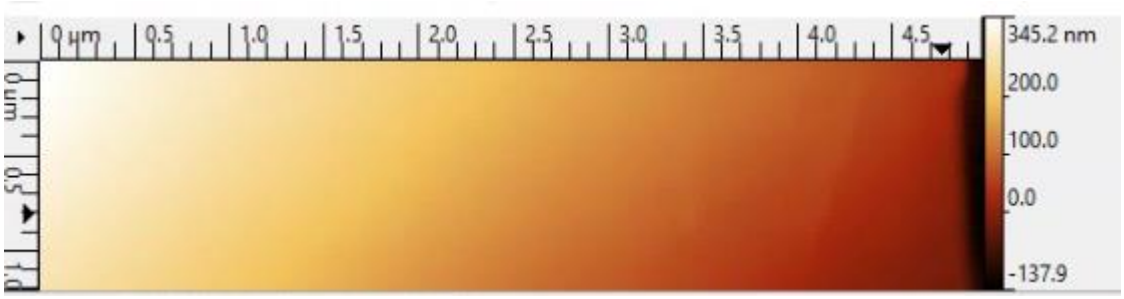

Figure 5. 10. The topography of VN790 sample surface.

The p-i-n structure GaAs-based LED sample has also been measured with resistive AFM. However, there are also some height differences across the imaged area. Figure 5. 11 and Figure 5. 12 show that the current and resistance measured of the same area are directly influenced by the surface topography information. The contrast from topography is too high near the right hand side, making the electrical contrast of the doped layers on the right-hand side near the surface disappear.

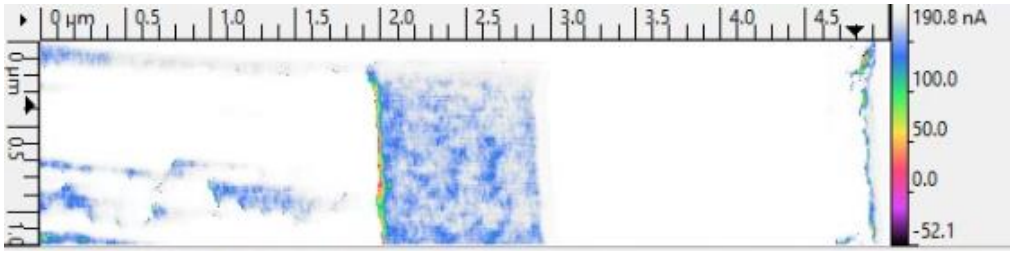

Figure 5. 11. The current map of sample VN790, the edge is at the right side of scan area.

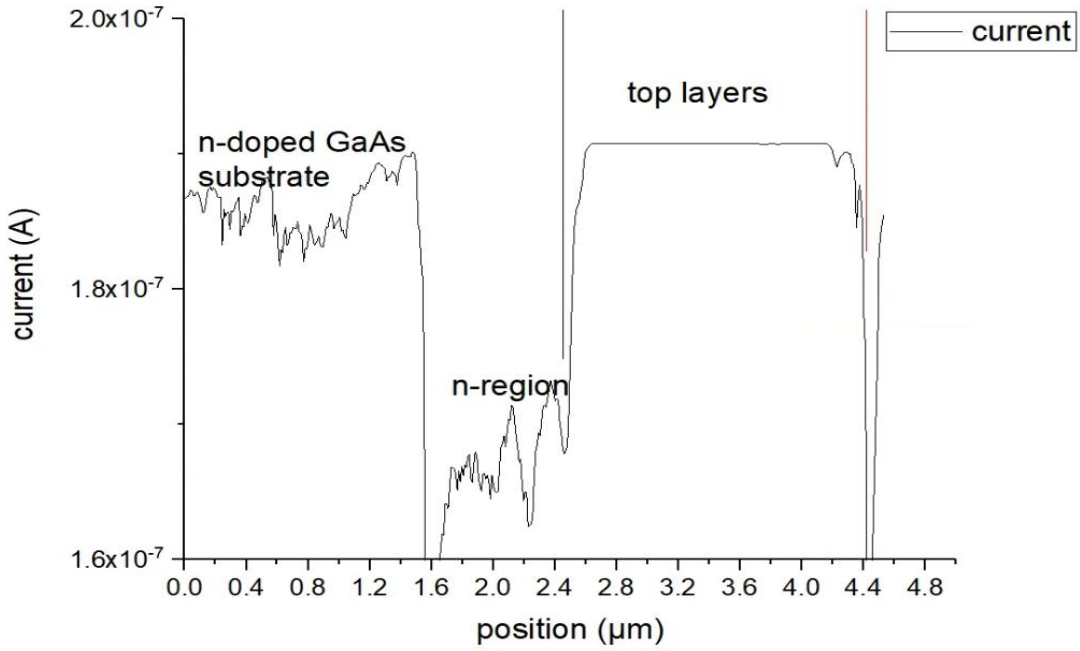

Figure 5. 12. The profile of current map and the regions that can be identified.

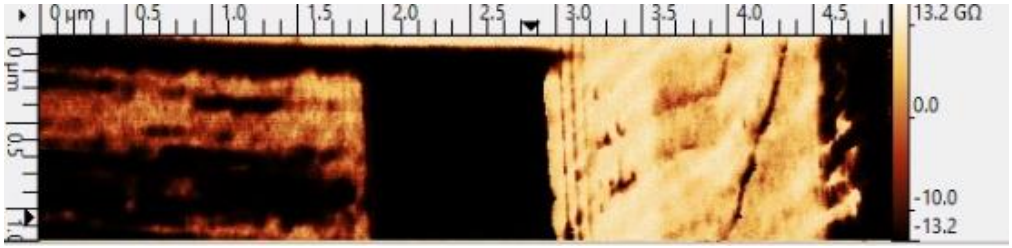

Figure 5. 13. The resistance map is also influenced by the surface defects, but it shows some contrast of the p-i-n structure.

In Figure 5. 11, the lowest current is measured at the interface of n-doped GaAs substrate and n-doped AlGaAs region. This is due to the discontinuity of AlGaAs/GaAs interface. The electrons are hard to come over the gap between valence band edges. The n-doped GaAs has better conductivity than AlGaAs (for intrinsic GaAs, the resistivity is $3.3 \times 10^8\ \Omega\text{cm}$ while for $Al_{0.4}Ga_{0.6}As$ it is $\approx 10^{13}\Omega\text{cm}$), hence the current is higher than n-doped AlGaAs region. The p-doped AlGaAs region is saturated, this might be due to the sample being reversed biased. To avoid this, it is better to use smaller voltage, or use positive bias.

From Figure 5. 13, we notice that there are positive and negative mark for the resistance, this is not due to the current direction. It is because the 0 resistance is set at the n-doped GaAs substrate, then the n-AlGaAs region must have negative value as its resistivity is worse than n-GaAs region.

The total layer thickness of the p-i-n structure is 2600nm from left of the black region in the middle up to the surface, which is close to the nominal thickness of 2550nm. The substrate used for the LED structure is n-doped GaAs, thus the variation of conductivity is minimised, and effective contact area of tip and sample did not change dramatically. The dark vertical stripes in the brightest region are the layers with InAs QDs (about 10nm in size). This suggests that the resistive AFM can do good quality measurements of nanostructures. The problem of the experiment on VN790 sample is there are too many surface defects on the scanned area.

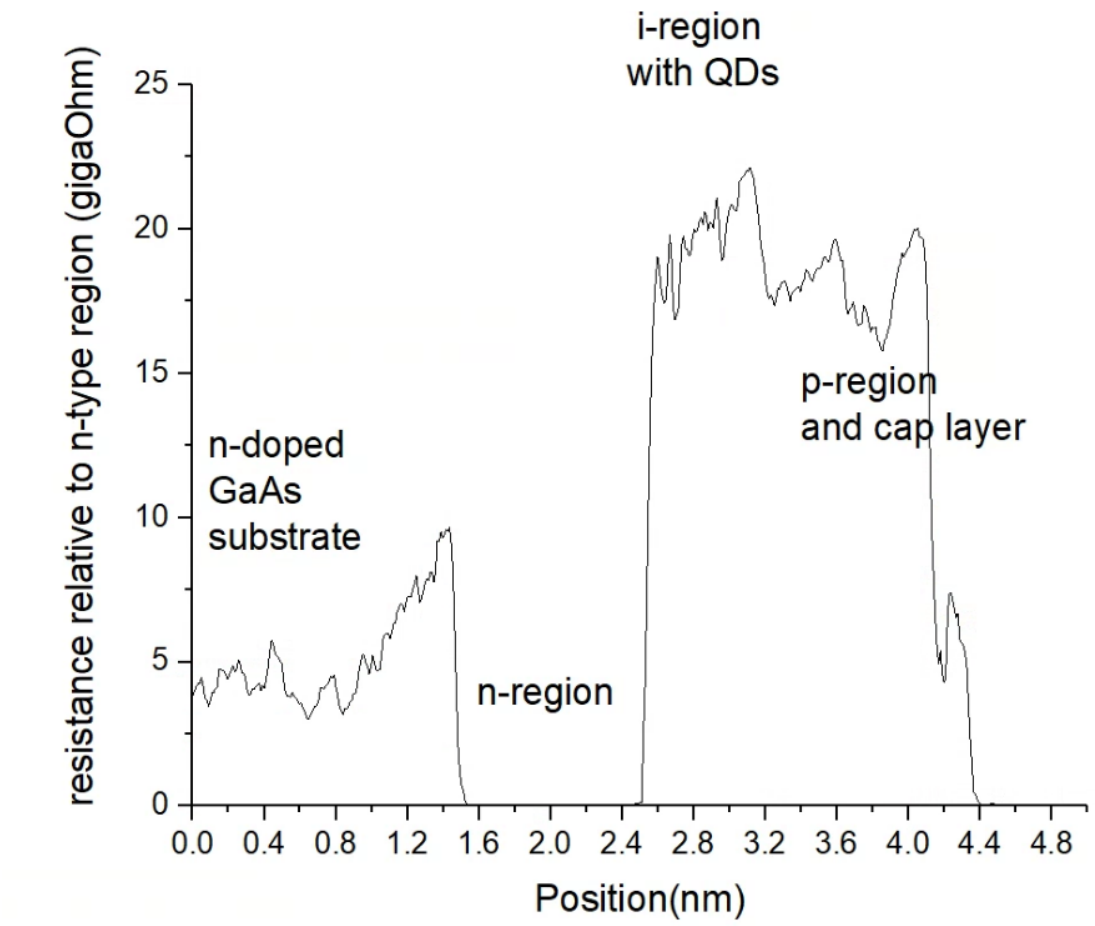

Figure 5. 14. The resistance increases relative to n-region in different regions of VN790 sample.

5.1.3 Conclusion

Resistive AFM measurements of the Be doped GaAs staircase sample and the GaAs-based LED sample VN790 have been performed. We can conclude from Park data that KPFM for doping measurement should be better performed under vacuum or protective atmosphere as the GaAs is easily oxidized in air due to high humidity in winter. KPFM can be used for p-n junction detection or doped region-intrinsic region interface alignment by measuring the contact potential difference (CPD), however, in order to measure the work function shift due to slightly changed doping concentrations, the energy resolution of KPFM needs to be improved.

The spatial resolution change related to the effective contact area of the tip has been discussed by combining resistive AFM and SEM measurements. As the scanning speed in resistive AFM is limited by the response of cantilever and feedback circuits [295] it is slower than SEM, and a slow scan rate could cause local charging by the current passing through the resistors, resulting in additional drift which may influence the accuracy of measurements [296].

The relationship between specific resistivity and resistance is

$$\rho = R\frac{A_{\text{eff}}}{l}, \qquad (5.1)$$

where l is the length of vertical current flow path (equals the specimen thickness without tilt). To get a quantitative analysis of the specific resistivity, an effective model for A_{eff} is needed as well as a measurement of l.

In this work, the measured resistance of Be doped layers is plotted as a function of doping concentration. The SE images showed that 10^{19} atoms/cm^3 or 200 ppm is a high doping concentration at which dopants start to segregate.

The measurement of VN790 sample is not in optimised condition, but we can still point out that the spatial resolution of resistive AFM is better than 12 nm as we can see the ~10nm quantum dots. As the conductive AFM is working in contact mode, one must avoid damaged surfaces when choosing the scan area, otherwise, the signal detected will be disturbed by surface steps or cleavage facets and make data interpretation difficult.

5.2 Results of KPFM

5.2.1 Be-doped GaAs sample

Due to surface contamination, the Si doped GaAs staircase sample did not provide useful data for analysis. The KPFM result for the Be doped GaAs has shown some features difficult to explain.

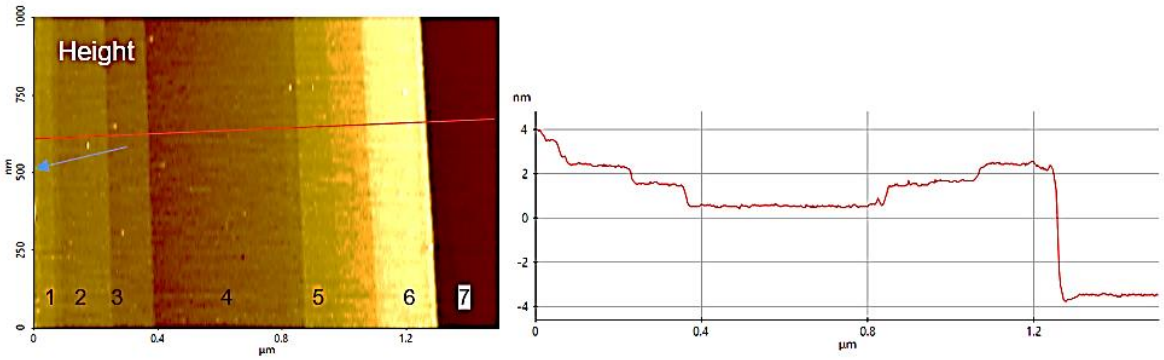

Figure 5. 15. The topography of the Be doped GaAs sample surface. The blue arrow points at specimen edge.

The mechanism of KPFM measurement is to keep the electrostatic force gradient constant, the resonance shift being corrected by moving the tip up and down. The relationship is described by [297]:

$$f_0^{'} = \frac{1}{2\pi}\sqrt{\frac{k-\delta F/\delta z}{m^*}} \approx f_0(1-\frac{1}{2k}\frac{\delta F}{\delta z}),$$

where *k* is the spring constant of the cantilever. However, due to the presence of electrical fields on the semiconductor surface, the electrostatic force would be modified; in order to re-adjust the resonance frequency of cantilever, the tip sample distance must be changed. So, the measured topography is not “height relative to a point on the surface” but “shift of the tip relative to its original height”. Thus, the contrast of regions 1-4 is possibly due to due to free carriers accumulating at the surface under the DC bias. Regions 5 and 6 are possibly revealing the depletion region at the buffer-substrate interface. Region 7 might be the GaAs substrate region without any effect of carrier depletion.

The simulation of internal electrical field across a p-i interface in GaAs by Padre is reproduced in Figure 5. 16. It suggested the depletion width of the i-region is about 400nm, which is quite similar to the 380nm total width of region5 and 6.

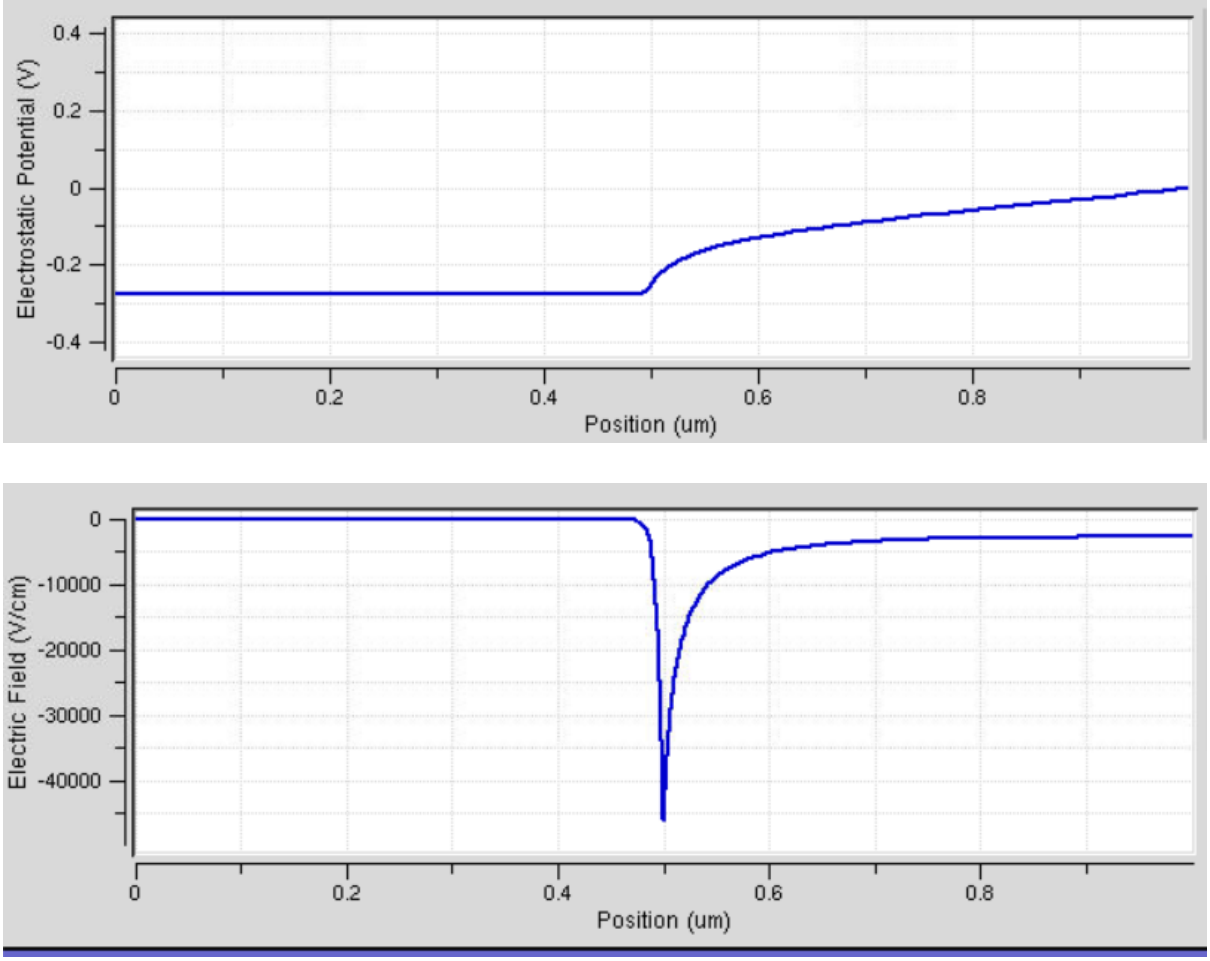

Figure 5. 16. The potential and electrical field between the p-i interface

I did not find any KPFM work to explain this kind of topography as a result of electrostatic force variation due to surface external field through literature survey. The mechanism is still unclear. The scan direction is left to right, so that it could be some cleaving steps at the sample surface.

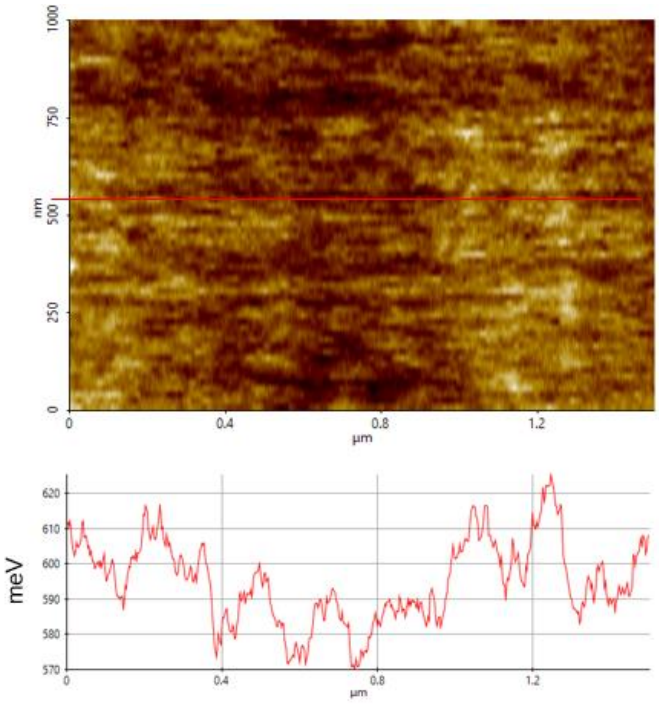

Figure 5. 17. The surface potential and its line profile for Be doped GaAs.

The potential map looks very noisy, but there is some similarity in the potential profile and the topography profile. I assume it is a product of the surface potential and the variation of the tip position. We need to build a method that can deconvolution the potential profile with the topography steps.

The KPFM measurements on sample VN790 shows less noise and it did not show the topography steps as the Be doped GaAs sample. The scanning direction of Be doped GaAs sample is from left to right, the steps are unfortunately indicating the cleaving of the surface. The other reason might be the potential difference of Be doped GaAs sample is 50mev while for VN790 is 500mev. When measuring small potential differences, the topography information obtain by probe-distance controller becomes dominating.

Figure 5. 18 shows the structure of the LED sample clearly. From the edge, there is a cap layer about 300nm thin, then a bright layer 750nm in thickness that is the p-doped AlGaAs region, then a thin very bright layer (what could this be), then several ultrathin layers of InAs QDs within undoped GaAs, then a dark region of 750nm n-AlGaAs region is sandwiched by p-AlGaAs region and the. The highest peak in the intensity profile is an evidence of an internal electrical field at the p-i interface. The top region of the potential map is for the n-doped GaAs substrate. The noise level is very low compared to the potential difference we obtained. With the change of scan direction up and down, the resolution of surface potential map looks better.

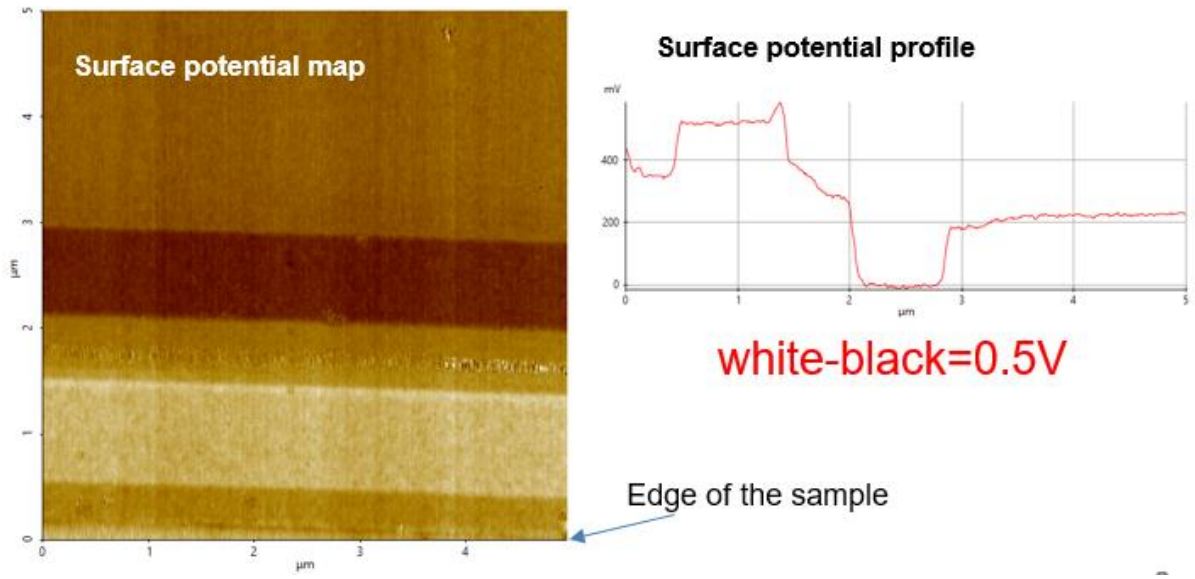

Figure 5. 18. The surface potential map for GaAs based LED structure VN 790.

5.2.2 KPFM measurement of VN790 sample

For the Be doped staircase sample, the calculation of doping level from the work function is difficult due to the external electric field effect and high noise level.

For the sample VN790, we lack the nominal doping concentrations for the doped layers. Though the sample has an undoped GaAs region, we cannot use it as a reference due to the undoped GaAs being embedded in doped cladding layers, and the measured work function will be influenced by the electrical field around the sample.

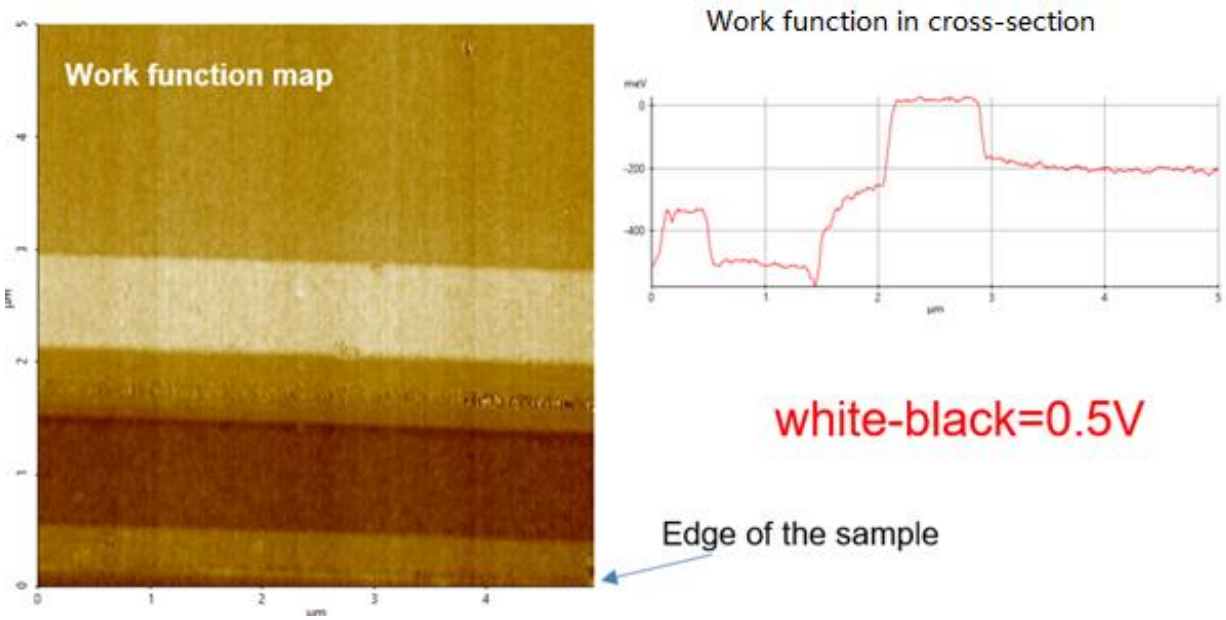

Figure 5. 19. The work function map of GaAs based LED structure VN790.

The work function of AlAs is 4.74eV, which is close to 4.72eV for GaAs, so we may assume the work function of AlGaAs will not change by much when the group III sub-lattice composition is changed by alloying [298]. However, it is interesting to note that the highly doped cap layer shows a smaller work function than the p-doped AlGaAs region. I would suggest that this is due to the Be dopant segregation in the cap layer modifying the effective work function as metallic Be would have a lower work function. The reduced work function of cap layer can improve the light emission efficiency.

5.2.3 Conclusion

KPFM can be sued to examine p-n junctions and p-i-n junctions, however, dopant distribution mapping for staircase samples with small variation in doping is difficult due to the lack of knowledge about the external field induced effect. More theoretical and experimental work needs to be done to improve the sensitivity of FM-KPFM.

Though KPFM can achieve direct measurement of the work function of material, there are still some issues remaining in investigating semiconductor devices

1. It needs to be investigated by simulations how the localised electrical field influences the work function measurement by KPFM; this is especially important for semiconductor devices as the device structure can be complex and the dimensions down to the nm level.
2. How can noise in KPFM measurements be reduced and what is the sensitivity for mapping?

5.3 Summary

The resistance changes in MΩ can be detected by CAFM. The several meV work function shift can be measured in KPFM. Comparing to SEM, the spatial resolution of CAFM and KPFM is better than 10nm, while SEM has about 20nm resolution.

6 Summary and future work

6.1 Summary

In the last decades, the high development speed of semiconductor industry has influenced the development of computing and telecommunications. As compound semiconductor devices, especially GaAs based devices, have some advantages over classical silicon-based devices, like higher power density, higher speed and higher optical efficiency, GaAs doping staircases and p-i-n structures with different doping levels are important systems to study systematically by SEM and AFM.

The most important factor that influences imaging contrast is the surface treatment method; it has been demonstrated by simulation and experiment that 10keV Ar^+ ion broad beam milling at shallow angle will destroy dopant contrast[299]. Further work should be using lower energy ions that have smaller ion ranges and damage the samples less, such as reduce the ion beam voltage to less than 1.5keV. As the SE1 signal is from primary beam and specimen interaction, it should not show much topography information for an on-axis (in-lens) SE detector. The SE image by using in-lens detector for SE1 should have the sensitivity for low energy ion milled surface.

The SE yield as a function of primary electron beam energy can be used to explain why low voltage is best used for dopant distribution mapping in an SEM. The effect of electron dose on dopant contrast is the following: when the dose is high, the local density of states can be changed dramatically by charges accumulating, pinning the Fermi level and hence increasing the work function. Then, formerly bright areas can show inversed SE contrast with increasing electron dose.

The change of working distance (WD) is like have external field applied to the sample. When the WD is small, the field lines extend from the specimen stage to the pole piece, helping those electrons without enough energy to overcome the barrier for emission from surface. When the WD is large, the field is from the pole piece to the specimen stage, suppressing the electron emission from the surface.

Surface carbon contamination and oxide layer formation will have influence on the SE contrast too. One must consider all the factors when interpreting the SEM results.

By combining SEM and resistive AFM together, we discussed the influence of effective contact area as a function of doping and the resistance as a function of doping.

From KPFM measurements we can get direct and quantitative maps of the work function shift in different areas of device structures.

The summary of this thesis is that the SEM image contrast is strongly dependent on the factors of surface treatment method, the electron beam energy, the electron dose, the image working distance and beam induced carbon deposition on the surface. By correlating SEM and AFM mapping, we can compare electrically active dopant distributions.

You should add your work on quantification as far as you have come, e.g. minimum doping visibility, how work function changes with doping, what spatial resolution was etc. (add some NUMBERS!)

6.2 Future work

Understand the doping contrast in SEM and cross-correlating it with other techniques like resistive AFM will release the full potential of these 2D dopant mapping methods and may improve further the sensitivity and data interpretation.

As discussed in chapters 3-5, dopant distribution mapping of GaAs based semiconductor structures and devices (doping staircase samples and p-i-n structure LEDs) by (a) using secondary electron imaging in SEM, (b) resistance mapping in resistive AFM and (c) surface potential mapping in KPFM mode can be combined. However, there are still many issues remaining.

For SEM, the complex dopant contrast mechanism makes SE image quantification difficult. Only parts of the contrast formation mechanism were investigated, like the influence on the SE contrast of surface treatment method, primary beam voltage, electron dose, working distance, and beam induced carbon contamination. Future experiments like chemical etching, or classical argon ion milled or focus ion beam sections and plasma cleaning can be used in specimen preparation to explore how surface structure influence dopant contrast.

In this work, etching of the surface has been applied, however, the etching rate is too fast for our sample with 0.17% Bromine-Methanol solvent, thus the future work should be continuing to reduce bromine concentration by adding more methanol into solvent and find a solution which etches the GaAs slower than 100Å/min. With smooth and clean etching surface, we expect the contrast can be enhanced.

The effect of plasma clean on the image contrast has not been performed due to laboratory closure during Covid. When the specimen is put into a plasma asher, the surface oxide thickness can be influenced by the plasma cleaning time[186]. By TEM or Auger electron microscopy measurements, the thickness of oxide layer can be obtained[300]. The relationship between surface oxide thickness and image contrast will be useful to quantify the SE images and comparing with simulation results.

How the surface treatment influences the GaAs dopant contrast would be interesting to study in future work. Paying more attention to ion milling strategies can be useful to get smooth surfaces, as the amorphous layer thickness might be reduced to nm level by low energy ions. Future work of ion milling the specimen surface should be conducted after the Ar ion source in implanted into the ion miller in our lab. If the amorphous dead layer can be reduced to nm level that means the dopant contrast can be detected by optimize the beam voltage and its interaction volume with specimen. And this will benefits other semiconductors which are difficult to get a good cleaved surface like silicon.

Coating the cleaved sample surface with metals to form metal- semiconductor interfaces can enhance the SE emission, and improve the surface conductivity to reduce charging effect. Etching of the specimen surface at room temperature without stirring or agitation of solution can reduce the undesirable etch pits for compound semiconductors [301]and specimens might be stored for longer as the etching process will give a passivated specimen surface more inert to ambient.

By well-established understanding of how ion milling time/energy/angle influence the ion milled surfaces, how metal coating species/thickness and how etchant/etch rate/with or with pressure/stir or not during etching, one can gain some pre-experimental calibration to set up a standard operation procedure. Besides, further understanding of dopant contrast mechanism, and how the SEM set-up influences contrast will improve the reproducibility of the SEM dopant contrast.

The further theoretical study of surface charge effect is also important. The surface charging includes the electrical field distribution, the Fermi level pinning and what will happen to the surface charge when an electron beam irradiates it. There are still many contributions to be made in this area.

As the staircase samples investigated in this study were MBE calibration samples, they were not optimised for the dopant contrast study as their doping only covers small doping ranges. As the field of view of SEM at 40kX is about 5µm, a much more extensive staircase with larger ranges of doping levels can be investigated if I had a chance to design the sample. And the nominal doping concentration provided by the grower is not accurate to better than 20% error from the information provided by grower. Though SIMs is a destructive method which is sensitive to all dopant atoms, not only the electrically active ones, but it is also still a quantitative method foe one dimensional dopant profile. If any future work can incorporate SIMS, a more accurate doping concentration and depth profile can be obtained, so that the dopant contrast in SEM can be compared with other techniques and explained better.

For conductive AFM measurements, we can make some improvements by designing a sample with higher concentration gradients of dopants to fully explore the detection rang of AFM. Besides, we can also add a 1000nm cap layer to the top of staircase samples, which can stop the tip of AFM fall off a cliff at the edge of the of specimen in cross section, and then the stability of measurement can be improved.

Here in Figure 6. 1 shows a sketch of ideal p-doped GaAs sample for both SEM and SPM measurements which has multiple layers covers 6 doping levels ranging from 10^{15}-10^{20} atoms/cm^3 being 500nm thickness. Large doping concentration difference will show better intensity contrast than the samples used in this work.

Cap layer 1000nm
500nm Be doped GaAs layer at 10^{20} atoms/cm^3
500nm Be doped GaAs layer at 10^{19} atoms/cm^3
500nm Be doped GaAs layer at 10^{18} atoms/cm^3
500nm Be doped GaAs layer at 10^{17} atoms/cm^3
500nm Be doped GaAs layer at 10^{16} atoms/cm^3
500nm Be doped GaAs layer at 10^{15} atoms/cm^3
300nm Buffer layer
GaAs substrate

Figure 6. 1. The ideal Be Doped GaAs staircase sample which covers larger rang of doping

The presence of AlGaAs and doped GaAs in the sample is not a problem, although it is possible that the work function value of AlGaAs is like that of doped GaAs layers resulting same SE intensity, the region can still be identified as most SEM can acquire both BSE (which contains Z contrast relative to atomic number) and SE images at the same time. We did not get the BSE image due to BSE detector broken but we can still try to use EDS at low kV (5kV, for example, which is enough to active the Al K, Ga L and As L lines in the spectrum) for longer mapping time to collect enough X-rays. Having n and p type layer in the same sample could also be a good idea, as they are in same sample, the influence of instrumental parameter is the same, thus the n and p dopant contrast can be quantitative analysed at same time. Considering the limited field of view at high magnification in a SEM, we can design another sample which concentrate on heavily doped p and n layers as heavily doped n layer contrast shows little or no dependence on doping level due to hot electron generation. By combine SPM method, 2D quantitative dopant contrast could be even achieve for heavily doped n-GaAs layers.

For resistive AFM, in order to get quantitative data on carrier concentration, a model for the correction of effective contact area and thermal drift correction must be developed both theoretically and experimentally. We can avoid the thermal drift by increasing the scan speed by tapping mode and do the resistance measurement within cooling system. We can also try to collaborate the AFM and SEM together to calibrate the spatial resolution of CAFM.

For KPFM measurement in AFM, the calibration of the tip work function with samples like pure metal with known work function is very important as the effective work function of a material equals the sum of contact potential difference CPD and tip work function. To improve sensitivity, it is better to perform experiments in ultra-high vacuum or under protecting gas atmosphere. This is because FM-KPFM is very sensitive to the electrostatic force gradient.

The KPFM sample used in this study was not transferred in vacuum or freshly cleaved. During posting to Park Ltd and before putting it into KPFM, the sample surface has had sufficient time to become damaged/ contaminated. Humidity has proven to be a problem too. So in-situ cleaving of the sample under vacuum or other sample transfer method should be considered in the future. The scanning direction could be changed to 90^{o} of the specimen growth direction or 45^{o} to clarify whether visible topography steps are due to cleavage or not.

For all the SEM or SPM methods used in this thesis, the spatial resolution is very high, the Hitachi SEM showed the QDs at about 10nm resolution at 1.5kV. In the foreseeable future, better spatial resolution and higher sensitivity methods for doping characterisation will be required due to the continued down-scaling of MOSFET devices. Other methods like electron holography or atom probe tomography could be used both in research and industrial areas by people who know how to conduct reproducible experiments.

References

[1] "Handbook of Compound Semiconductors | ScienceDirect." https://www-sciencedirect-com.sheffield.idm.oclc.org/book/9780815513742/handbook-of-compound-semiconductors (accessed Nov. 28, 2020).

[2] F. B. Insights, "Semiconductor Market Worth USD 726.73 Billion at 4.7% CAGR; Industry Giants Such as Intel and NVIDIA to Focus on Managing Finances amid the COVID-19 Pandemic: Fortune Business Insights™," *GlobeNewswire News Room*, Oct. 16, 2020. http://www.globenewswire.com/news-release/2020/10/16/2109767/0/en/Semiconductor-Market-Worth-USD-726-73-Billion-at-4-7-CAGR-Industry-Giants-Such-as-Intel-and-NVIDIA-to-Focus-on-Managing-Finances-amid-the-COVID-19-Pandemic-Fortune-Business-Insight.html (accessed Nov. 28, 2020).

[3] "Historical Survey," in *The Pauli Exclusion Principle*, John Wiley & Sons, Ltd, 2016, pp. 1–24. doi: 10.1002/9781118795309.ch1.

[4] B. Van Zeghbroeck, "Principles of semiconductor devices," *Colarado Univ.*, vol. 34, 2004.

[5] C. E. Housecroft and A. G. Sharpe, *Inorganic Chemistry*. Pearson Education, 2008.

[6] C. J. Bradley and A. P. Cracknell, *The mathematical theory of symmetry in solids: representation theory for point groups and space groups*. in Oxford classic texts in the physical sciences. Oxford: Clarendon Press, 2010.

[7] L. Pauling, "International Tables for X-ray Crystallography. Volume I. Symmetry Groups edited by N. F. M. Henry and K. Lonsdale," *Acta Crystallogr.*, vol. 7, no. 3, Art. no. 3, Mar. 1954, doi: 10.1107/S0365110X54000874.

[8] S. M. Sze and K. K. Ng, *Physics of Semiconductor Devices*. Hoboken, NJ, USA: John Wiley & Sons, Inc., 2006. doi: 10.1002/0470068329.

[9] D. Shi, Z. Guo, and N. Bedford, "1 - Basic Properties of Nanomaterials," in *Nanomaterials and Devices*, D. Shi, Z. Guo, and N. Bedford, Eds., in Micro and Nano Technologies. Oxford: William Andrew Publishing, 2015, pp. 1–23. doi: 10.1016/B978-1-4557-7754-9.00001-9.

[10] S. L. Kakani, *Electronics Theory and Applications*. India: New Age International, 2005.

[11] Y. Wan, J. Norman, and J. Bowers, "Quantum dot microcavity lasers on silicon substrates," in *Semiconductors and Semimetals*, Elsevier, 2019, pp. 305–354. doi: 10.1016/bs.semsem.2019.05.002.

[12] J.-C. Lavocat, "Active photonic devices based on liquid crystal elastomers," 2014. doi: 10.13140/RG.2.1.1053.4644.

[13] A. Beyer, W. Stolz, and K. Volz, "Metastable cubic zinc-blende III/V semiconductors: Growth and structural characteristics," *Prog. Cryst. Growth Charact. Mater.*, vol. 61, no. 2, pp. 46–62, Jun. 2015, doi: 10.1016/j.pcrysgrow.2015.10.002.

[14] A. Bett, D. Frank, G. Stollwerck, and O. Sulima, "III-V compounds for solar cell applications," *Appl. Phys. A*, vol. 69, pp. 119–129, Jan. 1999, doi: 10.1007/s003390050983.

[15] "Temperature dependence of the energy gap in semiconductors," *Physica*, vol. 34, no. 1, pp. 149–154, Jan. 1967, doi: 10.1016/0031-8914(67)90062-6.

[16] R. Rodrigues, T. Jiang, and D. Das, *Comparison of Cooling Solutions to Improve Overload Capability of Power Semiconductor Devices*. 2018, p. 5080. doi: 10.1109/ECCE.2018.8558263.

[17] G. Sun, "Intersubband approach to silicon based lasers—circumventing the indirect bandgap limitation," *Adv. Opt. Photonics*, vol. 3, no. 1, p. 53, Mar. 2011, doi: 10.1364/AOP.3.000053.

[18] W. Shockley and W. T. Read, "Statistics of the Recombinations of Holes and Electrons," *Phys. Rev.*, vol. 87, pp. 835–842, Sep. 1952, doi: 10.1103/PhysRev.87.835.

[19] A. R. Denton and N. W. Ashcroft, "Vegard's law," *Phys. Rev. A*, vol. 43, no. 6, pp. 3161–3164, Mar. 1991, doi: 10.1103/PhysRevA.43.3161.

[20] J. A. Van Vechten and T. K. Bergstresser, "Electronic Structures of Semiconductor Alloys," *Phys. Rev. B*, vol. 1, no. 8, pp. 3351–3358, Apr. 1970, doi: 10.1103/PhysRevB.1.3351.

[21] I. Vurgaftman, J. R. Meyer, and L. R. Ram-Mohan, “Band parameters for III–V compound semiconductors and their alloys,” *J. Appl. Phys.*, vol. 89, no. 11, pp. 5815–5875, Jun. 2001, doi: 10.1063/1.1368156.
[22] A. Y. Cho, “Film Deposition by Molecular-Beam Techniques,” *J. Vac. Sci. Technol.*, vol. 8, no. 5, pp. S31–S38, Sep. 1971, doi: 10.1116/1.1316387.
[23] A. Ichimiya, P. I. Cohen, and P. I. Cohen, *Reflection High-Energy Electron Diffraction*. Cambridge University Press, 2004.
[24] F. W. Smith, A. R. Calawa, C.-L. Chen, M. J. Manfra, and L. J. Mahoney, “New MBE buffer used to eliminate backgating in GaAs MESFETs,” *IEEE Electron Device Lett.*, vol. 9, no. 2, pp. 77–80, Feb. 1988, doi: 10.1109/55.2046.
[25] T. Lamas, S. Martini, M. Silva, A. Quivy, and J. Leite, “Morphological and optical properties of p-type GaAs(001) layers doped with silicon,” *Microelectron. J.*, vol. 34, pp. 701–703, May 2003, doi: 10.1016/S0026-2692(03)00106-X.
[26] C.-H. Chen, U. M. Gösele, and T. Y. Tan, “Thermal equilibrium concentrations of the amphoteric dopant Si and the associated carrier concentrations in GaAs,” *J. Appl. Phys.*, vol. 86, no. 10, pp. 5376–5384, Nov. 1999, doi: 10.1063/1.371534.
[27] S. B. Dugdale, “Life on the edge: a beginner’s guide to the Fermi surface,” *Phys. Scr.*, vol. 91, no. 5, p. 053009, Apr. 2016, doi: 10.1088/0031-8949/91/5/053009.
[28] C. Kittel, *Introduction to Solid State Physics.*, Third edition. New York: Wiley, 1967.
[29] S. S. Li, “THE DOPANT DENSITY AND TEMPERATURE DEPENDENCE OF HOLE MOBILITY AND RESISTIVITY IN BORON DOPED SILICON?,” p. 9.
[30] C. Hilsum, “Simple empirical relationship between mobility and carrier concentration,” *Electron. Lett.*, vol. 10, no. 13, p. 259, 1974, doi: 10.1049/el:19740205.
[31] M. Sotoodeh, A. H. Khalid, and A. A. Rezazadeh, “Empirical low-field mobility model for III–V compounds applicable in device simulation codes,” *J. Appl. Phys.*, vol. 87, no. 6, pp. 2890–2900, Mar. 2000, doi: 10.1063/1.372274.
[32] D. Ferry, *Semiconductor Transport*, 1st ed. London: CRC Press, 2000. doi: 10.4324/9781315267548.
[33] N. W. Ashcroft and N. D. Mermin, *Solid State Physics*. Philadelphia: Saunders College publishing, 1976.
[34] W. Ł. Nakwaski, “Effective masses of electrons and heavy holes in GaAs, InAs, A1As and their ternary compounds,” *Phys. B Condens. Matter*, vol. 210, pp. 1–25, Feb. 1995, doi: 10.1016/0921-4526(94)00921-H.
[35] A. Fick, “Ueber Diffusion,” *Ann. Phys.*, vol. 170, pp. 59–86, Jan. 1855, doi: 10.1002/andp.18551700105.
[36] J. W. Mayer and O. J. Marsh, “Ion Implantation in Semiconductors,” in *Applied Solid State Science*, R. Wolfe, Ed., Elsevier, 1969, pp. 239–342. doi: 10.1016/B978-0-12-002901-3.50009-X.
[37] A. Mokhberi, “Dopant-dopant and dopant-defect processes underlying activation kinetics,” Jan. 2003.
[38] R. Levy, *Microelectronic Materials and Processes*. Springer Science & Business Media, 1989.
[39] D. Bullock, “Growth Rate Calculations for Epitaxially Grown Thin Films,” vol. 62, p. 4, 2008.
[40] H. P. Meyers, *Introductory Solid State Physics, Second Edition*, 2 edition. London: CRC Press, 1997.
[41] G. Burns, *Solid State Physics*, International edition. Boston: Academic Press, 1990.
[42] M. Levinshtein and M. Shur, *Handbook Series on Semiconductor Parameters: Ternary and quaternary III-V compounds*, vol. 1.1. World Scientific, 1999.
[43] G. W. Gobeli and F. G. Allen, “Photoelectric Properties of Cleaved GaAs, GaSb, InAs, and InSb Surfaces; Comparison with Si and Ge,” *Phys. Rev.*, vol. 137, no. 1A, pp. A245–A254, Jan. 1965, doi: 10.1103/PhysRev.137.A245.

[44] T. Yamada, J. Fujii, and T. Mizoguchi, “STM, STS, and local work function study of Cs/p-GaAs (1 1 0),” *Surf. Sci.*, vol. 479, no. 1–3, pp. 33–42, 2001.
[45] L. Adamowicz and M. Zbroszczyk, “LMTO calculations of surface energy and work function for GaAs,” *Surf. Sci.*, vol. 352, pp. 730–733, 1996.
[46] U. Strauss *et al.*, “Minority-Carrier Lifetime in Heavily Doped GaAs:C,” *Jpn. J. Appl. Phys.*, vol. 32, no. 1S, p. 495, Jan. 1993, doi: 10.1143/JJAP.32.495.
[47] C. J. Hwang, “Optical Properties of n -Type GaAs. I. Determination of Hole Diffusion Length from Optical Absorption and Photoluminescence Measurements,” *J. Appl. Phys.*, vol. 40, no. 9, pp. 3731–3739, Aug. 1969, doi: 10.1063/1.1658263.
[48] C. S. Fuller and K. B. Wolfstirn, “Changes in Electron Concentration of Donor-Doped GaAs Crystals Caused by Annealing,” *J. Appl. Phys.*, vol. 34, no. 8, pp. 2287–2289, Aug. 1963, doi: 10.1063/1.1702731.
[49] C. S. Fuller, K. B. Wolfstirn, and H. W. Allison, “Defect Centers in GaAs Produced by Cu Diffusion,” *J. Appl. Phys.*, vol. 38, no. 11, pp. 4339–4345, Oct. 1967, doi: 10.1063/1.1709126.
[50] M. Otsubo, H. Miki, and S. Mitsui, “Photoluminescence Study of Defects in GaAs Formed by Annealing in an H2 Gas Flow,” *Jpn. J. Appl. Phys.*, vol. 16, no. 11, p. 1957, Nov. 1977, doi: 10.1143/JJAP.16.1957.
[51] M. R. Pinto *et al.*, *Padre*. 2006. doi: 10.4231/D30C4SK7Z.
[52] M. Kuzuhara and S. Tanaka, “GaAs-based high-frequency and high-speed devices,” p. 8.
[53] G. W. Wang and M. Feng, “Quarter-micrometer gate ion-implanted GaAs MESFET’s with an f/sub 1/ of 126 GHz,” *IEEE Electron Device Lett.*, vol. 10, no. 8, pp. 386–388, Aug. 1989, doi: 10.1109/55.31765.
[54] P. D. Ye *et al.*, “GaAs metal–oxide–semiconductor field-effect transistor with nanometer-thin dielectric grown by atomic layer deposition,” *Appl. Phys. Lett.*, vol. 83, no. 1, pp. 180–182, Jul. 2003, doi: 10.1063/1.1590743.
[55] C. E. Weitzel, “RF power amplifiers for wireless communications,” in *24th Annual Technical Digest Gallium Arsenide Integrated Circuit (GaAs IC) Symposiu*, Oct. 2002, pp. 127–130. doi: 10.1109/GAAS.2002.1049044.
[56] M. E. Kim, A. K. Oki, G. M. Gorman, D. K. Umemoto, and J. B. Camou, “GaAs heterojunction bipolar transistor device and IC technology for high-performance analog and microwave applications,” *IEEE Trans. Microw. Theory Tech.*, vol. 37, no. 9, pp. 1286–1303, Sep. 1989, doi: 10.1109/22.32211.
[57] A. Christou *et al.*, “Failure Mechanism Study of GaAs MODFET Devices and Integrated Circuits,” in *23rd International Reliability Physics Symposium*, Mar. 1985, pp. 54–59. doi: 10.1109/IRPS.1985.362075.
[58] G. E. Stillman, “Amphoteric impurities in gallium arsenide,” ILLINOIS UNIV AT URBANA ENGINEERING RESEARCH CENTER FOR COMPOUND SEMICONDUCTOR MICROELECTRONICS, Annual technical rept ADA173160, Jul. 1986.
[59] K. Ikegami, *Gallium Arsenide and Related Compounds 1992, Proceedings of the 19th INT Symposium, 28 September-2 October 1992, Karuizawa, Japan*. CRC Press, 1993.
[60] R. H. Maurer, K. Chao, C. B. Bargeron, R. C. Benson, and E. Nhan, “Reliability of gallium arsenide devices,” *Johns Hopkins APL Tech. Dig.*, vol. 13, pp. 407–417, Sep. 1992.
[61] J. L. Pan, J. E. McManis, T. Osadchy, L. Grober, J. M. Woodall, and P. J. Kindlmann, “Gallium arsenide deep-level optical emitter for fibre optics,” *Nat. Mater.*, vol. 2, no. 6, pp. 375–378, Jun. 2003, doi: 10.1038/nmat887.
[62] D. Bhattacharya, “Gallium arsenide digital integrated circuits,” *Bull. Mater. Sci.*, vol. 13, no. 1, pp. 135–150, Mar. 1990, doi: 10.1007/BF02744867.
[63] R. S. Pengelly, “Gallium Arsenide Integrated Circuits,” *Microw. Field-Eff. Transistors Theory Des. Appl.*, pp. 465–628, Jan. 1994, doi: 10.1049/SBEW016E_ch10.

[64] M. Gloanec, J. Jarry, and G. Nuzillat, “GaAs digital integrated circuits for very high-speed frequency division,” *Electron. Lett.*, vol. 17, pp. 763–765, Oct. 1981, doi: 10.1049/el:19810536.
[65] M. J. Howes and D. V. Morgan, Eds., *Gallium Arsenide: Materials, Devices and Circuits*. London: Wiley–Blackwell, 1985.
[66] N. G. Einspruch and W. R. Wisseman, *GaAs microelectronics*. Orlando: Academic Press, 1985.
[67] A. J. Seeds and K. J. Williams, “Microwave Photonics,” *J. Light. Technol.*, vol. 24, no. 12, pp. 4628–4641, Dec. 2006, doi: 10.1109/JLT.2006.885787.
[68] R. N. Hall, G. E. Fenner, J. D. Kingsley, T. J. Soltys, and R. O. Carlson, “Coherent Light Emission From GaAs Junctions,” *Phys. Rev. Lett.*, vol. 9, no. 9, pp. 366–368, Nov. 1962, doi: 10.1103/PhysRevLett.9.366.
[69] V. Petrova-Koch, R. Hezel, and A. Goetzberger, *High-Efficient Low-Cost Photovoltaics: Recent Developments*. in Springer Series in Optical Sciences, no. 140. Berlin: Springer, 2009.
[70] J. Yin *et al.*, “Charge Redistribution at GaAs/P3HT Heterointerfaces with Different Surface Polarity,” *J. Phys. Chem. Lett.*, vol. 4, no. 19, pp. 3303–3309, Oct. 2013, doi: 10.1021/jz401485t.
[71] W. Shockley and H. J. Queisser, “Detailed Balance Limit of Efficiency of *p-n* Junction Solar Cells,” *J. Appl. Phys.*, vol. 32, no. 3, pp. 510–519, Mar. 1961, doi: 10.1063/1.1736034.
[72] E. Inuzuka and H. Suzuki, “Emission microscopy in semiconductor failure,” in *Conference Proceedings. 10th Anniversary. IMTC/94. Advanced Technologies in I M. 1994 IEEE Instrumentation and Measurement Technolgy Conference (Cat. No.94CH3424-9)*, May 1994, pp. 1492–1496 vol.3. doi: 10.1109/IMTC.1994.352178.
[73] Y. Li, M. Pacheco, D. Goyal, J. W. Elmer, H. D. Barth, and D. Parkinson, “High resolution and fast throughput-time X-ray computed tomography for semiconductor packaging applications,” in *2014 IEEE 64th Electronic Components and Technology Conference (ECTC)*, May 2014, pp. 1457–1463. doi: 10.1109/ECTC.2014.6897485.
[74] P. L. Martin, *Electronic Failure Analysis Handbook: Techniques and Applications for Electronic and Electrical Packages, Components, and Assemblies*. McGraw-Hill Education, 1999. Accessed: Jun. 22, 2021. [Online]. Available: https://www.accessengineeringlibrary.com/content/book/9780070410442
[75] L. Reimer, *Scanning Electron Microscopy: Physics of Image Formation and Microanalysis*, 2nd ed. in Springer Series in Optical Sciences. Berlin Heidelberg: Springer-Verlag, 1998. doi: 10.1007/978-3-540-38967-5.
[76] L. Allen, A. alfonso, B. Forbes, B. Freitag, and D. Klenov, “Atomic-resolution elemental mapping using energy-dispersive x-ray (EDX) spectroscopy,” Aug. 2012.
[77] A. C. Twitchett, R. E. Dunin-Borkowski, and P. A. Midgley, “Quantitative Electron Holography of Biased Semiconductor Devices,” *Phys. Rev. Lett.*, vol. 88, no. 23, p. 238302, May 2002, doi: 10.1103/PhysRevLett.88.238302.
[78] H. Sasaki, S. Otomo, R. Minato, K. Yamamoto, and T. Hirayama, “Direct observation of dopant distribution in GaAs compound semiconductors using phase-shifting electron holography and Lorentz microscopy,” *Microscopy*, vol. 63, no. 3, pp. 235–242, Jun. 2014, doi: 10.1093/jmicro/dfu008.
[79] I. C. Noyan, T. C. Huang, and B. R. York, “Residual stress/strain analysis in thin films by X-ray diffraction,” *Crit. Rev. Solid State Mater. Sci.*, vol. 20, no. 2, pp. 125–177, Jan. 1995, doi: 10.1080/10408439508243733.
[80] S. Valeri and M. Lolli, “AES, EELS and XPS study of ion-induced GaAs and InP(110) surface and subsurface modifications,” *Surf. Interface Anal.*, vol. 16, no. 1–12, pp. 59–64, 1990, doi: https://doi.org/10.1002/sia.740160115.
[81] D. Häussler *et al.*, “Aberration-corrected transmission electron microscopy analyses of GaAs/Si interfaces in wafer-bonded multi-junction solar cells,” *Ultramicroscopy*, vol. 134, pp. 55–61, Nov. 2013, doi: 10.1016/j.ultramic.2013.07.005.

[82] D. D. Perovic, M. R. Castell, A. Howie, C. Lavoie, T. Tiedje, and J. S. W. Cole, “Field-emission SEM imaging of compositional and doping layer semiconductor superlattices,” *Ultramicroscopy*, vol. 58, no. 1, pp. 104–113, Apr. 1995, doi: 10.1016/0304-3991(94)00183-N.
[83] L. A. Giannuzzi, R. Geurts, and J. Ringnalda, “2 keV Ga+ FIB Milling for Reducing Amorphous Damage in Silicon,” *Microsc. Microanal.*, vol. 11, no. S02, Art. no. S02, Aug. 2005, doi: 10.1017/S1431927605507797.
[84] Y. Huh, K. J. Hong, and K. S. Shin, “Amorphization Induced by Focused Ion Beam Milling in Metallic and Electronic Materials,” *Microsc. Microanal.*, vol. 19, no. S5, pp. 33–37, Aug. 2013, doi: 10.1017/S1431927613012282.
[85] S. J. Pearton, U. K. Chakrabarti, A. P. Perley, and K. S. Jones, “Ion milling damage in InP and GaAs,” *J. Appl. Phys.*, vol. 68, no. 6, pp. 2760–2768, Sep. 1990, doi: 10.1063/1.346453.
[86] Y. Ohno *et al.*, “Impact of focused ion beam on structural and compositional analysis of interfaces fabricated by surface activated bonding,” *Jpn. J. Appl. Phys.*, vol. 59, no. SB, p. SBBB05, Nov. 2019, doi: 10.7567/1347-4065/ab4b15.
[87] P. Kazemian, C. Rodenburg, and C. J. Humphreys, “Effect of experimental parameters on doping contrast of Si p–n junctions in a FEG-SEM,” *Microelectron. Eng.*, vol. 73–74, pp. 948–953, Jun. 2004, doi: 10.1016/j.mee.2004.03.080.
[88] I. Volotsenko *et al.*, “Secondary electron doping contrast: Theory based on scanning electron microscope and Kelvin probe force microscopy measurements,” *J. Appl. Phys.*, vol. 107, no. 1, p. 014510, Jan. 2010, doi: 10.1063/1.3276090.
[89] P. J. Sellin, “Recent advances in compound semiconductor radiation detectors,” *Nucl. Instrum. Methods Phys. Res. Sect. Accel. Spectrometers Detect. Assoc. Equip.*, vol. 513, no. 1, pp. 332–339, Nov. 2003, doi: 10.1016/j.nima.2003.08.058.
[90] B. Kaestner, C. Rodenburg, and C. J. Humphreys, “Mapping the potential within a nanoscale undoped GaAs region using a scanning electron microscope,” *Appl. Phys. Lett.*, vol. 84, no. 12, pp. 2109–2111, Mar. 2004, doi: 10.1063/1.1689755.
[91] S. Kasap, C. Koughia, and H. E. Ruda, “Electrical Conduction in Metals and Semiconductors,” in *Springer Handbook of Electronic and Photonic Materials*, S. Kasap and P. Capper, Eds., in Springer Handbooks. Cham: Springer International Publishing, 2017, pp. 1–1. doi: 10.1007/978-3-319-48933-9_2.
[92] T. M. Wallis and P. Kabos, “Chapter 11. Dopant profiling in semiconductor nanoelectronics,” Sep. 2017, Accessed: Jun. 25, 2021. [Online]. Available: https://www.nist.gov/publications/chapter-11-dopant-profiling-semiconductor-nanoelectronics
[93] R. C. Jaeger, *Introduction to Microelectronic Fabrication: Volume 5 of Modular Series on Solid State Devices*. Upper Saddle River, N.J: Pearson, 2001.
[94] E. H. Hall, “On a New Action of the Magnet on Electric Currents,” *Am. J. Math.*, vol. 2, no. 3, pp. 287–292, 1879, doi: 10.2307/2369245.
[95] F. Ermanis and K. Wolfstirn, “Hall Effect and Resistivity of Zn-Doped GaAs,” *J. Appl. Phys.*, vol. 37, no. 5, pp. 1963–1966, Apr. 1966, doi: 10.1063/1.1708648.
[96] S. Joo and H. Liang, “Secondary Ion Mass Spectroscopy (SIMS),” in *Encyclopedia of Tribology*, Q. J. Wang and Y.-W. Chung, Eds., Boston, MA: Springer US, 2013, pp. 2989–2994. doi: 10.1007/978-0-387-92897-5_1218.
[97] L. Pillatsch, F. Östlund, and J. Michler, “FIBSIMS: A review of secondary ion mass spectrometry for analytical dual beam focussed ion beam instruments,” *Prog. Cryst. Growth Charact. Mater.*, vol. 65, no. 1, pp. 1–19, Feb. 2019, doi: 10.1016/j.pcrysgrow.2018.10.001.
[98] Y. Kataoka and T. Itani, “Ultrashallow depth profiling using SIMS and ion scattering spectroscopy,” *Surf. Interface Anal.*, vol. 39, no. 10, pp. 826–831, 2007, doi: 10.1002/sia.2597.
[99] M. J. Goeckner *et al.*, “Profiling of ultrashallow junctions,” *J. Vac. Sci. Technol. B Microelectron. Nanometer Struct. Process. Meas. Phenom.*, vol. 18, no. 1, pp. 472–476, Jan. 2000, doi: 10.1116/1.591214.

[100] A. Budrevich and J. Hunter, “Metrology aspects of SIMS depth profiling for advanced ULSI processes,” in *The 1998 international conference on characterization and metrology for ULSI technology*, Gaithersburg, Maryland (USA): ASCE, 1998, pp. 169–181. doi: 10.1063/1.56792.
[101] A. Priebe, T. Xie, G. Bürki, L. Pethö, and M. Johann, “The matrix effect in TOF-SIMS analysis of two-element inorganic thin films,” *J. Anal. At. Spectrom.*, p. 1156 (11 pp.), 2020, doi: 10.1039/C9JA00428A.
[102] J. Jussila, F. Granberg, and K. Nordlund, “Effect of random surface orientation on W sputtering yields,” *Nucl. Mater. Energy*, vol. 17, pp. 113–122, Dec. 2018, doi: 10.1016/j.nme.2018.08.002.
[103] E. Slavcheva, G. Ganske, G. Topalov, W. Mokwa, and U. Schnakenberg, “Effect of sputtering parameters on surface morphology and catalytic efficiency of thin platinum films,” *Appl. Surf. Sci.*, vol. 255, no. 13, pp. 6479–6486, Apr. 2009, doi: 10.1016/j.apsusc.2009.02.033.
[104] C. M. Mahoney and C. M. Mahoney, *Cluster Secondary Ion Mass Spectrometry: Principles and Applications*. Somerset, UNITED STATES: John Wiley & Sons, Incorporated, 2013. Accessed: Sep. 05, 2020. [Online]. Available: http://ebookcentral.proquest.com/lib/sheffield/detail.action?docID=1169505
[105] T. Wirtz, P. Philipp, J.-N. Audinot, D. Dowsett, and S. Eswara, “High-resolution high-sensitivity elemental imaging by secondary ion mass spectrometry: from traditional 2D and 3D imaging to correlative microscopy,” *Nanotechnology*, vol. 26, no. 43, p. 434001, Oct. 2015, doi: 10.1088/0957-4484/26/43/434001.
[106] L. A. McDonnell and R. M. A. Heeren, “Imaging mass spectrometry,” *Mass Spectrom. Rev.*, vol. 26, no. 4, pp. 606–643, 2007, doi: 10.1002/mas.20124.
[107] R. Levi-Setti, G. Crow, and Y. L. Wang, “Imaging SIMS at 20 nm Lateral Resolution: Exploratory Research Applications,” in *Secondary Ion Mass Spectrometry SIMS V*, A. Benninghoven, R. J. Colton, D. S. Simons, and H. W. Werner, Eds., in Springer Series in Chemical Physics. Berlin, Heidelberg: Springer, 1986, pp. 132–138. doi: 10.1007/978-3-642-82724-2_31.
[108] R. Levi-Setti, G. Crow, and Y. L. Wang, “Progress in high resolution scanning ion microscopy and secondary ion mass spectrometry imaging microanalysis,” *Scan. Electron Microsc.*, no. Pt 2, pp. 535–552, 1985.
[109] L. de Broglie, “The reinterpretation of wave mechanics,” *Found. Phys.*, vol. 1, no. 1, pp. 5–15, Mar. 1970, doi: 10.1007/BF00708650.
[110] M. Born and E. Wolf, *Principles of Optics: Electromagnetic Theory of Propagation, Interference and Diffraction of Light*. Elsevier, 2013.
[111] D. B. Williams and C. B. Carter, “The Transmission Electron Microscope,” in *Transmission Electron Microscopy*, Springer US, 2009, pp. 3–22. doi: 10.1007/978-0-387-76501-3_1.
[112] L. Reimer and H. Kohl, *Transmission Electron Microscopy*, vol. 36. in Springer Series in Optical Sciences, vol. 36. New York, NY: Springer New York, 2008. Accessed: Jan. 25, 2017. [Online]. Available: http://link.springer.com/10.1007/978-0-387-40093-8
[113] R. F. Egerton, *Physical Principles of Electron Microscopy-An Introduction to TEM, SEM, and AEM*. New York, USA: Springer, 2007.
[114] B. Rp and S. M, “Visualization of subsurface structures in cells and tissues by backscattered electron imaging.,” *Scan. Electron Microsc.*, no. 2, pp. 835–870, 1979.
[115] H. Xin and D. Muller, “Aberration-Corrected STEM Imaging and 2-D Elemental-Resolved Valence-EELS Mapping of Ru-TaN Ultrathin Barrier Layer,” *Microsc. Microanal.*, vol. 15, no. S2, pp. 1198–1199, Jul. 2009, doi: 10.1017/S1431927609095294.
[116] J. J. LePore, “An improved technique for selective etching of GaAs and Ga1−xAlxAs,” *J. Appl. Phys.*, vol. 51, no. 12, pp. 6441–6442, Dec. 1980, doi: 10.1063/1.327598.
[117] W. D. Rau, P. Schwander, and A. Ourmazd, “Two-Dimensional Mapping of pn Junctions by Electron Holography,” *Phys. Status Solidi B*, vol. 222, no. 1, pp. 213–217, 2000, doi: 10.1002/1521-3951(200011)222:1<213::AID-PSSB213>3.0.CO;2-H.

[118] W. D. Rau, P. Schwander, F. H. Baumann, W. Höppner, and A. Ourmazd, “Two-Dimensional Mapping of the Electrostatic Potential in Transistors by Electron Holography,” *Phys. Rev. Lett.*, vol. 82, no. 12, pp. 2614–2617, Mar. 1999, doi: 10.1103/PhysRevLett.82.2614.
[119] M. El-Gomati, F. Zaggout, H. Jayacody, S. Tear, and K. Wilson, “Why is it possible to detect doped regions of semiconductors in low voltage SEM: a review and update,” *Surf. Interface Anal.*, vol. 37, no. 11, pp. 901–911, 2005, doi: 10.1002/sia.2108.
[120] N. D. Jäger, M. Marso, M. Salmeron, E. R. Weber, K. Urban, and Ph. Ebert, “Physics of imaging p − n junctions by scanning tunneling microscopy and spectroscopy,” *Phys. Rev. B*, vol. 67, no. 16, p. 165307, Apr. 2003, doi: 10.1103/PhysRevB.67.165307.
[121] R. M. Feenstra, E. T. Yu, J. M. Woodall, P. D. Kirchner, C. L. Lin, and G. D. Pettit, “Cross-sectional imaging and spectroscopy of GaAs doping superlattices by scanning tunneling microscopy,” *Appl. Phys. Lett.*, vol. 61, no. 7, pp. 795–797, Aug. 1992, doi: 10.1063/1.107804.
[122] R. M. Feenstra, “Tunneling spectroscopy of the (110) surface of direct-gap III-V semiconductors,” *Phys. Rev. B*, vol. 50, no. 7, pp. 4561–4570, Aug. 1994, doi: 10.1103/PhysRevB.50.4561.
[123] R. M. Feenstra, “Cross-sectional scanning tunnelling microscopy of III-V semiconductor structures,” *Semicond. Sci. Technol.*, vol. 9, no. 12, pp. 2157–2168, Dec. 1994, doi: 10.1088/0268-1242/9/12/001.
[124] W. Treberspurg, T. Bergauer, M. Dragicevic, J. Hrubec, M. Krammer, and M. Valentan, “Measuring doping profiles of silicon detectors with a custom-designed probe station,” *J. Instrum.*, vol. 7, no. 11, pp. P11009–P11009, Nov. 2012, doi: 10.1088/1748-0221/7/11/P11009.
[125] D. K. Schroder, “Contact Resistance and Schottky Barriers,” in *Semiconductor Material and Device Characterization*, IEEE, 2006, pp. 127–184. doi: 10.1002/0471749095.ch3.
[126] A. L. Fripp, “Dependence of resistivity on the doping level of polycrystalline silicon,” *J. Appl. Phys.*, vol. 46, no. 3, pp. 1240–1244, Mar. 1975, doi: 10.1063/1.321687.
[127] S. M. Sze and J. C. Irvin, “Resistivity, mobility and impurity levels in GaAs, Ge, and Si at 300°K,” *Solid-State Electron.*, vol. 11, no. 6, pp. 599–602, Jun. 1968, doi: 10.1016/0038-1101(68)90012-9.
[128] D. Álvarez, J. Hartwich, M. Fouchier, P. Eyben, and W. Vandervorst, “Sub-5-nm-spatial resolution in scanning spreading resistance microscopy using full-diamond tips,” *Appl. Phys. Lett.*, vol. 82, no. 11, pp. 1724–1726, Mar. 2003, doi: 10.1063/1.1559931.
[129] P. De Wolf, M. Geva, T. Hantschel, W. Vandervorst, and R. B. Bylsma, “Two-dimensional carrier profiling of InP structures using scanning spreading resistance microscopy,” *Appl. Phys. Lett.*, vol. 73, no. 15, pp. 2155–2157, Oct. 1998, doi: 10.1063/1.122408.
[130] R. Subrahmanyan, “Measurement of two-dimensional doping profiles,” *Microelectron. Eng.*, vol. 19, no. 1, pp. 585–592, Sep. 1992, doi: 10.1016/0167-9317(92)90502-I.
[131] A. C. Diebold, *Handbook of Silicon Semiconductor Metrology*. CRC Press, 2001.
[132] E. H. Nicollian and J. R. Brews, *MOS (Metal Oxide Semiconductor) Physics and Technology*. John Wiley & Sons, 2002.
[133] D. K. Schroder, *Semiconductor Material and Device Characterization*. John Wiley & Sons, 2015.
[134] E. Lanzoni, C. Costa, Y. Filho, F. Galembeck, and C. Deneke, *Scanning Capacitance Microscopy (SCM): high resolution mapping of the electrostatic surface properties*. 2016. doi: 10.13140/RG.2.1.3123.6246.
[135] C. C. Williams, “Two-Dimensional Dopant Profiling by Scanning Capacitance Microscopy,” *Annu. Rev. Mater. Sci.*, vol. 29, no. 1, pp. 471–504, 1999, doi: 10.1146/annurev.matsci.29.1.471.
[136] C.-C. Chang *et al.*, “Carrier dynamics and doping profiles in GaAs nanosheets,” *Nano Res.*, vol. 7, no. 2, pp. 163–170, Feb. 2014, doi: 10.1007/s12274-013-0383-x.

[137] M. Tare, O. Puli, S. Oros, and A. Singh, “Drosophila adult eye model to teach Scanning Electron Microscopy in an undergraduate cell biology laboratory,” *Popul. Data Inf. Serv.*, vol. 92, pp. 174–180, Jan. 2009.
[138] H. Abudayyeh, “Synthesis and Analysis of ZnO Nanowires,” Hebrew University of Jerusalem, Accessed: Jan. 25, 2017. [Online]. Available: . 2012 https://www.researchgate.net/publication/263849645_Synthesis_and_Analysis_of_ZnO_Nanowires
[139] V. Morandi, P. G. Merli, and M. Ferroni, “Dopant regions imaging in scanning electron microscopy,” *J. Appl. Phys.*, vol. 99, no. 4, p. 043512, Feb. 2006, doi: 10.1063/1.2173685.
[140] C. Schönjahn, C. J. Humphreys, and M. Glick, “Energy-filtered imaging in a field-emission scanning electron microscope for dopant mapping in semiconductors,” *J. Appl. Phys.*, vol. 92, no. 12, pp. 7667–7671, Dec. 2002, doi: 10.1063/1.1525862.
[141] F. Fantini and C. Morandi, “Failure modes and mechanisms for VLSI ICs—a review,” in *IEE Proceedings G (Electronic Circuits and Systems)*, IET, 1985, pp. 74–81. Accessed: Jan. 25, 2017. [Online]. Available: http://digital-library.theiet.org/content/journals/10.1049/ip-g-1.1985.0018
[142] D. D. Perovic, R. Turan, and M. R. Castell, *Quantitative imaging of semiconductor doping distributions using a scanning electron microscope*. London: Inst Materials, 1998.
[143] H. S. Lin and R. Wang, “Using nanoprobing and SEM doping contrast techniques for failure analysis of current leakage in CMOS HV technology,” in *2009 16th IEEE International Symposium on the Physical and Failure Analysis of Integrated Circuits*, Jul. 2009, pp. 24–27. doi: 10.1109/IPFA.2009.5232705.
[144] L. Xu *et al.*, “Secondary Electron Microscopy Dopant Contrast Image (SEMDCI) for Laser Doping,” *IEEE J. Photovolt.*, vol. 3, no. 2, pp. 762–768, Apr. 2013, doi: 10.1109/JPHOTOV.2013.2241820.
[145] K. Nakayama, K. Tanabe, and H. A. Atwater, “Plasmonic nanoparticle enhanced light absorption in GaAs solar cells,” *Appl. Phys. Lett.*, vol. 93, no. 12, p. 121904, Sep. 2008, doi: 10.1063/1.2988288.
[146] C. Rodenburg, M. A. E. Jepson, B. J. Inkson, E. Bosch, A. K. W. Chee, and C. J. Humphreys, “Energy filtered scanning electron microscopy: Applications to dopant contrast,” *J. Phys. Conf. Ser.*, vol. 209, p. 012053, Feb. 2010, doi: 10.1088/1742-6596/209/1/012053.
[147] D. Drouin, A. R. Couture, D. Joly, X. Tastet, V. Aimez, and R. Gauvin, “CASINO V2.42—A Fast and Easy-to-use Modeling Tool for Scanning Electron Microscopy and Microanalysis Users,” *Scanning*, vol. 29, no. 3, pp. 92–101, 2007, doi: 10.1002/sca.20000.
[148] P. Hovington, D. Drouin, and R. Gauvin, “CASINO: A new monte carlo code in C language for electron beam interaction —part I: Description of the program,” *Scanning*, vol. 19, no. 1, pp. 1–14, 1997, doi: 10.1002/sca.4950190101.
[149] D. Drouin, P. Hovington, and R. Gauvin, “CASINO: A new monte carlo code in C language for electron beam interactions—part II: Tabulated values of the mott cross section,” *Scanning*, vol. 19, no. 1, pp. 20–28, 1997, doi: 10.1002/sca.4950190103.
[150] P. Hovington, D. Drouin, R. Gauvin, D. C. Joy, and N. Evans, “CASINO: A new monte Carlo code in C language for electron beam interactions—part III: Stopping power at low energies,” *Scanning*, vol. 19, no. 1, pp. 29–35, 1997, doi: 10.1002/sca.4950190104.
[151] J. Goldstein *et al.*, *Scanning Electron Microscopy and X-Ray Microanalysis: Third Edition*, 3rd edition. New York: Springer, 2007.
[152] H. Seiler, “Secondary electron emission in the scanning electron microscope,” *J. Appl. Phys.*, vol. 54, no. 11, pp. R1–R18, Nov. 1983, doi: 10.1063/1.332840.
[153] N. Marturi, “Vision and visual servoing for nanomanipulation and nanocharacterization in scanning electron microscope.,” Nov. 2013.

[154] A. G. Xie, S. R. Xiao, and H. Y. Wu, “Mean escape depth of secondary electrons emitted from semiconductors and insulators,” *Indian J. Phys.*, vol. 87, no. 11, pp. 1093–1097, Nov. 2013, doi: 10.1007/s12648-013-0355-8.
[155] A. Hussain *et al.*, “Theoretical calculations of the mean escape depth of secondary electron emission from compound semiconductor materials,” *J. Appl. Phys.*, vol. 127, no. 12, p. 125304, Mar. 2020, doi: 10.1063/1.5144721.
[156] D. R. Pendse and A. K. Chin, “Cathodoluminescence and Transmission Cathodoluminescence,” in *Encyclopedia of Materials: Science and Technology*, K. H. J. Buschow, R. W. Cahn, M. C. Flemings, B. Ilschner, E. J. Kramer, S. Mahajan, and P. Veyssière, Eds., Oxford: Elsevier, 2001, pp. 1–7. doi: 10.1016/B0-08-043152-6/00190-X.
[157] S. Tanuma, H. Yoshikawa, H. Shinotsuka, and R. Ueda, “Calculations of mean escape depths of photoelectrons in elemental solids excited by linearly polarized X-rays for high-energy photoelectron spectroscopy,” *J. Electron Spectrosc. Relat. Phenom.*, vol. 190, pp. 127–136, Oct. 2013, doi: 10.1016/j.elspec.2013.08.011.
[158] T. E. Everhart and R. F. M. Thornley, “Wide-band detector for micro-microampere low-energy electron currents,” *J. Sci. Instrum.*, vol. 37, no. 7, pp. 246–248, Jul. 1960, doi: 10.1088/0950-7671/37/7/307.
[159] K.-R. Peters, “Generation, Collection and Properties of an SE-I Enriched Signal Suitable for High Resolution SEM on Bulk Specimens,” *Scan. Electron Microsc.*, vol. 1982, no. 1, Jan. 1982, [Online]. Available: https://digitalcommons.usu.edu/electron/vol1982/iss1/31
[160] D. C. Joy, C. S. Joy, and R. D. Bunn, “Measuring the performance of scanning electron microscope detectors,” *Scanning*, vol. 18, no. 8, pp. 533–538, Nov. 1996, doi: 10.1002/sca.4950180802.
[161] D. C. Joy and D. E. Newbury, “Advanced SEM imaging,” in *The 1998 international conference on characterization and metrology for ULSI technology*, Gaithersburg, Maryland (USA): ASCE, 1998, pp. 653–666. doi: 10.1063/1.56851.
[162] J. Ludwick, G. Tripathi, M. Cahay, S. B. Fairchild, P. T. Murray, and T. C. Back, “A new fit to secondary emission yield in the low impact voltage regime: An improvement of Vaughan’s expression,” *AIP Adv.*, vol. 8, no. 8, p. 085017, Aug. 2018, doi: 10.1063/1.5031006.
[163] S. Kitamura and M. Iwatsuki, “High-resolution imaging of contact potential difference with ultrahigh vacuum noncontact atomic force microscope,” *Appl. Phys. Lett.*, vol. 72, no. 24, pp. 3154–3156, Jun. 1998, doi: 10.1063/1.121577.
[164] B. J. Griffin, “A comparison of conventional Everhart-Thornley style and in-lens secondary electron detectors-a further variable in scanning electron microscopy,” *Scanning*, vol. 33, no. 3, pp. 162–173, May 2011, doi: 10.1002/sca.20255.
[165] K. Kumagai, T. Sekiguchi, K. Fukuda, and T. Sasaki, “Secondary Electron Imaging of Monolayer Titania Nanosheets,” *Appl. Phys. Express*, vol. 2, no. 10, p. 105504, Oct. 2009, doi: 10.1143/APEX.2.105504.
[166] B. Griffin, D. Joy, and J. Michael, “Characteristics of Secondary Electron Images From In-lens and Conventional Everhart-Thornley Detectors - Evidence for the Energy-based Differentiation of High Resolution SE1 and Delocalized SE2 Signals,” *Microsc. Microanal.*, vol. 15, no. S2, pp. 46–47, Jul. 2009, doi: 10.1017/S1431927609097384.
[167] K. Kumagai and T. Sekiguchi, “Sharing of secondary electrons by in-lens and out-lens detector in low-voltage scanning electron microscope equipped with immersion lens,” *Ultramicroscopy*, vol. 109, no. 4, pp. 368–372, Mar. 2009, doi: 10.1016/j.ultramic.2009.01.005.
[168] I. Volotsenko *et al.*, “Secondary electron doping contrast: Theory based on scanning electron microscope and Kelvin probe force microscopy measurements,” *J. Appl. Phys.*, vol. 107, no. 1, p. 014510, Jan. 2010, doi: 10.1063/1.3276090.
[169] A. Howie, “Recent developments in secondary electron imaging,” *J. Microsc.*, vol. 180, no. 3, pp. 192–203, Dec. 1995, doi: 10.1111/j.1365-2818.1995.tb03678.x.

[170] S. L. Elliott, R. F. Broom, and C. J. Humphreys, “Dopant profiling with the scanning electron microscope—A study of Si,” *J. Appl. Phys.*, vol. 91, no. 11, Art. no. 11, May 2002, doi: 10.1063/1.1476968.
[171] L. Frank, M. Hovorka, M. M. El-Gomati, I. Müllerová, F. Mika, and E. Mikmeková, “Acquisition of the dopant contrast in semiconductors with slow electrons,” *J. Electron Spectrosc. Relat. Phenom.*, vol. 241, p. 146836, May 2020, doi: 10.1016/j.elspec.2019.03.004.
[172] D. Venables and D. M. Maher, “Quantitative two-dimensional dopant profiles obtained directly from secondary electron images,” *J. Vac. Sci. Technol. B Microelectron. Nanometer Struct. Process. Meas. Phenom.*, vol. 14, no. 1, pp. 421–425, Jan. 1996, doi: 10.1116/1.588486.
[173] M. R. Castell, D. A. Muller, and P. M. Voyles, “Dopant mapping for the nanotechnology age,” *Nat. Mater.*, vol. 2, no. 3, Art. no. 3, Mar. 2003, doi: 10.1038/nmat840.
[174] A. Howie, “Recent developments in secondary electron imaging,” *J. Microsc.*, vol. 180, no. 3, pp. 192–203, 1995.
[175] G. S. Plows and W. C. Nixon, “Stroboscopic scanning electron microscopy,” *J. Phys. [E]*, vol. 1, no. 6, pp. 595–600, Jun. 1968, doi: 10.1088/0022-3735/1/6/302.
[176] C. P. Sealy, M. R. Castell, and P. R. Wilshaw, “Mechanism for secondary electron dopant contrast in the SEM,” *J. Electron Microsc. (Tokyo)*, vol. 49, no. 2, pp. 311–321, Jan. 2000, doi: 10.1093/oxfordjournals.jmicro.a023811.
[177] S. L. Elliott, R. F. Broom, and C. J. Humphreys, “Dopant profiling with the scanning electron microscope—A study of Si,” *J. Appl. Phys.*, vol. 91, no. 11, pp. 9116–9122, Jun. 2002, doi: 10.1063/1.1476968.
[178] M. M. El-Gomati and T. C. R. Wells, “Imaging doped regions in a semiconductor with very low energy SEM and Auger electrons.,” *ELECTRON Microsc. Anal. 2001*, no. 168, pp. 489–492, 2001.
[179] M. El-Gomati, F. Zaggout, H. Jayacody, S. Tear, and K. Wilson, “Why is it possible to detect doped regions of semiconductors in low voltage SEM: a review and update,” *Surf. Interface Anal.*, vol. 37, no. 11, pp. 901–911, 2005, doi: 10.1002/sia.2108.
[180] A. K. W. Chee, R. F. Broom, C. J. Humphreys, and E. G. T. Bosch, “A quantitative model for doping contrast in the scanning electron microscope using calculated potential distributions and Monte Carlo simulations,” *J. Appl. Phys.*, vol. 109, no. 1, p. 013109, Jan. 2011, doi: 10.1063/1.3524186.
[181] I. Zhebova, M. Molotskii, Z. Barkay, G. Meshulam, E. Grunbaum, and Y. Rosenwaks, “HRSEM Secondary Electron Doping Contrast: Theory based on Band Bending and Electron Affinity Measurements,” in *EMC 2008 14th European Microscopy Congress 1–5 September 2008, Aachen, Germany*, M. Luysberg, K. Tillmann, and T. Weirich, Eds., Springer Berlin Heidelberg, 2008, pp. 639–640. doi: 10.1007/978-3-540-85156-1_320.
[182] L. Reimer and C. Tollkamp, “Measuring the backscattering coefficient and secondary electron yield inside a scanning electron microscope,” *Scanning*, vol. 3, no. 1, pp. 35–39, 1980, doi: 10.1002/sca.4950030105.
[183] P. B. Vose, “CHAPTER 4 - Detection Systems and Instrumentation,” in *Introduction to Nuclear Techniques in Agronomy and Plant Biology*, P. B. Vose, Ed., in Pergamon International Library of Science, Technology, Engineering and Social Studies. Pergamon, 1980, pp. 46–76. doi: 10.1016/B978-0-08-024924-7.50011-9.
[184] R. Jenkins and J. L. de Vries, *Practical X-ray Spectrometry*. Macmillan International Higher Education, 1970.
[185] A. M. Ilyin, “Chapter 11 - Auger Electron Spectroscopy,” in *Microscopy Methods in Nanomaterials Characterization*, S. Thomas, R. Thomas, A. K. Zachariah, and R. K. Mishra, Eds., in Micro and Nano Technologies. Elsevier, 2017, pp. 363–381. doi: 10.1016/B978-0-323-46141-2.00011-0.

[186] A. J. V. Griffiths and T. Walther, “Quantification of carbon contamination under electron beam irradiation in a scanning transmission electron microscope and its suppression by plasma cleaning,” *J. Phys. Conf. Ser.*, vol. 241, no. 1, p. 012017, Jul. 2010, doi: 10.1088/1742-6596/241/1/012017.
[187] C. M. Demanet and M. A. Marais, “A multilayer model for GaAs oxides formed at room temperature in air as deduced from an XPS analysis,” *Surf. Interface Anal.*, vol. 7, no. 1, pp. 13–16, 1985, doi: 10.1002/sia.740070104.
[188] R. Waser, *Nanoelectronics and Information Technology: Advanced Electronic Materials and Novel Devices*. John Wiley & Sons, 2012.
[189] P. Schmuki, G. I. Sproule, J. A. Bardwell, Z. H. Lu, and M. J. Graham, “Thin anodic oxides formed on GaAs in aqueous solutions,” *J. Appl. Phys.*, vol. 79, no. 9, pp. 7303–7311, May 1996, doi: 10.1063/1.361524.
[190] H.-H. Wang, J.-Y. Wu, Y.-H. Wang, and M.-P. Houng, “Effects of pH Values on the Kinetics of Liquid-Phase Chemical-Enhanced Oxidation of GaAs,” *J. Electrochem. Soc.*, vol. 146, no. 6, p. 2328, Jun. 1999, doi: 10.1149/1.1391935.
[191] H.-Y. Lee, “Growth of GaAs Oxide Layer Using Photoelectrochemical Method,” *J. Electrochem. Soc.*, vol. 155, no. 7, p. G141, May 2008, doi: 10.1149/1.2907751.
[192] H.-Y. Lee and Y.-F. Lin, “GaAs metal-oxide-semiconductor devices with a complex gate oxide composed of SiO$\less$sub$\greater$2$\less$/sub$\greater$and GaAs oxide grown using a photoelectrochemical oxidation method,” *Semicond. Sci. Technol.*, vol. 25, no. 1, p. 015005, Dec. 2009, doi: 10.1088/0268-1242/25/1/015005.
[193] H. Sharma, K. Moumanis, and J. J. Dubowski, “pH-Dependent Photocorrosion of GaAs/AlGaAs Quantum Well Microstructures,” *J. Phys. Chem. C*, vol. 120, no. 45, pp. 26129–26137, 2016, doi: 10.1021/acs.jpcc.6b08844.
[194] A. Pakes *et al.*, “Composition and growth of anodic and thermal oxides on InP and GaAs,” *Surf. Interface Anal.*, vol. 34, no. 1, pp. 481–484, 2002, doi: 10.1002/sia.1343.
[195] F. Gucmann *et al.*, “III-As heterostructure field-effect transistors with recessed ex-situ gate oxide by O2 plasma-oxidized GaAs cap,” *J. Vac. Sci. Technol. B*, vol. 33, no. 1, p. 01A111, Jan. 2015, doi: 10.1116/1.4905938.
[196] D. A. Allwood, R. T. Carline, N. J. Mason, C. Pickering, B. K. Tanner, and P. J. Walker, “Characterization of oxide layers on GaAs substrates,” *Thin Solid Films*, vol. 364, no. 1, pp. 33–39, Mar. 2000, doi: 10.1016/S0040-6090(99)00959-1.
[197] T. Walther, C. J. Humphreys, M. P. Grimshaw, and A. C. Churchill, “Detection of random alloy fluctuations in high-resolution transmission electron micrographs of AlGaAs,” *Philos. Mag. A*, vol. 72, no. 4, pp. 1015–1030, Oct. 1995, doi: 10.1080/01418619508239950.
[198] H. E. Maes, “Microscopy of Semiconducting Materials 1995. Proceedings of the Institute of Physics Conference held at Oxford University, 20 - 23 March 1995,” *Semicond. Sci. Technol.*, vol. 11, no. 7, p. 1131, Jul. 1996, doi: 10.1088/0268-1242/11/7/027.
[199] M. A. E. Jepson, K. Khan, T. J. Hayward, B. J. Inkson, and C. Rodenburg, “The effect of oxidation and carbon contamination on SEM dopant contrast,” *J. Phys. Conf. Ser.*, vol. 241, p. 012078, Jul. 2010, doi: 10.1088/1742-6596/241/1/012078.
[200] S. I. Raider, R. Flitsch, and M. J. Palmer, “Oxide Growth on Etched Silicon in Air at Room Temperature,” *J. Electrochem. Soc.*, vol. 122, no. 3, p. 413, Mar. 1975, doi: 10.1149/1.2134225.
[201] X. Zou *et al.*, “Carrier Recombination Processes in GaAs Wafers Passivated by Wet Nitridation,” *ACS Appl. Mater. Interfaces*, vol. 12, no. 25, pp. 28360–28367, Jun. 2020, doi: 10.1021/acsami.0c04892.
[202] G. Binnig, H. Rohrer, Ch. Gerber, and E. Weibel, “Tunneling through a controllable vacuum gap,” *Appl. Phys. Lett.*, vol. 40, no. 2, pp. 178–180, Jan. 1982, doi: 10.1063/1.92999.
[203] G. Binnig and H. Rohrer, “SCANNING TUNNELING MICROSCOPY,” p. 9.

[204] Y. Hasegawa, J. F. Jia, K. Inoue, A. Sakai, and T. Sakurai, “Elemental contrast of local work function studied by scanning tunneling microscopy,” *Surf. Sci.*, vol. 386, no. 1, pp. 328–334, Oct. 1997, doi: 10.1016/S0039-6028(97)00332-4.
[205] J. Tersoff and D. R. Hamann, “Theory of the scanning tunneling microscope,” *Phys. Rev. B*, vol. 31, no. 2, pp. 805–813, Jan. 1985, doi: 10.1103/PhysRevB.31.805.
[206] J. Bardeen, “Tunnelling from a Many-Particle Point of View,” *Phys. Rev. Lett.*, vol. 6, no. 2, pp. 57–59, Jan. 1961, doi: 10.1103/PhysRevLett.6.57.
[207] M. Nonnenmacher, M. P. O’Boyle, and H. K. Wickramasinghe, “Kelvin probe force microscopy,” *Appl. Phys. Lett.*, vol. 58, no. 25, pp. 2921–2923, Jun. 1991, doi: 10.1063/1.105227.
[208] M. Nonnenmacher, M. P. O’Boyle, and H. K. Wickramasinghe, “Kelvin probe force microscopy,” p. 4.
[209] C. Manfredotti, “Imaging at the Nanoscale,” in *Characterization of Semiconductor Heterostructures and Nanostructures*, Elsevier, 2013, pp. 467–507. doi: 10.1016/B978-0-444-59551-5.00011-X.
[210] G. Binnig, C. F. Quate, and Ch. Gerber, “Atomic Force Microscope,” *Phys. Rev. Lett.*, vol. 56, no. 9, pp. 930–933, Mar. 1986, doi: 10.1103/PhysRevLett.56.930.
[211] F. J. Giessibl, “High-speed force sensor for force microscopy and profilometry utilizing a quartz tuning fork,” *Appl. Phys. Lett.*, vol. 73, no. 26, pp. 3956–3958, Dec. 1998, doi: 10.1063/1.122948.
[212] S. Nishida, D. Kobayashi, T. Sakurada, T. Nakazawa, Y. Hoshi, and H. Kawakatsu, “Photothermal excitation and laser Doppler velocimetry of higher cantilever vibration modes for dynamic atomic force microscopy in liquid,” *Rev. Sci. Instrum.*, vol. 79, no. 12, p. 123703, Dec. 2008, doi: 10.1063/1.3040500.
[213] T. Göddenhenrich, H. Lemke, U. Hartmann, and C. Heiden, “Force microscope with capacitive displacement detection,” *J. Vac. Sci. Technol. Vac. Surf. Films*, vol. 8, pp. 383–387, Jan. 1990, doi: 10.1116/1.576401.
[214] F. J. Giessibl and B. M. Trafas, “Piezoresistive cantilevers utilized for scanning tunneling and scanning force microscope in ultrahigh vacuum,” *Rev. Sci. Instrum.*, vol. 65, no. 6, pp. 1923–1929, Jun. 1994, doi: 10.1063/1.1145232.
[215] N. Mullin and J. K. Hobbs, “A non-contact, thermal noise based method for the calibration of lateral deflection sensitivity in atomic force microscopy,” *Rev. Sci. Instrum.*, vol. 85, no. 11, p. 113703, Nov. 2014, doi: 10.1063/1.4901221.
[216] F. J. Giessibl, “Advances in atomic force microscopy,” *Rev. Mod. Phys.*, vol. 75, no. 3, pp. 949–983, Jul. 2003, doi: 10.1103/RevModPhys.75.949.
[217] Y. Martin and H. K. Wickramasinghe, “Magnetic imaging by ‘“force microscopy”’ with 1000 Å resolution,” *Appl. Phys. Lett.*, vol. 50, no. 20, pp. 1455–1457, May 1987, doi: 10.1063/1.97800.
[218] Y. Martin, D. Abraham, and K. Wickramasinghe, “High-Resolution Capacitance Measurement and Potentiometry by Force Microscopy,” *Appl. Phys. Lett.*, vol. 52, pp. 1103–1105, Apr. 1988, doi: 10.1063/1.99224.
[219] Y. Taur and T. H. Ning, *Fundamentals of Modern VLSI Devices:*, 2nd ed. Cambridge University Press, 2009. doi: 10.1017/CBO9781139195065.
[220] M. E. Levinshteĭn, S. L. Rumyantsev, and M. Shur, Eds., *Handbook series on semiconductor parameters*. Singapore ; New Jersey: World Scientific, 1996.
[221] R. Jia, M. Zhang, L. Zhang, W. Zhang, and F. Guo, “Correlative change of corrosion behavior with the microstructure of AZ91 Mg alloy modified with Y additions,” *J. Alloys Compd.*, vol. 634, pp. 263–271, Jun. 2015, doi: 10.1016/j.jallcom.2015.02.019.
[222] K. Okamoto, K. Yoshimoto, Y. Sugawara, and S. Morita, “KPFM imaging of Si(1 1 1)53×53-Sb surface for atom distinction using NC-AFM,” *Appl. Surf. Sci.*, vol. 210, no. 1, pp. 128–133, Mar. 2003, doi: 10.1016/S0169-4332(02)01492-7.

[223] S. Watanabe *et al.*, “In Situ KPFM Imaging of Local Photovoltaic Characteristics of Structured Organic Photovoltaic Devices,” *ACS Appl. Mater. Interfaces*, vol. 6, no. 3, pp. 1481–1487, Feb. 2014, doi: 10.1021/am4038992.
[224] R. A. Oliver, “Advances in AFM for the electrical characterization of semiconductors,” *Rep. Prog. Phys.*, vol. 71, no. 7, p. 076501, Jun. 2008, doi: 10.1088/0034-4885/71/7/076501.
[225] A. K. Henning *et al.*, “Two-dimensional surface dopant profiling in silicon using scanning Kelvin probe microscopy,” *J. Appl. Phys.*, vol. 77, no. 5, pp. 1888–1896, Mar. 1995, doi: 10.1063/1.358819.
[226] M. Tanimoto and O. Vatel, “Kelvin probe force microscopy for characterization of semiconductor devices and processes,” *J. Vac. Sci. Technol. B Microelectron. Nanometer Struct. Process. Meas. Phenom.*, vol. 14, no. 2, pp. 1547–1551, Mar. 1996, doi: 10.1116/1.589136.
[227] Th. Glatzel, S. Sadewasser, R. Shikler, Y. Rosenwaks, and M. Ch. Lux-Steiner, “Kelvin probe force microscopy on III–V semiconductors: the effect of surface defects on the local work function,” *Mater. Sci. Eng. B*, vol. 102, no. 1, pp. 138–142, Sep. 2003, doi: 10.1016/S0921-5107(03)00020-5.
[228] W. Melitz, J. Shen, A. C. Kummel, and S. Lee, “Kelvin probe force microscopy and its application,” *Surf. Sci. Rep.*, vol. 66, no. 1, pp. 1–27, Jan. 2011, doi: 10.1016/j.surfrep.2010.10.001.
[229] P. De Wolf, R. Stephenson, T. Trenkler, T. Clarysse, T. Hantschel, and W. Vandervorst, “Status and review of two-dimensional carrier and dopant profiling using scanning probe microscopy,” *J. Vac. Sci. Technol. B Microelectron. Nanometer Struct. Process. Meas. Phenom.*, vol. 18, no. 1, pp. 361–368, Jan. 2000, doi: 10.1116/1.591198.
[230] J. Colchero, A. Gil, and A. M. Baró, “Resolution enhancement and improved data interpretation in electrostatic force microscopy,” *Phys. Rev. B*, vol. 64, no. 24, p. 245403, Nov. 2001, doi: 10.1103/PhysRevB.64.245403.
[231] J. Murawski, T. Graupner, P. Milde, R. Raupach, U. Zerweck-Trogisch, and L. M. Eng, “Pump-probe Kelvin-probe force microscopy: Principle of operation and resolution limits,” *J. Appl. Phys.*, vol. 118, no. 15, p. 154302, Oct. 2015, doi: 10.1063/1.4933289.
[232] H. Lüth, *Solid Surfaces, Interfaces and Thin Films*, 6th ed. in Graduate Texts in Physics. Springer International Publishing, 2015. doi: 10.1007/978-3-319-10756-1.
[233] S. Sadewasser, C. Leendertz, F. Streicher, and M. C. Lux-Steiner, “The influence of surface topography on Kelvin probe force microscopy,” *Nanotechnology*, vol. 20, no. 50, p. 505503, Nov. 2009, doi: 10.1088/0957-4484/20/50/505503.
[234] W. Mönch and N. J. Dinardo, “Semiconductor Surfaces and Interfaces”.
[235] M. A. Berding, S. Krishnamurthy, A. Sher, and A. -B. Chen, “Cleavage energies in semiconductors,” *J. Appl. Phys.*, vol. 67, no. 10, pp. 6175–6178, May 1990, doi: 10.1063/1.345181.
[236] J. Chen, F. Ding, X. Luo, X. Rao, and J. Sun, “Fundamental study of ductile-regime diamond turning of single crystal gallium arsenide,” *Precis. Eng.*, vol. 62, pp. 71–82, Mar. 2020, doi: 10.1016/j.precisioneng.2019.11.010.
[237] J. E. Ayers, *Heteroepitaxy of Semiconductors: Theory, Growth, and Characterization*. Boca Raton: CRC Press, 2018. doi: 10.1201/9781315221915.
[238] R. Pérez and P. Gumbsch, “Directional Anisotropy in the Cleavage Fracture of Silicon,” *Phys. Rev. Lett.*, vol. 84, no. 23, pp. 5347–5350, Jun. 2000, doi: 10.1103/PhysRevLett.84.5347.
[239] W. Lei, A. Kumar, and R. Yalamanchili, “Die singulation technologies for advanced packaging: A critical review,” *J. Vac. Sci. Technol. B Microelectron. Nanometer Struct.*, vol. 30, pp. 040801–1~040801, Jul. 2012, doi: 10.1116/1.3700230.
[240] L. A. Giannuzzi, R. Geurts, and J. Ringnalda, “2 keV Ga+ FIB Milling for Reducing Amorphous Damage in Silicon,” *Microsc. Microanal.*, vol. 11, no. S02, Aug. 2005, doi: 10.1017/S1431927605507797.

[241] J. F. Ziegler, M. D. Ziegler, and J. P. Biersack, “SRIM - The stopping and range of ions in matter (2010),” *Nucl. Instrum. Methods Phys. Res. B*, vol. 268, no. 11–12, pp. 1818–1823, Jun. 2010, doi: 10.1016/j.nimb.2010.02.091.
[242] Y. Kudriavtsev, A. Villegas, A. Godines, and R. Asomoza, “Calculation of the surface binding energy for ion sputtered particles,” *Appl. Surf. Sci.*, vol. 239, no. 3, pp. 273–278, Jan. 2005, doi: 10.1016/j.apsusc.2004.06.014.
[243] H. L. Bay and J. Bohdansky, “Sputtering yields for light ions as a function of angle of incidence,” *Appl. Phys.*, vol. 19, no. 4, pp. 421–426, Aug. 1979, doi: 10.1007/BF00930106.
[244] O. S. Oen and M. T. Robinson, “Computer studies of the reflection of light ions from solids,” *Nucl. Instrum. Methods*, vol. 132, pp. 647–653, Jan. 1976, doi: 10.1016/0029-554X(76)90806-5.
[245] K. F. Galloway and P. Roitman, “Some aspects of using a scanning electron microscope for total dose testing,” National Bureau of Standards, Gaithersburg, MD, NBS IR 77-1235, 1977. doi: 10.6028/NBS.IR.77-1235.
[246] “HITACHI TM3030 PLUS INSTRUCTION MANUAL,” *ManualsLib*. https://www.manualslib.com/manual/1338510/Hitachi-Tm3030-Plus.html (accessed Oct. 07, 2022).
[247] “Sigma.” https://www.zeiss.com/microscopy/en/products/sem-fib-sem/sem/sigma.html (accessed Apr. 19, 2023).
[248] “NSM Archive - Physical Properties of Semiconductors.” http://www.ioffe.ru/SVA/NSM/Semicond/ (accessed Sep. 05, 2022).
[249] M. D. McCluskey and E. E. Haller, *Dopants and Defects in Semiconductors*, 1st edition. Boca Raton, FL: CRC Press, 2012.
[250] J. E. Greene, “Quantitative Electrical Measurements with Atomic Force Microscopy,” *Microsc. Today*, vol. 23, no. 6, pp. 32–37, Nov. 2015, doi: 10.1017/S1551929515000991.
[251] M. P. Murrell *et al.*, “Spatially resolved electrical measurements of SiO2 gate oxides using atomic force microscopy,” *Appl. Phys. Lett.*, vol. 62, no. 7, pp. 786–788, Feb. 1993, doi: 10.1063/1.108579.
[252] F. Houzé, R. Meyer, O. Schneegans, and L. Boyer, “Response to ‘Comment on “Imaging the local electrical properties of metal surfaces by atomic force microscopy with conducting probes” ’ [Appl. Phys. Lett. **70** , 3618 (1996)],” *Appl. Phys. Lett.*, vol. 70, no. 26, pp. 3619–3619, Jun. 1997, doi: 10.1063/1.119257.
[253] P. Narchi, “Investigation of crystalline silicon solar cells at the nano-scale using scanning probe microscopy techniques,” 2016.
[254] C. Renard *et al.*, “High current density GaAs/Si rectifying heterojunction by defect free Epitaxial Lateral overgrowth on Tunnel Oxide from nano-seed,” *Sci. Rep.*, vol. 6, no. 1, p. 25328, May 2016, doi: 10.1038/srep25328.
[255] Y. Calahorra, W. Kim, J. Vukajlovic-Plestina, A. F. i Morral, and S. Kar-Narayan, “Time-resolved open-circuit conductive atomic force microscopy for direct electromechanical characterisation,” *Nanotechnology*, vol. 31, no. 40, p. 404003, Jul. 2020, doi: 10.1088/1361-6528/ab9b4b.
[256] R. Muenstermann *et al.*, “Correlation between growth kinetics and nanoscale resistive switching properties of SrTiO3 thin films,” *J. Appl. Phys.*, vol. 108, no. 12, p. 124504, Dec. 2010, doi: 10.1063/1.3520674.
[257] A. Bayerl *et al.*, “Nanoscale and Device Level Gate Conduction Variability of High-k Dielectrics-Based Metal-Oxide-Semiconductor Structures,” *IEEE Trans. Device Mater. Reliab.*, vol. 11, no. 3, pp. 495–501, Sep. 2011, doi: 10.1109/TDMR.2011.2161087.
[258] A. Bayerl *et al.*, “Nanoscale and device level electrical behavior of annealed ALD Hf-based gate oxide stacks grown with different precursors,” *Microelectron. Reliab.*, vol. 53, no. 6, pp. 867–871, Jun. 2013, doi: 10.1016/j.microrel.2013.02.005.

[259] M. Ravier, F. Carmona, F. Houze, U. Nilsson, and A. Campus, “A new tool for investigating the electrical structure of carbon black filled polymers,” in *ICSD’01. Proceedings of the 20001 IEEE 7th International Conference on Solid Dielectrics (Cat. No.01CH37117)*, Jun. 2001, pp. 361–364. doi: 10.1109/ICSD.2001.955656.
[260] T. G. Ruskell, R. K. Workman, D. Chen, D. Sarid, S. Dahl, and S. Gilbert, “High resolution Fowler-Nordheim field emission maps of thin silicon oxide layers,” *Appl. Phys. Lett.*, vol. 68, no. 1, pp. 93–95, Jan. 1996, doi: 10.1063/1.116782.
[261] C. Rodenbücher *et al.*, “Local surface conductivity of transition metal oxides mapped with true atomic resolution,” *Nanoscale*, vol. 10, no. 24, pp. 11498–11505, Jun. 2018, doi: 10.1039/C8NR02562B.
[262] C. Pan, Y. Shi, F. Hui, E. Grustan-Gutierrez, and M. Lanza, “History and Status of the CAFM,” p. 28.
[263] Fei Hui *et al.*, “Graphene Coated Nanoprobes: A Review,” *Crystals*, vol. 7, no. 9, p. 269, Sep. 2017, doi: 10.3390/cryst7090269.
[264] R. Shimizu, “Secondary electron yield with primary electron beam of kilo-electron-volts,” *J. Appl. Phys.*, vol. 45, no. 5, pp. 2107–2111, May 1974, doi: 10.1063/1.1663552.
[265] J. E. Cunningham, K. W. Goossen, and T. H. Chiu, “Dimerization induced Be segregation in GaAs,” p. 4.
[266] V. Drexel, E. Weimer, and J.-P. Martin, “Ultra-high resolution column for the scanning electron microscope,” *Proc. Annu. Meet. Electron Microsc. Soc. Am.*, vol. 52, pp. 486–487, Jan. 1994, doi: 10.1017/S0424820100170165.
[267] P. Gnauck, P. Hoffrogge, and J. Greiser, “A New CrossBeam® Inspection Tool Combining an Ultrahigh Resolution Field emission SEM and a High Resolution FIB,” *Proc SPIE*, vol. 4689, Jul. 2002, doi: 10.1117/12.473530.
[268] M. Al-Khashab and N. Sadie, “The Electron Optical Performance of the Gemini Lens Design for Low Voltage Scanning Electron Microscope,” vol. 38, pp. 52–60, Dec. 2010.
[269] A. Recknagel, “Theorie des elektrischen Elektronenmikroskops fQr Selbststrahler.,” p. 20.
[270] *The Growth of Electron Microscopy*. Academic Press, 1996.
[271] J. Jiruše, M. Havelka, and F. Lopour, “Novel field emission SEM column with beam deceleration technology,” *Ultramicroscopy*, vol. 146, pp. 27–32, Nov. 2014, doi: 10.1016/j.ultramic.2014.05.006.
[272] Š. Mikmeková, H. Nakamichi, and M. Nagoshi, “Contrast of positively charged oxide precipitate in out-lens, in-lens and in-column SE image,” *Microscopy*, vol. 67, no. 1, pp. 11–17, Feb. 2018, doi: 10.1093/jmicro/dfx117.
[273] R. F. Egerton, *Electron Energy-Loss Spectroscopy in the Electron Microscope*. Springer Science & Business Media, 2011.
[274] D. Wang, Y. Cai, Y. He, Y. Xu, and Q. Jia, “Electron emission properties of silver oxide and its impact on the secondary emission yield of air-exposed silver,” *Results Phys.*, vol. 33, p. 105231, Feb. 2022, doi: 10.1016/j.rinp.2022.105231.
[275] C. S. Fuller and H. W. Allison, “A Polishing Etchant for III–V Semiconductors,” *J. Electrochem. Soc.*, vol. 109, no. 9, p. 880, Sep. 1962, doi: 10.1149/1.2425576.
[276] D. A. Allwood, R. T. Carline, N. Mason, B. K. Tanner, and P. J. Walker, “Characterization of oxide layers on GaAs substrates,” *Thin Solid Films*, vol. 364, pp. 33–39, Mar. 2000, doi: 10.1016/S0040-6090(99)00959-1.
[277] M. L. Reed and G. K. Fedder, “2 - Photolithographic Microfabrication,” in *Handbook of Sensors and Actuators*, T. Fukuda and W. Menz, Eds., in Micro Mechanical Systems, vol. 6. Elsevier Science B.V., 1998, pp. 13–61. doi: 10.1016/S1386-2766(98)80003-0.
[278] Y. Tarui, Y. Komiya, and Y. Harada, “Preferential Etching and Etched Profile of GaAs,” *J. Electrochem. Soc.*, vol. 118, no. 1, p. 118, Jan. 1971, doi: 10.1149/1.2407921.

[279] W. W. Pan *et al.*, “Defect Engineering in MBE-Grown CdTe Buffer Layers on GaAs (211)B Substrates,” *J. Electron. Mater.*, vol. 51, no. 9, pp. 4869–4883, Sep. 2022, doi: 10.1007/s11664-022-09725-1.
[280] S. E. H. Turley and P. D. Greene, “LPE growth on structured {100} InP substrates and their fabrication by preferential etching,” *J. Cryst. Growth*, vol. 58, no. 2, pp. 409–416, Jul. 1982, doi: 10.1016/0022-0248(82)90289-5.
[281] M. V. Sullivan and G. A. Kolb, “The Chemical Polishing of Gallium Arsenide in Bromine-Methanol,” *J. Electrochem. Soc.*, vol. 110, no. 6, p. 585, 1963, doi: 10.1149/1.2425820.
[282] J. G. Grabmaier and C. B. Watson, “Dislocation Etch Pits in Single Crystal GaAs,” *Phys. Status Solidi B*, vol. 32, no. 1, pp. K13–K15, 1969, doi: 10.1002/pssb.19690320155.
[283] J. L. Weyher and J. J. Kelly, “Defect-Selective Etching of Semiconductors,” in *Springer Handbook of Crystal Growth*, G. Dhanaraj, K. Byrappa, V. Prasad, and M. Dudley, Eds., in Springer Handbooks. Berlin, Heidelberg: Springer, 2010, pp. 1453–1476. doi: 10.1007/978-3-540-74761-1_43.
[284] A. S. Jordan, “An evaluation of the thermal and elastic constants affecting GaAs crystal growth,” *J. Cryst. Growth*, vol. 49, no. 4, pp. 631–642, Aug. 1980, doi: 10.1016/0022-0248(80)90287-0.
[285] E. Billig and J. J. Dowd, “p-n Junction revealed by Electrolytic Etching,” *Nature*, vol. 172, no. 4368, Art. no. 4368, Jul. 1953, doi: 10.1038/172115a0.
[286] C. Wu, “An investigation on p—n junction etch stop,” *Sens. Actuators Phys.*, vol. 35, no. 3, pp. 181–187, Feb. 1993, doi: 10.1016/0924-4247(93)80149-B.
[287] D. E. Holmes, R. T. Chen, K. R. Elliott, and C. G. Kirkpatrick, “Stoichiometry-controlled compensation in liquid encapsulated Czochralski GaAs,” *Appl. Phys. Lett.*, vol. 40, no. 1, pp. 46–48, Jan. 1982, doi: 10.1063/1.92913.
[288] L. B. Ta, H. M. Hobgood, A. Rohatgi, and R. N. Thomas, “Effects of stoichiometry on thermal stability of undoped, semi-insulating GaAs,” *J. Appl. Phys.*, vol. 53, no. 8, pp. 5771–5775, Aug. 1982, doi: 10.1063/1.331412.
[289] A. G. Cullis, P. D. Augustus, and D. J. Stirland, “Arsenic precipitation at dislocations in GaAs substrate material,” *J. Appl. Phys.*, vol. 51, no. 5, p. 2556, 1980, doi: 10.1063/1.327979.
[290] M. M. Carrabba, N. M. Nguyen, and R. D. Rauh, “Effects of Doping and Orientation on Photoelectrochemically Etched Features in n - GaAs,” *J. Electrochem. Soc.*, vol. 134, no. 7, pp. 1855–1859, Jul. 1987, doi: 10.1149/1.2100769.
[291] C.-S. Tan and M. H. Huang, “Density Functional Theory Calculations Revealing Metal-like Band Structures and Work Function Variation for Ultrathin Gallium Arsenide (111) Surface Layers,” *Chem. – Asian J.*, vol. 14, no. 13, pp. 2316–2321, 2019, doi: 10.1002/asia.201900597.
[292] “LEED, Auger, and work function studies of clean and Na-covered surfaces of GaAs,” *Surf. Sci.*, vol. 25, no. 2, pp. 305–314, Apr. 1971, doi: 10.1016/0039-6028(71)90251-2.
[293] H. Matsunami, “Chemical Vapor Epitaxy of Silicon Carbide,” in *Encyclopedia of Materials: Science and Technology*, K. H. J. Buschow, R. W. Cahn, M. C. Flemings, B. Ilschner, E. J. Kramer, S. Mahajan, and P. Veyssière, Eds., Oxford: Elsevier, 2001, pp. 1192–1197. doi: 10.1016/B0-08-043152-6/00223-0.
[294] V. Umansky and M. Heiblum, “Chapter 6 - MBE growth of high-mobility 2DEG,” in *Molecular Beam Epitaxy*, M. Henini, Ed., Oxford: Elsevier, 2013, pp. 121–137. doi: 10.1016/B978-0-12-387839-7.00006-3.
[295] H.-J. BUTT *et al.*, “Scan speed limit in atomic force microscopy,” *J. Microsc.*, vol. 169, pp. 75–84, Aug. 2011, doi: 10.1111/j.1365-2818.1993.tb03280.x.
[296] R. V. Lapshin, “Feature-oriented scanning methodology for probe microscopy and nanotechnology,” *Nanotechnology*, vol. 15, no. 9, pp. 1135–1151, Jul. 2004, doi: 10.1088/0957-4484/15/9/006.

[297] A. Axt, I. M. Hermes, V. W. Bergmann, N. Tausendpfund, and S. A. L. Weber, “Know your full potential: Quantitative Kelvin probe force microscopy on nanoscale electrical devices,” *Beilstein J. Nanotechnol.*, vol. 9, pp. 1809–1819, Jun. 2018, doi: 10.3762/bjnano.9.172.
[298] W. Liu, W. T. Zheng, and Q. Jiang, “First-principles study of the surface energy and work function of III-V semiconductor compounds,” *Phys. Rev. B*, vol. 75, no. 23, p. 235322, Jun. 2007, doi: 10.1103/PhysRevB.75.235322.
[299] W. Chen, L. M. Walpita, C. C. Sun, and W. S. C. Chang, “Ion beam etching of InGaAs, InP, GaAs, Si, and Ge,” *J. Vac. Sci. Technol. B Microelectron. Process. Phenom.*, vol. 4, no. 3, pp. 701–705, May 1986, doi: 10.1116/1.583600.
[300] I. Shiota, N. Miyamoto, and J. Nishizawa, “Auger Analysis of Thermally Oxidized GaAs Surfaces,” *J. Electrochem. Soc.*, vol. 124, no. 9, p. 1405, Sep. 1977, doi: 10.1149/1.2133663.
[301] N. J. Kadhim, S. H. Laurie, and D. Mukherjee, “Chemical Etching of Group III - V Semiconductors,” *J. Chem. Educ.*, vol. 75, no. 7, p. 840, Jul. 1998, doi: 10.1021/ed075p840.

Appendix

Sample description

As intrinsic density n_i for GaAs used in this report is $2.1 \times 10^6\ cm^{-3}$ from Ioffe insitute[42]. The work function shifts for different doping levels are listed below:

200nm Si doped GaAs layer at doping level 9×10^{18} atoms/cm^3
200nm Si doped GaAs layer at doping level 1.2×10^{18} atoms/cm^3
200nm Si doped GaAs layer at doping level 2.14×10^{18} atoms/cm^3
300nm Si doped GaAs buffer layer at doping level 3.8×10^{17} atoms/cm^3
350µm un-doped GaAs substrate

Table 0.1: nominal structure of the n-doped GaAs wafer sample number A

200nm Be doped GaAs layer at doping level 1.6×10^{19} atoms/cm^3
200nm Be doped GaAs layer at doping level 5.6×10^{18} atoms/cm^3
200nm Be doped GaAs layer at doping level 2.8×10^{18} atoms/cm^3
500nm Be doped GaAs buffer layer at doping level 1.0×10^{18} atoms/cm^3
350µm un-doped GaAs substrate

Table 0.2: nominal structure of the p-doped GaAs wafer sample number B

p^{++} GaAs cap layer
750nm $Al_{0.33}Ga_{0.67}As$ p^+ layer
500nm undoped GaAs containing three InAs quantum dot layers
750nm $Al_{0.33}Ga_{0.67}As$ n^+ layer
GaAs n^+ substrate

Table 0.3: p-i-n structure of LED sample number VN790

layer sequence of p-doped GaAs	nominal doping level N_D(atoms/cm^3)	N_D (ppm)	work function shift from intrinsic value (eV)
Layer 3	1.6×10^{19}	355	-0.7654
Layer 2	5.6×10^{18}	124	-0.7382
Layer 1	2.8×10^{18}	62	-0.7201
buffer	1.0×10^{18}	22	-0.6934

Table 0.4 the work function shift expected for different doping levels in p-doped GaAs *sample A.*

Images acquired by Hitachi Regulus 8100

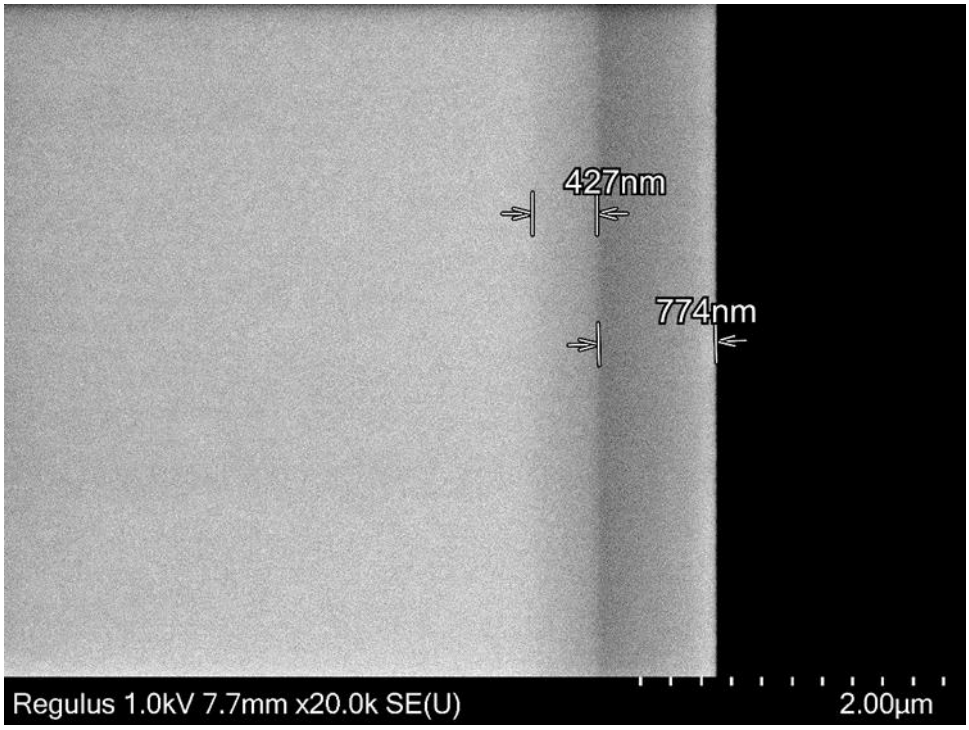

Figure 6. 1. The fresh cleaved Si-doped GaAs staircase dopant contrast by 1.0kV beam voltage at 7.7mm working distance. The magnification is 20kX, and upper in lens detector is used.

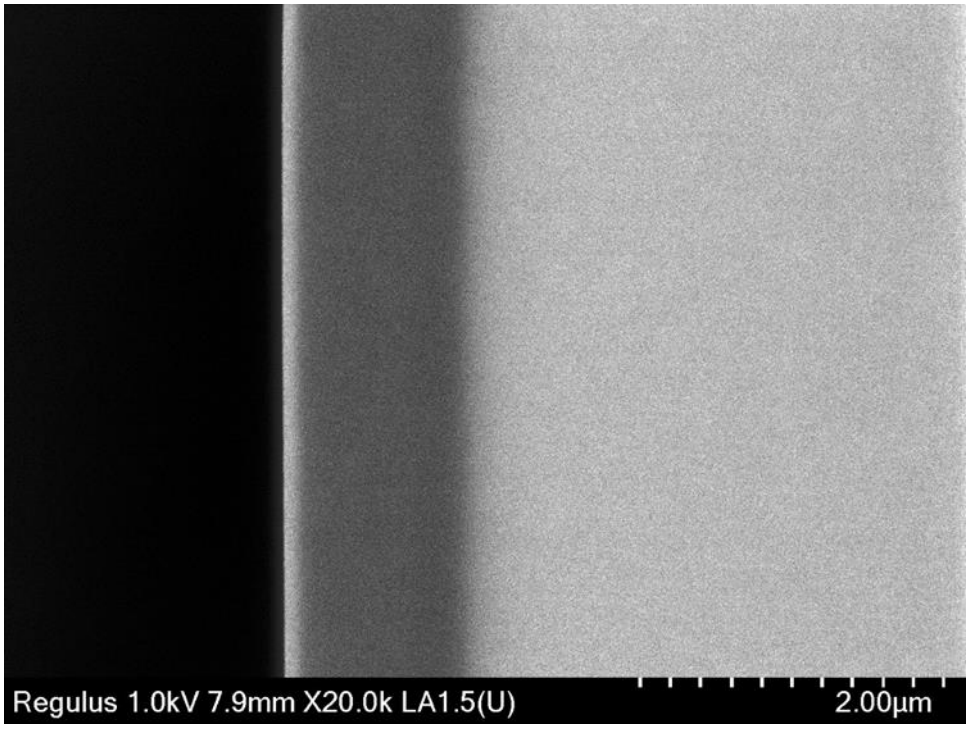

Figure 6. 2. The ion milled Si-doped GaAs staircase dopant contrast by 1.0kV beam voltage at 7.9mm working distance. The magnification is 20kX, and upper in lens detector is used. Electrode in pole piece is positively bias with 2.25V to supress SE3 to get image with SE1 and SE2. The contrast is disappeared after argon ion milling for 5 mins.

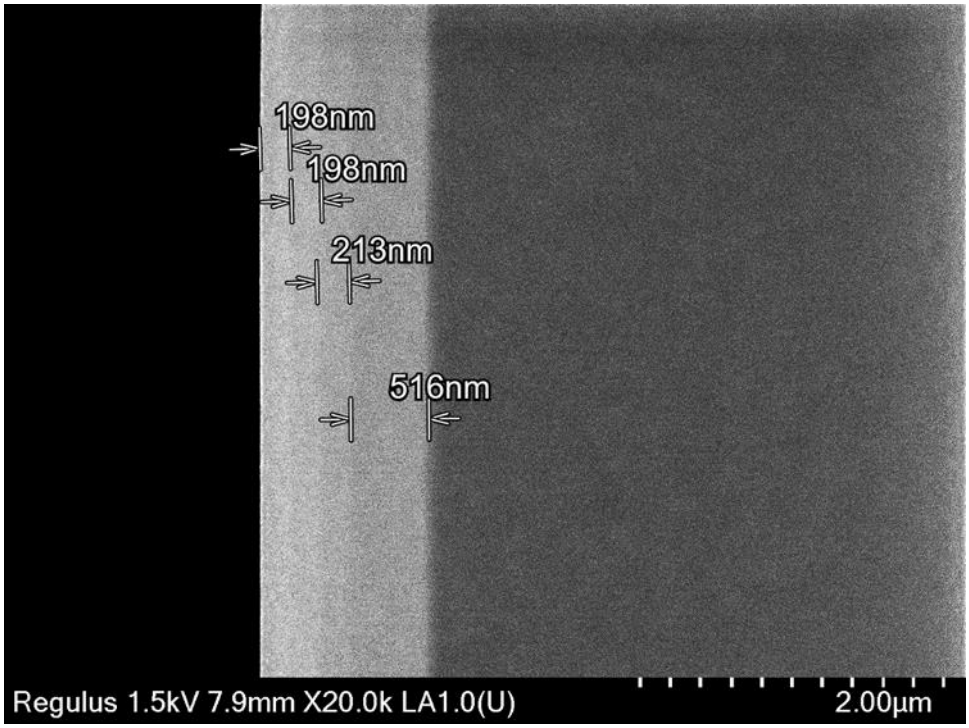

Figure 6. 3. The fresh cleaved Be-doped GaAs staircase dopant contrast by 1.5kV beam voltage at 7.9mm working distance. The magnification is 20kX, and upper in lens detector is used. 1.5V bias is applied to enhance the contrast.

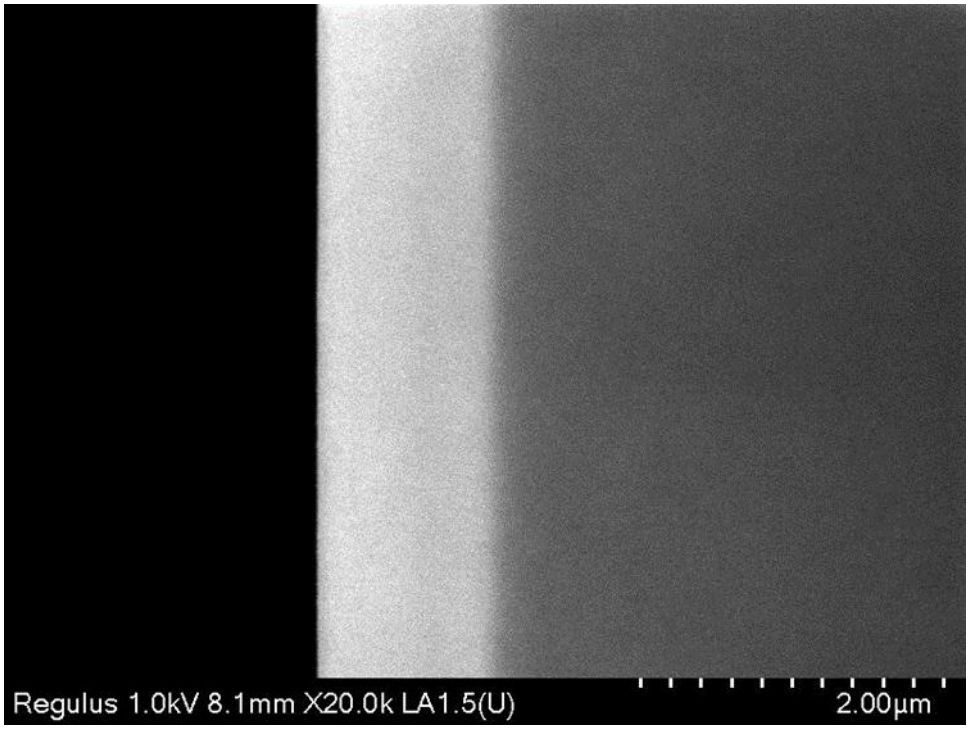

Figure 6. 4. The ion milled Be-doped GaAs staircase dopant contrast by 1.0kV beam voltage at 8.1mm working distance. The magnification is 20kX, and upper in lens detector is used. Electrode in pole piece is positively bias with 2.25V to supress SE3 to get image with SE1 and SE2. The staircase structure is not clear as Figure 6. 3 .

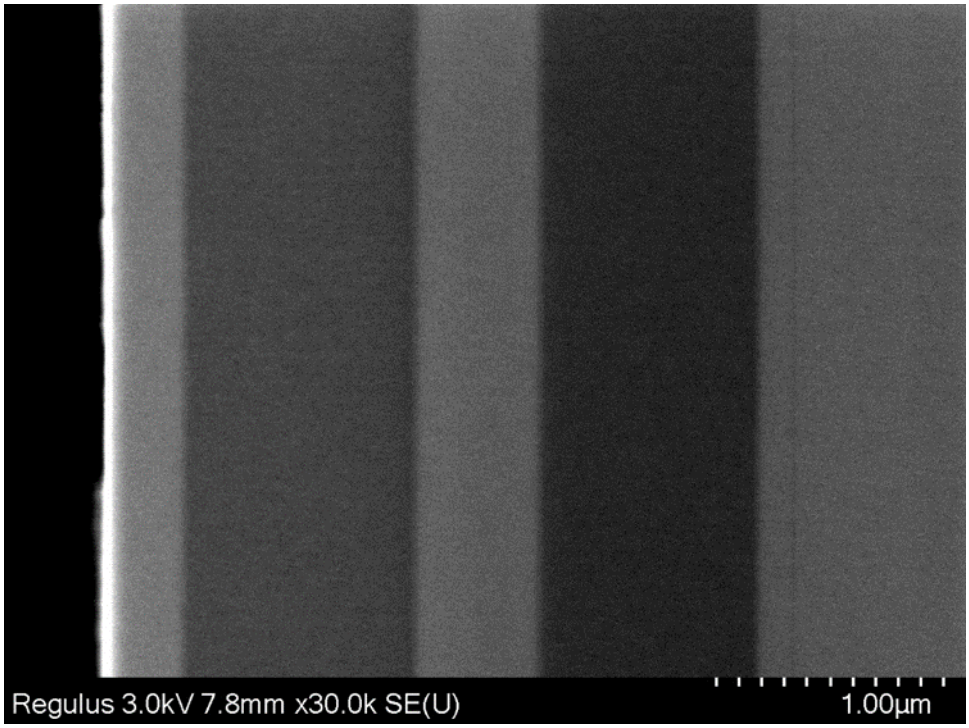

Figure 6. 5. The fresh cleaved VN790 sample imaged with 3.0kV beam voltage at 7.8mm working distance. The magnification is 30kX, and upper in lens SE detector is used. Electrode in pole piece is bias so that SE3 from low angle BSEs hitting the polo piece will be collected.

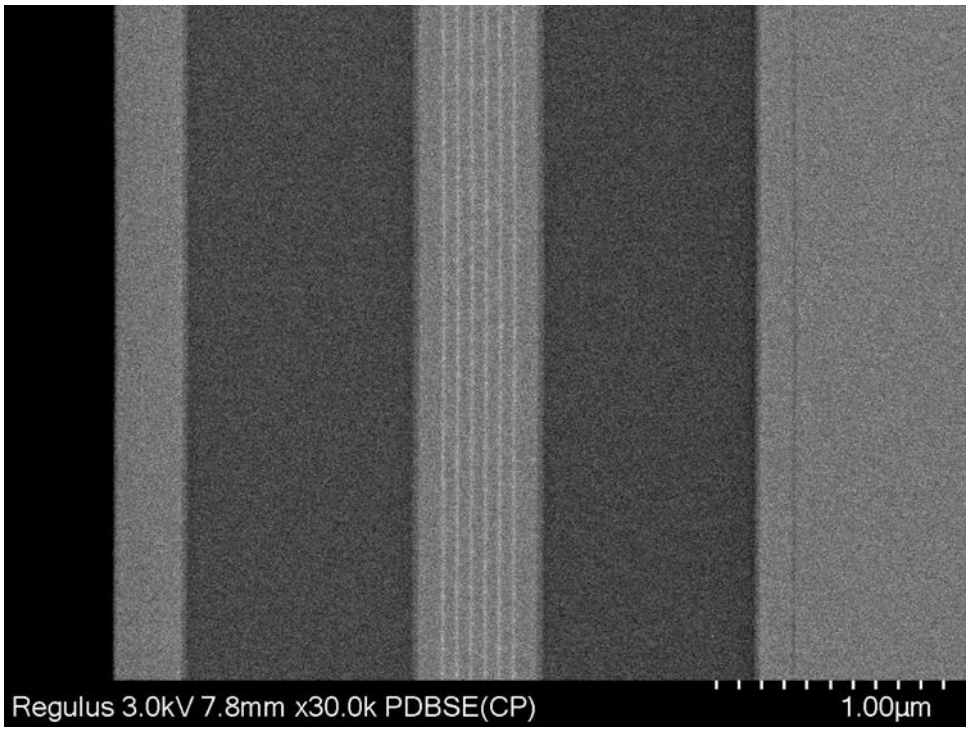

Figure 6. 6. The BSE image of the sample in Figure 6. 5. The atomic contrast is much stronger than doping contrast. The image has resolved 10nm quantum dot layer in the middle intrinsic region.